



**Politecnico
di Torino**

POLITECNICO DI TORINO
DEPARTMENT OF MECHANICAL AND AEROSPACE ENGINEERING

Master degree in Mechanical Engineering
Master thesis

Experimental and numerical analyses on a foot blade prosthetic

Supervisor

Prof. Alessandro Vigliani

Co-supervisor

Prof. Maryam GhandchiTehrani

Candidate

Claudia Barattini

April 2023

Acknowledgement

First of all I would like to thanks Professors and PhD students of DIMEAS department of Politecnico of Torino. Prof. Bonisoli believed in my capacities and in this project, supporting me even remotely, spending his weekends and evenings helping me. He taught me a lot and transmitted his passion for his work. Then, once I came back in Italy, the professional support of Prof. Vigliani, Prof. Rosso, Ing. Vella and Ing. Dimauro, was fundamental for continuing and finishing this research work. All of them were always available to help me and share their knowledge.

I thanks also Prof. Tehrani who host and support me in the University of Groningen.

This thesis work would not have been possible also without my family. They had to bear the worst part of me, they assist me in the most difficult moments and support me in any choice I did, they allowed me to go first to Barcelona and then to Gronigen.

Last but not least, my friends have been essential in this long path toward the graduation, they are my “foundation”. In particular, thanks to Chiara, my reference point both in life as in the professional field; to Rebecca and Andrea, my psychologists and my focal points here in Torino; to Rosario, Martina, Gianluca, Laura and “ i cooptati”.

I would like also to thanks all the people I met in Groningen which made me feel a little more at home and tried to help me in any issue I had. In particular I would like to mention my flatmate Nithin and Livia and Caterina.

Abstract

This master thesis is the result of a collaboration between Politecnico of Torino, the University of Groningen and Össur company. The main aim of this work is analysing the dynamic behaviour the blade prosthetic Cheetah Xcel, Össur.

Firstly, a bibliographic research on the state of art of the blade prosthetic knowledge was carried out.

Then, a static test was supposed to be performed on the MTS machine available in the DIMEAS department of Politecnico of Torino. Given the shape of the blade prosthetic and the unknown deformation which will be verified during the static test, it was necessary to design and produce new grippers to be able to perform the test on the MTS machine. Due to timing and costs issues, the test was not performed, but the entire design was completed, ready for the manufacturing process. In Paragraph 3, the entire design is described and in the Appendix the technical drawings are reported.

Further, a series of dynamic tests were performed in the laboratory of the Vibration and Dynamics department at the University of Groningen (Paragraph 4) and in the DIMEAS laboratory at Politecnico of Torino (Paragraph 0). From these tests, the natural frequencies and mode shapes of the prosthesis were estimated. In Paragraph 5.4, the comparison between the experimental results obtained in the two laboratories is presented. Given the more advanced devices used, the EMA performed in Italy is considered more reliable.

In the final part, numerical FE models are built and the resulting natural frequencies and mode shapes are compared to the experimental outcomes. A discussion about the limitations in simulating the actual prosthetic modal behaviour are presented in Paragraph 6.

In conclusion, in Paragraph 7, considerations about future works to perform in order to better understand the blade prosthetic behaviour are reported.

Index

1.	Introduction.....	1
1.1	Gait cycle and functionality of the prosthetic foot.....	1
1.2	Running biomechanics	4
1.3	Commercial prosthetics.....	5
1.4	Mechanical characterization of ESAR prostheses for running	6
1.4.1	Studies on the stiffness variation of prosthetic feet	6
1.4.2	Analyses on the best test method for stiffness measurements	8
1.4.3	Prosthetic mechanical characterization through FE analysis.....	10
1.4.4	Dynamic characterization of blade prostheses.....	12
2.	Model creation on Solidworks 2015	14
2.1	Model information.....	14
2.2	CAD creation.....	17
3.	Static test, grippers design for the MTS machine	23
3.1	Static test prevision	23
3.2	Issues in performing the static test on the MTS machine	24
3.2.1	General issues for the design of new grippers	25
3.2.2	BOM of the entire design.....	27
3.2.2.1	Aluminium blocks.....	30
3.3	Pin assembly.....	32
3.4	Upper gripper	34
3.4.1	Friction evaluation	36
3.5	Lower gripper assembly	40
3.5.1	Lower gripper BOM.....	40
3.5.2	Rotating and non-rotating parts.....	41
3.5.3	Symmetry	43
3.5.4	Linear sled.....	43
3.5.5	Rotating table	44
3.5.5.1	FEM analysis	45
4.	Hammer test at the Vibration and Dynamics department at the University of Groningen.....	52
4.1	Experimental setup.....	52
4.1.1	Experimental test definition and hardware	54
4.1.2	Reference system definition.....	58
4.1.3	Geometry of input and output points	60
4.1.4	Acquisition software setup and parameter settings.....	64
4.2	Post-processing on Matlab	65
4.2.1	Matlab code.....	66
4.3	Experimental results.....	67
4.4	Numerical results.....	73
4.4.1	FE analysis on SW2015	73
4.4.2	FE analysis on Lupos2023	75
4.4.3	Comparison of the FEA results.....	76
4.5	EMA - FEA comparison	77
5.	Hammer test at DIMEAS, Politecnico di Torino.....	81
5.1	Experimental setup.....	81

5.1.1	Experimental test definition and hardware	82
5.1.2	Reference system definition.....	85
5.1.3	Geometry of input and output points	86
5.1.4	Acquisition parameter settings.....	91
5.2	Experimental data.....	91
5.3	Post-processing results	94
5.3.1	Auto-inertances	95
5.3.2	Maxwell reciprocity	96
5.4	Comparison between the EMA performed at Politecnico of Torino and at the University of Groningen.....	98
5.5	Numerical analysis	99
5.5.1	Shell models.....	99
5.5.1.1	Model 1	101
5.5.1.2	Model 2	103
5.5.2	3D models	105
5.5.2.1	H-convergence analysis	107
5.5.2.2	Analysis on the constraints definition	113
5.5.2.3	Isotropic material tuning	114
5.5.2.4	Characterization of the carbon fiber composite as an anisotropic material	117
5.5.2.5	Laminate definition.....	128
5.5.2.6	EMA-FEA comparison	134
5.5.2.7	Changes of the stiffness along the prosthetic shape	137
6.	Discussion	141
7.	Conclusions and future works.....	145
Appendix.....		147
A.1	Drawings of the aluminium plates and blocks produced by the University of Groningen ..	147
A.2	Drawings of the supports designed for the static test on the MTS machine	149
A.2.1	Assemblies	149
A.2.2	Parts to be drilled	153
A.2.3	Parts to be produced.....	155
Reference		163

1. Introduction

The American Academy of Physical Medicine and Rehabilitation defines a prosthesis as an *artificial substitute for a missing body part that is used to restore the function of that body part or for cosmetic purposes* [2].

The human foot has a bivalent behaviour: it acts as a rigid structure, during weight-bearing and forward propulsion, but also as flexible one, to conform to uneven terrain. Furthermore, the foot does not only provide a base of support, but it also contributes, with dorsiflexion, in decreasing energy expenditure during a gait cycle. Therefore, the foot and the ankle functions are: supporting body weight, providing balance, shock-absorbing and transferring ground reaction forces to the upper limb structures.

1.1 Gait cycle and functionality of the prosthetic foot

To analyse the mechanics of a prosthetic, it is important to investigate the gait cycle of a human foot. This is composed by two main phases: the stance and the swing one. The first one lasts around 60% of the entire gait cycle; it is composed by two phases of double support (from 0% to 10% and from 50% to 60%), in which two feet are in contact with the ground, and one single support phase, where the bodyweight is supported just by one foot.

The gait events which characterize the gait cycle are displayed in Figure 1.1.1.

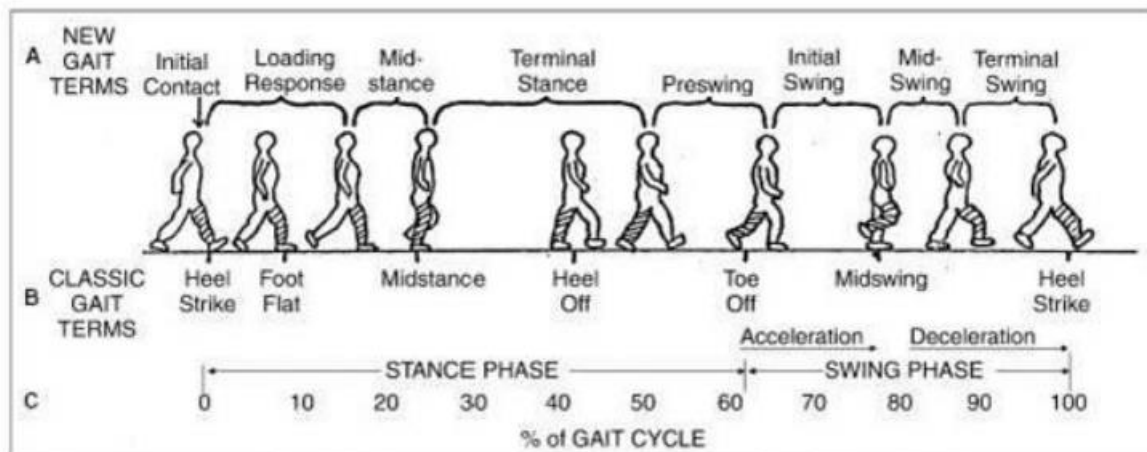


Figure 1.1.1 – Gate cycle according to the classical terminology.

Below, the phases just displayed in Figure 1.1.1 are listed and described, with a final resume in Table 1.1.1.

- Initial Contact (0% of the gait cycle) – It corresponds to heel strike. The heel touches the ground and the double support phase starts. Ground reaction force (GRF) is focused in the hind foot. During heel strike the hip is flexed by 30° and the knee is full-extended.
- Loading Response (0-10% of the gait cycle) – It goes from heel strike to slightly after foot flat. Foot flat is verified at 8-10% of the gait cycle, here the foot absorbs the forces generated from the impact with the ground by rolling in pronation. The knee shows a 15° - 20° flexion, while ankle plantarflexion increases to 10 - 15° . GRF keep increasing.
- Mid-stance (10-25% of the gait cycle) – It goes from slightly after foot flat to midstance. GRF keeps on increasing; at 15-20% of gait cycle it reaches a first maximum peak of amplitude that nearly corresponds to the body weight.

- Terminal Stance (25-40% of the gait cycle) – It goes from midstance to slightly after heel-off. Here the forward propulsion phase begins. Between midstance and heel-off, the knee reaches maximal flexion and then begins to extend, and the ankle reaches 5° dorsiflexion. Then, the hindfoot leaves the floor, the knee becomes flexed (0-5°) and the ankle gets supinated and plantarflexed. During this phase, the weight-bearing is performed by single limb support. The GRF slowly moves from hind to mid and then to forefoot. Its amplitude decreases until 30% of gait cycle and then starts to re-increase.
- Pre-swing (40-60% of the gait cycle) – It goes from slightly after heel-off to toe-off. Here the bodyweight is shared between the metatarsal heads of the leading foot, while the contralateral foot approaches the ground. The hip goes into flexion. GRF reaches the second maximum peak at 45-50% of gait cycle, and then it decreases, reaching 0 N value at toe-off, since the foot is no more in touch with the ground.
- Initial Swing (60-75% of gait cycle) – The knee flexes to 40-60°, and the ankle goes from 20° of plantarflexion to dorsiflexion, ending in neutral position (90° with respect to the shank). Here an acceleration of the movement of the leg is verified.
- Mid-swing (75-85% of the gait cycle). The leg starts to decelerate its movement.
- Terminal swing (85-100% of the gait cycle) – The hip flexes to 30° and ankle dorsiflexion is verified. The knee from a 60° flexion extends approximately to 30°.

Table 1.1.1 – Gain cycle resume.

Phase	% of gait cycle	Knee flexion	Ankle flexion	GRF
Initial contact	0%	Full-extended	30°	Is focused in the hind foot.
Loading response	0-10%	15°-20°	Increase in the plantarflexion to 10°-15°	It keeps on increasing. To absorb the impact force, the foot rolls in pronation.
Mid-stance	10-25%			Increases till reaching the first maximum at 15-20%.
Terminal Stance	25-40%	Maximal flexion, then extension and finally flexion of 5°	5° dorsiflexion, then supination and finally plantarflexion	Single limb support. The GRF slowly moves from hind to mid and then to forefoot. Amplitude: decreases until 30% of gait cycle and then re-increases.
Pre-swing	40-60%	Flexion	Plantar flexion	Bodyweight is shared between the metatarsal heads of the leading foot, while the contralateral foot approaches the ground. Amplitude: increases till 45-50% of the gait cycle (second peak) and then decreases till 0N.
Initial swing	60-75%	Increases till 40-60°	Form 20° plantarflexion, to dorsiflexion and finally neutral position	0 N
Mid-swing	75-85%	Decreases		0 N
Terminal swing	85-100%	Reaches the full extension	Dorsiflexion	0 N

As mentioned at the beginning, the prosthetic foot has to replace the same main functionalities of the human one. Below are reported the operating features it has to grant for each gait cycle phase.

- Standing: allowing the person to balance COM's (Centre of Mass) oscillations.
- Heel strike: absorbing the Ground Reaction Forces (GRF) in order to lower the interarticular forces acting on the knee and the hip and prevent joint injuries like osteoarthritis.
- Stance phase: transferring the bodyweight from heel to toe. This function is normally controlled by plantar flexor muscles of the ankle joint, which are lost after the amputation.
- Push-off: returning the energy stored during the heel strike to promote the forward propulsion of the body. This role is normally promoted by the flexor muscles of the ankle joint.

Furthermore, the prosthetic has to grant stability during the entire gait cycle and a physiological Rang of Motion (RoM).

1.2 Running biomechanics

The running biomechanics [4] differs a lot from the walking one. The joint range of motion, the muscle activity and the joint reaction forces vary on the basis of the speed and often from one step to the other. Three different condition of running can be individuated: jogging (3 m/s), running (5 m/s) and sprinting (11 m/s).

As displayed in Figure 1.2.1, with respect the walking gait, increasing the speed, there is a decrease in the stance phase period, while there is an increase of the swing phase and a third phase, the non-supportive float phase, develops.

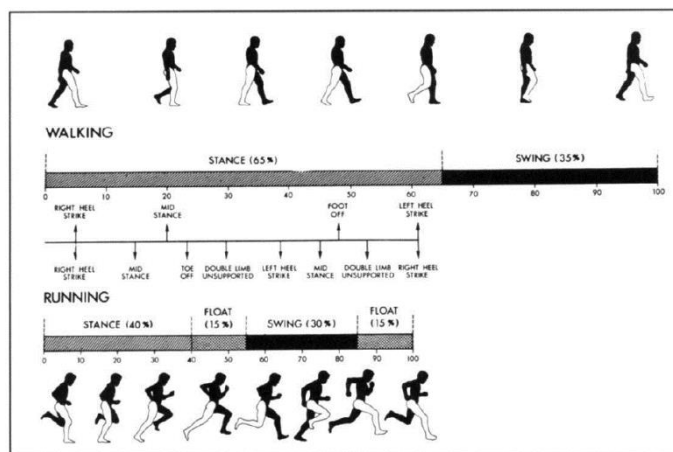


Figure 1.2.1 – Comparison of phases of walking and running cycles

Long-distance runners initially contact the ground with the heel or with the foot flat, while sprinters commonly land on the midfoot. At the time of heel strike, there is a rapid dorsiflexion. Even during sprinting, dorsiflexion generally occurs, although insufficient for the heel to touch the ground, the foot is in mild plantar flexion at impact because foot strike typically occurs on the more distal part of the foot. Dorsiflexion peaks at midstance, after which plantar flexion rapidly occurs in the foot until toe-off. Just after toe-off, progressive dorsiflexion occurs until foot strike, except that during sprinting, plantar flexion begins during the terminal part of the swing phase just before contact.

During running, the vertical force approaches the 275% of the body weight. Furthermore, in this case, there is just a peak after impact, while in walking two peaks occur, as shown in Figure 1.2.2. This is a consequence of the fact that more force is generated with propulsion rather than with impact, it results that the impact peak is lower than the one related to the propulsion.

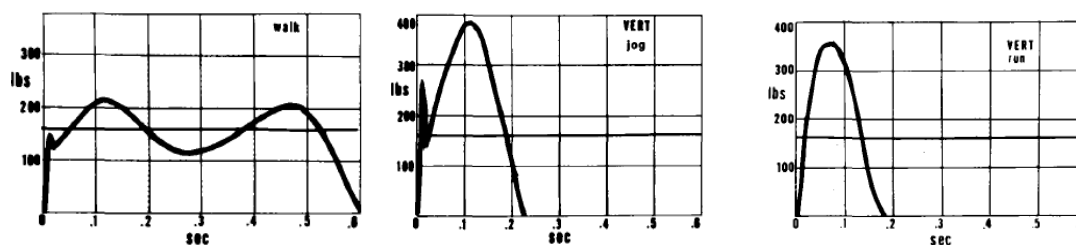


Figure 1.2.2 – Vertical ground reaction forces comparison between walking (left), jogging (right) and running (right).

1.3 Commercial prosthetics

According to the different level of amputation, different lower limb prosthetics are produced. In this study, the ones produced for foot amputation are considered. They are composed by a stump socket, eventually by an ankle joint and a foot device (Figure 1.3.1).



Figure 1.3.1 – Foot prosthetic for foot amputation.

There are different kind of foot prosthetic in the market, they are listed below and shown in Figure 1.3.2.

- Rigid feet – They are called Solid Ankle Cushioned Heel (SACH). They have a rigid wooden, plastic or metallic keel cover. This type of prosthetic foot is cheap, durable and almost maintenance-free. They can store (absorb) energy during heel-strike, but they are not very effective to return it during the push-off phase.
- Articulated feet – They have a mechanical joint which connect them to shank. Depending on their design, they are free to move or just in one direction or in multiple ones. They are usually employed for above-the -knee prostheses.
- ESAR feet – It is the acronym of: Energy Storing And Return feet. They are the best in coping the foot physiological function of energy storage and return, even though they are not able to perform it as well as the human feet. In fact, these lasts return the 240% of the energy stored, while ESAR just around the 80%. SACH feet are even worse: they only return 30% of stored energy. The impossibility of having the same amount of energy stored and realised with respect to the human feet, is due to the absence of plantar-dorsiflexor muscles that help the foot to store and return energy during gait. Such prosthetics also confer better symmetry to the gait and they improve the subject's comfort and reactivity; also, they reduce the ground reaction forces generated on the contralateral heel when it strikes the ground.
- Sport purpose feet – They are ESAR feet with extreme optimization in order to be used for high-level sport.



Figure 1.3.2 – Foot prosthetics on the market. From left to right: SACH, articulated foot prosthetic, ESAR foot and ESAR for sport applications.

The suitable prosthetics for the work which will be carried out are the ESAR one. The aim of this activity is indeed to apply piezoelectric patches in the prosthetic in order to take advantage from the deformations of the prosthetic and produce electrical energy.

1.4 Mechanical characterization of ESAR prostheses for running

In the case of prosthetics used for high level of activity, such as sprinting, no standardize test is currently present. The existing test protocol, the ISO 10328 [5], defines loads and inclinations of the platform to perform the static test according to the walking conditions. Even the blade prosthetic for running purposes are verified through this standard. However, to have a real access to the mechanical characteristics of the blade prosthetic in the conditions it is intended to be used, different parameters from the standard ones have to be applied during the test. Thus, before planning the tests to perform on the component, it is necessary to perform bibliographic researches to understand how to perform stiffness measurements on ESR blade prosthetics.

1.4.1 Studies on the stiffness variation of prosthetic feet

In the research of Beck et al. [13] the stiffness of two different blade prosthetic models, one with C shape and one with J shape, was analysed. Indeed, as pointed out from this study, it is important to properly test the running prosthetic, since its stiffness is affected by multiple factors which are listed below.

- When the speed increases from 3 m/s, the stiffness decreases.
- Due to conflict evidence in literature and the insufficient information provided by the manufacturers, it is not known if the force-displacement profiles are linear or curvilinear. For example, the mechanical tests of Dyer et al. [14] on Elite Blade prosthetics, demonstrate that the stiffness is dependent on the load, since the force-displacement obtained are not linear.
- The dimension of the prosthetic affects the proximal bending moment value and thus the vertical displacement, resulting in different stiffness values, as better described below.

The stiffness testing was performed on an Instron machine. In order to know how to perform the test in such a way to simulate as much as possible the running condition, the ground reaction force and the sagittal plane angles inclination were measured for 11 athletes with unilateral transtibial amputation while running at 3 m/s and 6 m/s on a force-measuring treadmill. The average angles on the trials performed were calculated. For the C shape the α_3 is the angle measured at 3 m/s and α_6 at

6 m/s. while for the J-shape: β_3 at 3 m/s and β_6 at 6 m/s. From the tests $\alpha_3=15.1^\circ\pm 4.8^\circ$ with a GRF peak of 2.5 ± 0.3 times the body. In Table 1.4.1.1 a resume of the results obtained.

Table 1.4.1.1 – Resume of the angles and GRFs obtained by the experimental measurements of running tests at 3 m/s and 6 m/s of amputee athletes, C-shape (α) and J-shape (β) are considered.

Angle from measurements	Angle value considered for the test	GRF peak
$\alpha_3 = 15.1^\circ\pm 4.8^\circ$	$\alpha_3 = 15.0^\circ$	2.5 ± 0.3 times the body weight
$\alpha_6 = 10.0^\circ\pm 4.2^\circ$	$\alpha_6 = 10.0^\circ$	2.7 ± 0.3 times the body weight
$\beta_3 = 20.9^\circ\pm 8.9^\circ$	$\beta_3 = 20.0^\circ$	2.5 ± 0.3 times the body weight
$\beta_6 = 24.2^\circ\pm 9.3^\circ$	$\beta_6 = 25.0^\circ$	2.8 ± 0.3 times the body weight

Hence, the prosthetics were tested at different inclination of the platform: at 0° , α_3 or β_3 , α_6 or β_6 (Figure Figure 1.4.1.1). For each condition three loading and unloading cycles at 100 N/s were performed. For the GRF peak the corresponding max body weight suggested by the manufacturer was considered. To replicate the 3 m/s running condition the body weight was multiplied for 3, while for the 6 m/s running case, it was multiplied for 3.5.

To minimize the shearing force, the low-friction roller system was used. It allows anterior and posterior translation while the angle of the platform is maintained constant. The threshold for force detection was 10 N and at 10 Hz the force magnitude and prosthetic displacements were recorded. To analyse the influence of the height on the stiffness, the aluminum pylon height was varied for each model. For example, in the Cheetah Xtend prosthesis, the vertical distance between contract point with the platform and the attachment point of the prosthetic to the machine was set to 31.5, 38.0 and 41.5 cm.

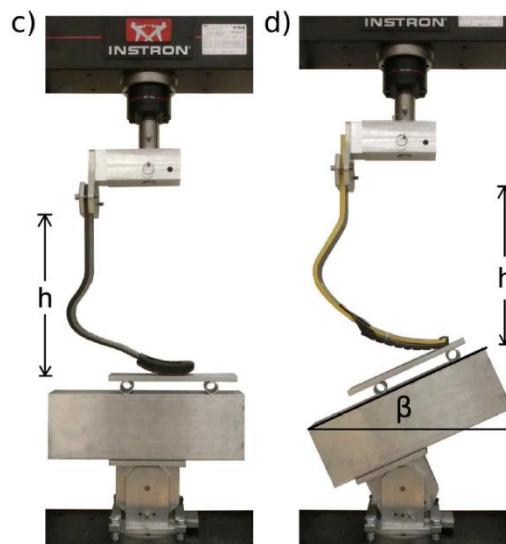


Figure 1.4.1.1 – Static test performed on Cheetah Xtend prosthesis, null (left) and β (right) inclinations applied.

Curvilinear force-displacement profiles were obtained, indicating that prosthetic stiffness varies with the magnitude of applied force. It was also demonstrated that stiffness changes between the prosthetic models and is inversely dependent to the height of J-shaped RSPs. Moreover, prosthetic stiffness results to be much greater at 0° than at angles representative of those that occur during

running. Hence, an overestimation of the stiffness results if the prosthetic is tested with no inclination of the platform. As a result, when athletes with leg amputations change prosthetic models, height, and/or sagittal plane alignment, prosthetic stiffness also changes; therefore variations in comfort and performance, may be indirectly due to altered stiffness. The stiffness results obtained for each category of the different models analyzed are reported in Table Figure 1.4.1.1 Table 1.4.1.2.

Table 1.4.1.2 – Average prosthetic stiffness across models based on running 3 m/s and 6 m/s. All values include the rubber sole that comes with the prosthetic model, with the exception of the Össur Cheetah Xtend, which was equipped with the Össur Flex-Run's rubber sole.

Users Mass (kg)	3 m/s				6 m/s			
	Flex-Run (kN/m)	Catapult (kN/m)	1E90 Sprinter (kN/m)	Cheetah Xtend (kN/m)	Flex-Run (kN/m)	Catapult (kN/m)	1E90 Sprinter (kN/m)	Cheetah Xtend (kN/m)
55	18.0	17.4	16.2	20.7	20.4	20.4	19.0	21.5
60	20.6	20.1	18.6	23.2	22.6	25.8	19.5	23.5
65	22.1	20.8	19.1	23.7	23.7	27.6	22.7	23.9
70	22.9	22.8	21.8	26.1	26.1	29.9	23.1	26.4
75	23.7	23.5	22.2	26.6	27.7	30.7	23.5	26.8
80	26.2	25.9	22.7	28.8	29.2	33.7	26.4	28.9
85	26.1	26.5	23.2	29.3	31.3	34.5	26.8	29.4
90	29.5	29.9	25.9	32.3	33.4	41.2	27.2	32.4
95	31.4	30.5	26.3	32.7	34.7	42.0	27.6	32.8
100	31.8	31.1	26.7	33.2	35.3	42.8	32.1	33.1

1.4.2 Analyses on the best test method for stiffness measurements

The research of Dyer et al. [14] aims not only to find the most appropriate method to analyse the stiffness of a blade prosthetic, but also to understand if it is possible to derive a mechanical stiffness value when other bodyweight conditions, with respect the one tested, are applied.

In this study, two Elite Blade composite ESAR were analysed fixing them in an inverted position on a Testomic strength testing machine and compressing them vertically. They were mounted to an aluminum fixing block which aligns the prosthetic shank at 60° with respect the horizontal plane . In this way, a correct alignment is verified, having a theoretical centerline from the distal end of the prosthetic to the midpoint of the fixing bolt that would attach the prosthetic socket. Three different test techniques, shown in Figure 1.4.2.1, were realised, in order to understand which one is the most reliable. They are the following:

- fixed at the prostheses distal end (FDE): the distal end of the prosthesis butts against a ledge that prevents it from sliding when compressed;
- partial slide then fixed (PSF): the prosthesis is allowed to slide 28 mm before the distal end butts against a ledge, then no further slide is permitted;
- unfixed distal end (UDE): the distal end of the prosthesis can slide freely under the load cell platen when compressed.

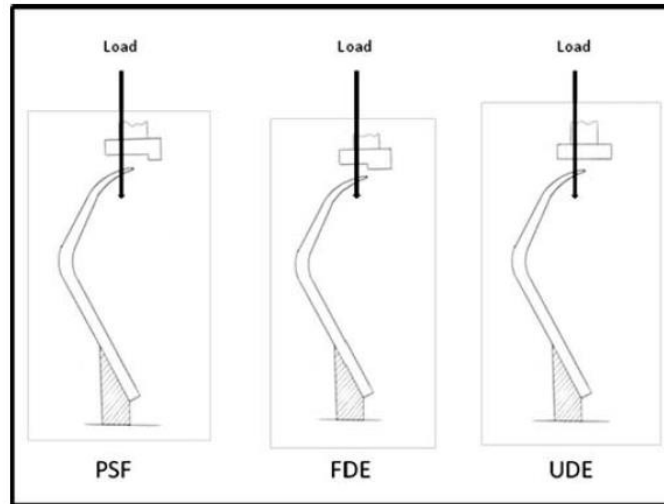


Figure 1.4.2.1 – Testometric loading tests, PSF (left), FDE (centre) and UDE (right).

Ten compression tests were run for both the prosthetic, loading them till 1500-2000 N at a rate of 50 mm/min.

The two prosthetic reported different levels of stiffness between each other. This highlights how composite manufacture can alter the mechanical properties by changing parameters such as cloth lay-up, fiber orientation or resin application, even though they are physically identical. However, each experiment reported a low variation of data between the 10 repetitions, thus less than 10 tests are sufficient for each experiment method.

The highest stiffness was recorded with the FDE method. This is probably due to the fact that in the UDE and PSF methods, since slippage is allowed, a relative rather than an actual displacement was recorded by the loading machine. It is possible that such slippage of the PSF and UDE methods may effectively shorten the spring length causing further measurement inaccuracy. Nevertheless, all the measurements result in a non-linear behaviour of the prosthetics stiffness.

Hence, while the prosthesis performance itself is repeatable, the change in methods produces a significant enough change in the results, preventing data to be referenceable between methods. However, the FDE method is recommended by Dyer et al. [14] for the future analysis on the ESR prostheses, since the stiffness results always higher than the other approaches and fixing the distal end is likely a more accurate representation of the mechanical performance. Furthermore, the UDE method leads to an underestimation of the prosthetic performance, is not recommended to have a unfixed distal end when measuring the stiffness.

It must be underlined that, in this research, the absolute distal end point is loaded, actually the ground reaction strike point is not properly that one. This point is determined by different variables, such as race length, running round the bend, athlete fatigue. Given that, since this strike point would be different between all runners, an alternative approach is to identify a standardized.

Another issue is whether to consider the average stiffness or the one verified at maximum load. Given the non-linearity of such mechanical characteristic, the difference between the maximum and mean value is high. Since a run of 100 m is composed by three phases, high acceleration, acceleration to maximal running speed and maintenance of maximal running speed, an average stiffness would be the suitable to take the varying phases into account. On the other hand, the maximal speed phases are likely far larger as a percentage of the overall 100 m race compared to the lower load efforts plus lower speeds have been demonstrated not to cause reductions in ankle joint stiffness, suggesting that the stiffness peak would be more representative of a larger percentage of the limbs actual experience in the 100 m run.

Finally, given the overall non-linearity of the stiffness, in which the sole use of a linear or polynomial trend line is not enough to describe the stiffness behaviour, it is really difficult to predict such

mechanical characteristic for different bodyweights. The best method would be to take the highest load and deflection data graph trace available and then apply a linear line to that aspect to predict higher load stiffness.

In Table 1.4.2.1, the stiffness results obtained in the FDE test under 3500 N loading condition on the second prosthetic and the predicted stiffness value through polynomial and linear trend line are reported.

Table 1.4.2.1 – FDE test stiffness results for 3500 N loading and stiffness prediction through linear and polynomial trend.

Data Set	Sample	Stiffness (N/mm)
1st Experiment FDE test	Average stiffness of 0–1,950 N sample	39
	Actual stiffness at 1,950 N loading	48
2nd Experiment FDE test	Average stiffness of 0–1,950 N sample	37
	Actual stiffness at 1,950 N loading	45
	Actual stiffness at 3,500 N loading	53
Predictive stiffness @3500N	2nd order polynomial trend line	55
	1,500–1,950 N loading linear trend line	49

1.4.3 Prosthetic mechanical characterization through FE analysis

In the research of Rigney et al. [12] the suitability of the FEA for standardizing the mechanical characterisation of the ESAR feet is analysed. With respect to other studies, here, also the horizontal force, thus the friction, between prosthetic and load cell, is taken into account.

Two quasi-static tests were conducted on the prosthetic on the Instron material testing machine in order to find out E and μ values. The carbon fiber prosthetic materials were considered to be linearly viscoelastic, isotropic and homogenous because the result of importance belonged to the global prosthesis behaviour as opposed to the small-scale mechanical characteristics of the material.

Afterwards, also the simulation of the dynamic loading response was carried out and the Rayleigh parameters α and β , stiffness and energy efficiency were evaluated.

In Figure 1.4.3.1 the flowchart of the of the proposed methodology is displayed. Through a combination of experimental and finite element analysis (FEA), the stored energy E_{IN} , the energy efficiency E_{EFF} and the overall stiffness k of ESAR prostheses are determined.

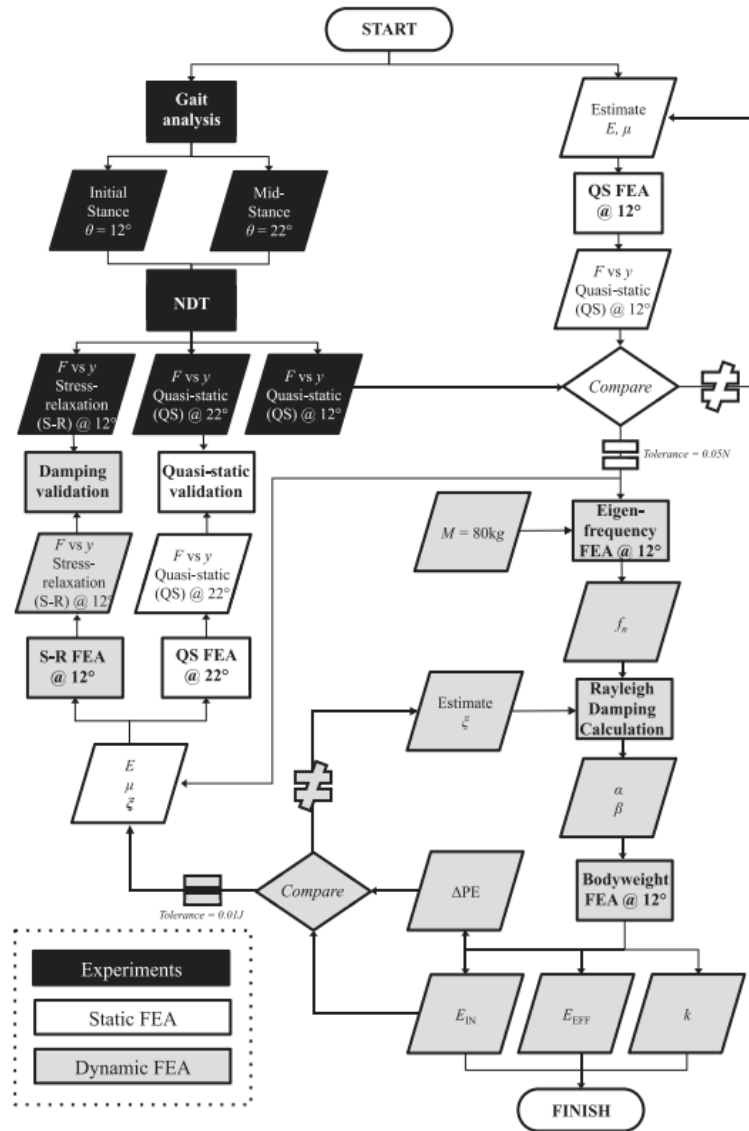


Figure 1.4.3.1 – Flowchart of the of the proposed methodology to determine the stored energy E_{IN} , the energy efficiency E_{EFF} and the overall stiffness k of ESAR prostheses.

From this research, it resulted that the transition from ‘stick’ to ‘slip’ condition during unloading, caused a decrease in the apparent stiffness. The values of stiffness obtained during constant strain rate test and bodyweight loading were different, highlighting an influence of the loading condition on the prosthesis stiffness.

The prosthetics resulted to be slightly over-damped, with a damping ratio around 100-200% of the critical damping at 1Hz, which is the first mode, corresponding to a lateral vibration mode shape. The results were in agreement with the experimental one of the stress-relaxation tests.

From the dynamic loading response it was possible to deduce that ESAR prostheses with high stiffness result in a low energy loss but a high impulse (assuming reduced compression upon impact equates to a reduced time of impact), potentially increasing the residual limb reaction force. Since the prostheses possessed similar viscoelasticity and their major differentiating feature was their geometry, it then follows that the biggest contributing factor to energy lost by an ESAR prosthesis, when dynamically loaded, is its shape and thickness.

1.4.4 Dynamic characterization of blade prostheses

In the researches of Noroozi et al. [[16],[17]], the free behaviour of nine prosthetic blades was considered.

In the research [16], all the prostheses analysed were the same model, Össur Flex-Run, but all of a different stiffness category, which for the Össur models goes from 1LO to 9LO. 1LO is the category which can hold the lowest maximum weight (44 kg), while 9LO is stiffer one and it can hold till 130 kg. The aim was to evaluate the changes of undamped natural frequency and stiffness between the different categories of the prosthetics. In the work [17], instead, two Elite Blade composite feet models, one solid and the other one spitted at the distal end, were examined. Five different masses were applied on the two models, and their dynamic response was evaluated. The foot mass arrangement of both the research works is depicted in Figure 6.2.1.1. In Figure 1.4.4.1.

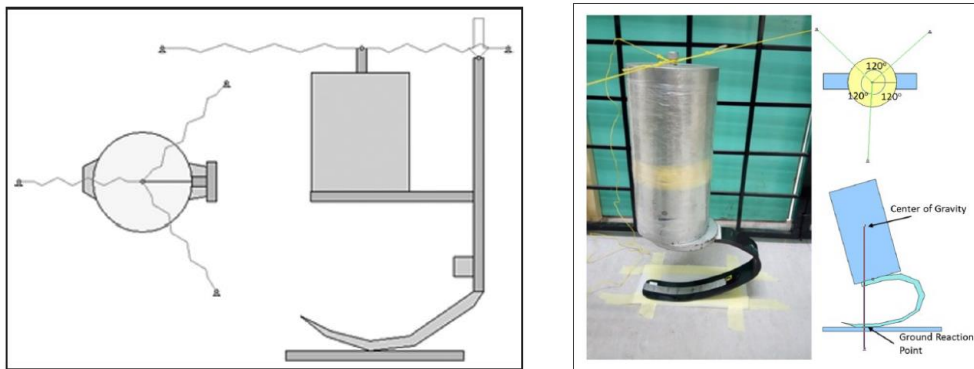


Figure 1.4.4.1 – Foot-mass arrangement of the Elite Blade model (left) and Flex-Run model (right).

The dynamic characterization of the structure is particularly useful because the damping characteristic cannot be determined through simulations such as FEA, but it must be physically measured.

From the hammering test, for each prosthetic category, it resulted that, whatever is the excitation direction between X (horizontal) and Z (vertical), the mode shape and the natural frequency is the same. Although, the natural frequency increases by increasing the prosthetic category from 1LO to 9LO. This results in higher stiffness by going up in the category: it is computed a stiffness of 32161.72 N/m for 1LO Flex-Run, while for 9LO it is 59011.67 N/m.

According to Noroozi et al. [16] statement, once the stiffness is known, the natural frequency can be predicted based on different masses to be used on the prosthetic, assuming that the boundary conditions are fixed. This because linearity of the data is considered. By predicting the natural frequency, it can be selected the right stiffness category foot in order to match the activity level or vice versa for a better gait performance. Indeed, in the case of matched frequencies, the bouncing action is amplified with less effort and loss of energy, preserving a more steady periodic motion and promoting better gait performance. Hence the effect of underload and overload considered in this work, can be utilized to vary the natural frequencies and match the user's performance requirements. In other words, the foot is not just prescribed based on the weight of the amputees but based on the activity level of the amputees.

The first four eigenmodes obtained were: first twisting, first bending, second twisting and second bending. From this analysis, it is verified that there are a number of natural frequencies and mode shapes that can be excited as a result of impact, such as the one due to jumping, walking or running. Since the first bending mode produces vertical displacement, potentially contributes the most to this process. In this study, it is verified that the twisting modes can occur close to or even before the first bending mode, at a relatively low frequency. Hence there is a strong elastic coupling which links bending to twisting indicating the load is not passing through the shear centre of the section. Such

result can be due to many factors, such as unsymmetrical loading, an unsymmetrical section or shear coupling due to high material anisotropy.

Form the damping decay rate and damping ratio evaluations, it resulted that the energy loss due to damping is higher at higher modes. Hence, all the modes damp out quickly unless they match the excitation frequency of an external source. The first bending mode registered the lowest damping.

Using simple regression, the frequency against $1/\sqrt{m}$, of the first bending mode, was plotted and an high level of nonlinearity was observed: the prosthetic foot did not exhibit constant stiffness. The biggest contribution to the nonlinearity comes from large deflections and changing boundary conditions due to variation in contact surface. This results in varying bending moments when using larger masses.

Noroozi et al. [17] concluded that, for practical purposes, it may be possible to approximate anyway the stiffness as linear to closely predict the frequency of the first bending mode of vibration irrespective of the mass or the weight of the amputee.

2. Model creation on Solidworks 2015

In this chapter, firstly information about the Cheetah Xcel model are presented and then, the CAD creation on Solidworks 2015 of the model is described.

2.1 Model information

The prosthetic foot Cheetah Xcel, displayed in Figure 2.1.1, is realized for professional runners, with transtibial or transfemoral amputation, which have to perform short-distance sprinting of 100-200 m.



Figure 2.1.1 – Cheetah Xcel blade prosthetic foot, Össur.

Depending on the height of the user, the model can have two different geometrical dimensions, as reported in Figure 2.1.2. The small size can be used for people below 1.70 m height and 55 kg weight. The prosthetic which will be tested in this research is the Large version. Notice that, for both the Large and Small versions, two heights are pointed out, they represent the maximum and minimum height that a prosthetic can have. Thus, for example, the Large model can be cut maximum at 513 mm. The model tested has not been cut, thus its height is the maximum one: 569 mm.

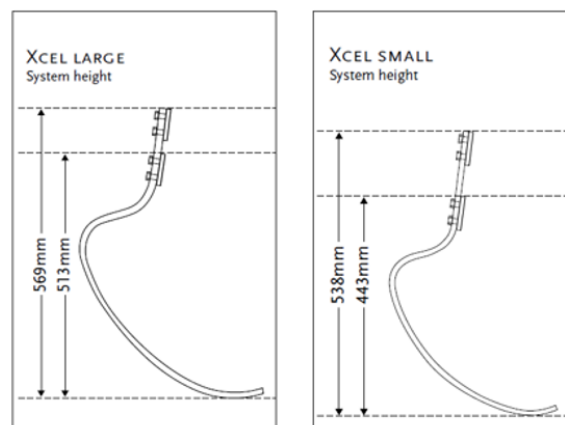


Figure 2.1.2 – Sketches of the Cheetah Xcel Large (left) and Small (right) prosthetic models, Össur.

In Table 2.1.1, data of the prosthetic which will be analysed are reported.

Table 2.1.1 – Cheetah Xcel Large data.

	Product weight [kg]	Max. system height [mm]	Max. user weight [kg]
Cheetah Xcel Large	0.98	569	147

Each foot prosthetic model is further divided in stiffness categories. Indeed, depending on the actual weight of the user, different prosthetics have to be utilized. Össur distinguishes the foot prosthetics in 9 categories [19], as reported in Table 2.1.2. The tested prosthetic is of category 6, thus is intended for users of around 89-100 kg.

Table 2.1.2 – Categories of the Cheetah Xcel prosthetic model.

Weight kg	45-52	53-59	60-68	69-77	78-88	89-100	101-116	117-130	131-147
Weight lbs	99-115	116-130	131-150	151-170	171-194	195-220	221-256	257-287	288-325
Extreme Impact Level	1	2	3	4	5	6	7	8	9

The Cheetah Xcel model is an improved, more sprinting, version of the existing blade prosthetics Cheetahs, Xtend and Xtreme. In Figure 2.1.3 the three models are displayed, while in Figure 2.1.4 a superposition of the lateral view of the models is reported. Cheetah Xcel Large presents a more aggressive curve, this supports larger displacements. The upper and lower bends are moved upwards, causing a larger lever and enhancing the energy return, the lever arm is 10% longer than the Xtrem model. Furthermore, the more plantarflexed shape, supports a better angle of force forward. The toe is more extended and curved, this improves the ground contact and the starting phase in competitions.



Figure 2.1.3 – Cheetahs Xcel (left), Xtend (centre) and Xtreme(right), Össur.

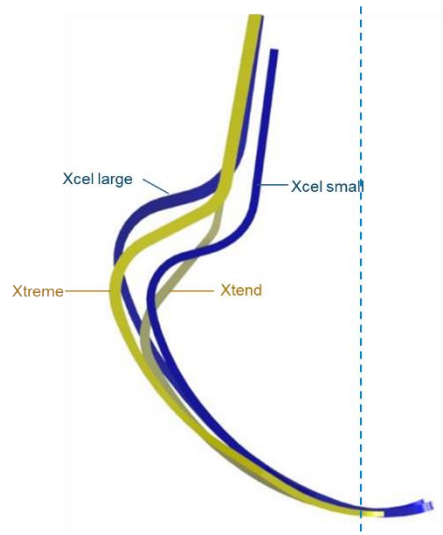


Figure 2.1.4 – Lateral comparison of the Cheetahs models, Cheetah Xcel Large and Small (blue) and Cheetahs Xtreme and Xtrend (yellow).

A photo of the lateral view of the prosthetic is reported in Figure 2.1.5, the thickness is visibly not constant along the whole component. In general, the upper part, the one which have to be attached to the socket and the adjacent curved region, is thicker; while the lowest thickness is reached at the toe level.



Figure 2.1.5 – Cheetah Xcel Össur, photo of the lateral view.

This component is realised composed by carbon fiber layers, as visible in the photo of the lateral part of the prosthetic, Figure 2.1.6 left image. On the surface of the component, the fibers are left visible, thus it is possible to observe that at least the external layers are bidirectional carbon woven fabrics inclined of $45^{\circ}/-45^{\circ}$, Figure 2.1.6 right image. Notice that, from the lateral view of Figure 2.1.6, it is also clear that the edges are chamfered, in such a way to avoid stress concentration verified at sharp edges.



Figure 2.1.6 – Cheetah Xcel Össur material, photos of the frontal (left) and lateral (right) views.

2.2 CAD creation

From the information reported in Paragraph 2.1 obtained from the technical documents of the Össur foot prosthetic model [18] - [21], the CAD model of the prosthetic is realised. Then, starting from this model, another CAD is generated, updating the measurements with the ones directly evaluated on the real model through the use of a calibre.

Preliminary CAD model

Firstly a new part is created and called “CheetahXcelDrawing.SLDPRT”. A sketch in plane XZ is created an horizontal construction line is created and its distance from the origin is set equal to the maximum height of the prosthetic: 569 mm.

Then the image is inserted in the sketch using the following commands: *Sketch tools*, *Sketch Picture*. The image can be rotated, moved and rescaled. Thus, the lowest point of the prosthetic picture model is set coincident with the origin of the part and resized in such a way that the maximum height of it will be 569 mm (the highest edge have to be coincident with the horizontal construction line drawn previously). It is also possible to set the transparency of the image, in this case it is set to 0.65. Then, splines are drawn on the image, following the model drawing, as depicted in Figure 2.2.1. In sketching the lower spline, the point which is in contact with the ground, the one set coincident to the origin, is even defined as the tangent point the horizontal construction line representing the floor.

Notice, from Figure , that the thickness of the prosthetic is not constant. Furthermore, since the spine lines are drawn just following the image in background, the sketch is not define, thus, the function “Fully define sketch” is used to make all the sketch entities determined.

From the sketch just defined, the maximum width along X is evaluated: 355 mm.

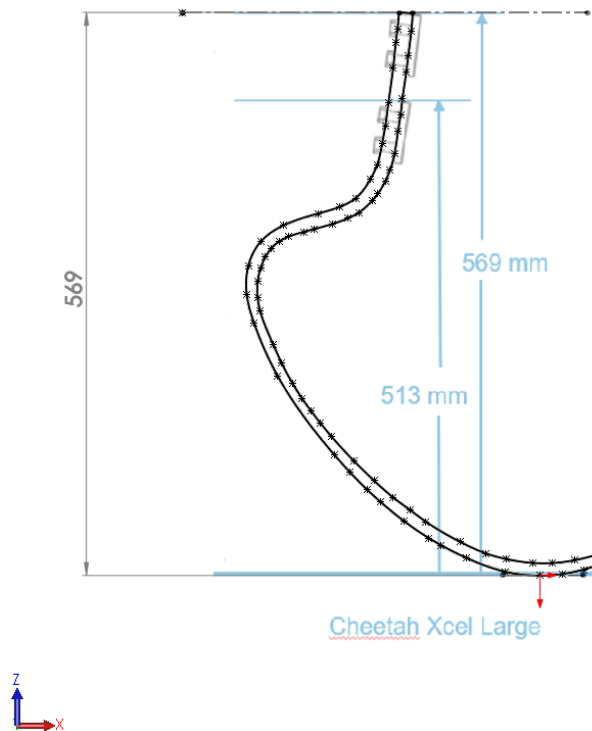


Figure 2.2.1 – Sketch creation on the Cheetah Xcel prosthetic model picture.

Afterwards, a new part is created and called “CheetahXcel.SLDPRT”. On plane XZ a sketch is opened and the 2D drawing realised before is copied and pasted here. Through the command *Sketch Tools, Move*, the sketch is translated in such a way that the lower point, the one tangent to the ground, coincides with the origine of the part.

All the dimension and relations which were defined before are not anymore defined, thus the command “Fully define sketch” is again used.

Finally, the 2D representation of the prosthetic is extruded. The only information about the width is that at the toe level it is 70 mm. Hence this dimension is considered for the extrusion, where the sketch plane is maintained the mid one. The only information about the width is indeed that at the toe level it is Finally, *Fillet* of radius 25 mm are performed at the distal end of the foot prosthetic. This geometry allows a better fit of the sole to the prosthetic. There are, indeed, different kind of soles which are sold with the Cheetah Xcel model depending on the kind of ground the user is going to run. In general their aim is to have a better ground contact and improve the running performances. The final result is displayed in Figure 2.2.2.

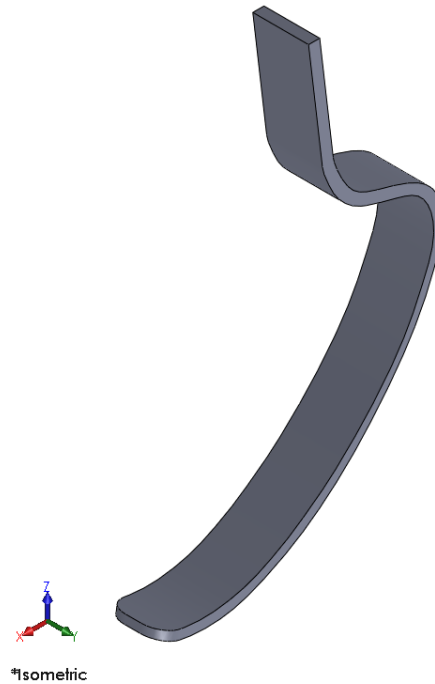


Figure 2.2.2 – Extrusion of the 2D sketch of Cheetah Xcel Large prosthetic model.

The file “CheetahXcelDrawing.SLDPRT” is again used to measure the holes position. In the image, four holes are displayed because are represented the positions of the holes for the version with maximum and minimum height. Actually, as explained in the dossier of the instruction for use [4], just two holes are present in the component. The representative image of how to attach the prosthetic to the socket [21], is reported in Figure 2.2.3.

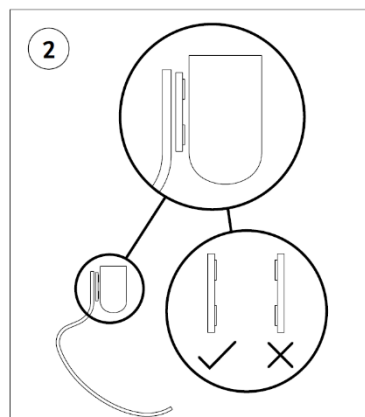


Figure 2.2.3 – Sketch of how to attach the prosthetic to the socket, instructions for use.

In the case analysed, since the component is 569 mm high, the sketch of the two upper holes is considered. Thus, the lines which define these two holes are sketched and the vertical measurements from the origin are evaluated, as displayed in Figure 2.2.4. The dimension of the holes results to be 10 mm.

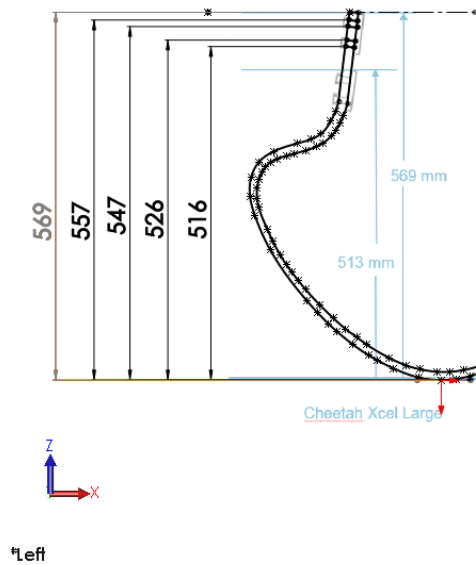


Figure 2.2.4 – Evaluation of the holes position through which the prosthetic is fixed to the socket.

Thus, on the “CheetahXcel.SLDPRT” model, a new sketch is opened in the lateral plane, XZ. The rectangles representing just half of the hole are drawn perpendicular to the line and the locations, computed in the “CheetahXcelDrawing.SLDPRT” file, are reported, as displayed in Figure 2.2.5, left. Then a *Revolved Cut* is performed for each hole. The result is displayed in Figure 2.1.5, right image.

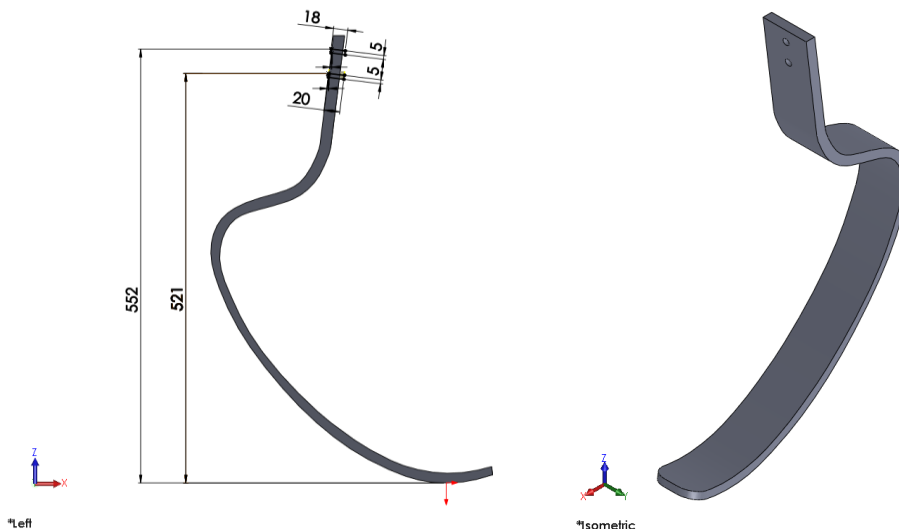


Figure 2.2.5 – Creation of the holes for fixing the prosthetic to the socket; sketch in the lateral view (left) and final result in the isometric view (right); Cheetah Xcel, Össur.

Adjustments on the CAD model

Once the prosthetic was available, the CAD model has been updated with the actual measurements evaluated directly on the component.

Through the use of the calibre, the thickness is evaluated along the prosthetic. The results obtained are really different from the ones considered in the creation of the previous CAD. For example, before at the upper and lower ends respectively a thickness of 14 and 10.91 mm were considered, while, as shown in Figure 2.2.6, the actual values are 17 and 9.5 mm.



Figure 2.2.6 – Evaluation of the thickness upper (left) and lower (right) ends on the real model through the use of a calibre.

Starting from the sketch realised for the first CAD, the thickness measurements have been adjusted. To reproduce the prosthetic shape, multiple adjacent splines have been used. Hence, to have a continuity in the model, the spline tool *Fit Spline* is used to convert all the adjacent curves in just one.

The further passages are maintained the same of the ones described in Paragraph 2.1. However, after the extrusion of the sketch, another step is needed. Indeed, actually the width of the component, a part from the toe, is large 60 mm. Thus a sketch on the XY plane, of the part to cut, is realised and then the *Extruded Cut* is performed along the whole part. In Figure 2.2.7 the result is displayed.

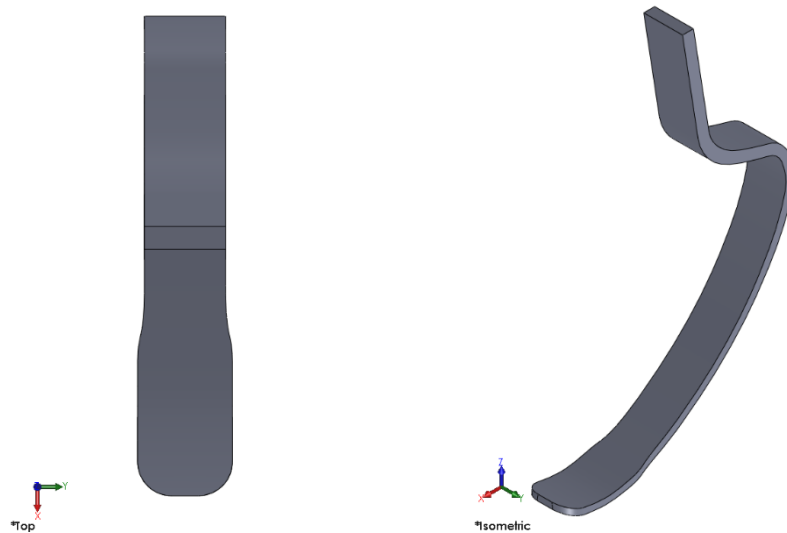


Figure 2.2.7 – Result of the *Extruded Cut* performed along the width of the prosthetic; top (left) and isometric (right) views.

Although, the creation of the holes, for the attachment of the prosthetic to the socket, is not performed since in the component available they are not present.

The updated CAD model, according to the features of the real component which will be tested, is displayed in Figure 2.2.8.

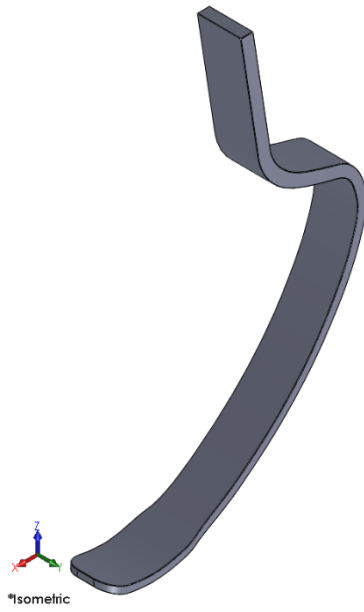


Figure 2.2.8 – Updated CAD model; isometric view.

3. Static test, grippers design for the MTS machine

The static test was intended to be performed on the MTS machine, available in the DIMEAS laboratory at Politecnico of Torino. Due to time and costs issues, the tests was not performed, but the design of the grippers to perform the experimental activity was entirely prepared. Indeed, as explained in Paragraph 3.2, the shape of the Cheetah Xcel does not allow to perform the test using the grippers already present on the machine, thus it was necessary to design new ones.

The description of the design is broken down into three main assemblies: the pin assembly, Paragraph 3.3, upper gripper assembly, Paragraph 3.4, and lower gripper assembly, Paragraph 3.5. Given the necessity to rotate and move linearly the prosthetic during the test, the description of the design of the lower gripper needs more considerations and a FEM analysis (Paragraph 3.5.5.1) to verify the flow of forces when load is applied on the prosthetic.

3.1 Static test prevision

The static test intended to be performed is the result of bibliographic researches about methods of how to perform stiffness measurements on ESR blade prosthetics for athletes. Indeed, in the case of prosthetics used for high level of activity, such as sprinting, no standardize test is currently present. The existing test protocol, such as ISO 10328, defines load and inclination of the platform to perform the static test according to the walking condition. Even the blade prosthetic for running purposes are verified through this standard. However, to have a real access to the mechanical characteristic of the prosthetic in the conditions it is intended to be used, different parameters from the standard ones have to be considered and applied in the test.

All the researchers conducted on blade prosthetic stiffness [14], [13], [12], demonstrate that such mechanical characteristic varies depending on multiple conditions, indeed such component does not have a linear force-displacement behaviour when speed of the gait is higher than 3 m/s, which is the velocity for which jogging is defined. Stiffness depends on load value, velocity of gait and dimension of the prosthetic. The manufacturers do not report the stiffness values, but they classify the prosthetic models in stiffness categories based on the body mass of the user and the intended activity.

In the ISO 10328 [8], two loading conditions are considered to analyse statically the prosthetic. In this way, the two moments in which the force peak is verified are simulated. Such moments are at the early stance phase of walking (defined in the standard as “loading condition I”), in which the heel is loaded, and at the late stance phase (“loading condition II”), in which the forefoot is loaded. Studies on the running biomechanics [4] demonstrated that just one peak of the force is verified in a gait just after the impact, corresponding to the propulsion moment. For this reason, the just one loading condition is performed in the static test, corresponding to the moment in which the GRF peak is verified.

Given the empirical results obtained by empirical measurements on running situations by different researches [14], [13], [12], the prosthetic is usually inclined of 60-80° with respect the horizontal plane, in such a way to have a theoretical centerline from the distal end of the prosthetic, which is the loaded part, to the midpoint of the fixing bolt that would attach the prosthetic socket. As suggested by the Dyer at al. [14]] analysis, it the distal end horizontal motion should be constrained. Furthermore, it underlines the fact that the ground reaction strike point is determined by different variables, such as race length, running round the bend, athlete fatigue. Given that, since this strike point would be different between all runners, usually distal end is loaded area.

The static test designed on the MTS machine at DIMEAS allows to have a flexible configuration: the prosthetic can be rotated and moved in such a way to load the distal end and avoid slippage with

the load cell. However, the initial position of the blade prosthesis is already inclined of 60° with respect the horizontal direction.

During running, the peak force ranges between 2.1 and 3.3 times the body weight for speeds from 2.5 m/s to 10.8 m/s. Hence, for this test 3 times the maximum weight of the prosthetic category, which is 147 kg, is considered: 4300 N.

In general, the load is applied at a constant rate of 100N/s. Indeed, the standard ISO 10328, indicate a rate in between 100 and 250 N/s.

3.2 Issues in performing the static test on the MTS machine

To analyse the material properties of the prosthetic, it is necessary to perform a static test. From the evaluation of the deformation assumed by the component when a vertical load is applied, its stiffness properties can be evaluated.

The machine available in the mechanical laboratory, DIMEAS, at Politecnico of Torino is the MTS machine, shown in Figure 3.2.1.



Figure 3.2.1 – MTS machine, DIMEAS Politecnico of Torino.

The lower gripper of the machine clamps the prosthetic vertically. Aluminium blocks, inclined of 60° where produced to incline the prosthetic and be able to perform the static test, but they cannot fit properly in the lower clamping system.

Given the shape of the blade, the tangential point, to the horizontal plane, at the toe level, does not coincide with the vertical plane where the upper part of the prosthetic is clamped and where the load cell, placed at the upper gripper, is. What just explained can be better understood by looking at the CAD model in Figure 3.2.2.

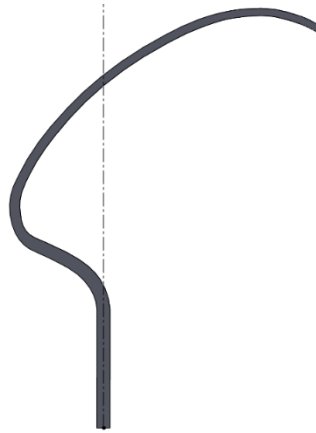


Figure 3.2.2 – CAD model positioned according to the clamping system of the MTS machine, DIMEAS, Politecnico of Torino.

Given this problem, the necessity of designing new grippers rose.

3.2.1 General issues for the design of new grippers

For the design of the grippers some constraints have to be taken into account. At the lower gripper level, the aim is to not have a creation of moments and additional forces with respect to the ones applied from the upper gripper and the frictional ones caused by the contact in between upper plate and prosthetic toe. To avoid this, the centre of contact in between prosthetic and the clamping system should lie on the plane of symmetry of the lower gripper and of the contact point with the upper gripper. Overall, the plane of symmetry of the upper gripper, the contact point with the prosthetic toe, the centre of the clamped part of the prosthetic and the plane of symmetry of the lower gripper have to be aligned, as shown in Figure 3.2.1.1.

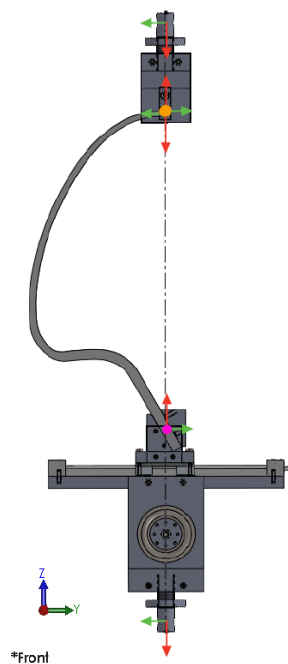


Figure 3.2.1.1 – Scheme of the upper and lower grippers, contact point (orange point) and centre of the prosthetic clamped part (violet point) on the same vertical axis. Representation of the free body forces.

By performing a FEM simulation on the prosthetic model, the deformed shape, when a load of 2400 N is applied, can be obtained. Given this approximative shape it is possible to visibly see the difference in the grippers setup at the end of the test, when the maximum load is reached, as shown in Figure 3.2.1.2. In this can the rotating part of the lower gripper is inclined of 5° and the sled is displaced of 15 mm. Notice that the two setups displayed in the two images is just an approximation to obtain a visual result. Indeed, the prosthetic model material will be calibrated after the static test and the horizontal plate of the upper gripper can be also inclined at the beginning of the test, depending on what will be decided just before starting the test.

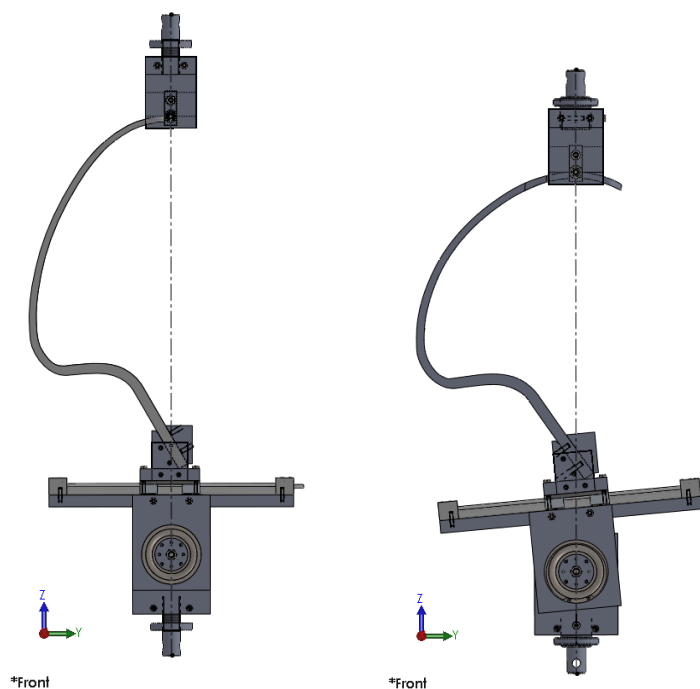


Figure 3.2.1.2 – Grippers setup with the undeformed prosthetic (left) and the deformed prosthetic (right).

To be sure to avoid the creation of additional forces and moments while loading the prosthetic, the force read on the load cell must be the equal to the one imposed minus the frictional force. If it is lower, it means that additional reaction forces and moments are created. Thus, during the test, it is important to be able to modify the prosthetic position in such a way to read always the maximum load on the load cell. As consequence, the design will have to provide flexible grippers in order to be able to adjust the position of the prosthetic and of the upper gripper plate before or during the test. In particular, the prosthetic must be able to rotate and displace, while the upper gripper contact plate must be able to rotate.

To reduce the production costs, the shapes of each part has been simplified, no rounds, cuttings, fillets or chamfers are designed where it is not necessary. Any additional manufacturing work increase the cost of the components. For this reason are mainly chosen hexagonal bots since they require an only simple drill, while other screws, as the flat head ones, require more complicated cuttings.

Regarding the height of the blind holes of the screws, the standard requirements are followed: the threaded depth must be at least $1.5/2$ times the nominal diameter of the bolt for steel alloy parts and 2.5 times for aluminium ones. Since during the design phase is was unknow the material of the parts, since the cheapest one between aluminium and steel alloy was preferred, the depth of the screw drills was set to 2.5 times the nominal diameter.

3.2.2 BOM of the entire design

In Figure 3.2.2.1, the isometric and right views of the entire assembly CAD model are displayed.

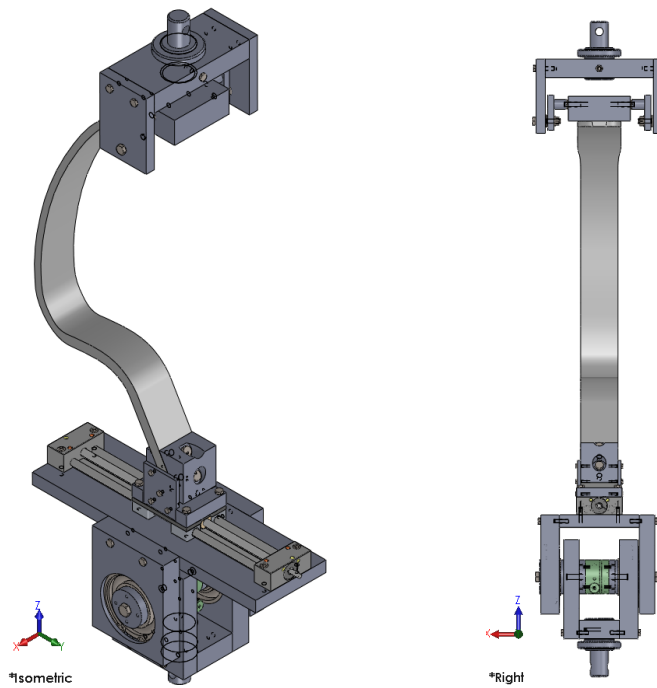


Figure 3.2.2.1 – Isometric (left) and right (right) views of the entire assembly.

The ballooned drawing of the entire assembly, is displayed in Figure 3.2.2.2, the corresponding BOM is reported in Table 3.2.2.1. In the BOM table, the material of the components to produce is not declared since it will be discussed with the producers if using aluminium or steel alloy, according to which one will require the lowest overall price. Indeed, aluminium purchasing results to be more expensive, but the manufacturing of it is easier and thus cheaper.

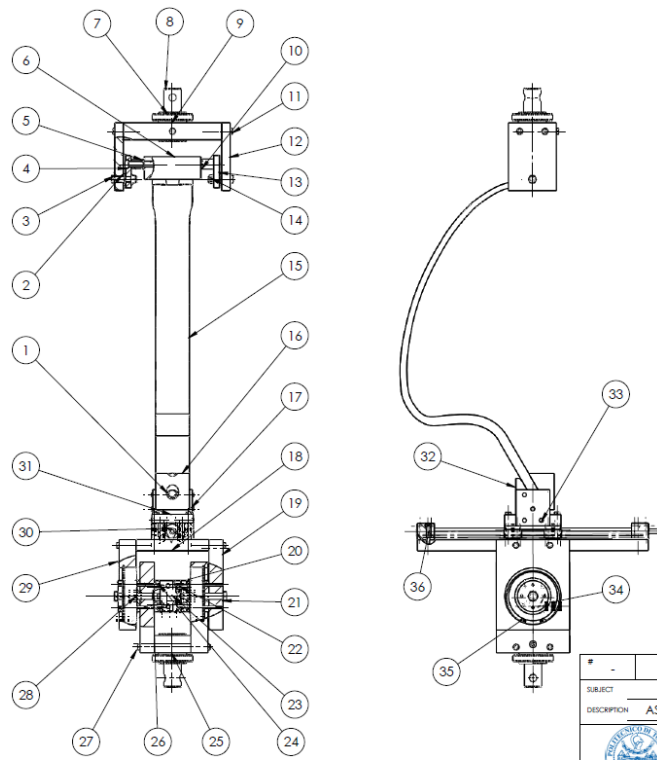


Figure 3.2.2.2 – Ballooned drawing of the entire assembly.

Table 3.2.2.1 – Legend (upper one) and BOM tables.

Legend	
	Parts to drill
	Parts to produce
	Comercial parts to buy
N. parts to produce	23

ITEM NO.	PART NUMBER	QTY.
1	ISO 4014 - M8 x 40 x 22-C	2
2	Washer ISO 7090 - 10	4
3	ISO 4014 - M8 x 40 x 22-C	2
4	ISO 1207 - M8 x 60 --- 38C	2
5	Washer ISO 7090 - 8	4
6	RotatingPlate_UpperGr	1
7	CircularNut	2
8	Pin	2
9	HorizontalSupport_UpperGr	1
10	Spacer_UpperGr	2
11	ISO 4014 - M6 x 30 x 18-C	5
12	VerticalSupport_UpperGr	2
13	VerticalPlate_UpperGr	2
14	Hexagon Flange Nut ISO - 4161 - M8 - C	2
15	CheetahXcel_CAD_real	1
16	AluminiumBlock2	1
17	AluminiumPlate	2
18	RotatingPlate_LowerGr	1
19	VerticalSupport_LowerGr	2
20	B27.7M - 3AM1-55	2
21	ISO 4014 - M10 x 70 x 26-C	2
22	ISO 4762 M5 x 12 --- 12C	8
23	MDV 55 AV1	1
24	Parallel Pin ISO 8734 - 4 x 26 - A - St	16
25	HorizontalSupport_LowerGr	1
26	Part1	2
27	ISO 4014 - M6 x 40 x 18-C	12
28	RotatingSpacer	2
29	VerticalSupport_LowerGr_Bearing	2
30	LinearSled	1
31	PlateSled	1
32	AluminiumBlock1	1
33	ISO 4015 - M4 x 20 x 14-C	8
34	ISO 15 ABB - 0255 - 14,SI,NC,14_68	2
35	B27.7M - 3BM1-100	2
36	ISO 4762 M6 x 35 --- 24C	5

The only component not marked in the BOM table is the rotating table, since it is already available in the DIMEAS department of Politecnico of Torino and does not need manufacturing adjustments,

3.2.2.1 Aluminium blocks

The components which have just to be drilled are two plates and two blocks in aluminium. They were already produced from the University of Groningen to perform the static test on the MTS machine of Politecnico of Torino. Indeed, remotely the issues in performing the static test with the clampings already available for the MTS machine were not known, thus a couple of aluminium plates and of aluminium block were designed and produced at the University of Groningen. Such components will be reused in the design of the new grippers to fix the prosthetic on the lower gripper. To avoid slippage of the Cheetah Xcel with respect the blocks, which are really smooth, it is decided to couple them through the use of bolts.

The drilling must be perpendicular to the inclination of the prosthetic, which is of 30° with respect the vertical direction, according to the slope of the inclined edge of the two aluminium blocks. The hexagonal bolts used are M8 since, according to the “Instructions for Use” indications of the Cheetah Xcel model [20], the prosthetic is fixed to the socket with bolts $3/8$ ”, which correspond to a M8 in the metric units of measurement. In Figure 3.2.2.1.11 the assembly prosthetic-aluminium blocks is displayed.

It is suggested to perform such holes putting all together the prosthetic and the two block and proceed with the drilling. Indeed, also the prosthetic has to be drilled.

To avoid damaging the prosthetic, chamferes have also to be relised at the corners in contact with the prosthetic, as visible in the right image of Figure 3.2.2.1.1.

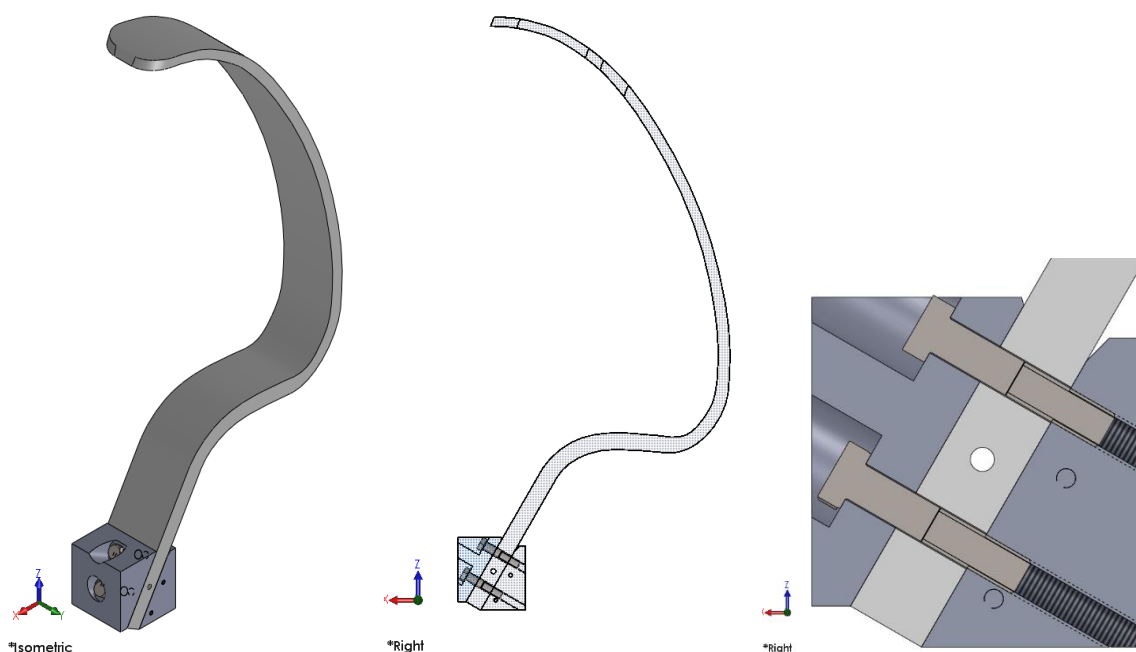


Figure 3.2.2.1.1 – Connection in between Cheetah Xcel and the two aluminium blocks.). Isometric view (left), right view with transparent components (centre) and zoom in of the section right view (right).

Although, the aluminium plates are used to fix the Cheetah Xcel assembly displayed in Figure 3.2.2.1.1 to the lower gripper, in particular to the linear sled. The connection designed happen through the use of bolts M4 on the two sides of the block. Thus, the function of the two plates is also to constrain laterally the assembly. For each side, two screws are threaded into the aluminium block which lies on the sled and other two to the sled plate designed. In Figure 3.2.2.1.2, the assemblage just explained is displayed.

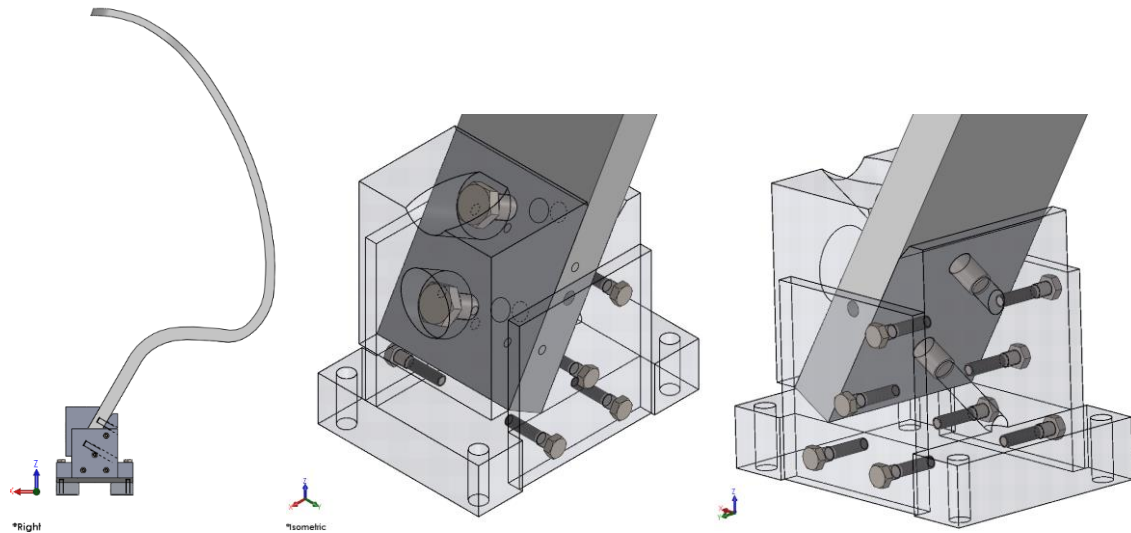


Figure 3.2.2.1.2 – Connection of Cheetah Xcel to the sled. Right view (left), zoom in of the isometric view with transparent components (centre) and zoom in with transparent components (right).

The aluminium components to be drilled are displayed in Figure 3.2.2.1.3. The aluminium plates have the same holes, unlike the blocks.

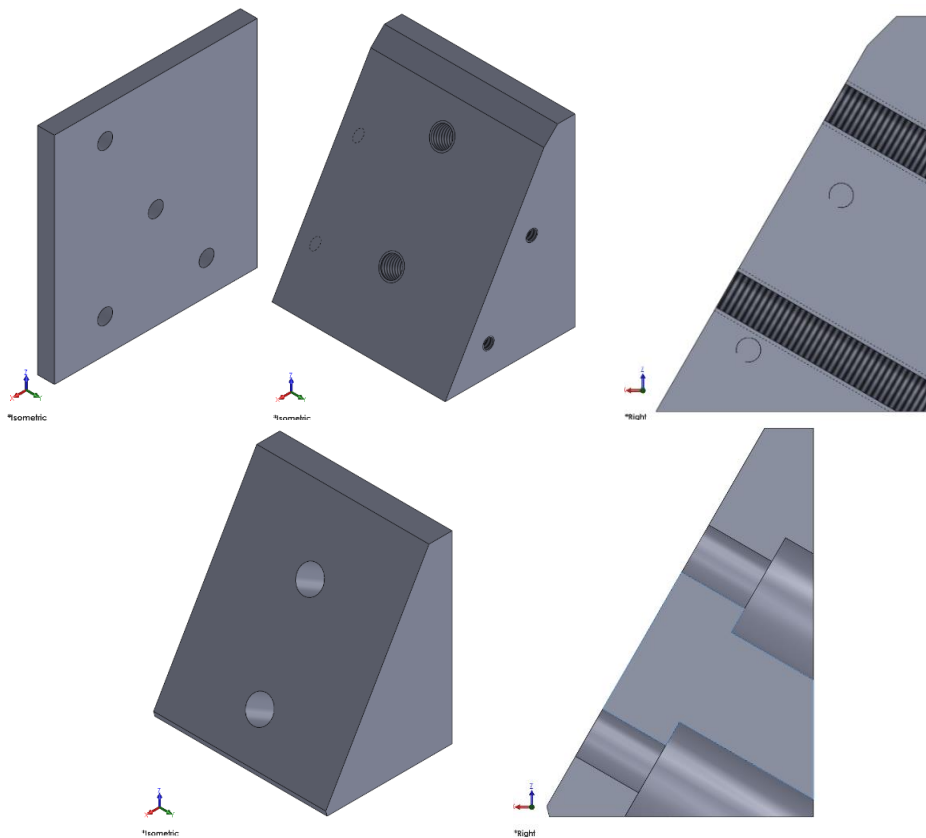


Figure 3.2.2.1.3 – Isometric view of the aluminium plates (up-left); isometric (up-center) and section right (up-right) views of the aluminium block to place downwards the prosthetic; isometric (down-left) and section right (down-right) views of the aluminium block to place upwards the prosthetic.

3.3 Pin assembly

At the beginning, the aim was to reuse the pin and the circular nut of the grippers already present in the MTS machine, Figure 3.3.1. Nevertheless, their thread is difficult to determine by measurements: the outer diameter is around 49 mm, but the ISO metric threads are M48 or M50. Thus, to avoid coupling problems, new parts are designed.

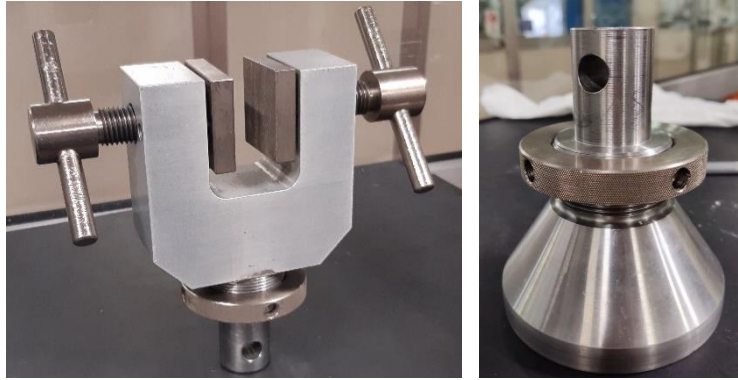


Figure 3.3.1 – Lower and upper grippers of the MTS machine already present in the DIMEAS laboratory, Politecnico of Torino.

The pin is set in the machine by placing it in a hollow component displayed in Figure 3.3.2. They are coupled through the use of a transversal parallel pin; the relative position is fixed threading the circular nut to be in contact with the hollow component, applying on the transversal pin a shear stress. Thus, to have the right coupling with the component already present in the machine, it is necessary to reproduce some dimensions of the pin already present.

The measurements of the pin and of the circular nut have been taken (Figure 3.3.3).

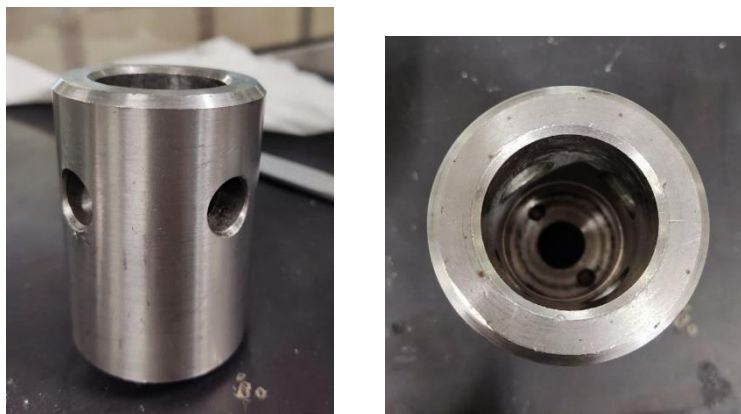


Figure 3.3.2 – Hollow component of the MTS machine grippers, already present in the DIMEAS laboratory, Politecnico of Torino.

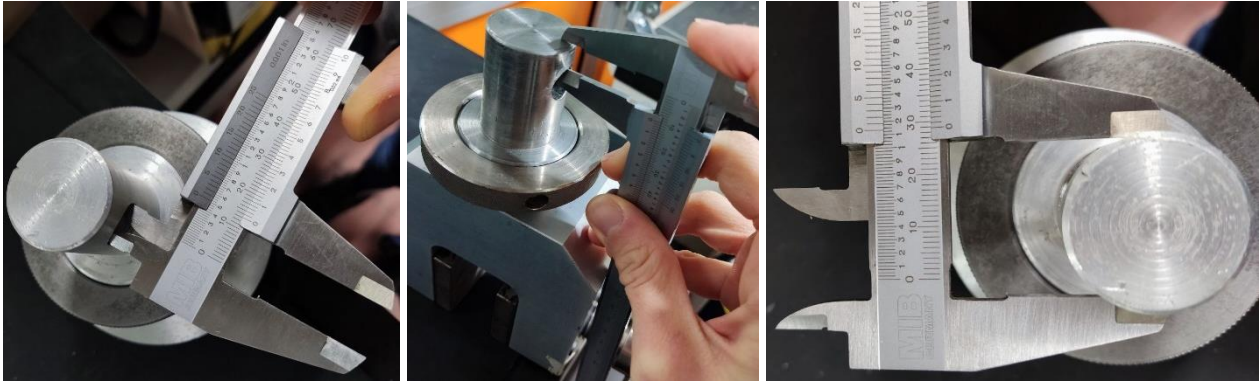


Figure 3.3.3 – Measurements of the pin already present in the DIMEAS laboratory, Politecnico of Torino.

The pin and circular nut designed are displayed in Figure 3.3.4. They are coupled through a thread M48x2, according to the ISO standard. The lower, no threaded part, of the pin is the same of the one already present, in such a way to have the right coupling with the hollow part. Even the circular nut has maintained the same overall dimensions.



Figure 3.3.4 – Isometric view of the pin assembly designed.

On the other hand, the upper thread is higher with respect the original one, in such a way to have more fillets gripping in between the pin and the horizontal plate of the grippers and so to have a better fastening. Furthermore, since the horizontal support of the grippers have a through-hole thread, the vertical position must be constrained through the use of a transversal bolt. Thus, on the upper part of the pin, a transversal through all threaded hole is realised and a simple one on the horizontal supports. The holes are through all the component in such a way to have easier and hence cheaper machining. Given the difference in the upper and lower gripper, for the lower gripper it is better to have the hole along the X direction, while for the upper one it is better along the Y direction. This because it is better to drill the horizontal component long the shortest width, to avoid using too long screws and having more complex machining operations. In any case, since the pin couples with an hollow component (Figure 3.3.2) which has 4 holes, the same pin can be used and just rotated of 90° one with respect to the other.

In Figure 3.3.5 the lower gripper coupling with the pin is displayed. A hole on the vertical support plate is realised to insert the bolt. The screw used is the same already utilised for the assembly of the linear sled: M6x35.

In Figure 3.3.6 the upper gripper coupling with the pin is displayed. Here the hexagonal bolt is used and it is the same already used in other parts of the entire assembly: M6x30.

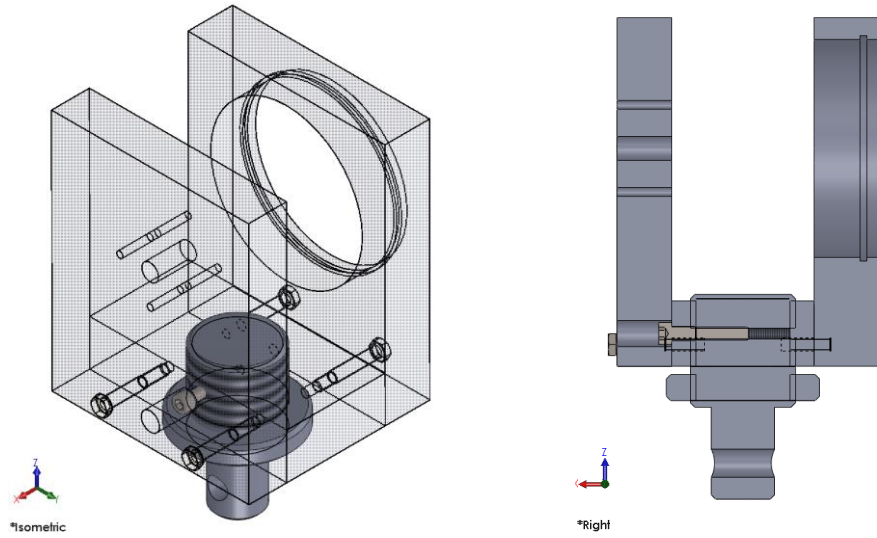


Figure 3.3.5 – Lower gripper coupling with the pin assembly. Isometric (left) and section right (right) views.

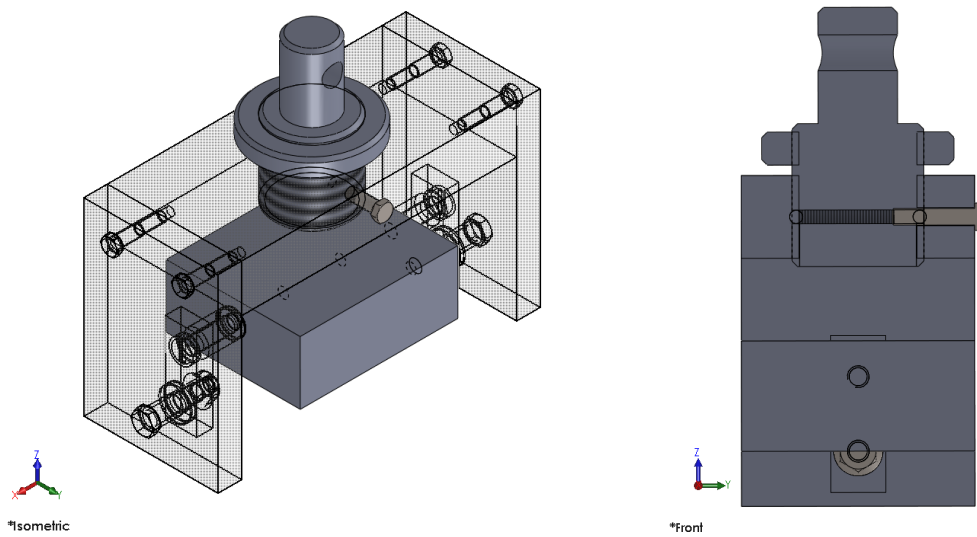


Figure 3.3.6 – Upper gripper coupling with the pin assembly. Isometric (left) and section right (right) views.

3.4 Upper gripper

In Figure 3.4.1, the upper gripper design is displayed.

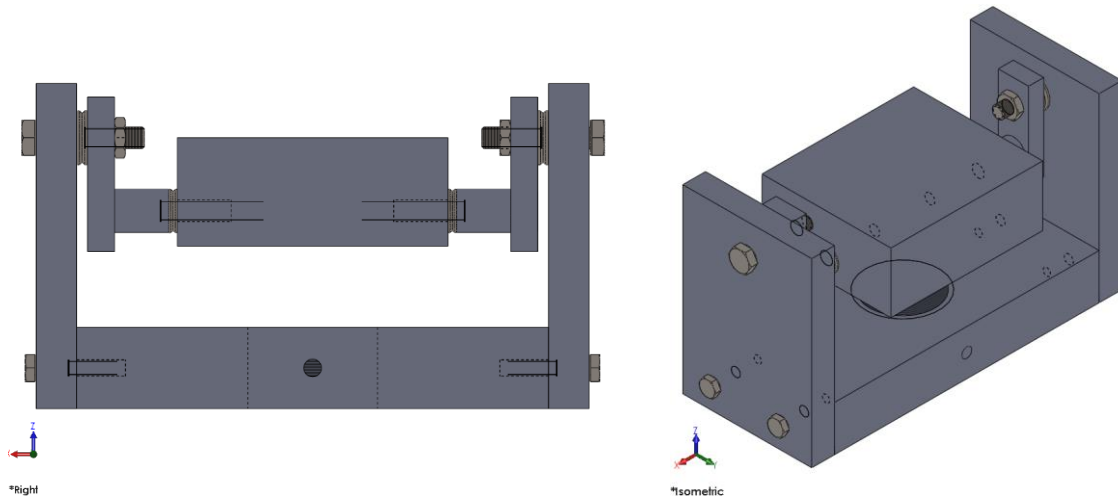


Figure 3.4.1 – Upper gripper; frontal (left) and isometric (right) views.

This gripper is mounted on the travers of the machine which, during the test displaces vertically applying, as consequence a defined amount of force, controlled by the load cell.

The plate is mounted in a U configuration to reach stability. The plate assembly is an inverted pendulum, so the stability is reached when the force applied to the prosthetic lies downwards with respect the centre of the screws which hold it. The best solution is to have the contact point at the level of the bolts which hold the plate, in such a way to not have creation of reaction moments which could stress excessively the load cell and break it. In Figure 3.4.2 a representative scheme of what just mentioned is displayed. Note that, as depicted in Figure 3.4.2, the force applied is vertical (F_z), but during the test, there is the creation of a frictional force along Y direction.

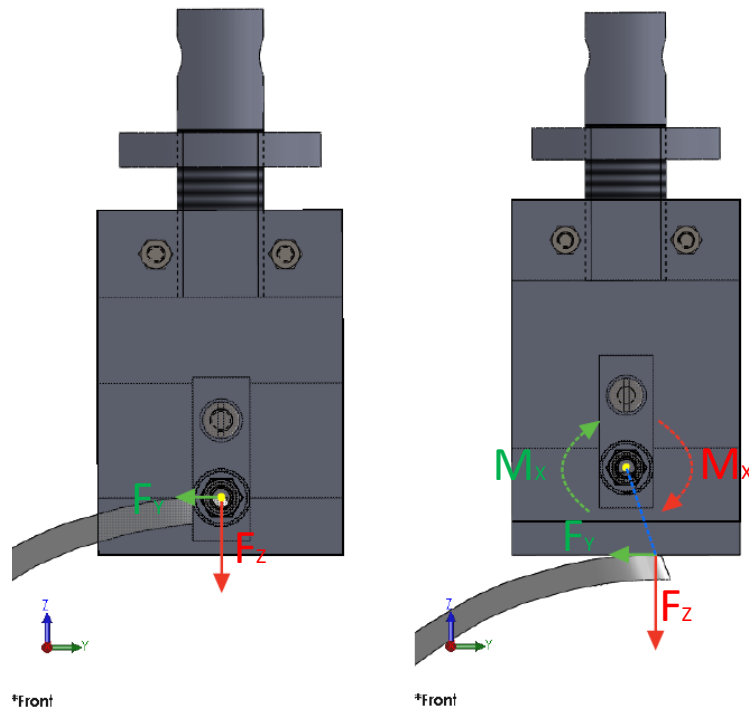


Figure 3.4.2 – Scheme of the moment creation on the upper gripper if the contact point is not concentric to the fastener which hold the contact plate; no moment creation (left) and moment creation (right) cases. The yellow point is concentric to the screws; the blue line (right image) represents the arm for which there is the creation of moments.

During the assembly, the contact plate can be rotated. In this way it is possible to control the tangency with the prosthetic in such a way that the contact point lies along the plane of symmetry of the gripper and the centre of the bolts, avoiding the creation of reaction moments.

The ballooned drawing of the upper gripper assembly, with the corresponding BOM table, is displayed in Figure 3.4.3.

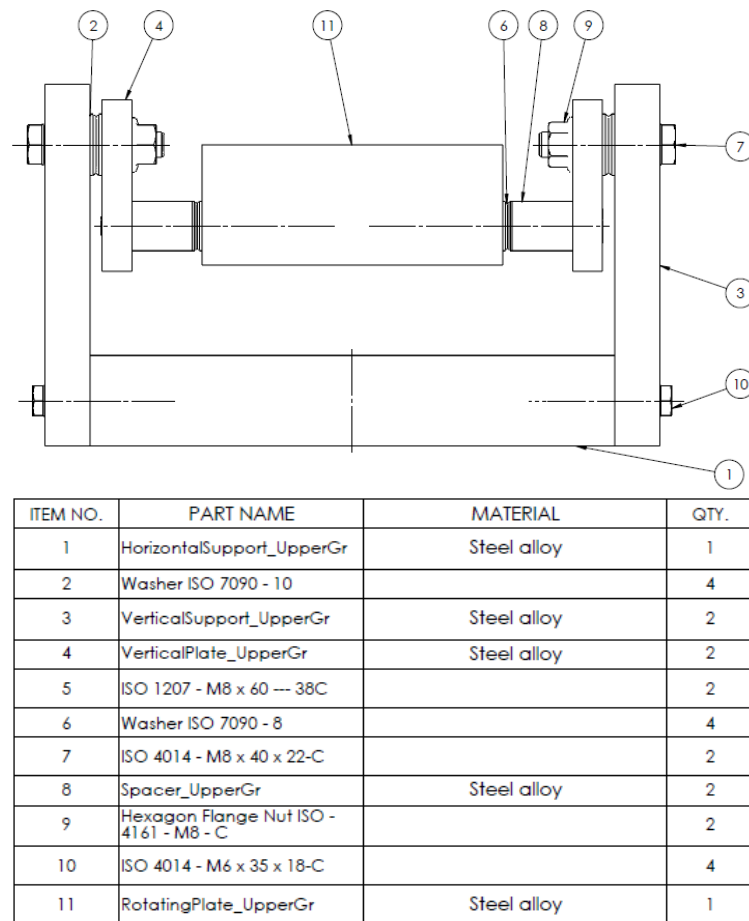


Figure 3.4.3 – Ballooned upper gripper assembly and corresponding BOM table.

3.4.1 Friction evaluation

As already mentioned, the aim of having a flexible design is to be able to change the position of the prosthetic and of the horizontal plate of the upper gripper in order to avoid stressing the load cell. In particular, the position is changed when an horizontal load is visibly sensed on the upper gripper. A simulation to understand the rough value which can assume the frictional force when the maximum load intended to be applied is reached.

In the simulation just the assembly of the upper gripper and the prosthetic CAD are considered.

Since it is still unknown the position that will be set during the test of the prosthetic and of the plate in contact with it, two configurations are run. The first configuration represents the initial condition when the prosthetic touches the ground, because the prosthetic is loaded at an upper point with respect the distal end. In the second one, instead, the contact plate is set horizontal, thus parallel to the XY plane. The contact point, which must lie on the YZ plane, occurs at the distal end. They are displayed in Figure 3.4.1.1.

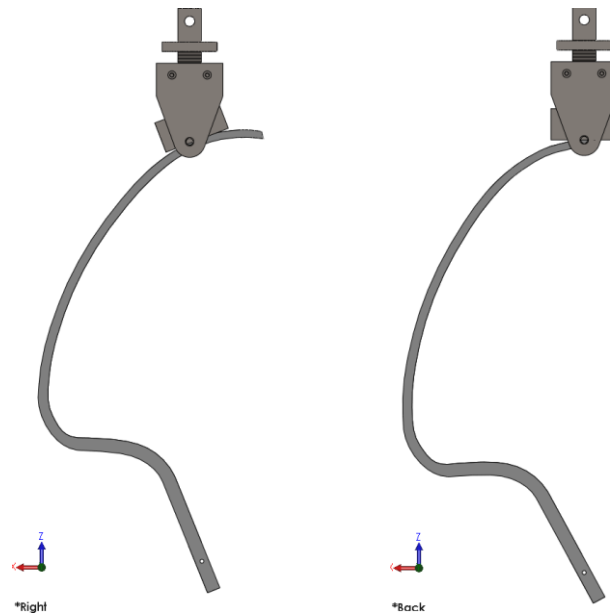


Figure 3.4.1.1 – Configuration 1 (with the contact plate of the upper gripper inclined of 20°) on the left and configuration 2 (with the contact plate horizontal) on the right.

To make the simulation lighter and avoid interference issues, all the fasteners and the nuts were not included in the analysis. For the other components the contact characteristics listed below are set.

- The bolted contact in between all the parts is maintained. In this way the nodes of the surfaces in contact coincide in between the parts.
- Since the pin is connected to the circular nut and the plate of the upper gripper assembly through a thread, interference is detected. To be able to mesh the assembly, the connection in between the pin and the other two parts was defined as “Shrink fit”.
- In between the contact plate of the upper gripper and the prosthetic a no penetration contact was set and a friction coefficient of 0.5 was defined. As suggested in the article of Taran Packer, the mesh of the bodies in between which there is a frictional contact should be different. In particular the “origin” face should have a finer mesh than the “target” one.

The load has been applied on the upper part of the contact plate, as displayed in Figure . Since the displacement of the upper gripper occurs vertically, the force has just a component along Z. nevertheless, in the second configuration, since the plate is horizontal, an initial value along the X direction was given just setting the force inclined of 1° with respect the vertical direction. The axial force due to friction, is the one this study is interested in.

The upper gripper has been constrained just at the pin with a circular constraint. This is the actual constraint which is present during the test. If just this constraint is applied at the gripper, a small displacement of 1 mm occurs along the Y direction and a frictional force, along this direction, at the contact with the prosthetic is present. If instead even roller constrained are applied at the other components of the upper gripper to allow just the vertical displacement, the Y frictional contact load is almost nil.

Moreover, at the prosthetic the two faces in contact with the lower gripper are constrained through rollers and the face in between them is fixed.

In Figure 3.4.1.2, the force and constraints applied are shown in both the configurations.

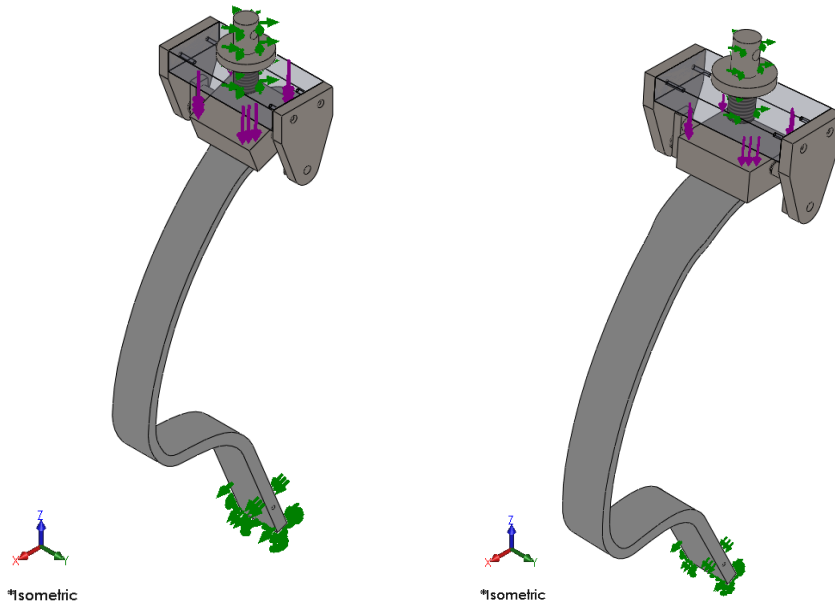


Figure 3.4.1.2 – Load and constraints applied, configuration 1(left) and 2 (right), isometric view.

All the analyses performed are linear because Solidworks failed in finding the solution through the large displacement method. Different trials were done changing the solver, the mesh magnitude and the force value, but the solution always failed. The non linearity regards the prosthetic behaviour, which in this case is not of interests, thus it is reasonable to perform a linear analysis. The parameters of the first simulation are resumed in Table 3.4.1.1.

Table 3.4.1.1 – Configuration 1 characteristics.

Parameter	Direction	Value
Prosthetic inclination	68° wtr XY plane	
Contact plate inclination	20° wtr XY plane	
Force [N]	Vertical direction (along Z)	2400
B.C. prosthetic	Two faces with roller constraint and one fixed	
B.C. upper gripper	Circular constrain at the pin	

In Figure 3.4.1.3, the frictional force due to the contact in between prosthetic and upper gripper are displayed. F_x results to be -1000 N.

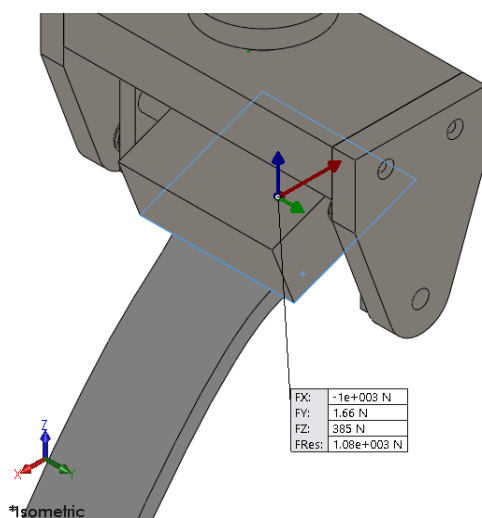


Figure 3.4.1.3 – Frictional force results configuration 1; isometric view.

The parameters reported in Table 3.4.1.2 are applied. The choice to incline the force of one degree with respect the vertical direction is just to give an initial friction condition: the component of the force along X direction is not completely zero.

Table 3.4.1.2 – Configuration 2 characteristics.

Parameter	Direction	Value
Prosthetic inclination	61° wtr XY plane	
Contact plate inclination	Parallel wtr XY plane	
Force [N]	1° wtr the vertical direction	2400
B.C. prosthetic	Two faces with roller and one fixed	
B.C. upper gripper	Circular constrain at the pin	

In Figure 3.4.1.4, the frictional force due to the contact in between prosthetic and upper gripper are displayed. F_x results to be -1200 N.

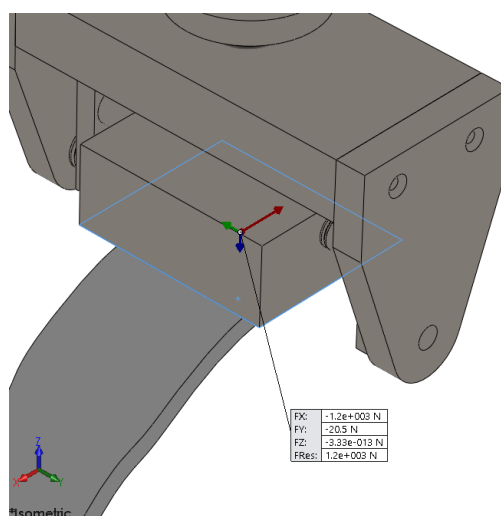


Figure 3.4.1.4 – Frictional force results configuration 1; isometric view.

3.5 Lower gripper assembly

In Figure 3.5.1, the lower gripper design is displayed. The rotating table and the linear sled are transparent, since they are commercial parts, thus not to be produced.

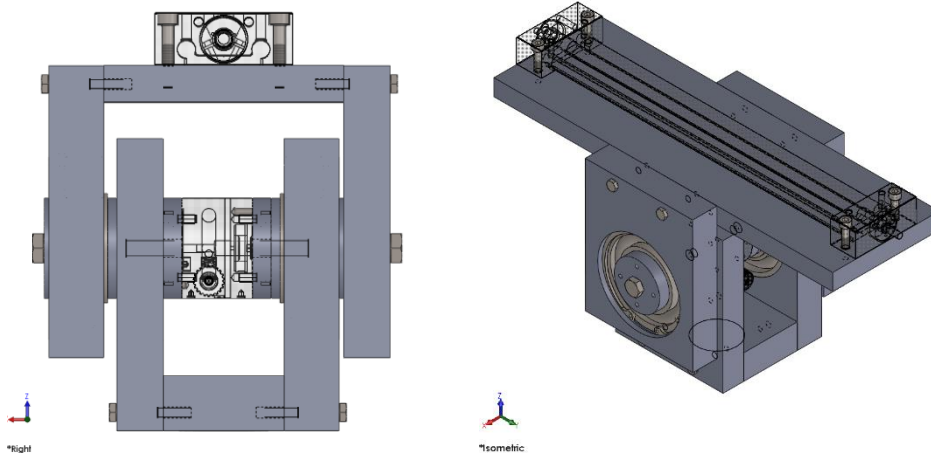


Figure 3.5.1 – Lower gripper; frontal (left) and isometric (right) views.

The entire assembly is divided in multiple subassemblies:

- “ASSEMBLY_FixedLowerGripper”; it is in contact with the pin and it is fixed;
- “ASSEMBLY_RotatingTable”; it connects the other two assemblies of the lower gripper, allowing a relative rotation in between the two;
- “ASSEMBLY_RotatingLowerGripper”; it can rotate during the test and holds the prosthetic.

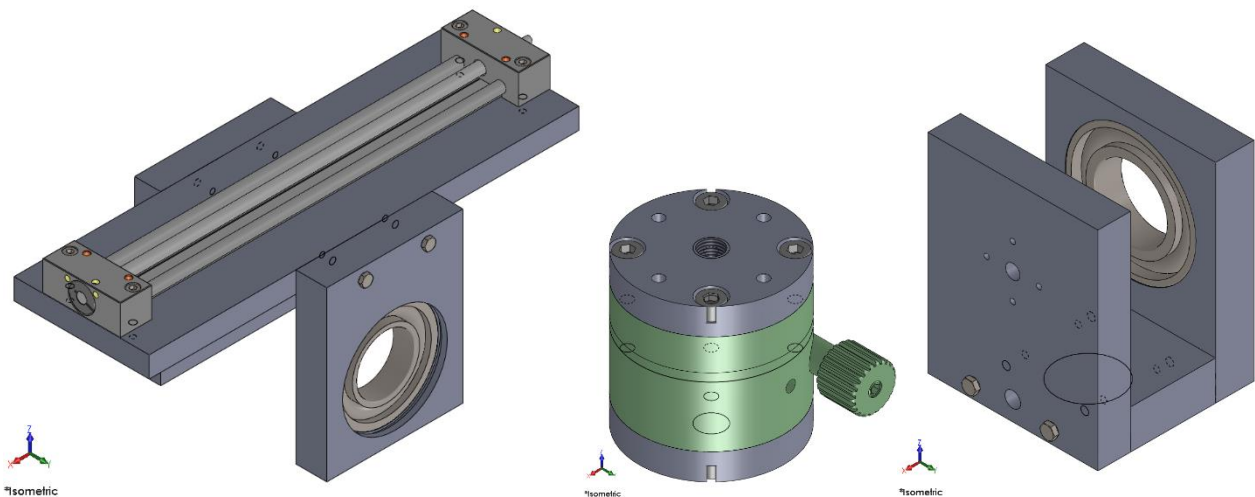


Figure 3.5.2 – Lower gripper subassemblies; “ASSEMBLY_FixedLowerGripper” (left), “ASSEMBLY_RotatingTable” (centre) and “ASSEMBLY_RotatingLowerGripper” (right).

3.5.1 Lower gripper BOM

The ballooned drawing of the upper gripper assembly, with the corresponding BOM table, is displayed in Figure 3.5.1.1. From the BOM information, it is possible to better understand how the three subassemblies are connected through the use of pins and screws. The role of the two screws M10 is

to constrain the assembly axially, in such a way that the rotating table will not hold axial loads. However, the parallel pins are used to position all the parts which have to be concentric: the rotating table and the vertical supports of the fixed and rotating lower gripper subassemblies.

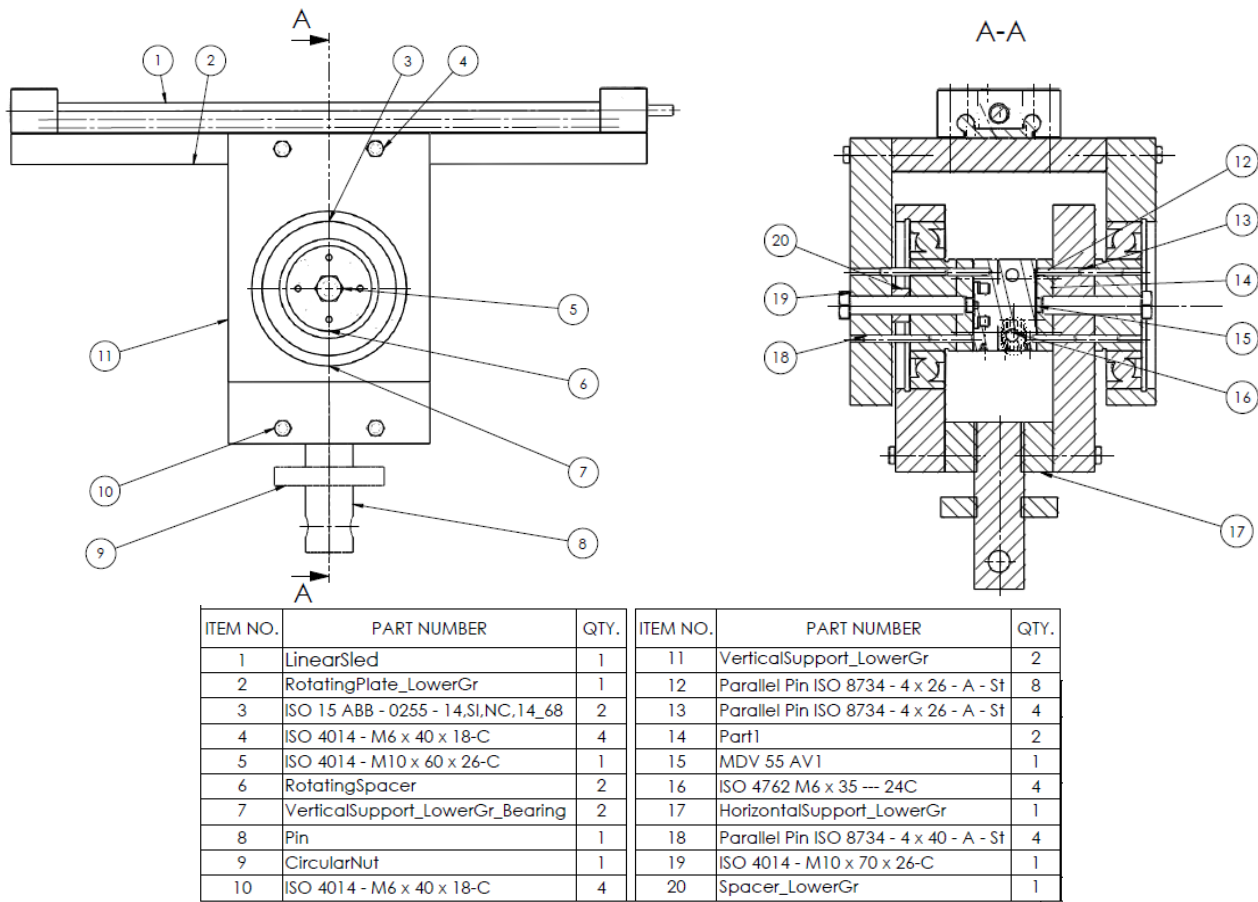


Figure 3.5.1.1 – Ballooned lower gripper assembly and corresponding BOM table.

3.5.2 Rotating and non-rotating parts

To better understand the assembly design, it is important to point out the parts in rotation and the one fixed, in such a way to understand which are the adjacent faces where there is a relative motion in between the parts. In Figure 3.5.2.1, the fixed part is grouped by orange lines, while the rotating part is pointed out through violet lines. To distinguish better the faces in between rotating and not rotating parts, they are marked through light blue lines.

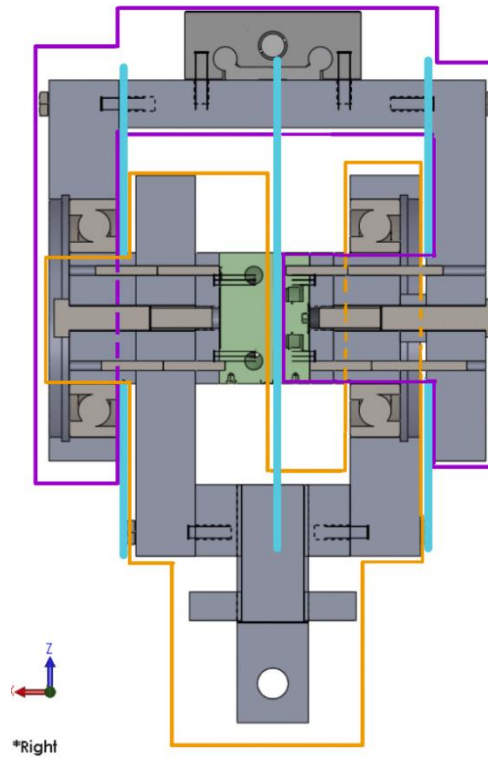


Figure 3.5.2.1 – Lower gripper assembly, distinction in between the rotating (violet curve) and the non-rotating (orange curve) parts. The adjacent faces in between parts in relative movement are marked in blue.

As visible in the Figure 3.5.2.2, there are internal parts which have a different motion from the ones which hold them, the relative motion between them is allowed by the use of bearings. In particular, in the assembly two angular contact ball bearings in X configuration are used. They have an inner diameter of 55 mm, an outer one of 100 mm and a width of 21 mm. For these type of bearings one inner and one outer ring have to be constrained axially to avoid the disassembly of the bearing. Hence, Seeger rings are used. According to the standards, the dimensions of the housing of the rings are followed. Figure 3.5.2.2 shows a zoom in of the disposition of the bearings and the presence of the housings of the Seegers are present on the two opposite sides for each bearing. The yellow dashed lines of the image represent the line of action of the bearings, which indeed is in X configuration.

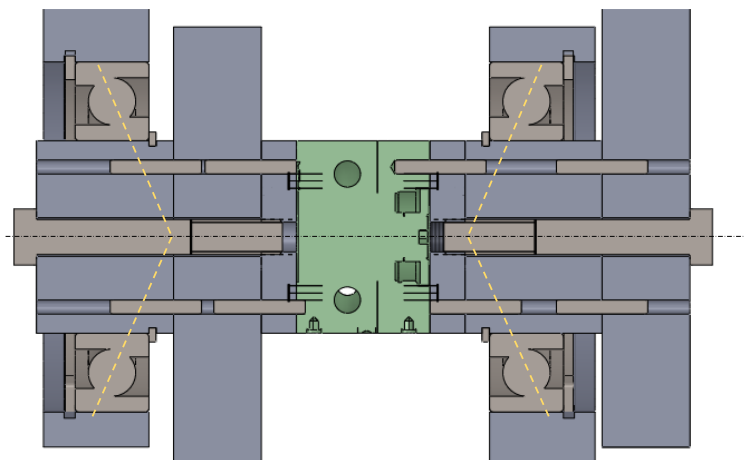


Figure 3.5.2.2 – Bearings disposition. The yellow dashed lines represent the line of action of the bearings, they are set in X configuration.

While in the rotating table no precaution in between the faces in relative movement have to be taken into account, since the aim of the device itself is to have the relative motion of the parts, for the other two faces where the two adjacent parts are in relative movement (marked in light blue in Figure 3.5.2.1), it is necessary to consider a space in between the rotating and the non-rotating components. While on the left the Seeger ring housing already created a gap itself, on the right, to create a space in between the two vertical supports, the RotatingSpacer has been extruded of 11 mm more with respect the minimum length given by the bearing width and the Seeger housing.

3.5.3 Symmetry

As visible in Figure 3.5.3.1, the assembly is not symmetric since the position of the bearings is required in not symmetric locations. However, the aim is to maintain the position of the linear sled and, as consequence, of the prosthetic on the plane of symmetry of the pin hole, which is represented by the vertical construction line of Figure 3.5.3.1.

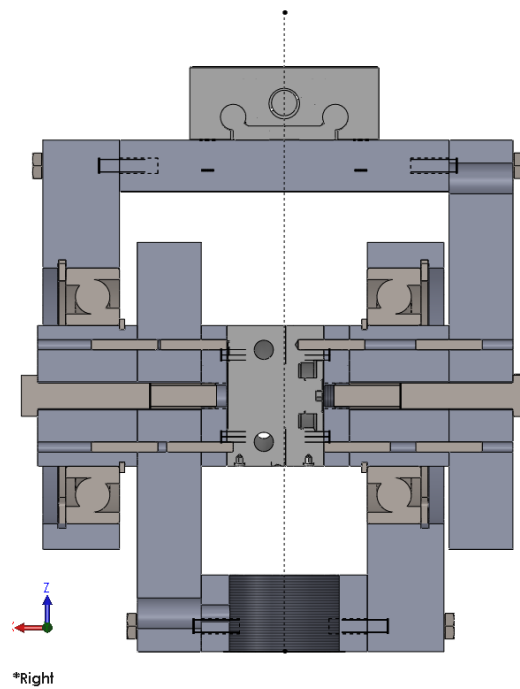


Figure 3.5.3.1 – Lower gripper assembly; the sled and pin must lie on the same vertical line.

3.5.4 Linear sled

To move and control the displacement of the prosthetic, a commercial linear sled is used. In particular the model Dryline SHT-12 linear module with trapezoidal thread of the brand Igus is selected (Figure 3.5.4.1).

Thanks to the coupling in between the trapezoidal screw and the central plate, by rotating the screw, the sled moves linearly. This mating allows a better control of the displacement. The material of the component is stainless steel and the stroke selected is 250 mm.

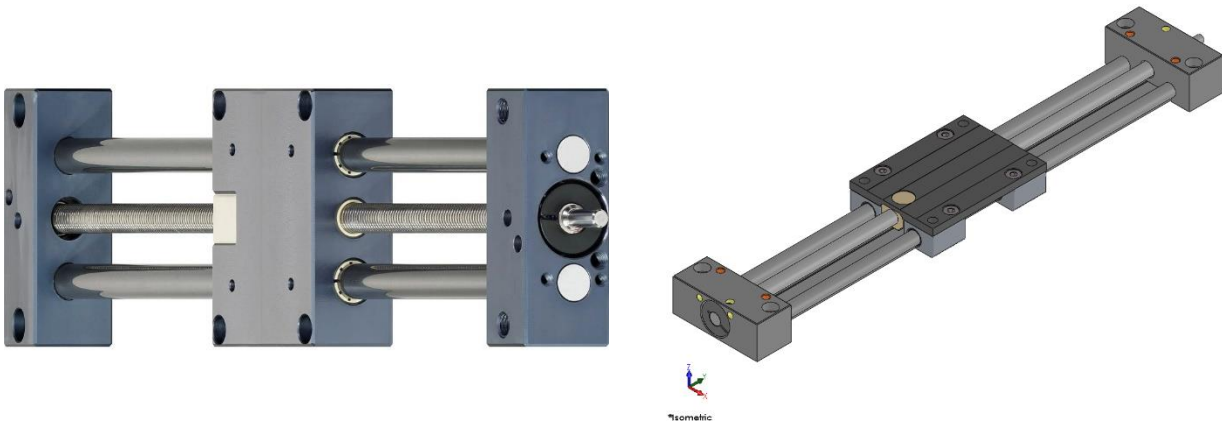


Figure 3.5.4.1 – Linear sled, Dryline SHT-12 linear module with trapezoidal thread, Igus. Photo (left) and CAD model (right).

3.5.5 Rotating table

In the DIMEAS department of Politecnico of Torino was already present a rotating table. The model is a manual MDV 55 (Figure 3.5.5.1), thus its external diameter is 55 mm. To connect the component to the other elements, on each face there are 4 drills M5 disposed in a square of edge of 32 mm. the functionality of this element is to allow and control the relative rotation in between two parts.

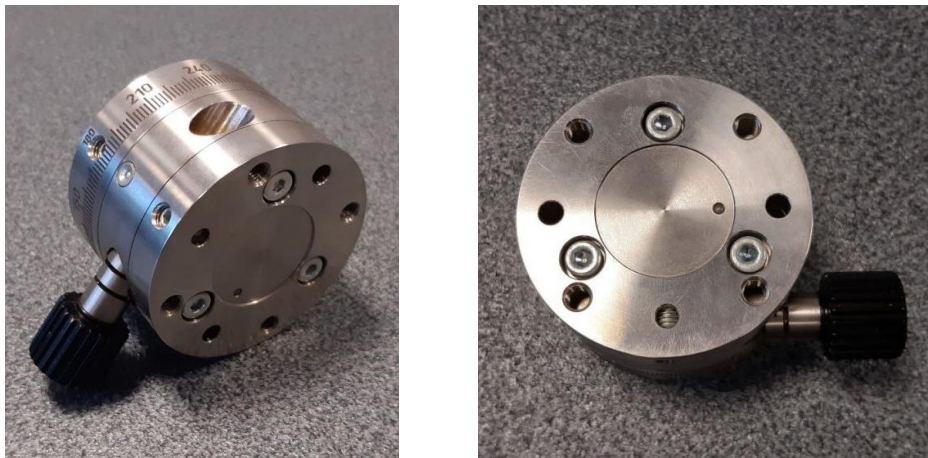


Figure 3.5.5.1 – Rotating table photos.

Since the rotating table does not present a central threaded hole, to connect it to the entire assembly, two intermediate equal parts are used. They are linked to the assembly through a central M10 screw and attached to the rotating table through 4 screws M5, as shown in Figure 3.5.5.2. This solution is chosen also to avoid sollicitating the rotating table in tension. Indeed, the bolt M10 sollicit the intermediate parts in tension, while the rotating table is in compression by coupling the intermediate parts with the 4 M5 screws.

Furthermore, in order to set all the parts concentric one to each other, pins of diameter 4 mm and height 26 mm are used.

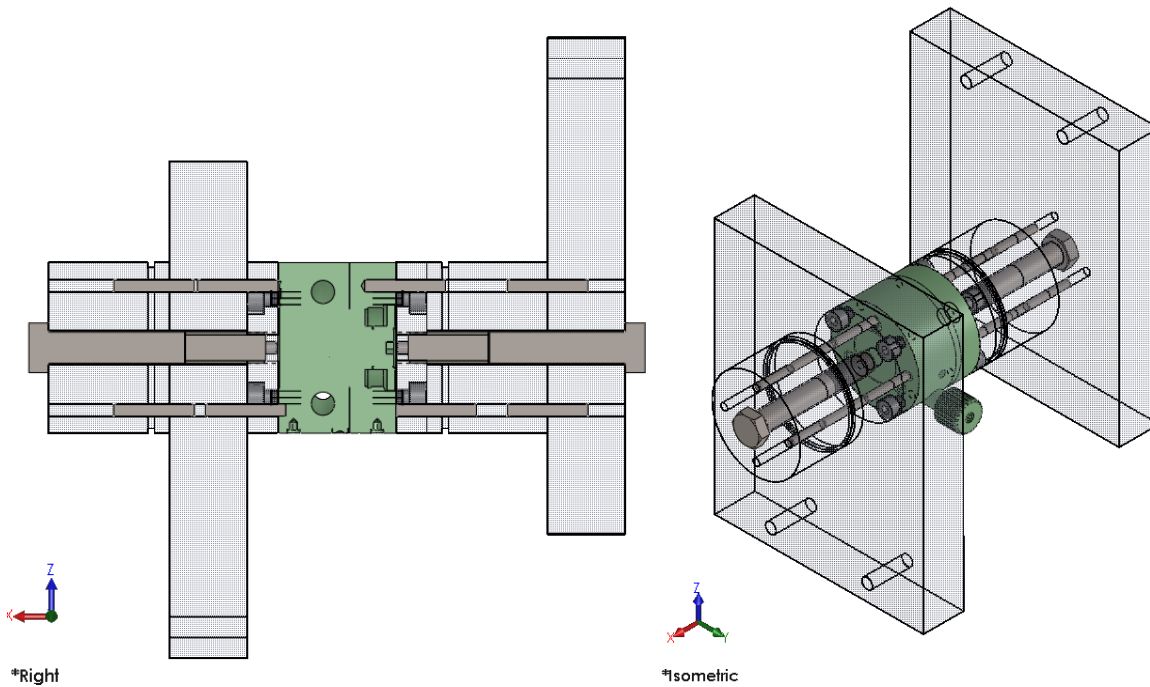


Figure 3.5.5.2 – How the rotating table is connected to the assembly. All the parts are transparent a part from the rotating table, the pins and the screws. Right section (left) and isometric view (right).

3.5.5.1 FEM analysis

As mentioned before, the rotating table cannot carry high loads. Hence, before proceeding with the production of the parts, it is necessary to perform a simulation to verify that the flow of forces goes directly down to the pin and does not flow through the rotating table.

A static analysis of the entire assembly is performed, just the upper gripper is omitted. Since the aim is just to understand the load flow and not an accurate results of stresses, a lot of simplifications are done. Indeed, when there are interferences in between the parts, special contacts in between the parts have to be defined or adequate adjustments must be done. Furthermore, for very small and particular shapes the mesh software is not able to create the mesh. For this reasons, the measures reported below are taken.

- All the bolts are cancelled a part from the two screws M10 at the level of the rotating table cause they are fundamental for describe the connection in between the intermediate parts attached to the rotating table and the lower part of the fixed lower gripper assembly.
- Since the threaded connection of the screws M10 creates interferences between the parts, the bolts are substituted by circular parts of diameter 10 mm and the holes, to which they are threaded, are edited to be simple cavities of 10 mm of diameter.
- The central tube of the “LinearSled” assembly is suspended since it is in interference with other parts of the assembly. It is reasonable to remove it since it has just the function of moving the sled and not of carrying its weight, this last is held by the other two lateral tubes.
- The sled of the “LinearSled” assembly is substituted with a simpler part (Figure 3.5.5.1.1). Indeed, the sled presents particular shapes which the software is not able to mesh, given the big dimensions of the curvature based mesh (Figure 3.5.5.1.2).
- Given the same issues encountered for the sled, the rotating table is substituted with a simpler part with the overall same dimensions (Figure 3.5.5.1.3).

- The defined mesh can neither be applied on the angular contact bearings of the assembly, for their particular shape. Thus, they are substituted with simple parts with the same overall dimensions: inner and outer diameter and width (Figure 3.5.5.1.4).

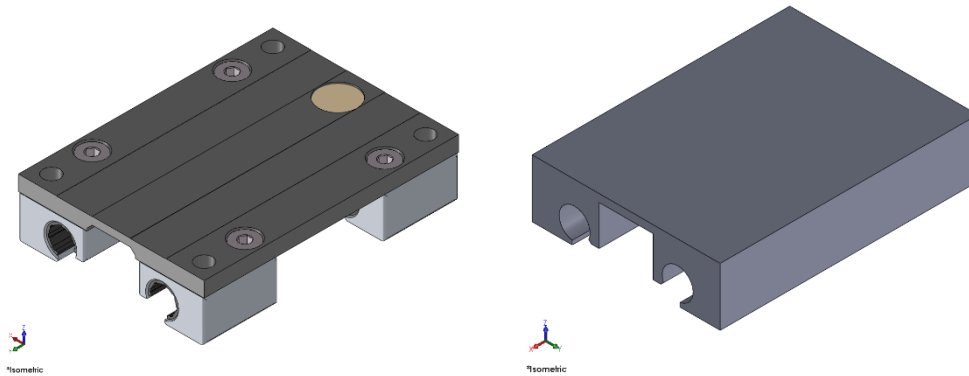


Figure 3.5.5.1.1 – Part3 of the LinearSled assembly; CAD model of the commercial element (left) and simplified part used to create the mesh (right).

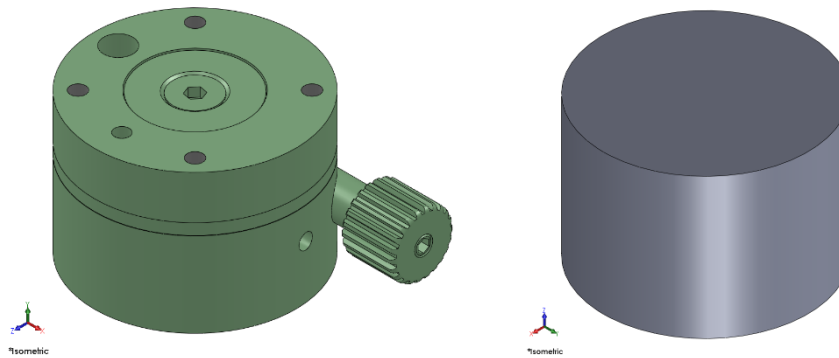


Figure 3.5.5.1.2 – Rotating table; CAD model of the commercial element (left) and simplified part used to create the mesh (right).

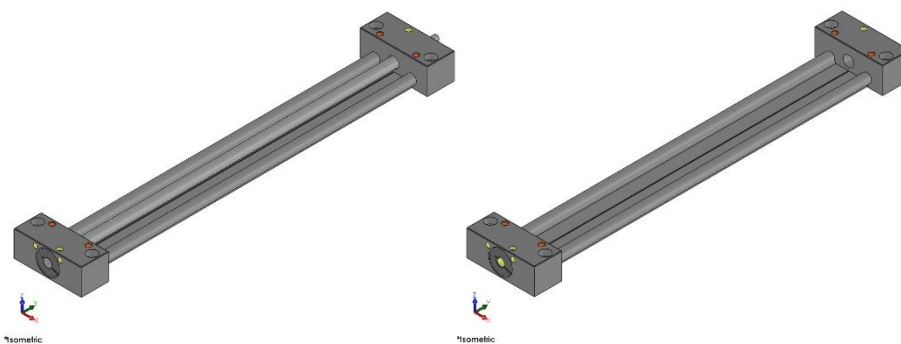


Figure 3.5.5.1.3 – LinearSled assembly without Part3; Part1 unsuppressed (left) and suppressed (right).

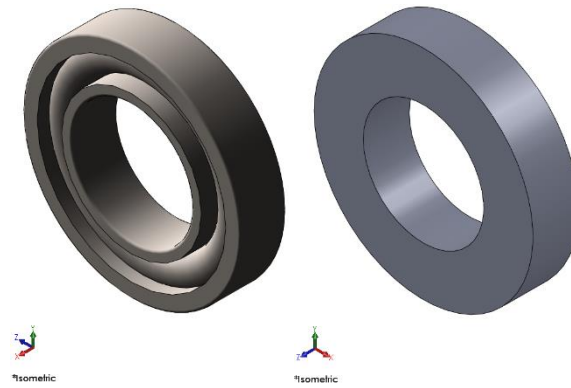


Figure 3.5.5.1.4 – Angular contact bearing; Toolbox element (left) and simplified part used to create the mesh (right).

On the new edited assembly it is then possible to perform a static analysis, called Static1. The characteristics below listed are defined before running the simulation.

- The material applied to the all the parts is aluminium alloy 1060. Indeed, the components will be realised in steel alloy or aluminium, since this last has a lower Young modulus, to be on the safety side, aluminium is selected. Just to the prosthetic different material properties are applied: the carbon fiber ones.
- No further connections are defined a part from the global bounded one. Thus, all the parts in contact behave as if they were welded. Furthermore, the mesh is defined compatible, thus the coincident nodes along the interface of the parts are merged. If the mesh is not defined compatible, the software applies constraint equations internally to simulate bonding.
- The threaded hole of the lower gripper horizontal support is fixed in all the directions (Figure 3.5.5.1.5). This constraint is a simplification which actually does not describe properly the real conditions, it is accepted for the qualitative analysis which is intended to be performed.
- The distributed external load is set vertically on the prosthetic toe (Figure 3.5.5.1.5). The value is set to 1 N since the analysis will be linear, so the results will be proportional to the amount of force applied.
- The defined mesh is a curvature based with maximum element size of 36 mm and minimum of 2 mm. The number of total nodes and elements is respectively 444080 and 295393.

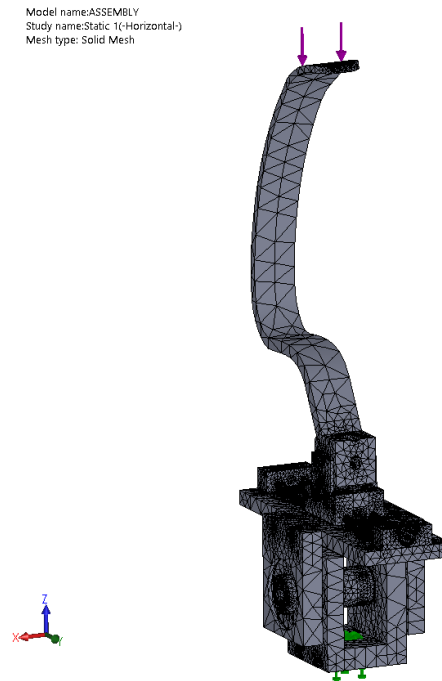


Figure 3.5.5.1.5 – Meshed assembly, force (violet arrows) applied at the toe and constrained (green arrows) applied at the threaded hole of the horizontal support of the lower gripper.

The result stress results, displayed in Figure 3.5.5.1.6, underlines that the prosthetic is the element sollecitated the most.

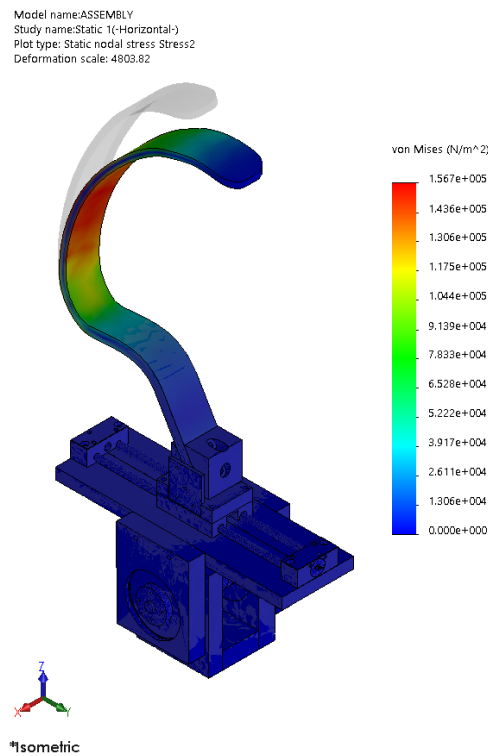


Figure 3.5.5.1.6 – Stress assembly results, isometric view.

Since the focus of this analysis is the flow of forces in the lower gripper assembly, the coloured scale is changed, the maximum load scale is set to 1000 Pa rather than $1.5 \cdot 10^5$ Pa. Furthermore, the section

view is set. In this way the flow of forces is clearly visible along all the components of the lower gripper, as shown in Figure 3.5.5.1.7.

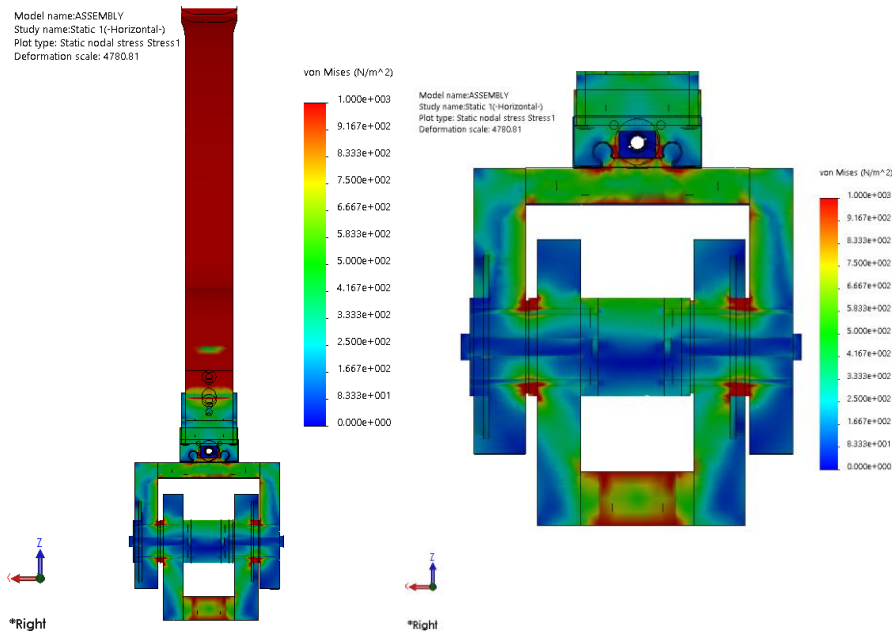


Figure 3.5.5.1.7 – Stress assembly results, section right view. The colour scale is edited setting a maximum value of 1000 Pa. View of the entire assembly (left) and zoom in on the lower gripper (right).

The same analysis is performed setting the maximum external force which it is intended to be applied during the test: 2400 N. Through this rough analysis the factor of safety can be evaluated, as shown in. Since the material of all the components are ductile, the Factor of Safety is defined considering the Von Mises criterion, thus the yielding stress is considered as the allowable one. Hence, the FOS is calculated by the software as follows:

$$\frac{\sigma_{\text{lim}}}{\sigma_{\text{VonMises}}} > 1 \quad (3.5.5.1.1)$$

If the ratio results to be lower than 1, the material achieved the yielding stress and failed. If the ratio it is equal to 1, the material just started to fail. If, instead, it is higher than 1 the component is in safety conditions when that amount of load is applied.

Firstly it is used the Solidworks option to display in red just the areas which are below the safety condition and in blue the safe ones. As it is visible from the upper image on the left of Figure 3.5.5.1.8, all the components are in safety conditions. Then, the same result is obtained by setting the FOS scale from 0.5, which represents an unsafety condition, and 2, which represents a condition in which the margin of safety, before the failure, is of 100%. Also in this case all the components are blue, thus they have a FOS of 2 or higher. Just the vertex of the commercial component of the linear sled is green: here it is evaluated a FOS of 1.5, thus there is a margin of safety of the 50% before reaching the yielding stress.

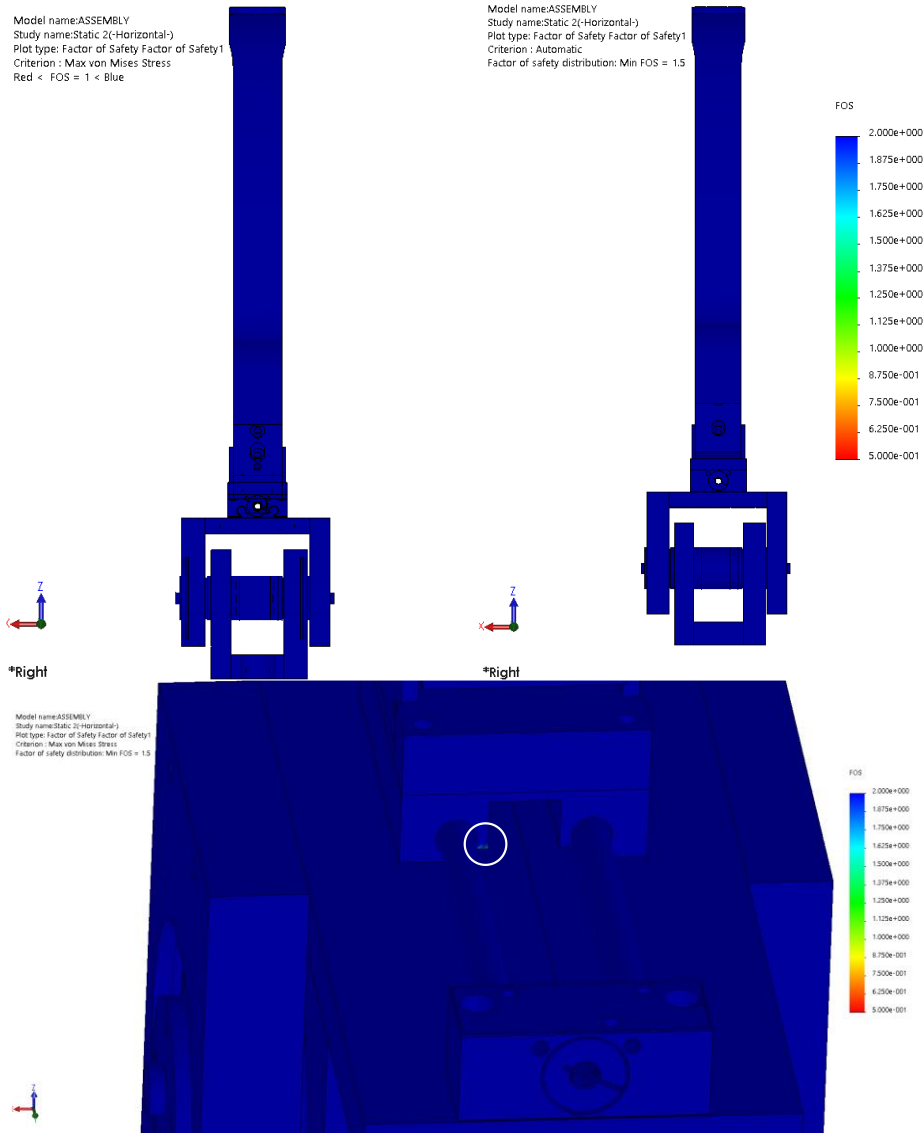


Figure 3.5.5.1.8 – Factor of safety results. Display option to see just the failed components in red (up-left); FOS results with a colour scale from 0.5 to 2 (up-right) and zoom in of the area with the lowest FOS, equal to 1.5, it is marked with a white circle (down).

From the results obtained it is verified that the rotating table is subjected to a low amount of load. The force is mainly transferred down to the pin. This is given to the fact that the two rotating spacers are subjected to flexional moment, indeed, as remarked in Figure 3.5.5.1.9 with violet circles, the two lateral parts, in red are subjected to load in tension and compression on the two opposite sides. Thus, part of this stress, the one on the lower part, flows down to the machine. Furthermore, it is interesting to notice the analogy with the fluids flow. When notches are present and the transversal section becomes smaller, there is an higher concentration of tension, as it happen with the fluid: the flow increases and turbolences rise at the notches. in the tension, as well known, there is a concentration of forces at the corners.

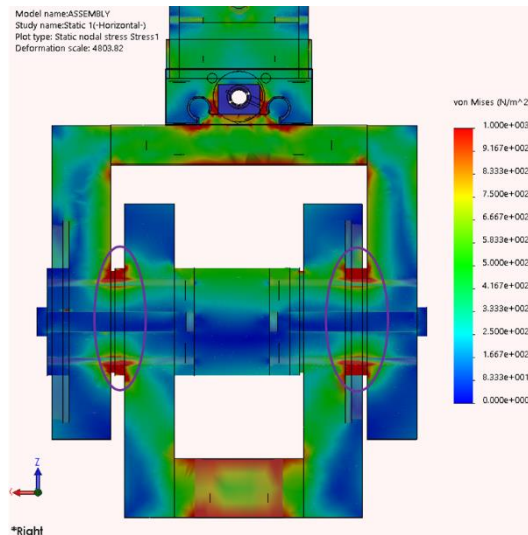


Figure 3.5.5.1.9 – Stress results, zoom in on the lower gripper. The part of the rotating spacer subjected to flexional moment is marked with violet circles.

Another important issue that has to be verified through this analysis is to not stress the two bolts M10 to shear tension. As it is visible from the results displayed above, it is verified that the two screws do not hold loads.

If instead another smaller spacer was used in the assembly to create a gap in between the two vertical supports, the one rotating and the other one not, as it was designed in previous steps, the bolts would have been subjected to higher loads. The result of this design is displayed in Figure 3.5.5.1.10. Since the spacer has a smaller diameter, it is subjected to an higher flexional moment. Moreover, not only the right bolt held a not negligible load, but also the transversal pins. These commercial pins have the aim of just positioning all the parts concentrically, they must not carry any load. Given these results, the design just shown is not applicable.

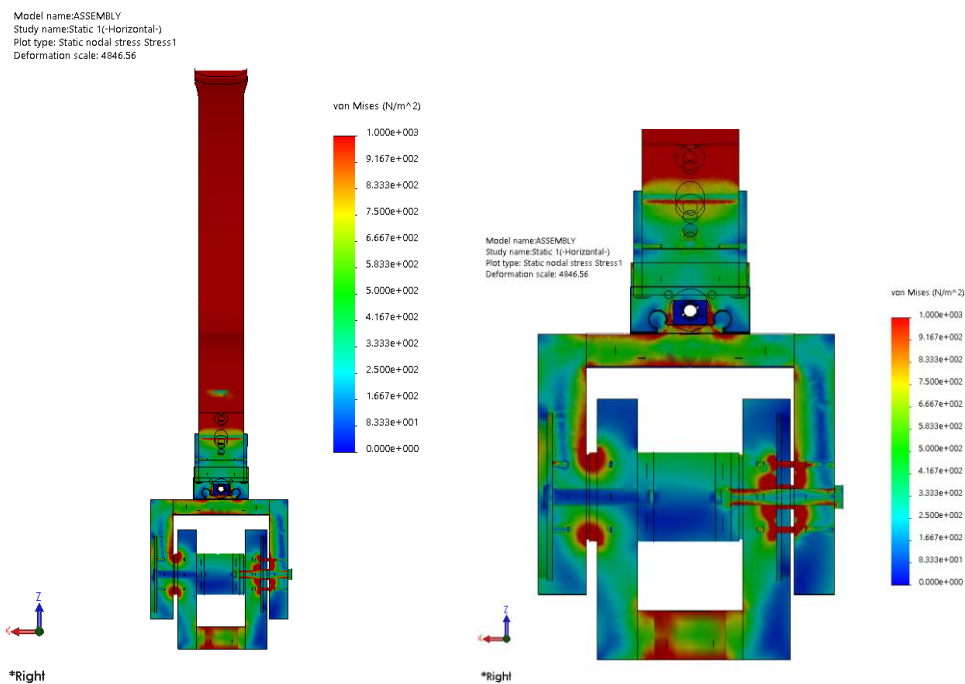


Figure 3.5.5.1.10 – Stress results of a previous design of the lower gripper. A smaller spacer is set in between the two vertical support on the right.

4. Hammer test at the Vibration and Dynamics department at the University of Groningen

A description of the roving hammer test performed on the Cheetah Xcel prosthetic at the University of Groningen is reported. The experimental activity on this component aims to characterise its structural properties by comparing the results in between EMA and FEA and properly tuning the model material. The FE simulations, performed both on Solidworks 2015 and Lupos 2023, are also described in this chapter.

The experimental test was performed at the Vibration and Dynamics department at the University of Groningen in 2023-01-31 and post-processed until 2023-02- on which the main activity was conducted.

4.1 Experimental setup

In this test, the clamped prosthetic Cheetah Xcel, Össur, is excited with a roving hammer and its response is analysed. The component will behave according to the equation of motion:

$$\mathbf{M} \ddot{\mathbf{x}} + \mathbf{C} \dot{\mathbf{x}} + \mathbf{K} \mathbf{x} = \mathbf{f}(t) \quad (4.1.1)$$

where the dofs of the system are the n overall of boundary conditions (i.e. in the case of an ideal clamp $\mathbf{x}_{clamp} \equiv \mathbf{0}$) and of relative kinematic relations (i.e. rigid body links, rigid joints, multi-point-constraints, etc.).

The experimental modal analysis is performed adopting a clamped condition. As shown in Figure 4.1.1, the prosthetic is fixed at the upper end. the clamping system is fixed to a really heavy table through the use of screws; thus the fixture is very stiff. To avoid ruining the component, two aluminium plates, of dimensions 60x64x5 mm, are set in between the clamp and the prosthetic. These plates were designed to perform the static test and produced by the University of Groningen (see Paragraph 3.2.2.1 and Appendix A.1).



Figure 4.1.1 – Prosthetic clamped condition with the aluminium plates.

The clamped area, $60 \times 64 \text{ mm}^2$, represents the exact dimension of the plate used to fix the prosthetic to the socket when the component is worn by the athletes. Actually, in this last case, just a face of the upper end is attached to the plate, through the use of two bolts, while the other one is free, as displayed in Figure 4.1.2. In this case, it is not possible to simulate the real clamping condition since the prosthetic model does not have the holes, which instead are present when the component is sold to the patients.

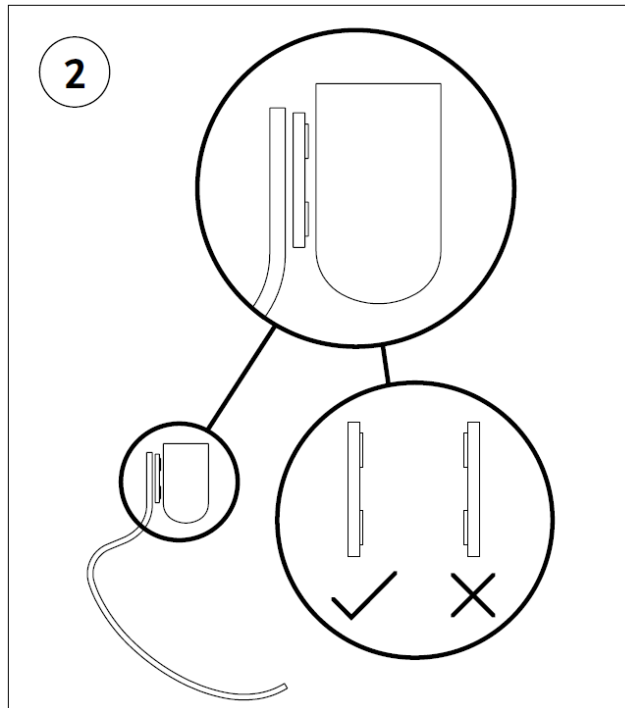


Figure 4.1.2 – Instructions for use Cheetah Xcel, Össur. How to fix the prosthetic to the socket.

It is important to notice that, given the fact that the prosthetic is in carbon fiber composite, the manufacturing of the component does not allow to have a perfect dimensional precision, as for the metals production. For this reason, when clamping the prosthetic, one face results to be completely clamped along the width, while the other one is a bit bigger than 60 mm, as shown in Figure 4.1.3. Furthermore, on the same face, there is a bit of space left in between the upper side of the aluminium plate and the prosthetic, thus the face is not perfectly straight.

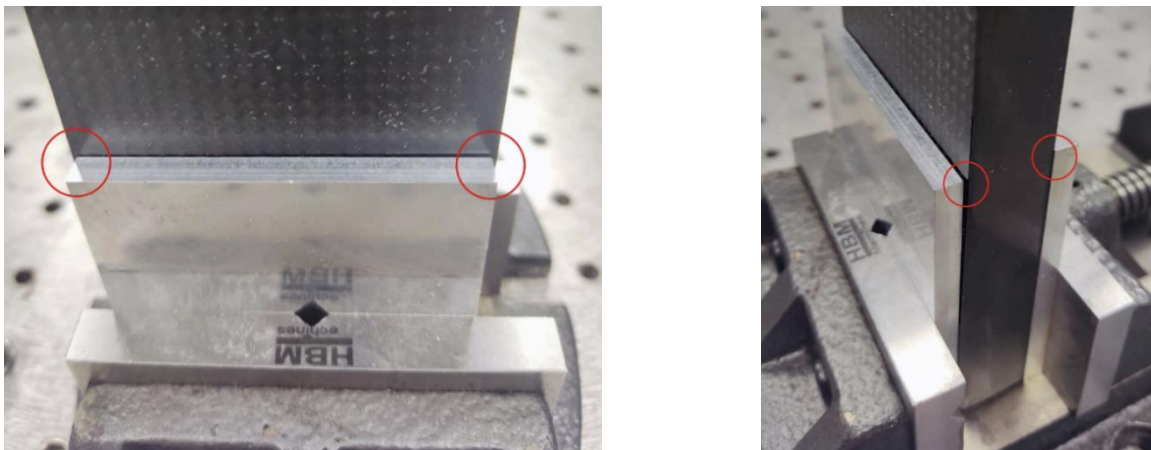


Figure 4.1.3 – Zoom in of the clamping system. On one face the aluminium plate does not cover the entire width of the prosthetic (left image), in contrast to the opposite surface (right image).

In Figure 4.1.4, the entire setup is displayed. The element is excited with a roving hammer and the response is evaluated through one mono-axial accelerometer. Both devices are connected to the data analyser dSpace, for the acquisition of the signals. The prosthetic is excited on 24 nodes along the possible directions allowed by its geometry, obtaining as an overall 31 excitations to the system. The response of node 128 is measured. The sensed node is always the same, in such a way to not vary the mass contribution of the device on the prosthetic. The response for each node is averaged on a set of 5 responses acquired to give more repeatability and stability to each measurement, eliminating the noise contribution.



Figure 4.1.4 – Overview of the experimental setup.

4.1.1 Experimental test definition and hardware

The experimental setup is displayed in Figure 4.1.1.1. In Figure 4.1.1.2, the different point of view of the hardware implementation are displayed. The sensor has been set at the toe level, where the curvature is tangential to the horizontal plane. At this level, the local reference frame results to be the same of the absolute one, thus just the Z displacements are sensed by the accelerometer.

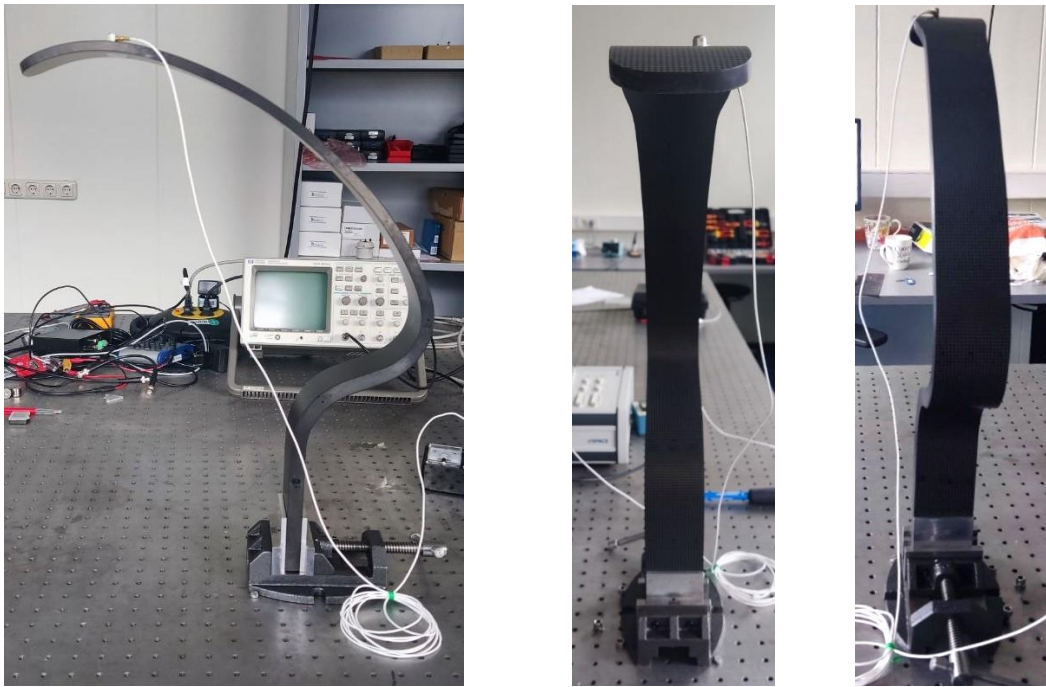


Figure 4.1.1.1 – Experimental setup.

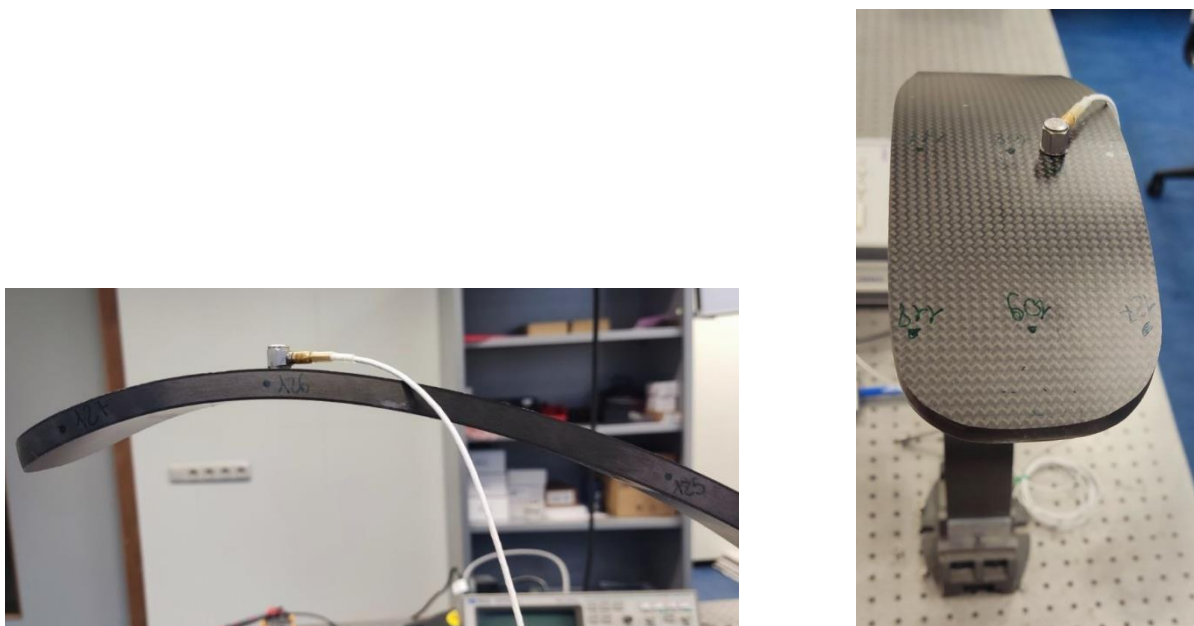


Figure 4.1.1.2 – Experimental setup of the accelerometer. Lateral (left) and upper (right) views.

A roving hammer EMA is performed with an impact hammer PCB 480E09 using the tip with medium hardness (Figure 4.1.1.3 and Figure 4.1.1.4) to avoid damaging the structure. Its characteristics are listed in Table 4.1.1.1.



Figure 4.1.1.3 – Impact Hammer PCB Model 5800B3.



Figure 4.1.1.4 – Hammer tips available: hard (left), medium (centre) and soft (right).

Table 4.1.1.1 – Impact hammer characteristics.

Component	Characteristics	Value
Impact Hammer DYTRAN Model 5800B3	Sensitivity [mV/N]	11.2
	Measurement range pk [N]	±444.8
	Hammer mass [kg]	0.10-0.22
	Resonant frequency [Hz]	>75000
	Tips number [-]	3

The sensor used is a IEPE miniature monoaxial accelerometer: 3035BG 7449, DYTRAN. Its technical characteristics are listed in Table 4.1.1.2.

Table 4.1.1.2 – Accelerometer technical characteristics.

Component	Channel ID	Accelerometer ID	Node ID	Weight [kg]	Sensitivity [mV/m/s ²]	Acc. Direction [-]
DYTRAN 3035BG 7449	6	Mono 1	127	2.5·10 ⁻³	10.2	-Z

The mass of the prosthetic, according to the technical information document of Cheetah Xcel [19], should be around 0.98 kg. The measured component mass is 1.0355 kg. Also the mass and dimensions of the aluminium plates, which are in contact with the prosthetic, are experimentally measured. Both the weight of the single part and the one of the two together is measured, as reported in Figure 4.1.1.6. One plate results to be 10⁻⁴ kg lighter than the other one.



Figure 4.1.1.5 – Cheetah Xcel weight.



Figure 4.1.1.6 – Mass of the two aluminium plates. Of the two together (left), of plate 1 (centre) and plate 2 (right).

Table 4.1.1.3 – Cheetah Xcel mass properties.

Component	Weight [kg]
Cheetah Xcel	1.0355
Aluminium plate 1	0.540
Aluminium plate 2	0.539

The CAD model of the component is created on Solidworks 2015 (Paragraph 2.2). Given the mass measured and the volume obtained from the CAD model, the density of the material is computed; it results to be 1548.93 kg/m^3 .

From the realised model, the properties of mass and barycentre can be obtained, as shown in Figure 4.1.1.7 and resumed in Table 4.1.1.4.

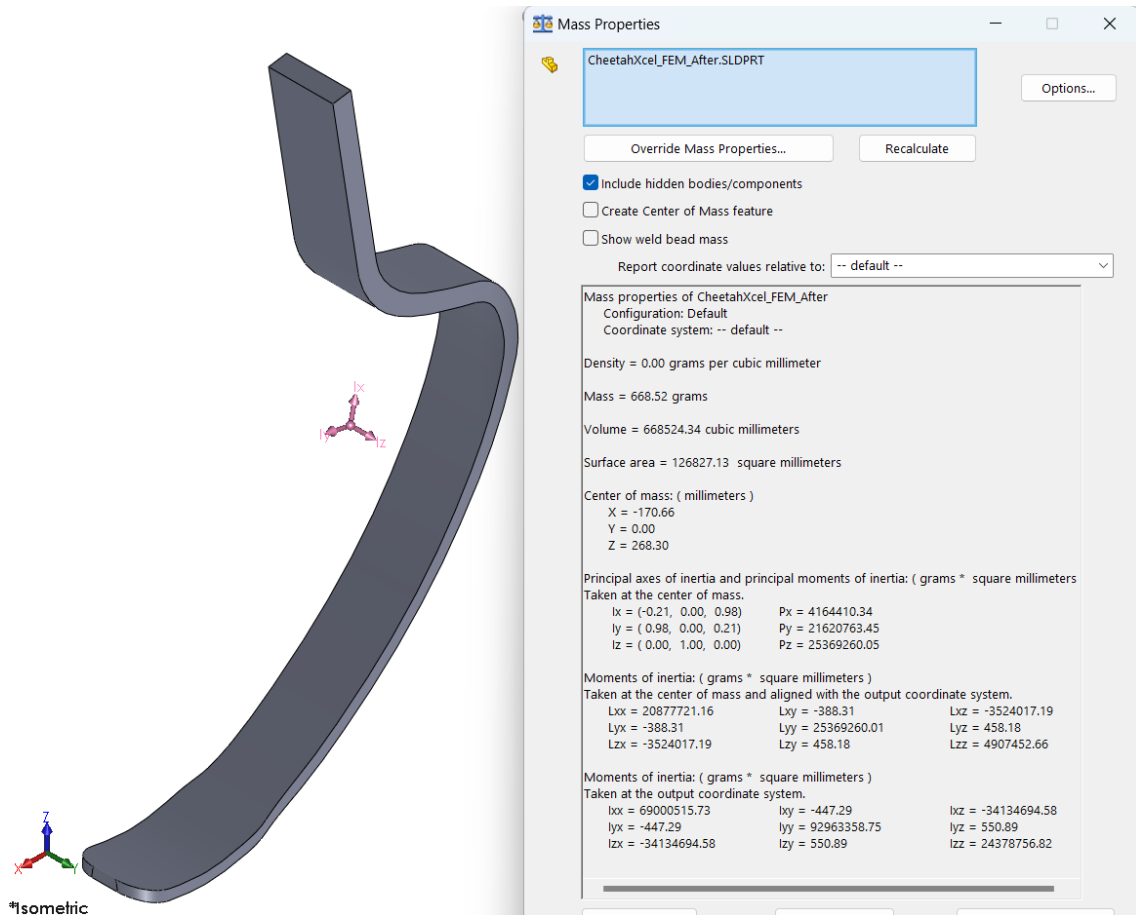


Figure 4.1.1.7 – Cheetah Xcel inertial properties.

Table 4.1.1.4 – Cheetah Xcel inertial properties.

Component	Properties	Value
Cheetah Xcel	x_{COG} , centroid x direction [m]	-0.17066
	y_{COG} , centroid x direction [m]	-0
	z_{COG} , centroid x direction [m]	-0.2683
	J_{XX} , barycentre moment of inertia [$kg \cdot m^2$]	0.00416441
	J_{YY} , barycentre moment of inertia [$kg \cdot m^2$]	0.00216207
	J_{ZZ} , barycentre moment of inertia [$kg \cdot m^2$]	0.00253692
	J_{XY} , barycentre moment of inertia [$kg \cdot m^2$]	-0.00000039
	J_{XZ} , barycentre moment of inertia [$kg \cdot m^2$]	-0.00352402
J_{YZ} , barycentre moment of inertia [$kg \cdot m^2$]	0.00000046	

4.1.2 Reference system definition

The definition of the nodes map is carried out from the prosthetic CAD model already created. The model has been moved to the same position the prosthetic has during the hammering test and the reference frame is defined. The coordinates of the nodes, which can describe a simplified shape of

the model, are measured from the drawing, according to the absolute reference system, as shown in Figure 4.1.2.1.

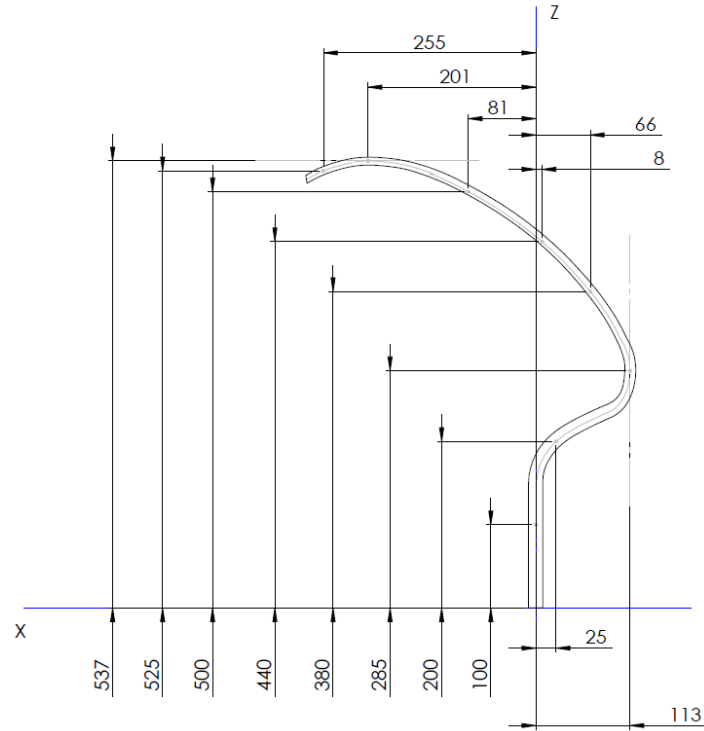


Figure 4.1.2.1 – Node coordinates evaluation from the CAD drawing of Cheetah Xcel prosthetic.

As an overall, 27 nodes are identified, 9 along the symmetric plane and 18 at the right and left borders of the prosthetic. They are used to create a simplified model geometry on Lupos, as shown in Figure 4.1.2.2.

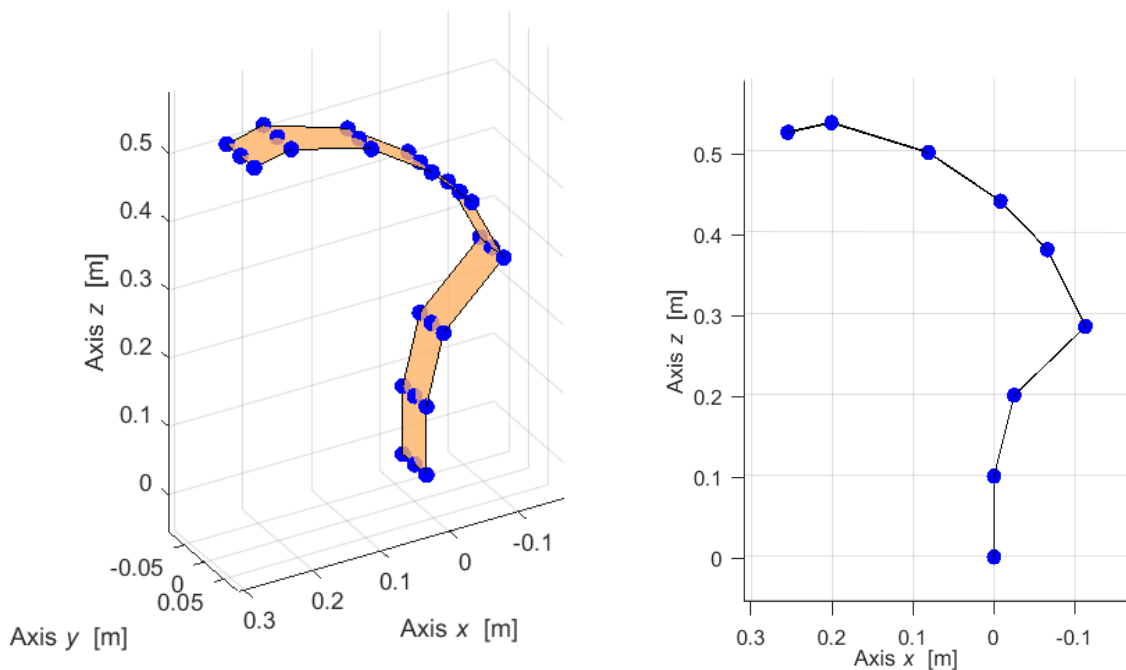


Figure 4.1.2.2 – Simplified model geometry of Cheetah Xcel on Lupos.

4.1.3 Geometry of input and output points

According to the reference system and the numerical model, definition of points and corresponding model nodes are listed in Table 1.3.1. A brief description of the node is defined in the table. In Table 4.1.3.1, the nodes ID is displayed on the Lupos model.

Table 4.1.3.1 – Geometry of I/O points. Hammer test at University of Groningen.

Identifier	Model node	x [m]	y [m]	z [m]	Notes
Clamped 1	100	0	0	0	Plane of symmetry - Prosthetic upper end and origin of the global reference system
Input hammer 1	101	0	0	0.1	Plane of symmetry - Closest hammered point to the clamping
Input hammer 2	102	-0.025	0	0.2	Plane of symmetry - Tangent to the first curvature
Input hammer 3	103	-0.113	0	0.285	Plane of symmetry - Tangent to the highest curvature and to the vertical axis
Input hammer 4	104	-0.066	0	0.38	Plane of symmetry - Along the curvature of the prosthetic
Input hammer 5	105	-0.008	0	0.44	Plane of symmetry - Along the curvature of the prosthetic
Input hammer 6	106	0.081	0	0.5	Plane of symmetry - Along the curvature of the prosthetic
Input hammer 7	107	0.201	0	0.537	Plane of symmetry - Tangent to the horizontal axis
Input hammer 8	108	0.255	0	0.525	Plane of symmetry - Distal end
Clamped 2	200	0	-0.03	0	Left border - Prosthetic upper end of the prosthetic and origin of the global reference system
Input hammer 9	201	0	-0.03	0.1	Left border -Closest hammered point to the clamping
Input hammer 10	202	-0.025	-0.03	0.2	Left border -Tangent to the first curvature
Input hammer 11	203	-0.113	-0.03	0.285	Left border -Tangent to the highest curvature and to the vertical axis
Input hammer 12	204	-0.066	-0.03	0.38	Left border - Along the curvature of the prosthetic
Input hammer 13	205	-0.008	-0.03	0.44	Left border - Along the curvature of the prosthetic
Input hammer 14	206	0.081	-0.03	0.5	Left border - Along the curvature of the prosthetic
Input hammer 15	207	0.201	-0.035	0.537	Left border - Tangent to the horizontal axis

Input hammer 16	208	0.255	-0.035	0.525	Left border - Distal end
Clamped 3	300	0	0.03	0	Right border - Prosthetic upper end of the prosthetic and origin of the global reference system
Input hammer 17	301	0	0.03	0.1	Right border - Closest hammered point to the clamping
Input hammer 18	302	-0.025	0.03	0.2	Right border - Tangent to the first curvature
Input hammer 19	303	-0.113	0.03	0.285	Right border - Tangent to the highest curvature and to the vertical axis
Input hammer 20	304	-0.066	0.03	0.38	Right border - Along the curvature of the prosthetic
Input hammer 21	305	-0.008	0.03	0.44	Right border - Along the curvature of the prosthetic
Input hammer 22	306	0.081	0.03	0.5	Right border - Along the curvature of the prosthetic
Input hammer 23	307	0.201	0.035	0.537	Right border - Tangent to the horizontal axis
Input hammer 24	308	0.255	0.035	0.525	Right border - Distal end
Accelerometer	400	0.201	0.02	0.537	Tangent to the horizontal axis, displaced from the plane of symmetry to the left

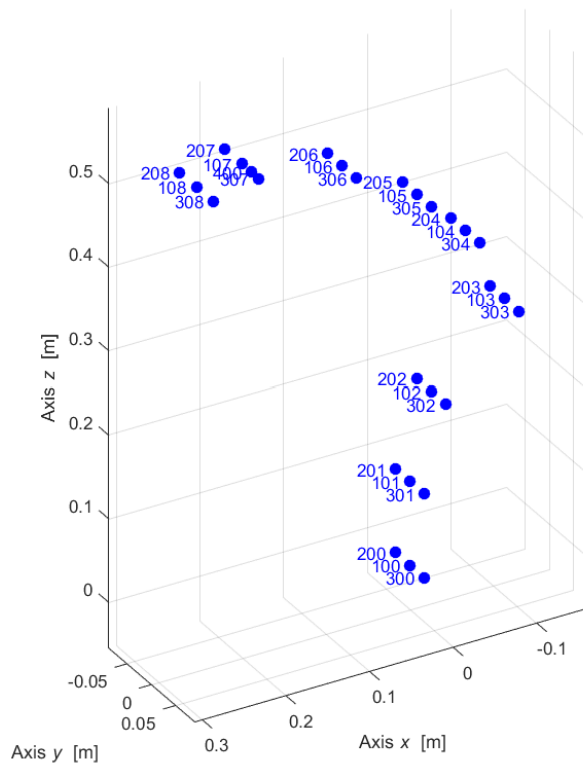


Figure 4.1.3.1 – Nodes ID of the simplified model geometry on Lupus.

As a reference approach, the hammered directions are always orthogonal to nearest surface to defined nodes. As consequence, the Euler angle at each node level must be measured, it defines the angle in between the local and the global reference frames. In this case, it is computed from the drawing of the Solidworks CAD, as shown in Figure 4.1.3.2 and reported in Table 4.1.3.2.

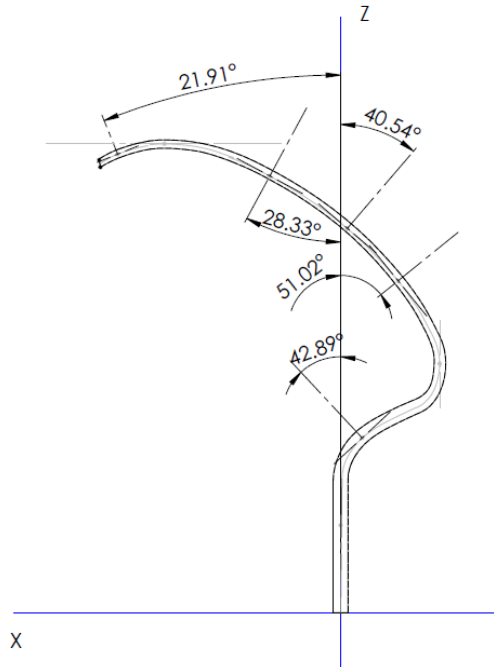


Figure 4.1.3.2 – Evaluation of the Euler angle at each node level on the CAD drawing, Solidworks 2015

Table 4.1.3.2 – Euler angles of the prosthetic nodes.

Node ID	Euler angle
101-201-301	-90°
102-202-302	42.89°
103-203-303	-90°
104-204-304	-51.02°
105-205-305	-40.54°
106-206-306	-28.33°
107-207-307	0°
108-208-308	21.91°

In Table 4.1.3.3, directions and versus of actuation during the experimental work are supplied. For some points at the border of the prosthetic, two hammering are performed: one along the width, Y direction, and the other one perpendicular to the component shape, composed direction X and Z. actually these points are not exactly the same on the prosthetic component, indeed the hammering direction must be tangential to the surface. Thus, the hammering along Y is performed at the middle of the prosthetic thickness, while along the X and Z direction is performed at the same level but on

the convex surface, close to the border. They are called with the same node number and identified with the same node on the 2D model, but it is a simplification.

Table 4.1.3.3 – Directions and versus of actuation during the experimental work for each excited node.

FRF num.	Node ID	Hammering directions
1	101	+Fx
2	102	-Fx;-Fz
3	103	+Fx
4	104	+Fx;-Fz
5	105	+Fx;-Fz
6	106	+Fx;-Fz
7	107	-Fz
8	108	-Fx;-Fz
9	201	+Fy
10	202	+Fy
11	203	+Fy
12	204	+Fy
13	205	+Fy
14	206	+Fy
15	207	+Fy
16	208	+Fy
17	301	-Fy
18	302	-Fy
19	303	-Fy
20	304	-Fy
21	305	-Fy
22	306	-Fy
23	307	-Fy
24	308	-Fy
25	201	-Fx
26	202	-Fx;-Fz
27	203	+Fx
28	208	-Fx;-Fz
29	305	+Fx;-Fz
30	307	-Fz
31	308	-Fx;-Fz

Given the information just reported in Table 4.1.3.3, overall the FRF which will be obtained are 31:

- 8 of the nodes which lie on the plane of symmetry, they are excited along the composed direction X and Z at the nodes;

- 16 of the nodes at the two borders of the prosthetic, when they are excited along the Y direction;
- 7 of some nodes at the two borders of the prosthetic, when they are excited along the composed direction X and Z at the nodes.

As already mentioned, each FRF is averaged over 5 test results, to delete the noise present during the experimental analysis.

4.1.4 Acquisition software setup and parameter settings

As mentioned before, for this analysis the data analyser dSpace is used. To perform the acquisition, dSpace requires a Simulink file, in which the channels from which acquiring the data are specified. In Figure 4.1.4.1, the Simulink program is displayed. In the first block of the first row, the hammer signal is recalled, the channel in which the hammer is connected to dSpace must be specified. Then the signal is multiplied for a gain of 10, because the data analyser divides all the signal acquired for 10. Since the hammer force is obtained in Volts, it must be converted in Newtons. To do this, another gain is needed and it is equal to the reverse of the hammer sensitivity; thus the signal is multiplied for $1000/11.2 \text{ N/V} = 89.28 \text{ N/V}$. Finally, the input force can be displayed using the scope block.

In the second row the response of the beam is processed. Firstly, it is recalled the input channel in which the accelerometer is connected to the dSpace device. Then the signal, as done for the hammer force, is multiplied for 10, corresponding to the ADC gain, and for $1000/10.2 \text{ V/m/s}^2 = 100 \text{ m/s}^2/\text{V}$, to convert the signal from V to m/s^2 . Then a discrete-time integration is performed to evaluate the velocity. The trapezoidal rule is used for the integration and then a filter is applied. The same integration is performed another time to compute the displacement. The filters applied after the integrations allow to cancel the downstream signal and avoid integration drifts. Indeed, the integration of signals which are really close to zero would cause progressively larger errors: a linear drift for the velocity and parabolic one for the displacement. Acceleration, velocity and displacement are displayed through the use of scope blocks.

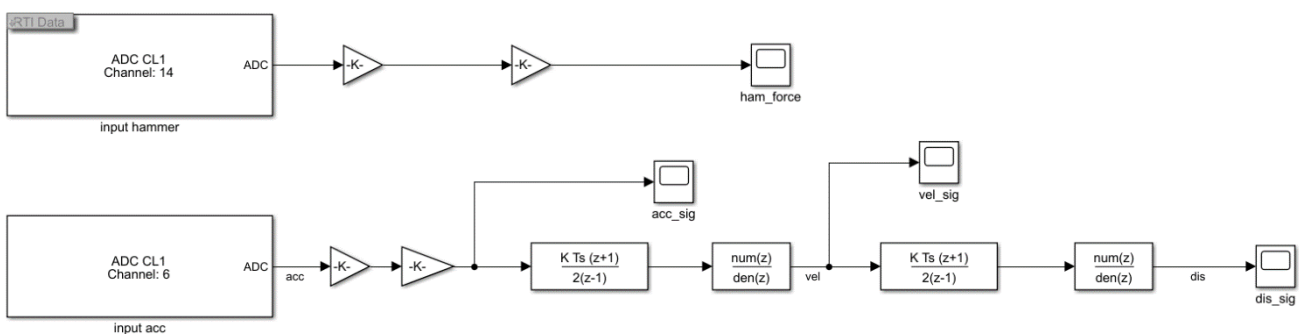


Figure 4.1.4.1 – Simulink program to load in dSpace.

The program is built pressing `Control+B`.

A new file on dSpace can now be created. As input, the .sdl file built on Simulink is uploaded.

The time plots of hammer force, acceleration, velocity and displacement are displayed in the workspace. In this way, during the test, it is possible to verify in real time if the test is being performed well. Indeed, sometimes there are visible problems of rebound during hammering which alter the results with respect the one attended, just one peak must be present in the force plot.

Among the solver parameters of the Simulink program, the frequency sample must be specified.

In order to obtain reliable results, multiple tests have been performed and their goodness is further evaluated during the post-processing phase. To be able to perform a comparison between the multiple tests performed, during the post-processing, the Trigger Recording is adopted. In this case, the Trigger

Recording is defined in such a way that the recording starts just 0.5 s before the moment in which a value of 20 N of the input force is measured, and it lasts 6 s. The acquisition parameters are reported in Table 4.1.4.1

Table 4.1.4.1 – Independent and dependent parameters of acquisition.

Quantity	Symbol	Relationship	Value	Units
Total acquisition time	T		6	s
Sample frequency	f_s		8192	Hz
Total samples	N	$N = f_s T$	49152	-
Bandwidth (max frequency)	f_b	$f_b \cong \frac{f_s}{2}$	4096	Hz
FRF frequency resolution	Δf	$\Delta f = \frac{f_s}{N} = \frac{1}{T}$	0.17	Hz
Number of spectral lines	N_f	$N_f = \frac{N}{2}$	24576	-

4.2 Post-processing on Matlab

In the post-processing, the receptance is extracted; it is a frequency response function (FRF) defined as the ratio between the displacement and the external forces. In the real case of a m dofs system, its formula is:

$$H_{j,k}(\omega) = \frac{x_j(\omega)}{F_k(\omega)} = \sum_{r=1}^m \frac{\Phi_{j,r} \Phi_{k,r}}{\omega_r^2 + 2i\zeta_r \omega_r \omega - \omega^2} \quad (4.2.1)$$

where:

- ω_r is the natural frequency of r -mode shape;
- ω is the excitation frequency;
- $\Phi_{j,r}$ and $\Phi_{k,r}$ are the mode shapes related to the j and k nodes respectively.

On Matlab, all the time-signals are loaded and converted in the frequency domain through the Fast Fourier transform. By analysing the force time and frequency plots, 5 tests are selected for each configuration. Then the FRF are evaluated and plotted.

Multiple other mathematical tools are available to evaluate the frequency response of the component, as studied in the hammer test of the beam (Report “2022-12-20_Hammer test on a clamped beam”). In this case, the power spectral density (PSD) is also calculated. It describes the distribution of power into frequency components composing that signal. It is defined as:

$$S_{xx}(\omega) = \lim_{T \rightarrow \infty} \frac{1}{T} |x_T(\omega)|^2 \quad (4.2.2)$$

Since, in this case, both signals are affected by disturbance, the transfer function estimator of the PSD to be considered is defined as:

$$T_{xy}(\omega) = \frac{\sqrt{S_{xx}(\omega)}}{\sqrt{S_{yy}(\omega)}} \quad (4.2.3)$$

where $S_{xx}(\omega)$ is the PSD of the input signal, $S_{yy}(\omega)$ is the PSD of the output.

Evaluating such quantity in the frequency domain, it is possible to understand the frequencies in which the power of the free response is higher, thus the natural frequencies of the component.

4.2.1 Matlab code

The time-signals acquired from dSpace are the hammer force, the acceleration, the velocity and the displacement. Through the Fast Fourier Transform function `fft`, they are converted in the frequency domain. The Fast Fourier Transform is performed choosing precise values of time window and overlapping, from which other parameters of the spectral analysis are derived, as reported in Table 4.2.1.1. The suggested overlapping value is of 97%, in this way it is avoided the loss of information given by the application of windowing. Indeed, if just the 50% of overlapping is adopted, there can be an attenuation of part of the signal and loss of information. The number of samples adopted is set equal to the value of the frequency sample defined in the Simulink program, thus the frequency resolution is 1 Hz. The number of the of samples directly affect the frequency and time resolution. The higher it is, the better is the resolution of in the frequency domain, but, consequently, the time one is lower, vice versa if the number of samples is lower.

Table 4.2.1.1 – Independent and dependent parameters of spectral analysis, three different trials are considered, the sample value is changed in between them.

Quantity	Symbol	Relationship	Value	Units
Overlap	<i>Overlap</i>		97.0	%
Samples	N_w		8192	-
FRF frequency resolution	Δf	$\Delta f = \frac{f_s}{N_w} = \frac{1}{T_w}$	1	Hz
Number of spectral lines	N_f	$N_f = \frac{N_w}{2}$	4096	-
Sample time	T_w	$T_w = \frac{N_w}{f_s}$	1	s
Time-shift	ΔT_w	$\Delta T_w = T_w \cdot (1 - \text{Overlap})$	0.03	s

In order to apply the windowing and overlapping, a function, called `fft_function`, is created.

Once the `fft` is applied to displacement and force, the FRF can be calculated. Since 5 tests are

considered for each configuration, the averaged receptance, according to eq. $A_{avg}(\omega) = \frac{\sum_{r=1}^5 x_r(\omega)}{\sum_{r=1}^5 F_r(\omega)}$

(4.2.1.1), must be considered:

$$A_{avg}(\omega) = \frac{\sum_{r=1}^5 x_r(\omega)}{\sum_{r=1}^5 F_r(\omega)} \quad (4.2.1.1)$$

The transfer function $T_{xy}(\omega)$ is evaluated by the computation of the PSDs of the two signals through the Matlab function `pwelch`, for the PSDs, and `cpsd`, for the CPSDs. The averaged value

on the 5 tests is evaluated, according to eq $T_{xy,avg}(\omega) = \frac{\sqrt{\sum_{r=1}^5 S_{xx,r}(\omega)}}{\sqrt{\sum_{r=1}^5 S_{yy,r}(\omega)}}$ (4.2.1.2).

$$T_{xy,avg}(\omega) = \frac{\sqrt{\sum_{r=1}^5 S_{xx,r}(\omega)}}{\sqrt{\sum_{r=1}^5 S_{yy,r}(\omega)}} \quad (4.2.1.2)$$

4.3 Experimental results

As already mentioned, dSpace provides the signals in time. Thus, in the post processing, firstly the signal in time are plotted to evaluate their shape. In Figure 4.3.1, the plots of hammer force, acceleration, velocity and displacement are evaluated. On the left image, all the plots display the signals till the end of the recording, which is 6 s.

It is also important to have a closer look to the signals acquired, thus all the four plots are zoomed in (right image of Figure 4.3.1). Firstly, it is important to have a close look to the hammering shape because excitation in time, in order to be an impulse, must present just a peak, if rebounds are present the measurement must be rejected. On the other hand, taking a closer look to the acceleration acquired, the signal is really dirty: the overall sinusoidal shape presents multiple up and down. Notice that, thanks to the filters applied in the integrations, the velocity shape is a bit better than the acceleration and the displacement is a clear sinusoidal shape. As a consequence, the FRF analysis will be conducted evaluating the receptance and not the inductance nor the mobility.

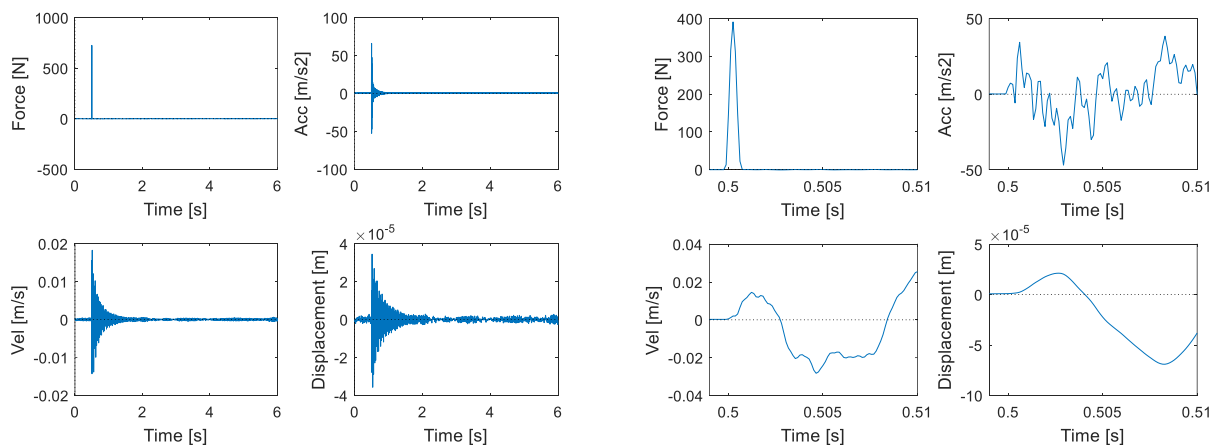


Figure 4.3.1 – Time plots of the force, acceleration, velocity and displacement of the first signal of the hammering on node 103 along X. The time range 0 s - 6 s (left) and 0.49 s - 0.51 s (right).

Before proceeding with the results evaluation, it is important to check the range of frequencies excited in hammering the prosthetic. Thus the Fast Fourier transform of the force is evaluated and plotted in the frequency domain. In Figure 4.3.2, the five impact forces applied to node 102 are displayed. The force signal is a monotonic decreasing function; indeed, the hammer is able to excite till a certain level of energy, afterwards it is no more able to provide power to the system. Usually, it is considered that, when a decrease of 3 dB is reached, the energy is no more comparable to the one fed at 0 Hz. 3 dB corresponds roughly to half of the power; for this reason, the range of frequency taken into consideration is called half power bandwidth. In this case, the hammer is no more able to feed power when 0.05 N of hammer force are reached (dashed line in Figure 4.3.2), thus the frequencies higher than 1200 Hz are not excited. Hence the component FRFs can be evaluated till 1200 Hz.

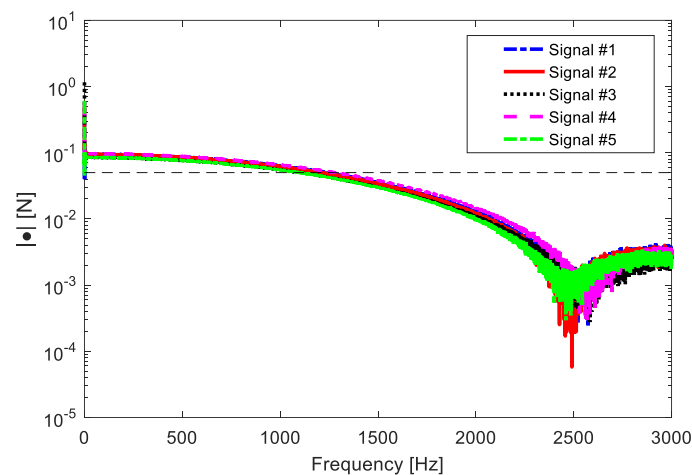


Figure 4.3.2 – ffts of the five hammer forces applied to node 103 along X direction.

The FRF obtained by hammering point 103 is displayed in Figure 4.3.3. The plot is displayed till the maximum frequency, which corresponds to the frequency sample: $2 \cdot 10^{13}$ Hz. In this way, the property of the fast Fourier transform is clearly visible: in the conversion from the time domain (real) to the frequency one (complex), the resulting modulus is symmetric with respect to the Nyquist frequency, which is roughly the half of the maximum frequency, while the phase is antisymmetric.

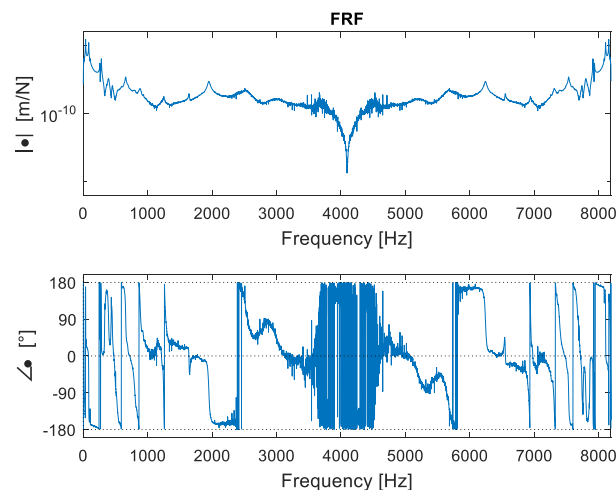


Figure 4.3.3 – Receptance resulting by exciting node 103 along X direction.

As mentioned before, the FRF evaluation is meaningful just till around 1200 Hz. Thus, in Figure 4.3.4 the receptance till 1200 Hz obtained by exciting node 103 along X and node 204 along Y are displayed. By taking a closer look to their modulus, the natural frequencies are graphically detected. Notice that two FRF of the hammering along two different directions are considered because, depending on the hammered node and on the excitation direction, some modes could not be excited. Indeed, in this case the FRF of node 204 presents less modes with respect the one of node 103. The natural frequencies obtained are resumed in Table 4.3.1.

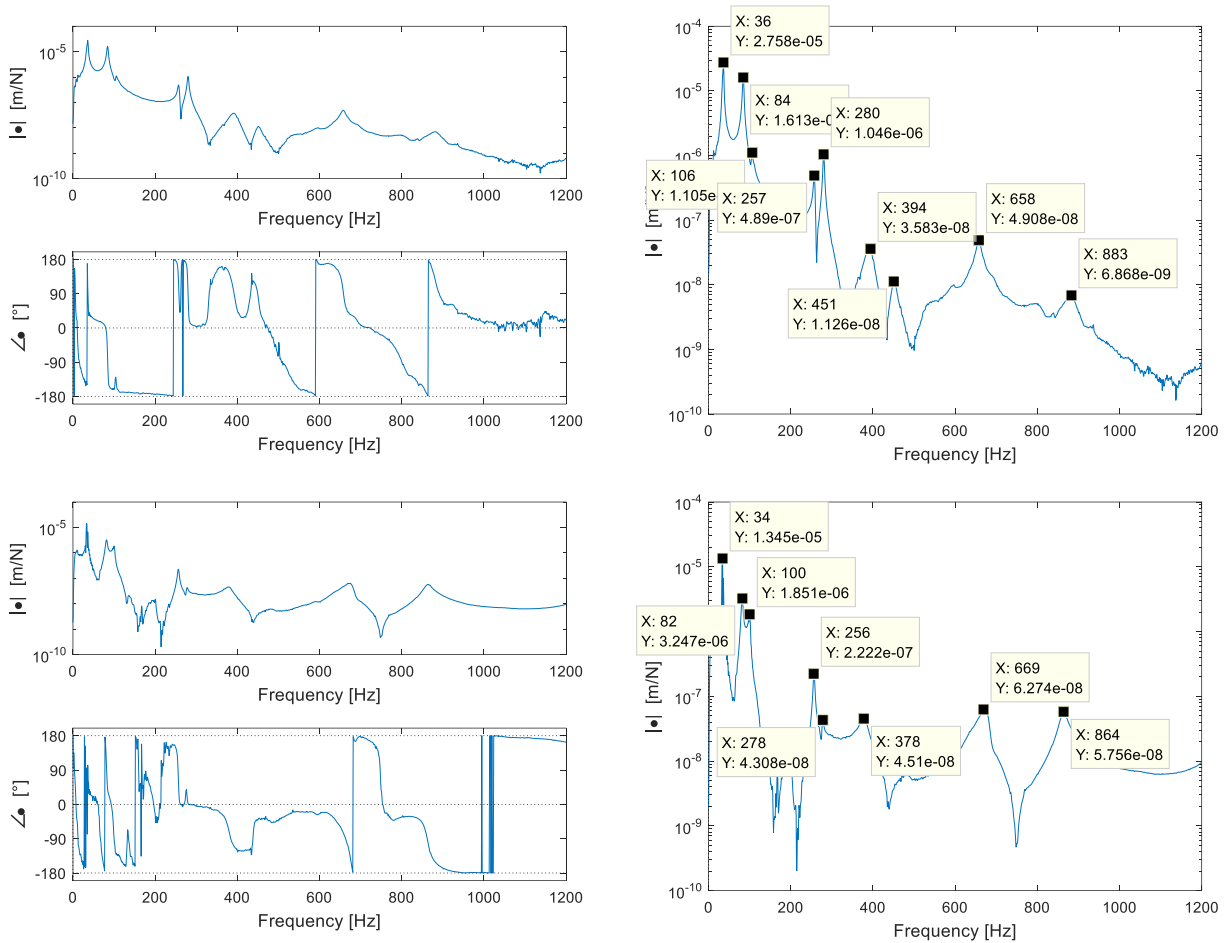


Figure 4.3.4 – Receptance till 1200 Hz resulting by exciting node 103 along X direction (top) and node 204 along Y (bottom). For both, modulus and phase are displayed on the left, while on the right just the modulus is plotted in order to evaluate the coordinates of the peaks.

Table 4.3.1 – Natural frequencies identified from the FRF graphs obtained experimentally till 1200 Hz.

Mode	f [Hz]
1	34
2	84
3	100
4	257

5	275
6	380
7	450
8	660
9	870

A deeper analysis is performed till 300 Hz in order estimate the mode shapes corresponding to each peak.

The dominant behaviour is just caused by the lowest frequency modes, while the high frequency ones die out really soon: after a really short time they stop contributing. Furthermore, when high frequency modes are analysed, it is very easy to incur in errors. Indeed, increasing the Hz values, the frequency distance between the modes keeps on reducing, thus, it is more frequent to have almost superposition of the eigenvectors and it is more difficult to properly identify all of them. Moreover, usually more local modes are verified, rather than global ones, thus, when modes at high frequencies are studied to tune the CAD model, the mesh magnitude becomes important, in order to be able to properly identify all the local modes.

As mentioned before, not all the modes are sensed by every excitation. From the comparison in between the FRFs obtained exciting different points, a prevision on the mode shapes assumed at each natural frequency can be done.

The FRF curves obtained by exciting the nodes along the middle of the width prosthetic are compared in Figure 4.3.5. In the graph the dashed lines correspond to the natural frequencies previously detected (Table 4.3.1). From this plot, the consideration listed below can be done.

- The amplitude of the response is generally lower when the node excited is further from the sensed point. Indeed, the curves 101x and 102xz have the lowest magnitude values, the contrary for the curves 107z and 108xz.
- The closest excited nodes to the sensed one present more antiresonances. When the hammered and the sensed point are further, there are more saddles rather than antiresonances.
- Some curves do not present a peak around 100 Hz and, when it is present, the magnitude is really low. Considering the fact that when the node 107 is excited along Z, such mode is not sensed, the mode shape at 100 Hz is probably a bending on the XY plane. Indeed, the bending on the XZ plane and the torsion are sensed when the excitation occurs along Z, just next to the accelerometer, just shifted along the Y direction.

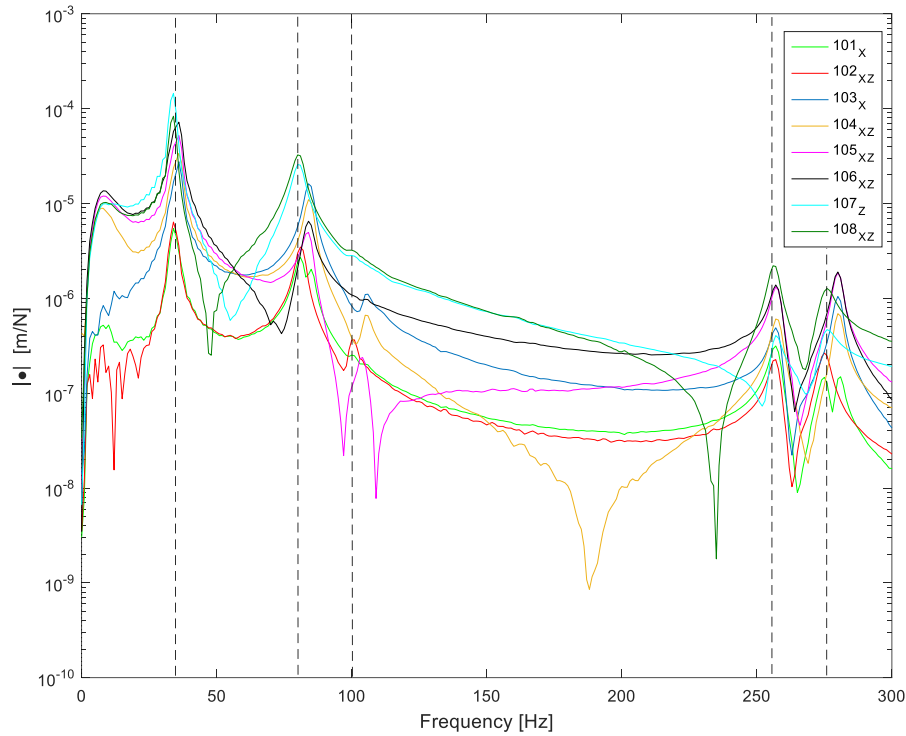


Figure 4.3.5 – Comparison of the receptance curves obtained by exciting the nodes along the middle of the width prosthetic. In correspondence of the natural frequencies, vertical dashed lines are reported.

It is also useful to compare the results obtained by exciting the nodes along Y direction. In this case, the FRF curves obtained are more affected by noise with respect the ones obtained exciting the other nodes. This can be probably a consequence of the fact that the mono-axial accelerometer is placed in such a way to measure the acceleration along Z, thus, when the component is excited along Y, the acquired signal is more affected by noise . Since in this case the plots of the PSD transfer function are smoother, they are considered and displayed in Figure 4.3.6. Here the excitations of all the nodes along the prosthetic border on the negative part of the Y axis (with an $+F_Y$ impact force) are compared.

All the receptance curves in the graph present the mode at 100 Hz and the peak is almost of the same height of the one at 80 Hz. This confirms the hypothesis mentioned before that the mode at 100 Hz is the bending in the XY plane.

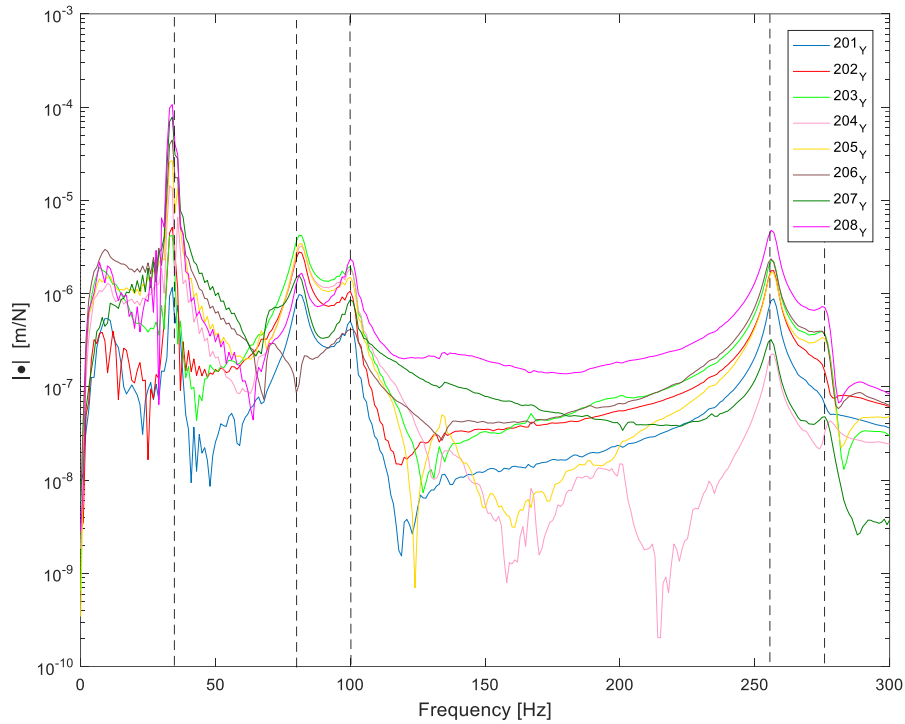


Figure 4.3.6 – Comparison of the PSD curves obtained by exciting the nodes along the border of the prosthetic along Y direction. In correspondence of the natural frequencies, vertical dashed lines are reported.

From the comparison of the transfer functions obtained by exciting nodes along the same Z and X coordinate, just shifted along Y, further consideration can be done. In Figure 4.3.7 the results of the hammering at the same level of the accelerometer position are displayed. In Figure 4.3.8, instead, the outcomes of exciting the structure at the maximum curvature level are compared. From both the graphs the deductions listed below can be done.

- The peaks at 36 Hz and 80 Hz are higher when the structure is excited along Z or X, with respect to Y. Thus, it is more likely that the first two modes are bending on the XZ plane.
- At 257 Hz, instead, the modes magnitude of the peaks is roughly the same or higher when exciting along Y with respect to exciting along X and Z. Thus, this mode is probably a torsional mode.
- Concerning the mode at 275 Hz, it is just slightly sensed when the structure is excited along Y, thus it is excluded to be a bending mode on the XY plane. Since it is sensed mainly by exciting the structure along X and Z at the middle of the prosthetic width, it is likely to be a bending mode on the XZ plane.

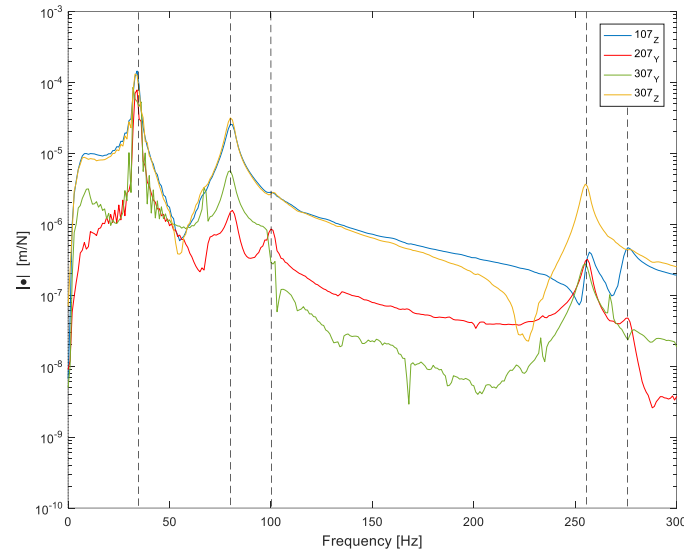


Figure 4.3.7 – Comparison of the receptance curves obtained by exciting the nodes at the same level of the accelerometer position. In correspondence of the natural frequencies, vertical dashed lines are reported.

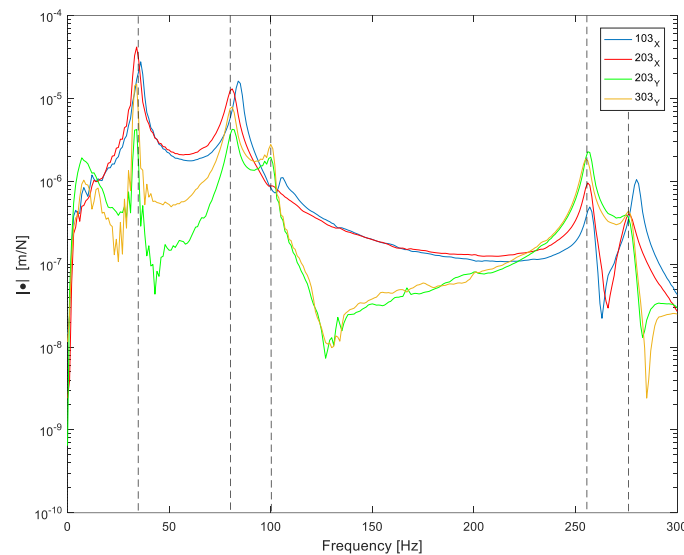


Figure 4.3.8 – Comparison of the receptance curves obtained by exciting the nodes at the maximum curvature level. In correspondence of the natural frequencies, vertical dashed lines are reported.

Having a look to Figure 4.3.9, where the receptance FRF curves of the closest nodes to the clamping, excited along X, are compared, the statements mentioned before are confirmed. Indeed, at 257 Hz, which is supposed to be a torsional mode, the magnitude of the receptance, when node 201 is excited is higher than the other two nodes. This is given to the fact that node 201 is further, along Y, to the accelerometer position, thus the arm for exciting the torsional mode is higher. On the other hand, the peaks at 36 Hz, 80 Hz and 275 Hz are almost the same in between the three nodes, this because the bending mode on the XZ plane has the same arm when exciting along the same direction and at the same X and Z coordinates, the shift along Y direction does not change the excitation of this mode. Finally, the mode at 100 Hz is mostly not sensed cause the hammering occurs along X and does not excite the bending on the XY plane.

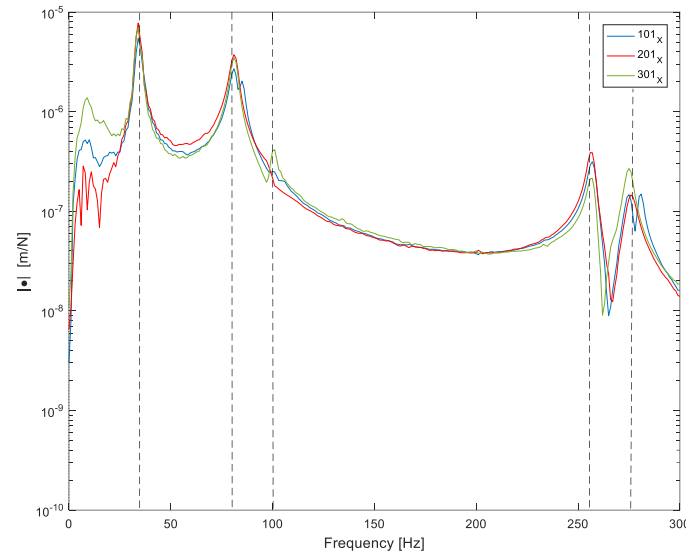


Figure 4.3.9 – Comparison of the receptance curves obtained by exciting, along X direction, the three nodes closest to the clamping.

Summarising, the mode shapes of each of the 5 natural frequencies pointed out are:

Table 4.3.2 – Natural frequencies identified experimentally and the assumed corresponding mode shapes.

Mode	f [Hz]	Mode shape
1	36	1 st bending on XZ plane
2	81	2 nd bending on XZ plane
3	101	1 st bending on XY plane
4	257	1 st torsion on YZ plane
5	275	3 rd bending on XZ plane

4.4 Numerical results

Numerical simulation are both performed on the Solidworks CAD created previously and also on Lupos 2023, where the model is composed by a low number of beams. The results obtained by the FEAs created are compared. Finally, the Solidworks results are compared to the EMA results.

4.4.1 FE analysis on SW2015

The modal analysis is performed on Solidworks 2015. The model CAD previously realised (Paragraph 2.2) is considered and, in the *New Study* panel, the *Frequency* analysis is selected. The prosthetic Cheetah Xcel model is made with carbon fibre fabrics. Its material properties vary a lot depending on the manufacturing: the disposition of the fibres, the quantity of resin, the matrix

material, the production process adopted. Indeed, the characteristics of the composite, are given both from the fibers, which have a very high strength and low density, and from the matrix, which is necessary to bond the fibers and it is more ductile. In theory, the properties of the material are indeed calculated using the so called rule of mixture.

Since the main free response behaviour of the component occurs on the XZ plane, the material is defined isotropic and homogeneous. In this case, the properties evaluated in the research of Rigney et al. [12] are considered. In the research the Cheetah Xtreme model, of category 5, was evaluated in the running conditions; the Young modulus obtained by this study is $6.4313 \cdot 10^{10}$ Pa. Below the material properties explicated for the modal simulation are reported:

Table 4.4.1.1 – Carbon fibre composite properties, Össur Cheetah Xcel.

Property	Value	Units
Elastic Modulus	6.4313e+010	N/m ²
Poisson's Ratio	0.3	N/A
Shear Modulus		N/m ²
Mass Density	1548.93	kg/m ³
Tensile Strength		N/m ²
Compressive Strength		N/m ²
Yield Strength		N/m ²
Thermal Expansion Coefficient		/K
Thermal Conductivity		W/(m·K)
Specific Heat		J/(kg·K)
Material Damping Ratio		N/A

To simulate the clamped condition, the constraints applied are:

- slider in the two regions of attachment of the prosthetic with the aluminium plates. Thus, through the command *Split line*, two areas of dimension 64x60 mm are created on the two opposite surfaces of the CAD model.
- fixture at the upper surface.

They are here displayed:

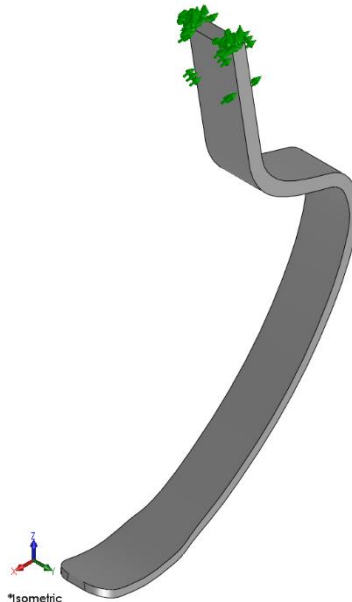


Figure 4.4.1.1 – Constraints applied to for the frequency analysis on SW2015.

Since the modal analysis is mainly a global analysis, it is not necessary to create a detailed mesh with an high number of Jacobian points. Thus, the mesh size was set to 3 mm, in order to have at least 3 elements along the thickness, with 4 Jacobian points. The details of the mesh are reported below:

Study name	Frequency1_10modes (-Default)
Mesh type	Solid Mesh
Mesher Used	Standard mesh
Automatic Transition	Off
Include Mesh Auto Loops	Off
Jacobian points	4 points
Element size	3 mm
Tolerance	0.15 mm
Mesh quality	High
Total nodes	228718
Total elements	150099
Maximum Aspect Ratio	9.7168
Percentage of elements with Aspect Ratio < 3	99.7
Percentage of elements with Aspect Ratio > 10	0
% of distorted elements (Jacobian)	0
Time to complete mesh(hh:mm:ss)	00:00:05
Computer name	

Figure 4.4.1.2 – Mesh details, SW2015 frequency analysis.

The results obtained are:

Table 4.4.1.2 – Natural frequencies and mode shapes resulting from the modal simulation performed on SW2015.

Mode	f [Hz]	Mode shape
1	37	bending XZ
2	64	bending XY
3	100	bending XZ
4	232	torsion
5	291	bending XZ
6	476	torsion
7	696	bending XZ
8	815	bending XZ
9	1264	torsion
10	1305	bending XZ

4.4.2 FE analysis on Lupos2023

On Lupos2023 three different models were created. All of them are composed just by beam elements.

- Model 1 – It is the simplest one: it is composed just by the nodes on the plane of symmetry, individuated previously for the ODE definition. They are the nodes from 100 to 108 (see Table 4.1.3.1). Just another node, numbered 109 (coordinates: (0; 0; 0.05) m), is additionally created in order to define better the same boundary conditions imposed on Solidworks. Hence node 100 is fixed along all the directions, while node 109 just along X direction.
- Model 2 – Starting from Model 1, the nodes at the border are also added, thus along the width three beams were created. The same nodes reported in Table 4.1.3.1 are considered and nodes 109, 209 and 309 are additionally defined. The nodes at the same Z level are coupled between them through rigid joints.
- Model 3 – Through the creation of the Matlab script “Interpolation_20nodes.m”, 36 additional nodes are defined in between the ones of Table 4.1.3.1.

The three models are displayed in Figure 4.4.2.1 and their number of nodes and dofs are resumed in Table 4.4.2.1.

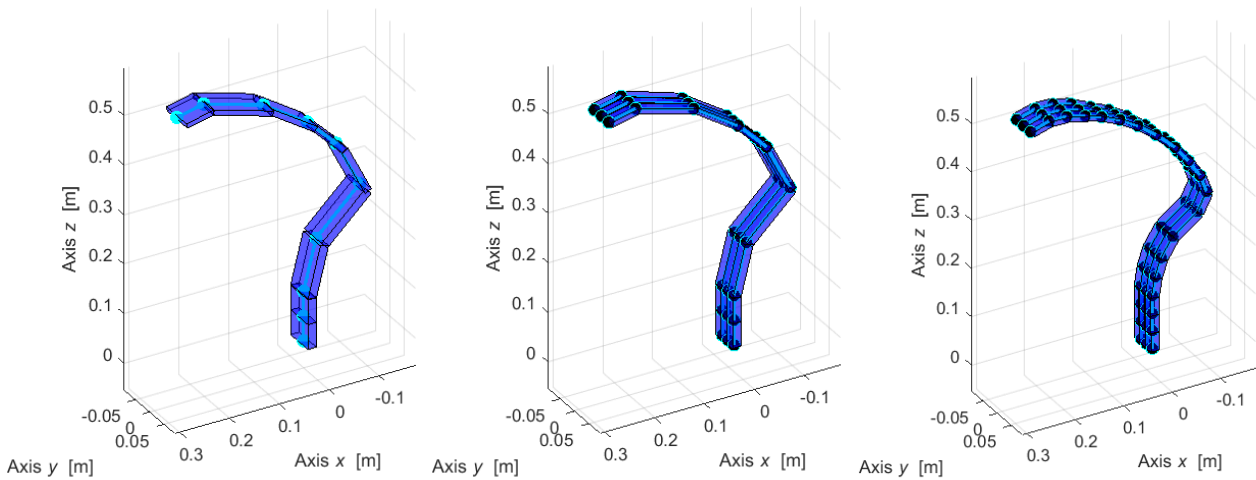


Figure 4.4.2.1 – Model 1 (left), Model 2 (centre) and Model 3 (right). Representation of the nodes (light blue) and of the rigid joints (black).

Table 4.4.2.1 – Number of nodes, elements and dofs of the three Lupos models.

	Model 1	Model 2	Model 3
Nodes n.	10	30	60
Element n.	9	27	57
Dofs	53	159	336

By running the tool “LUPOS_Gui.p”, the modal analyses of the three models were performed. The results obtained are reported and analysed in the following paragraph.

4.4.3 Comparison of the FEA results

Before performing a comparison of the results of the FE analyses performed, firstly the number of nodes, of elements and of the degrees of freedom describing each model are reported in Table 4.4.3.1. In between the Solidworks and the Lupos analysis there is an high difference in the quantity of elements describing the structure, there is a difference of at least 3 units of magnitude in between them.

Table 4.4.3.1 – Comparison of the number of nodes, elements and dofs in between the Solidworks and Lupos analyses

	SW2015	Model 1	Model 2	Model 3
Nodes n.	228718	10	30	60
Element n.	150099	9	27	57
Dofs	684555	53	159	336

In Table 4.4.3.2, the frequency and mode shapes results are compared.

The Lupos model defined just by the middle nodes, Model 1, is not able to detect the torsional modes. In place of them, there are multiple bending modes on the XY plane.

In order to simulate the foot performance, the prosthetic shape is designed to have as principal behaviour the bending on XZ plane. This is indeed what arises from the Solidworks simulation: the main free mode shapes of the prosthetic are the bending on the XZ planes and some torsions. Just one

bending in the XY plane is present among the first ten modes. This is exactly what results also from the frequency analyses of Model 2 and Model 3. In between these two LuPos models, there are just numerical differences in the natural frequencies obtained and a disagreement in the last mode shape resulting.

Of course, the Solidworks results are considered the most reliable, given the high number of degree of freedom describing it. Nevertheless, Model 3 results to be really trustworthy since the same mode shapes of SW2015 are detected. Also the natural frequencies values are very close in between Model 3 and the SW2015, in particular considering that there is a discrepancy of the 99.95% in the number of dofs describing the two models.

However, already Model 2 results to be very accurate: all the mode shapes till the 9th are the same of the SW model and the natural frequencies are also really similar. Moreover, this model is described by the half of the nodes of Model 3 and there is a discrepancy of the 99.98% in the dofs number with respect to the Solidworks model.

Table 4.4.3.2 – Comparison of the natural frequencies and mode shapes resulting from the Solidworks and LuPos simulations.

Mode	SW_2015		LUPOS					
			Model 1		Model 2		Model 3	
	f [Hz]	Mode shape	f [Hz]	Mode shape	f [Hz]	Mode shape	f [Hz]	Mode shape
1	37	bending XZ	42	bending XZ	42	bending XZ	44	bending XZ
2	64	bending XY	75	bending XY	68	bending XY	83	bending XY
3	100	bending XZ	106	bending XZ	106	bending XZ	113	bending XZ
4	232	torsion	230	bending XY	229	torsion	252	torsion
5	291	bending XZ	349	bending XZ	347	bending XZ	345	bending XZ
6	476	torsion	563	bending XY	534	torsion	636	torsion
7	696	bending XZ	773	bending XZ	771	bending XZ	811	bending XZ
8	815	bending XZ	920	bending XZ	916	bending XZ	1003	bending XZ
9	1264	torsion	1365	bending XY	1196	torsion	1430	torsion
10	1305	bending XZ	1701	bending XZ	1512	torsion	1604	bending XZ

4.5 EMA - FEA comparison

To perform the experimental and numerical results comparison, the simulation carried out on Solidworks is taken into consideration, since it is the most reliable.

In Table 4.5.1, the first nine natural frequencies obtained from the EMA and FEA are confronted. The their values are really similar till the fifth mode, then there is a mismatch. Actually, if the 6th mode of the EMA is deleted or if it is left a space in the 6th mode of the FEA, as done in Table 4.5.2, there is again a match in between the resulting natural frequencies. Indeed, what probably happen is that the sixth peak detected from the receptance curves of the experimental tests actually is not a mode or the sixth mode is not detected from the FE analysis.

Table 4.5.1 – Comparison of the first nine natural frequencies of the experimental and numerical results.

Mode	FEA - f [Hz]	EMA - f [Hz]
1	37	36
2	64	81
3	100	101
4	232	257
5	291	275
6	476	380
7	696	450
8	815	660
9	1264	870

Table 4.5.2 – Comparison of the first nine natural frequencies of the experimental and numerical results; a space is left for the 6th natural frequency of the FE analysis.

Mode	FEA - f [Hz]	EMA - f [Hz]
1	37	36
2	64	81
3	100	101
4	232	257
5	291	275
6	-	380
7	476	450
8	696	660
9	815	870

In Table 4.5.3, the first five mode shapes are confronted. There is a mismatch of the second and third ones in between the EM and FE analyses, they are switched. This sometimes can happen when two modes are really close in frequency.

Table 4.5.3 – Natural frequencies and corresponding mode shapes resulting from the EM and FE analyses.

Mode	FEA		EMA	
	f [Hz]	Mode shape	f [Hz]	Mode shape
1	37	1 st bending on XZ plane	36	1 st bending on XZ plane
2	64	1 st bending on XY plane	81	2 nd bending on XZ plane
3	100	2 nd bending on XZ plane	101	1 st bending on XY plane
4	232	1 st torsion on YZ plane	257	1 st torsion on YZ plane
5	291	3 rd bending on XZ plane	275	3 rd bending on XZ plane

Moreover, the receptance curves obtained experimentally and from the simulation are compared. In particular, the cases when nodes 103, along X, 203, along X and Y and 207, along Z and Y are considered, as displayed in Figure 5.1. In the plots, the natural frequencies detected from the FE analysis are displayed in vertical dashed lines. Even though obviously the natural frequencies values do not match perfectly, the trend of the curves compared is similar.

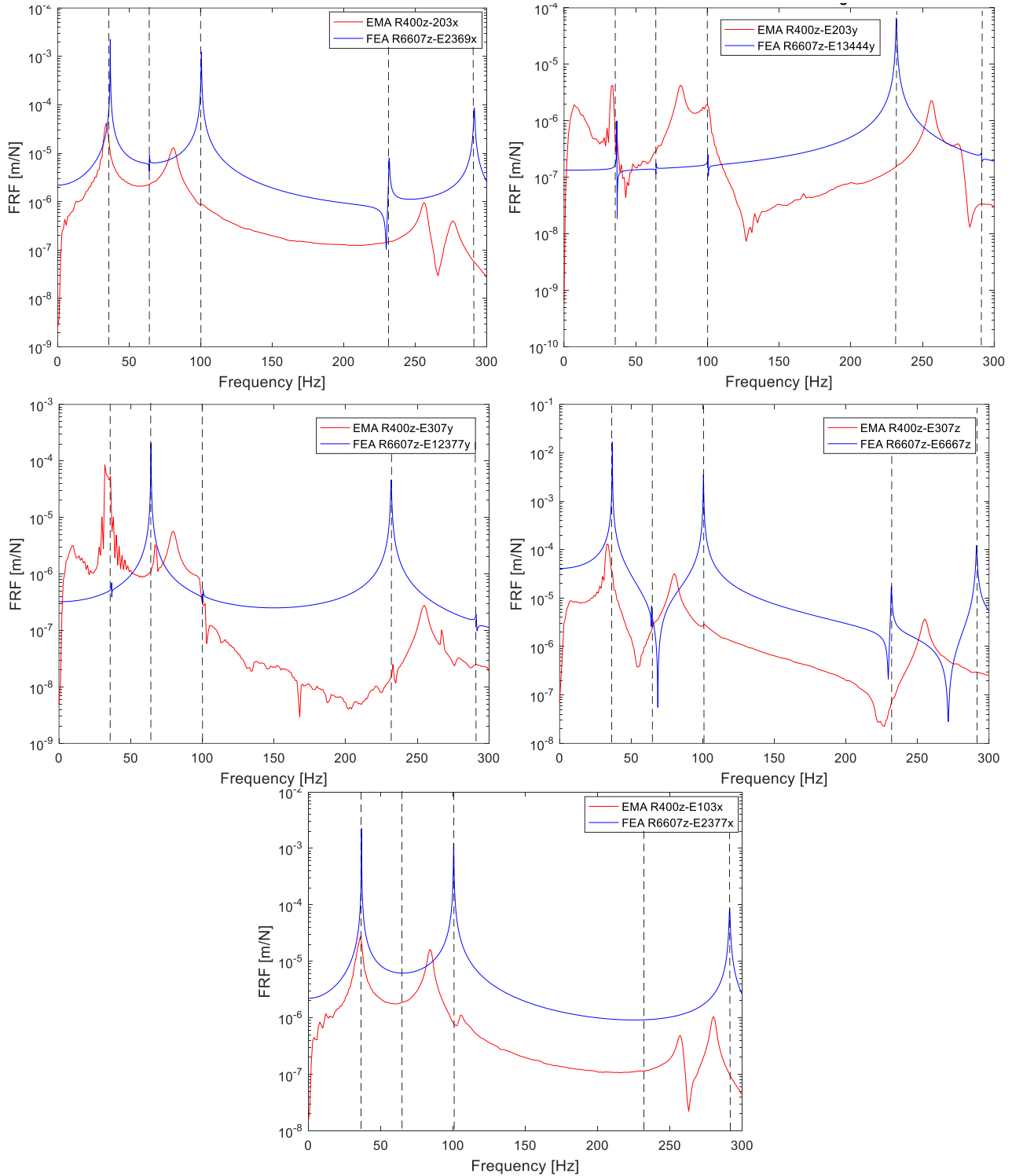


Figure 4.5.1 – Comparison of the receptance curves obtained from the EMA and FEA. Vertical dashed lines are plotted in correspondance of the natural frequencies detected from the Solidworks simulation. Receptance when nodes 203, along X (top-left) and Z (top-right), node 207, along Y (centre-left) and Z (centre-right), and node 103 along X (bottom) are excited.

Since the EMA mode shapes obtained are just deduced from the receptance curves, and the sensor used was just a mono-axial accelerometer, it is unknown which is the most reliable result in between EMA and FEA. When the other set of tests will be performed at Politecnico of Torino, with an higher number of tri-axial sensors, the outcomes will be compared (Paragraph 5.4).

5. Hammer test at DIMEAS, Politecnico di Torino

A description of the roving hammer test performed on the Cheetah Xcel prosthetic at the Politecnico di Torino is reported. The experimental activity on this component aims to characterise its structural properties.

Firstly, the experimental methodologies adopted, such as the definition of experimental setup, construction of the same, setting of the LMS.Testlab environment for impact testing, are described. In the second part, the identification of mode shapes is performed focussing on stabilisation diagram, stable point recognition and extraction of data from LMS.Testlab environment for data manipulation in common programming languages such as Matlab®.

Finally, post-processing is performed: Modal Assurance Criterion complex (MACX) for checking goodness of experimental activity and comparison with Finite Element (FE) models.

Multiple models are created on Lupos and their degree of complexity is progressively increased: firstly 2D elements are considered, then 3D ones, then orthotropic material properties are defined.

The experimental test was performed Department of Mechanical and Aerospace Engineering (DIMEAS) of Politecnico di Torino in 2023-02-24 and post-processed until 2023-03-20 on which the main activity was concluded.

5.1 Experimental setup

The experimental modal analysis is performed adopting clamping-free conditions, exciting the structure with roving hammer and evaluating the response through accelerometers, either mono-axial or tri-axial. The hammer is excited on 31 nodes along all the possible directions allowed by its geometry, obtaining as an overall 49 excitations to the system. The responses of 5 nodes are measured: 208, 305, 202, 3300, and 1200. The response for each node is averaged on a set of 3 responses acquired to give more repeatability and stability to each measurement.

For each response:

- the spatial coordinates are continuous for each instant of time;
- the time/frequency data and the modal content are acquired and identified with Siemens Test.Lab v.17;
- it evinces those modal coordinates enable approximate solutions, according to the number of modal coordinates used, thus in nonlinear problems this property can improve computational efforts in the best way.

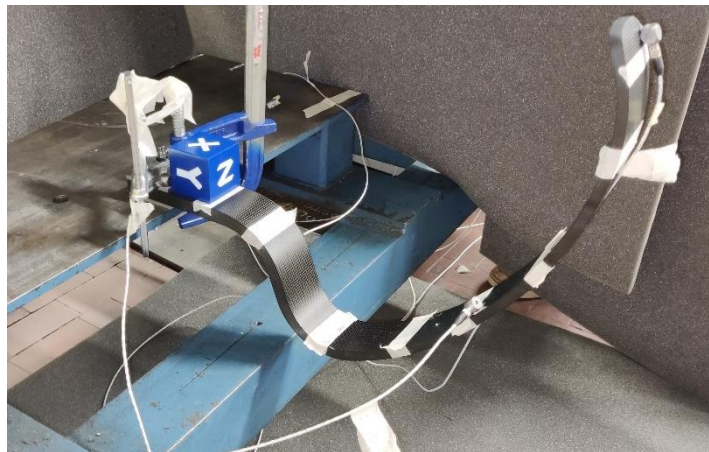


Figure 5.1.1 – Experimental setup scenario.

The prosthetic is clamped on a table of 2 tons. To avoid ruining the blade prosthesis, two aluminium plates, of dimensions 60x64x5 mm, are set in between the clamp and the prosthetic.

5.1.1 Experimental test definition and hardware

Both pictures of the entire system, with different points of view and details of the hardware implemented and of their location are requested information.

Importance has the reference system (x, y, z) used, according also to suitable models. The same reference system will be considered for the models which will be created.

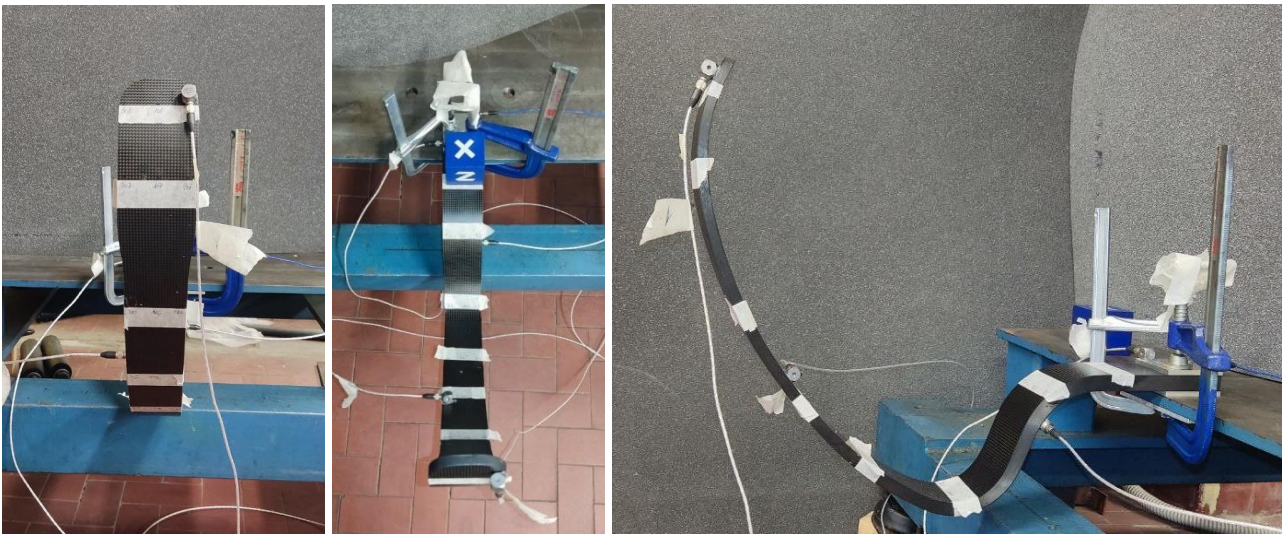


Figure 5.1.1.1 – Overview of the experimental setup.





Figure 5.1.1.2 – Details of the implemented hardware, from left to right in reading order: Tri-axial-node 208, Tri-axial-node 305, Tri-axial-node 202, Tri-axial-node 3300, Mono-axial-node 1200.

The acquisition is performed with a LMS SCADAS Mobile system. A roving hammer EMA is performed using an impact hammer PCB 086C03 using hard plastic tip (Figure 5.1.1.3 and Figure 5.1.1.4) to avoid damaging the structure. A series of 3 hammer repetitions is linearly averaged. The characteristics are listed in Table 5.1.1.1.



Figure 5.1.1.3 – Impact Hammer PCB Model 086C03.



Figure 5.1.1.4 – Hammer tip medium.

Table 5.1.1.1– Impact hammer characteristics.

Component	Characteristics	Value
Impact Hammer PCB Model 086C03	Sensitivity [mV/N]	2.199
	Measurement range pk [N]	±2224
	Hammer mass [kg]	0.16-0.235
	Resonant frequency [Hz]	>22000
	Tips number [-]	5

All the accelerometer acquire the signal in the frequency range 0-5000 Hz. Their location and their characteristics are reported in Table 5.1.1.2.

Table 5.1.1.2 – Accelerometer technical characteristics.

Component	Channel ID	Accelerometer ID	Node ID	Weight [kg]	Sensitivity [mV/g]	Acc. Direction [-]
SN5958474	1	Tri 1 x	208	$6.4 \cdot 10^{-3}$	105.28	+Z
	2	Tri 1 y			106.21	+Y
	3	Tri 1 z			103.38	-X
SN5958475	4	Tri 2 x	305	$6.4 \cdot 10^{-3}$	106.38	-Y
	5	Tri 2 y			104.27	-Z
	6	Tri 2 z			103.52	+X
SN5958472	9	Tri 3 x	202	$6.4 \cdot 10^{-3}$	100.10	+X
	10	Tri 3 y			103.52	+Y
	11	Tri 3 z			102.19	+Z
SN5958473	12	Tri 4 x	3300	$6.4 \cdot 10^{-3}$	102.45	+X
	13	Tri 4 y			107.23	-Y
	14	Tri 4 z			104.96	-Z
LW148801	15	Mono_1	1200	$5.8 \cdot 10^{-3}$	103.52	+X

The mass of the prosthetic and of the aluminium plates clamping the component were already evaluated for the hammer test performed at the University of Groningen, see Paragraph 4.1.1. In Table 5.1.1.3 and Table 5.1.1.4 their mass properties are again reported.

Table 5.1.1.3 – Mass properties.

Component	Weight [kg]
Cheetah Xcel	1.0355
Aluminium plate 1	0.540
Aluminium plate 2	0.539

Table 5.1.1.4 – Cheetah Xcel mass properties.

Component	Properties	Value
Cheetah Xcel	x_{COG} , centroid x direction [m]	-0.17066
	y_{COG} , centroid x direction [m]	-0
	z_{COG} , centroid x direction [m]	-0.2683
	J_{XX} , barycentre moment of inertia [kg·m ²]	0.00416441
	J_{YY} , barycentre moment of inertia [kg·m ²]	0.00216207
	J_{ZZ} , barycentre moment of inertia [kg·m ²]	0.00253692
	J_{XY} , barycentre moment of inertia [kg·m ²]	-0.00000039
	J_{XZ} , barycentre moment of inertia [kg·m ²]	-0.00352402
	J_{YZ} , barycentre moment of inertia [kg·m ²]	0.00000046

5.1.2 Reference system definition

To run the experimental modal analysis on the component it is necessary to create a model by identifying the most relevant nodes that allow to build a reference geometry as much close as the real one and at the same time could allow to give important information with regards to the response of the system.

The definition of the nodes map is carried out by obtaining the CAD geometry information of the prosthetic model developed in Solidworks, where the coordinates of each node are measured according to the reference system set on the component, as shown in Figure 5.1.2.1.

As an overall, 33 nodes are identified and used to develop the model geometry in Siemens LMS Test.Lab. Given the symmetry of the component, 11 nodes are evaluated along the symmetric plane, as shown in Figure 5.1.2.2, and 22 at the right and left borders.

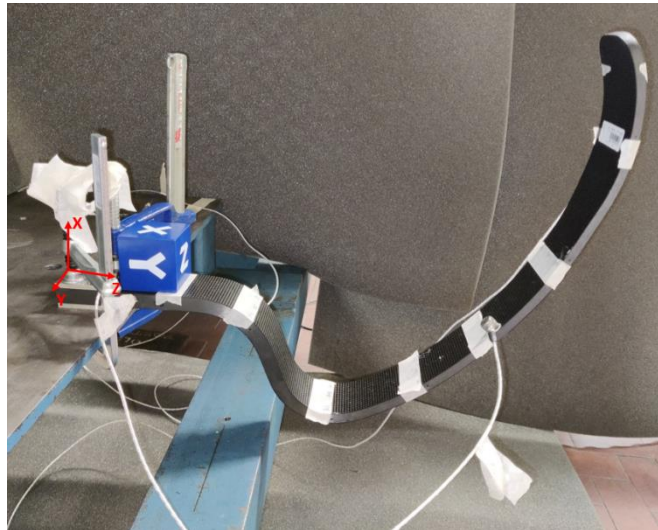


Figure 5.1.2.1 – Prosthetic reference frame

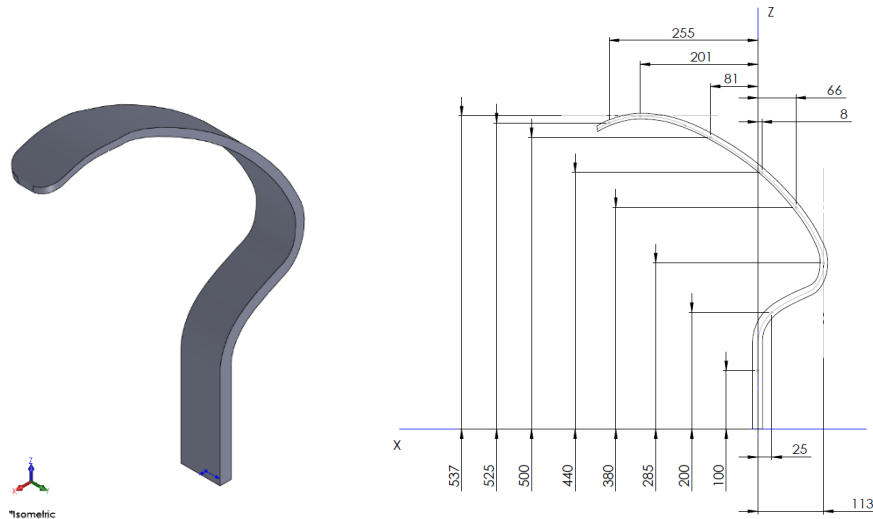


Figure 5.1.2.2 – Prosthetic CAD geometry (left) and node coordinates evaluation from the CAD drawing (right).

5.1.3 Geometry of input and output points

According to reference system and to numerical model, definition of points and corresponding model nodes are listed in Table 5.1.3.1. A part from the clamped part, 24 nodes are identified for the roving hammer EMA, 3 of them are used for accelerometer positioning and hammered in the neighbourhood for auto-inertance. In the constrained part, 9 nodes are identified, 7 of them are hammered and, among them, 2 are used for the accelerometers positioning. Node nomenclature is based on the following considerations:

- Left side prosthetic (Y+ surface) is numbered with 3XX;
- Right side prosthetic (Y- surface) is numbered with 2XX;
- Prosthetic first clamped row is numbered with 1XXX;
- Prosthetic second clamped row is numbered with 2XXX;
- Prosthetic third clamped row is numbered with 3XXX.

In Figure 1.3.1, the nodes ID is displayed on the Lupos model. Details of the experimental geometry are supplied in Table 5.1.3.1.

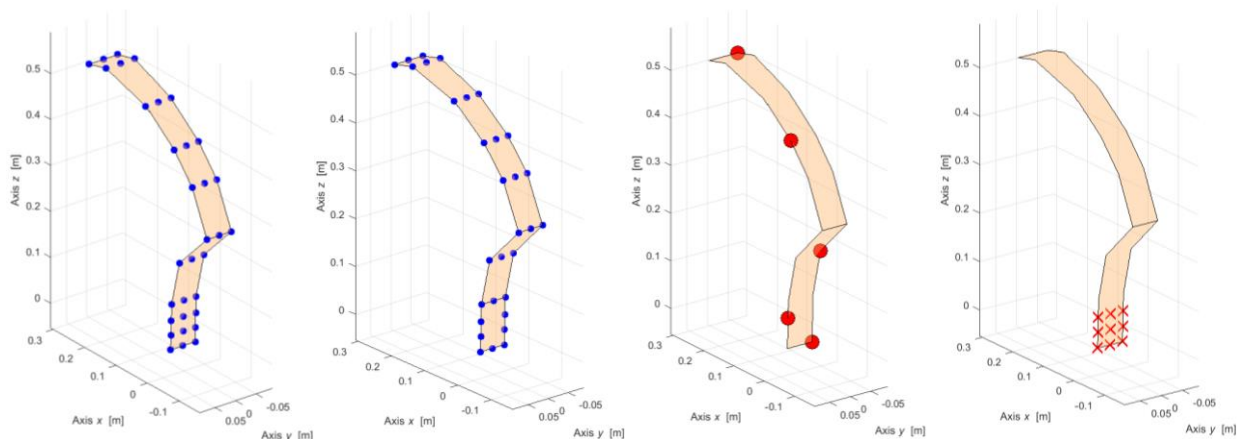


Figure 5.1.3.1 – Experimental geometry (from left to right): all the nodes defined, nodes excited, sensor nodes and constrained nodes.

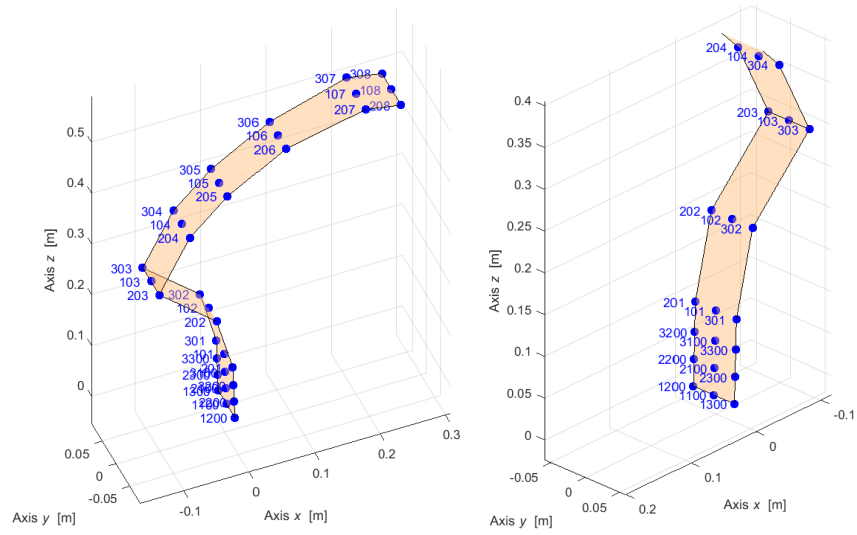


Figure 5.1.3.2 – Node nomenclature.

Table 5.1.3.1 – Geometry of I/O points.

Identifier	Exp. point	x [m]	y [m]	z [m]	Notes
	101	0.000	0.000	0.100	
	102	-0.025	0.000	0.200	
	103	-0.113	0.000	0.285	
	104	-0.066	0.000	0.380	
	105	-0.008	0.000	0.440	
	106	0.081	0.000	0.500	
	107	0.201	0.000	0.537	
	108	0.255	0.000	0.525	
	201	0.000	-0.030	0.100	
Acc. 3, x, y, z	202	-0.025	-0.030	0.200	SN5958472
	203	-0.113	-0.030	0.285	
	204	-0.066	-0.030	0.380	
	205	-0.008	-0.030	0.440	
	206	0.081	-0.030	0.500	
	207	0.201	-0.035	0.537	
Acc. 1, x, y, z	208	0.255	-0.035	0.525	SN5958474
	301	0.000	0.030	0.100	
	302	-0.025	0.030	0.200	
	303	-0.113	0.030	0.285	
	304	-0.066	0.030	0.380	
Acc. 2, x, y, z	305	-0.008	0.030	0.440	SN5958475
	306	0.081	0.030	0.500	
	307	0.201	0.035	0.537	
	308	0.255	0.035	0.525	
	1100	0.003	0.000	0.000	
Acc. 5, x	1200	0.003	-0.030	0.000	LW148801
	1300	0.003	0.030	0.000	
	2100	0.002	0.000	0.032	
	2200	0.002	-0.030	0.032	
	2300	0.002	0.030	0.032	
	3100	0.001	0.000	0.064	
	3200	0.001	-0.030	0.064	
Acc. 4, x, y, z	3300	0.001	0.030	0.064	SN5958473

As a reference approach, the hammered directions are always orthogonal to nearest surface to defined nodes. As consequence, the Euler angle at each node level must be measured and specified in the geometry definition on Siemens LMS Test.Lab. It defines the slope in between the local and the global reference frames. In this case, it is computed from the drawing of the Solidworks CAD, as shown in Figure 5.1.3.3. In Table 5.1.3.2, the Euler angles specified on the software are reported, notice that the majority of them is complementary with respect the ones evaluated on the drawing, in order to have the X direction of the local reference frame pointing inwards the prosthetic shape.

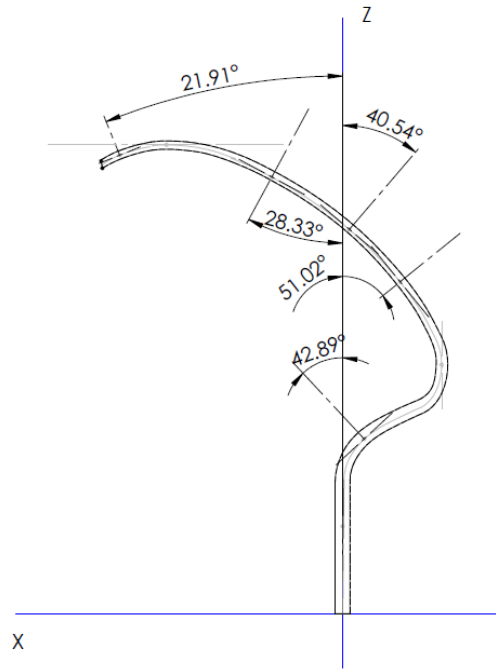


Figure 5.1.3.3 – Evaluation of the Euler angle at each node level on the CAD drawing, Solidworks 2015

Table 5.1.3.2 – Euler angles of the prosthetic nodes.

Node ID	Euler angle
1100-1200-1300	0°
101-201-301	0°
102-202-302	42.89°
103-203-303	0°
104-204-304	-38.98°
105-205-305	-49.46°
106-206-306	-61.67°
107-207-307	-90°
108-208-308	-111.91°

In Table 5.1.3.3, hammering directions during the experimental work are supplied. For some points at the border of the prosthetic, two hammering are performed: one along the width, Y direction, and the other one perpendicular to the component shape. Given the difficulties in exciting properly nodes 108, 208 and 308, they are not excited along X direction. Where possible, also some constrained points are excited, some along Y direction and some along Z. In the constrained area, just the points where the sensors are placed are also excited along X.

Table 5.1.3.3 – Hammering directions of the experimental work for each excited node.

Node ID	Hammering directions
101	X
102	X
103	X
104	X
105	X
106	X
107	X
108	Z
201	X; Y
202	X; Y
203	X; Y
204	X; Y
205	X; Y
206	X; Y
207	X; Y
208	Y
301	X; Y
302	X; Y
303	X; Y
304	X; Y
305	X; Y
306	X; Y
307	X; Y
308	Y
1100	Z
1200	X; Y; Z
1300	Y; Z
2100	-
2200	Y
2300	Y
3100	-
3200	Y
3300	X; Y

5.1.4 Acquisition parameter settings

During impact testing measurements, the parameters in Table 5.1.4.1 are selected:

Table 5.1.4.1 – Independent and dependent parameters of acquisition.

Quantity	Symbol	Relationship	Value	Units
Total acquisition time	T		4	s
Sample frequency	f_s		8192	Hz
Total samples	N	$N = f_s T$	32768	-
Bandwidth (max frequency)	f_b	$f_b = \frac{f_s}{2}$	4096	Hz
FRF frequency resolution	Δf	$\Delta f = \frac{f_s}{N} = \frac{1}{T}$	0.25	Hz
Number of spectral lines	N_f	$N_f = \frac{N}{2}$	16384	-

For the windowing a cut-off of 0.6 and a decay of 90% are set. The decay setting is useful if the signal is not nil at the end of the acquisition time: a damping is applied to the last part of the signal in order to have a zero value in the final part.

5.2 Experimental data

The experimental data are analysed in a frequency range 0÷ 1500 Hz, in Figure 5.2.1, the FRF sum is displayed, while in Figure 5.2.1 the natural frequencies and damping ratios are extracted.

In Figure 5.2.1, the vertical dashed lines represent the natural frequencies extracted; notice that, not for all of them the FRF sum plot shows a peak. Just the first 6 mode shapes are identified.

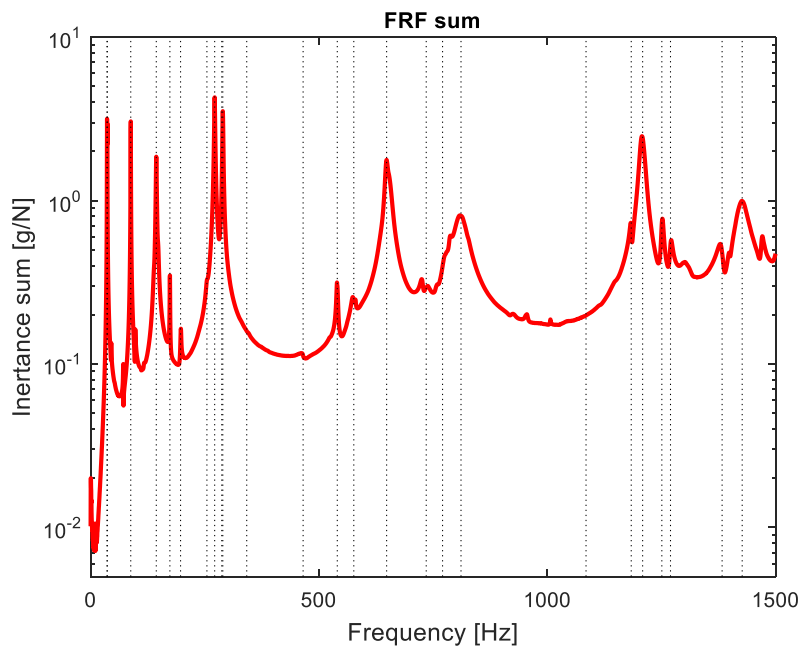


Figure 5.2.1 – Prosthetic FRF sum.

Table 5.2.1 – Experimental natural frequencies and damping ratios on Prosthetic.

Mode	Freq. [Hz]	ζ, damping ratio [%]	Description
1	35.95	0.0038	1 st bending XZ
2	36.58	0.0034	1 st bending XY
3	87.89	0.0027	2 nd bending XZ
4	143.8	0.0069	Torsional RZ
5	173.6	0.0017	3 rd bending XZ
6	197	0.0061	Torsional RZ
7	254.7	0.0074	-
8	271.7	0.0041	-
9	287.2	0.0130	-
10	289.5	0.0030	-
11	341.9	0.0127	-
12	465.4	0.0066	-
13	540.2	0.0026	-
14	576.4	0.0078	-
15	648.3	0.0043	-
16	735	0.0092	-
17	770.8	0.1028	-
18	811.2	0.0196	-
19	1085	0.0139	-
20	1184	0.0011	
21	1209	0.0042	
22	1251	0.0025	
23	1270	0.0031	
24	1383	0.0037	
25	1427	0.0097	

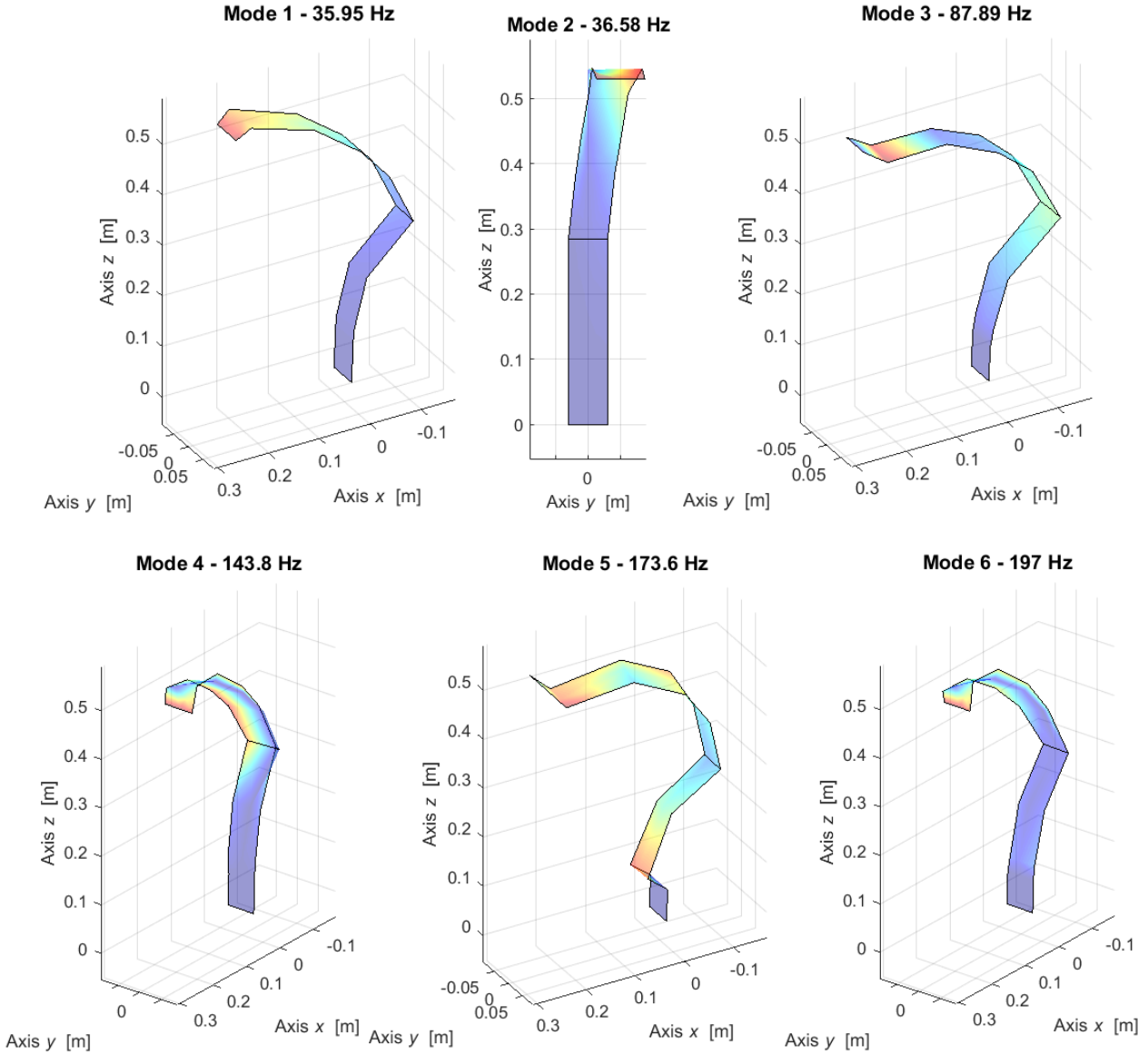


Figure 5.2.2 – Prosthetic first 6 mode shapes, experimental results.

In order to carry out a comparison of the independency of the mode shapes, the MACX (complex Modal Assurance Criterion) is adopted allowing to measure the correlation level between two complex mode shapes Ψ_j and Ψ_k respectively.

The MACX is defined as follow:

$$MACX_{j,k} = \frac{\left[|\Psi_j^H \Psi_k| + |\Psi_j^T \Psi_k| \right]^2}{\left[\Psi_j^H \Psi_j + |\Psi_j^T \Psi_j| \right] \left[\Psi_k^H \Psi_k + |\Psi_k^T \Psi_k| \right]} \quad (5.2.1)$$

where:

- the superscript H is the Hermitian, complex transposed;
- its value is always real and semi-positive, independently if the eigenvectors are real or complex;

- its value ranges from 0, corresponding to very far mode shapes or orthogonal, to 1, corresponding to equal or similar (scaled) shapes;
- it is independent on the norm and the phase of Ψ_j and Ψ_k , so the normalisation of eigenvectors is neglected;
- it is insensitive to conjugate operations on its arguments;
- $MACX(\Psi_j, \Psi_k) = 0$ is equivalent to $\Psi_j^H \Psi_k = 0$ and $\Psi_j^T \Psi_k = 0$;
- if $\Psi_k = z \Psi_j$ or $\Psi_k = z \Psi_j^*$, considering an arbitrary complex coefficient or unitary norm $z = e^{i\delta}$, then $MACX(\Psi_j, \Psi_k) = 1$, but it is worth noting that this is only a sufficient condition;
- if one of the vectors Ψ_j and Ψ_k is monophasic, then the MACX and MAC criteria are identical;
- conversely, vectors Ψ_j and Ψ_k can be found such that $MAC(\Psi_j, \Psi_k) = 0$ and $MACX(\Psi_j, \Psi_k) = 1$, but in this case both vectors are “full” complex since $MPC(\Psi_j) = 0$ and $MPC(\Psi_k) = 0$.

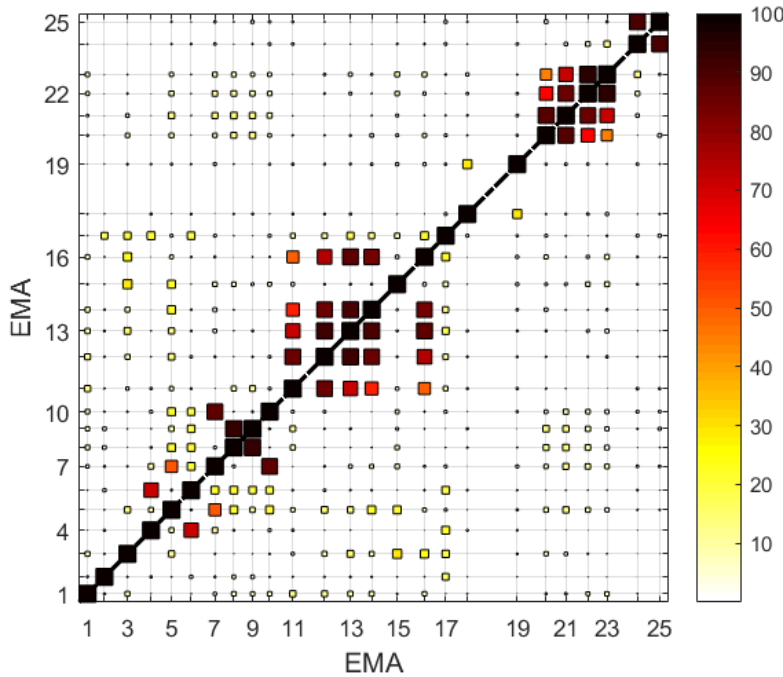


Figure 5.2.3 – Experimental mode shapes Auto-MAC.

The auto-MAC obtained is almost diagonal, meaning that the modes obtained are orthogonal. Just between few modes there is an high MACX value, such as between the 8th and 9th ones. These two modes are really close in frequency: 271.7 Hz and 287.2 Hz and have a MACX value of 92.9 %. This is just a consequence of experimental issues: the accelerometers and hammering locations cause the identification of two different modes where actually just one is present.

5.3 Post-processing results

The inertance is a frequency response function (FRF) that is defined in the frequency domain as the ratio between the acceleration and the external forces.

In the real case of a m dofs system the inertance formula can be defined as:

$$A_{j,k}(\omega) = \frac{\ddot{x}_j(\omega)}{F_k(\omega)} = -\omega^2 \frac{x_j(\omega)}{F_k(\omega)} = \sum_{r=1}^m \frac{-\omega^2 \Phi_{j,r} \Phi_{k,r}}{\omega_r^2 + 2i\zeta_r \omega_r \omega - \omega^2} \quad (5.3.1)$$

where:

- ω_r is the natural frequency of r -mode shape;
- ω is the excitation frequency;
- $\Phi_{j,r}$ and $\Phi_{k,r}$ are the mode shapes related to the j and k nodes respectively.

5.3.1 Auto-inertances

The auto-inertance can be defined as the FRF evaluated in the node k due to the excitation on the node j , where $j = k$ and along the same direction. Therefore, the node of excitation is the same as the node where the FRF is evaluated.

In the following figures the auto-inertances experimental (solid blue line), synthesised with lower and upper residuals (LR and UR) (dash-dot red line) and synthesised with modal superposition are presented.

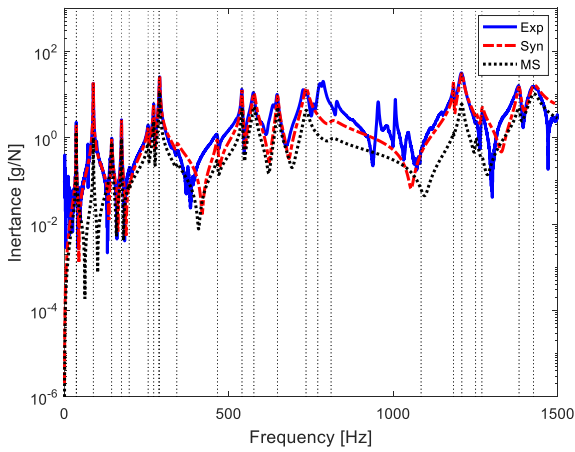


Figure 5.3.1.1 – Auto-inertance: E202x_R202x.

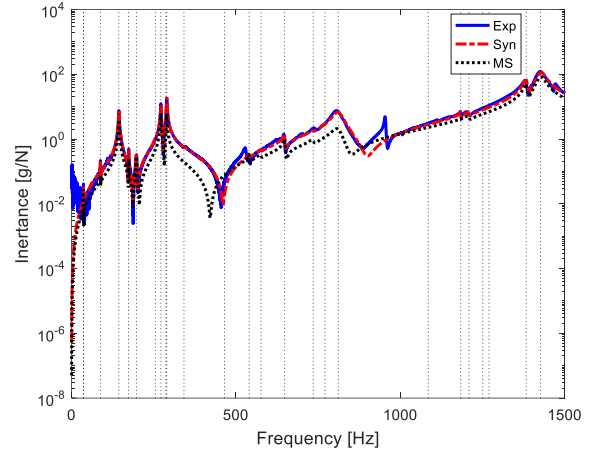


Figure 5.3.1.2 – Auto-inertance: E202y_R202y.

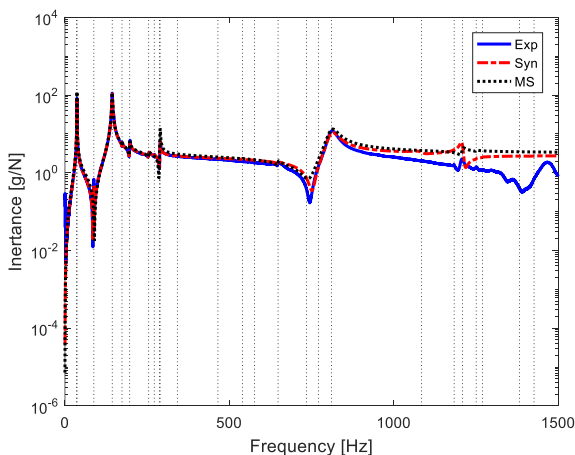


Figure 5.3.1.3 – Auto-inertance: E208y_R208y.

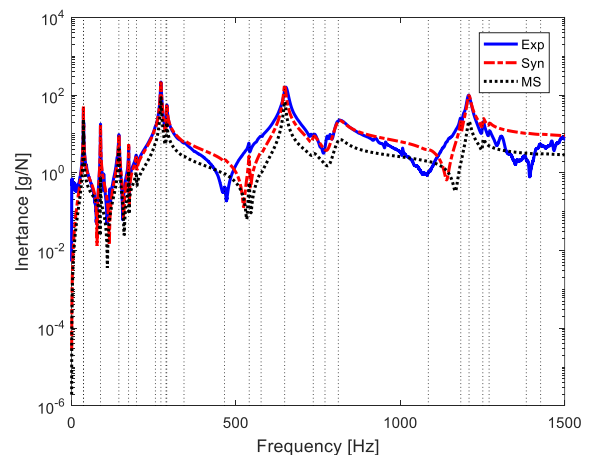


Figure 5.3.1.4 – Auto-inertance: E305y_R305y.

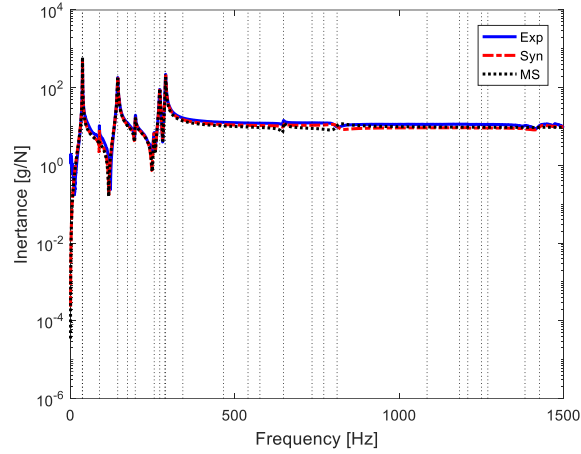


Figure 5.3.1.5 – Auto-inertance: E305x_R305x.

The plots just reported, show almost an overlapping of the three curves, demonstrating a good agreement in between the experimental and the computed results, thus proving the goodness of the experimental results.

5.3.2 Maxwell reciprocity

With real modal superposition of m modes or with complex modal superposition of $2m$ modes, a generic cross-receptance $\alpha_{j,k}$ (similarly to mobility $Y_{j,k}$ and inertance $A_{j,k}$), the Maxwell reciprocity imposes that input and output can be switched:

$$\alpha_{j,k}(\omega) = \frac{x_j(\omega)}{F_k(\omega)} = \alpha_{k,j}(\omega) = \frac{x_j(\omega)}{F_j(\omega)} = \sum_{r=1}^m \frac{\Phi_{j,r} \Phi_{k,r}}{\omega_r^2 + 2i\zeta_r \omega_r \omega - \omega^2} \quad (5.3.2.1)$$

$$\alpha_{j,k}(\omega) = \frac{x_j(\omega)}{F_k(\omega)} = \sum_{r=1}^{2m} \frac{\Psi_{j,r} \Psi_{k,r}}{a_r(i\omega - S_r)} \quad (5.3.2.2)$$

Below, the reciprocity test is performed by plotting the experimental and the synthesised inertances, switching the excited and sensed nodes and direction. Given the good agreement in between the curves compared, the linearity of the component is verified.

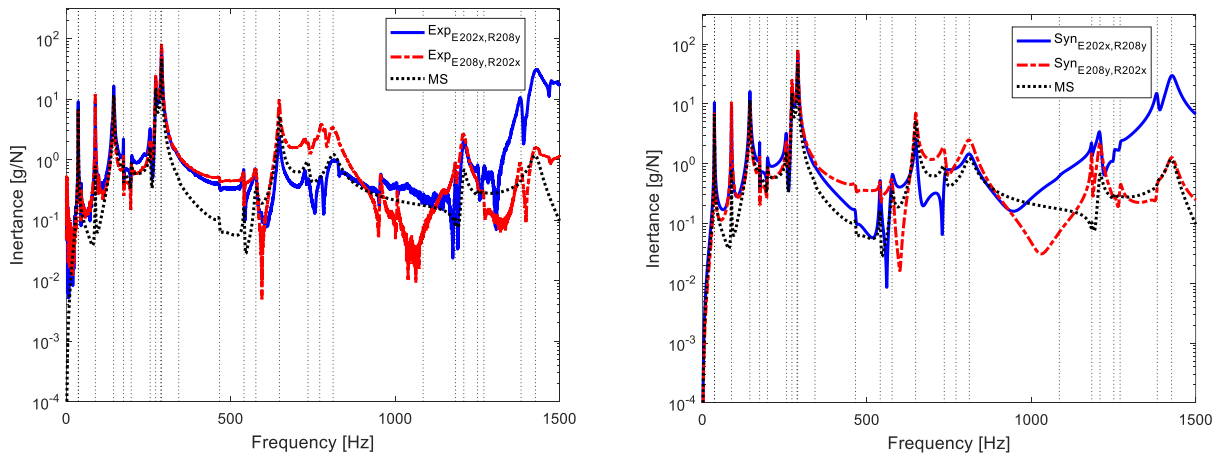


Figure 5.3.2.1 – Reciprocity test: E202x-R208y:
experimental inertance (left) and synthesised inertance by Test.Lab (right).

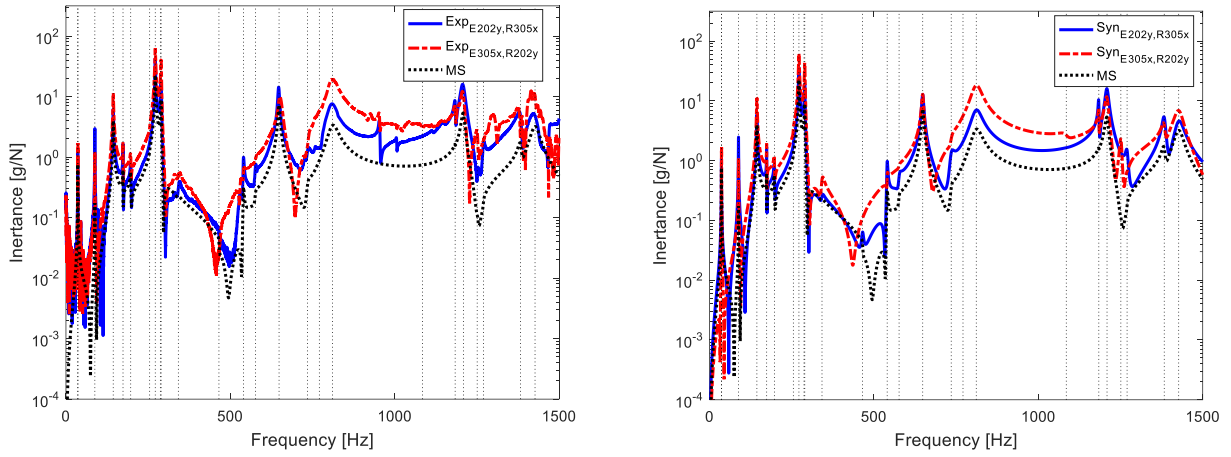


Figure 5.3.2.2 – Reciprocity test: E202y-R305y: experimental inertia (left) and synthesised inertia by Test.Lab (right).

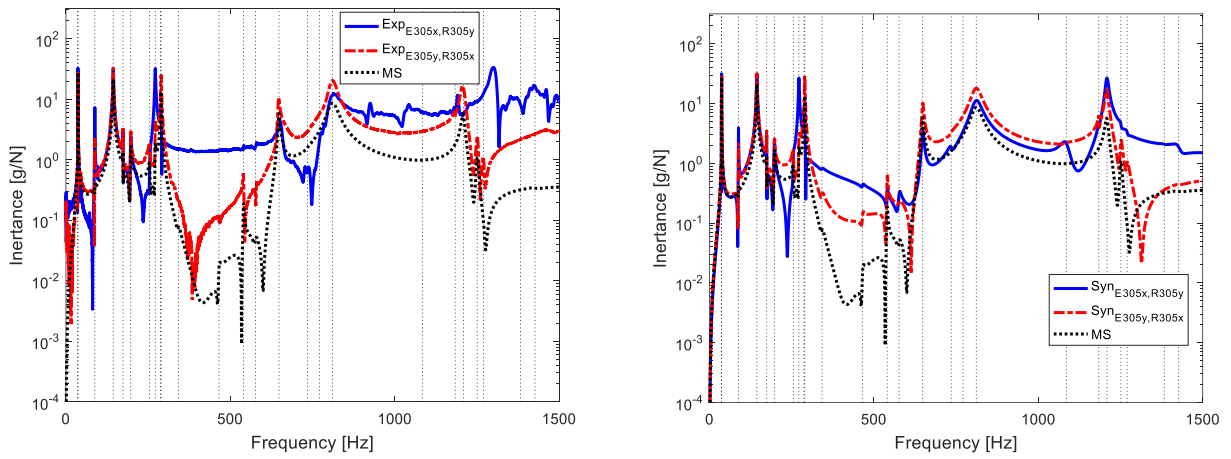


Figure 5.3.2.3 – Reciprocity test: E305x-R305y: experimental inertia (left) and synthesised inertia by Test.Lab (right).

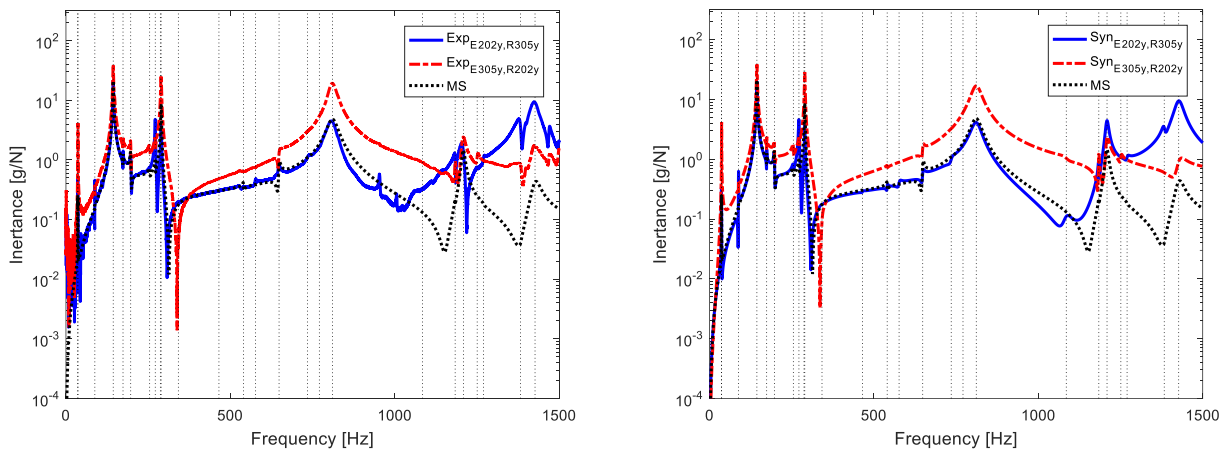


Figure 5.3.2.4 – Reciprocity test: E202y-R305y: experimental inertia (left) and synthesised inertia by Test.Lab (right).

5.4 Comparison between the EMA performed at Politecnico of Torino and at the University of Groningen

In Table 5.4.1 the results obtained from the two EMAs are compared. The outcomes obtained from the test performed in Italy are more reliable since multiple triaxial accelerometers were placed on the prosthetic and a more advanced data analyser was used. In the test performed at the University of Groningen (Paragraph 4), just one monoaxial accelerometer was available and it was possible just to acquire the data in time. Furthermore, the only check on the goodness of the hammering performed was the analysis of the force curve in the time and frequency domain, evaluated after the test. The natural frequencies were then obtained by looking at the FRF curves obtained in the post processing of the data performed on Matlab and the mode shapes were assumed by looking at the plot obtained. As consequence, the majority of the natural frequencies individuated in the test performed in Italy were not pointed out in the EMA carried out in the Netherlands. Indeed, thanks to the use of multiple triaxial accelerometers and of the data analysed Siemens Test.Lab v.17, in the test performed at DIMEAS, it was possible to investigate better the particular dynamic behaviour of the prosthetic which has some modes really close in frequency, such as the first and second ones.

From Table 5.4.1, it is remarkable the fact that just the first two bending modes on the XZ plane were correctly individuated in the first EMA test. Indeed, the accelerometer was placed at the toe level where the prosthetic is tangential to the horizontal plane, in such a way to evaluate mainly the bending in the XZ plane, which is considered the main one for the purpose for which the blade prosthetic is used.

The natural frequency at around 100 Hz instead, was confused to be a bending mode on the XY plane instead of a torsion, this is comprehensible since just one sensor was used, thus is really easy to mistake between flexural mode on the XY plane and torsion.

Overall, given the boundary conditions for which the test at the University of Groningen was performed, the disposition of the sensor and the good post processing evaluations performed, allowed to understand roughly the main dynamic behaviour of the blade prosthetic.

Table 5.4.1 – Results comparison of the EMA performed at University of Groningen and the one carried out at Politecnico of Torino.

Mode	EMA_University of Groningen		EMA_Politecnico of Torino	
	f [Hz]	Mode shape	f [Hz]	Mode shape
1	36	1 st bending XZ	35.95	1 st bending XZ
2	-	-	36.58	1 st bending XY
3	81	2 nd bending XZ	87.89	2 nd bending XZ
4	101	1 st bending XY	143.8	Torsional RZ
5	-	-	173.6	3 rd bending XZ
6	-	-	197	Torsional RZ
7	257	1 st torsion RZ	254.7	-
8	275	3 rd bending XZ	271.7	-

5.5 Numerical analysis

The numerical analysis is conducted on Lupos 2023 with the support, for the large models, of the MSC Nastran 2017 solver.

Firstly, the component is discretized in 2D shell with homogeneous isotropic material. Then, a 3D model is created through the use of hexagonal elements. The component is initially simulated considering isotropic properties and then orthotropic ones. Finally, along the thickness different material properties are considered in order to simulate a laminate stacking sequence in which the laminae orientation is different between each other.

For every model, before performing the simulations, it is verified that the total mass coincides with the one of the blade prosthetic measured.

5.5.1 Shell models

The component is discretized by shell elements made up of 4 nodes each (sh4).

The model creation is below described.

1. Firstly the nodes along the prosthetic shape (XZ plane) are discretized through the use of the Matlab function `interp1`. In particular, the interpolation method used is `pchipr`, a piecewise cubic interpolation. Given the shape of the prosthetic, in order to have a homogeneous nodes discretization, the Z coordinates are computed by setting a constant distance, calculated through the Pitagora's theorem, and then the corresponding X values where computed by using `interp1`.
2. Then, all the nodes which have been found in the 2D space are extruded adding the Y coordinate value:

$$Y_r = \pm \frac{w}{num_r - 1} \cdot count_r \quad (5.5.1.1)$$

where:

- r refers to the node along the prosthetic width;
- w is the width which is constant till around node 106. Starting from some nodes before the 106th till some nodes after this one (depending on the discretization level), there is a continuous width variation, till reaching a constant value of 70 mm;
- num_r is the number of nodes which describes the component along the width;
- $count_r$ is the loop counting which considers the r th node which is being computed;

The nodes ID along the width is, starting from the outset nodes, ID_p+100 on the right and ID_p+200 on the left (with respect the Y axis).

3. Finally, the shell elements are created. The information required for the .sh4 document are the ID of the 4 nodes describing the element, the colour and the material properties: density, Young modulus and Poisson ratio. The nodes must be indicated in a proper order, otherwise wrong shapes with respect a shell will be created and all the normal vectors have to point all inwards or outwards with respect the prosthetic shape. Below an example of a line of the .sh4 file and the imagine representing the hexa element created.

```
[211 10211 10411 411 231 10231 10431 431 11 1.5e+03 6.43e+10 3.0e-01]
```

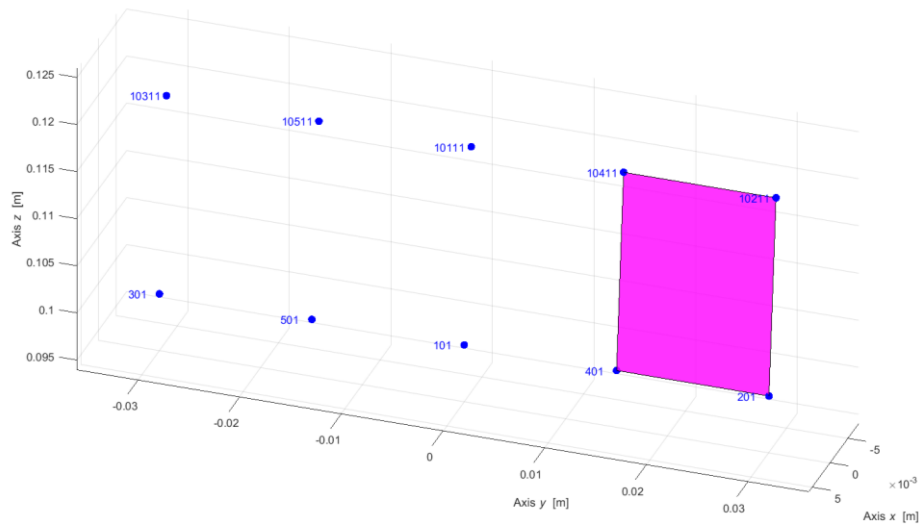


Figure 5.5.1.1 – Creation of one sh4 element. Test Rig Control Pannell, Lupos 2023.

H-convergence analyses are performed considering two different models: the first one with a constant mean thickness value along the prosthetic shape, while the second one with a discrete variation of the thickness.

To perform the H-convergence study, three different discretisations with an increasing number of elements are considered, as displayed in Figure 5.5.1.2 and reported in Table 5.5.1.1.

Notice that, since the finite element analysis works better with regular shapes, the same distance is tried to be kept both on the XZ plane and on the Y direction, in such a way to have shell in a square shape.

As boundary conditions, all the nodes in the constrained area are fixed in all the directions.

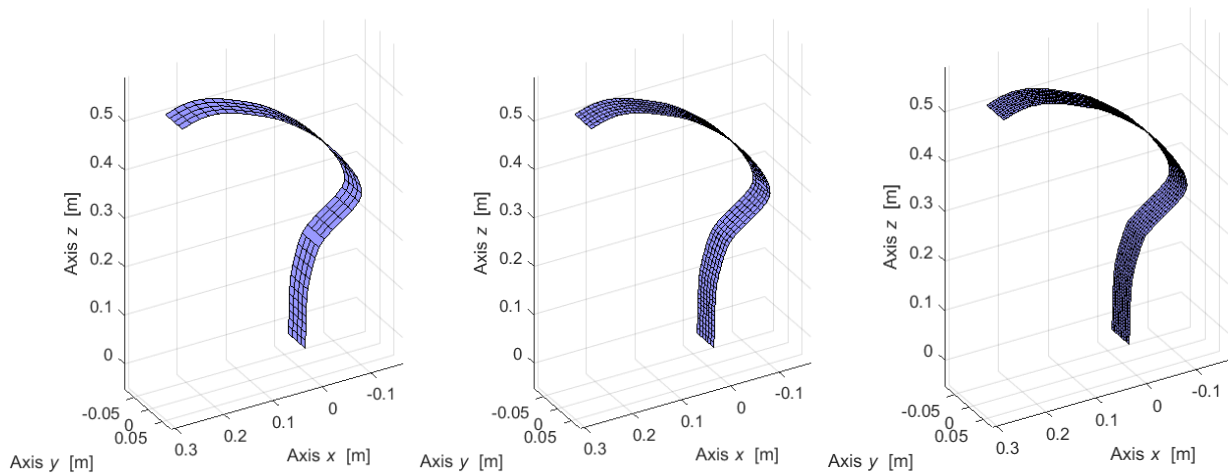


Figure 5.5.1.2– Models of the simulations. From left to right: Prosthetic_002, Prosthetic_001 and Prosthetic_0006.

Table 5.5.1.1– Characteristics of the three models considered for the simulation.

Characteristic	Prosthetic_002	Prosthetic_001	Prosthetic_0006
Nodes num.	205	574	1474
Elements num.	160	486	1330
BCs	180	420	996
Dofs	1050	3024	7848

A comparison in between the CAD model created on Solidworks 2015 and the model created on Lupos 2023 discretised with shell elements is displayed in Figure 5.5.1.3.

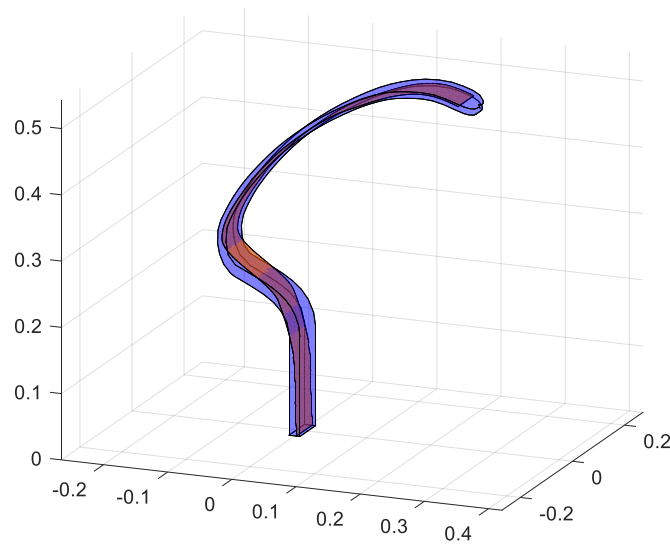


Figure 5.5.1.3 – Overlapping of the CAD model created on Solidworks 2015 and the model created on Lupos 2023 discretised with 2D shell elements.

The material parameters considered are reported in Table 5.5.1.2.

Table 5.5.1.2– Isotropic material properties, shell simulation.

Property	Value
Density [kg/m ³]	1548.93
Poisson ratio [-]	0.3
Young modulus [Pa]	$6.4 \cdot 10^{10}$

5.5.1.1 Model 1

In the first model a constant mean thickness value is considered in the definition of all the shell elements. The elements properties established are reported in Table 5.5.1.1.1.

Table 5.5.1.1.1 – Shell elements parameters.

Parameter	Value
Thickness [mm]	15
Density [kg/m ³]	1548.93
Young modulus [Pa]	6.4·10 ¹⁰
Poisson ratio [-]	0.3

The models are defined on Lupos and then converted in the .bdf files in order to perform the simulations on MSC Nastran 2017.

An H-convergence analysis is performed considering the first two natural frequencies, as displayed in **Errore. L'origine riferimento non è stata trovata.** A comparison of the first four natural frequencies among the three discretisations is also reported in Table 5.5.1.1.2. In the last column of

the table, the variance in between the results obtained is computed, according to eq $e = \frac{f_{\max,i} - f_{\min,i}}{f_{\max,i}}$

(5.5.1.1.1).

$$e = \frac{f_{\max,i} - f_{\min,i}}{f_{\max,i}} \quad (5.5.1.1.1)$$

where $f_{\max,i}$ and $f_{\min,i}$ are respectively the maximum and minimum natural frequencies of the i -th mode evaluated between the three discretisation.

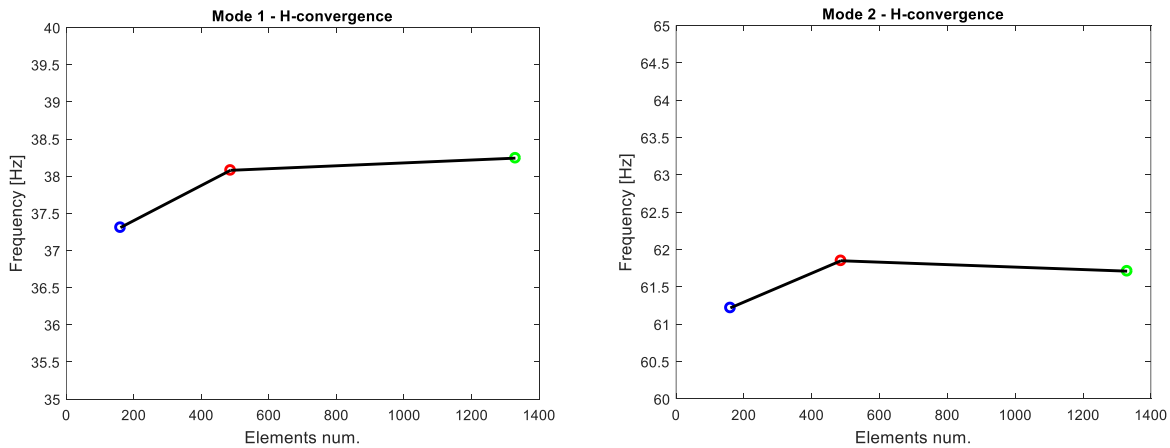


Figure 5.5.1.1.1– H-convergence results of the prosthetic models described by sh4 elements with the same thickness. First (left) and second (right) modes.

Table 5.5.1.1.2– Natural frequency results of the three discretisations; Model 1.

Natural frequency	Prosthetic_002	Prosthetic_001	Prosthetic_0006	e
f ₁ [Hz]	37.31	38.08	38.24	2.4%
f ₂ [Hz]	61.22	61.85	61.71	1.0%

f_3 [Hz]	117.60	120.91	121.65	3.3%
f_4 [Hz]	293.59	306.50	310.77	5.5%

The natural frequencies obtained are really close between the three discretisations, thus already with 160 shell elements a stability in the modal results is reached.

5.5.1.2 Model 2

In order to better simulate the real component, a discrete variation of the thickness is then considered along the prosthetic shape. In between the adjacent nodes identified for the experimental analysis, the same shell properties are maintained, thus there is a discrete thickness variation per area. The thickness values considered are reported in Table 5.5.1.2.1, for sake of completeness in Figure 5.5.1.2.1 the nodes mentioned in the table are represented.

Table 5.5.1.2.1 – Thickness values defined along the prosthetic shape.

Starting node	Ending node	Thickness [mm]
1100	102	17
102	103	14
103	104	12
104	105	11
105	106	10
106	107	9.7
107	108	9.5

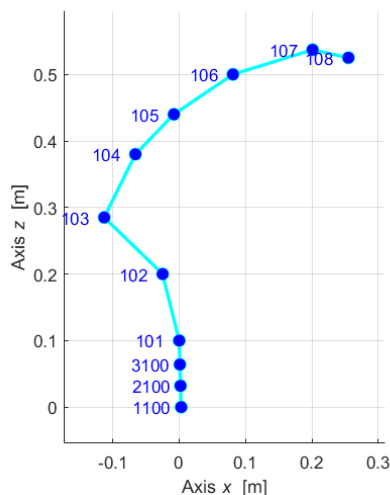


Figure 5.5.1.2.1 – Prosthetic central nodes identified for the EMA. A part from the constrained nodes, the others represent the nodes in which there is a discrete variation of thickness.

In Figure 5.5.1.2.2, the H-convergence graphs are reported. Just the first two natural frequencies are considered. A comparison of the first four natural frequencies among the three discretisations is also

reported in Table 5.5.1.2.2 with the variance computation of the results, according to

$$\text{eq } e = \frac{f_{\max,i} - f_{\min,i}}{f_{\max,i}} \quad (5.5.1.1.1).$$

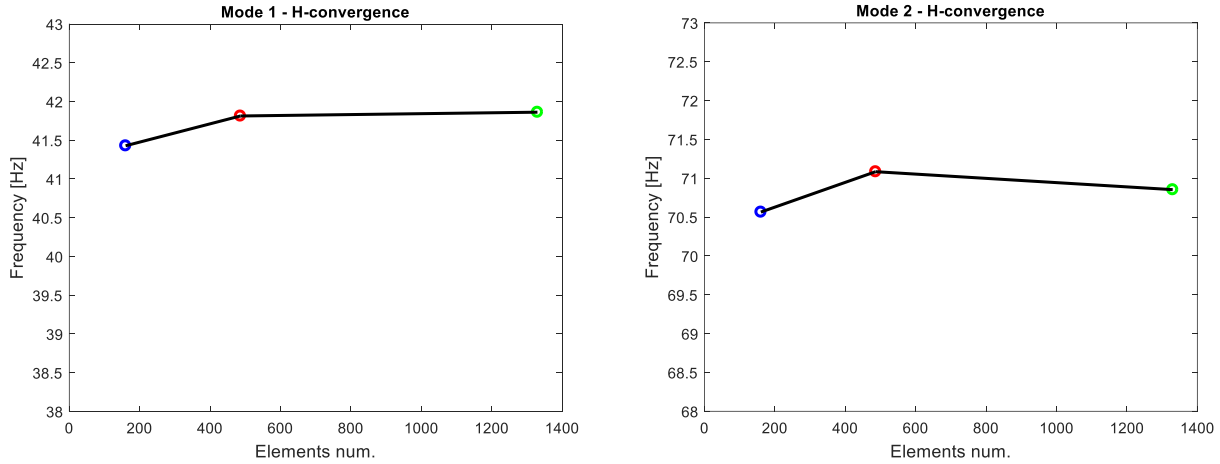


Figure 5.5.1.2.2 – H-convergence results of the prosthetic models described by sh4 elements, varying the thickness. First (left) and second (right) modes.

Table 5.5.1.2.2 – Natural frequency results of the three discretisations, Model 2.

Natural frequency	Prosthetic_002	Prosthetic_001	Prosthetic_0006	e
f ₁ [Hz]	41.43	41.81	41.86	1.0%
f ₂ [Hz]	70.56	71.08	70.85	0.7%
f ₃ [Hz]	118.38	121.76	122.52	3.4%
f ₄ [Hz]	323.10	324.54	324.56	0.5%

The natural frequencies obtained are higher with respect the ones obtained by maintaining a constant thickness value along all the model. The variance in the outcomes is smaller with respect what obtained in Model 1.

For completeness, the first 6 natural frequencies and mode shapes of the finest model, Prosthetic_0006, are compared to the EMA results (see Table 5.5.1.2.3). Between the fourth and the fifth mode shapes there is switch: 4th mode is a bending in XZ while the 5th is the first torsion. Furthermore, there is a remarkable discrepancy between the FEA and the EMA natural frequencies obtained, for higher modes the mismatch becomes always bigger.

Table 5.5.1.2.3 – EMA-FEA comparison. Shell model Prosthetic_006, isotropic material.

Mode	FEA		EMA	
	Nat freq. [Hz]	Mode shape	Nat. freq. [Hz]	Mode shape
1	41.86	1 st bending XZ	35.95	1 st bending XZ
2	70.85	1 st bending XY	36.58	1 st bending XY
3	122.50	2 nd bending XZ	87.89	2 nd bending XZ
4	324.60	3 rd bending XZ	143.80	Torsional RZ

5	340.40	Torsional RZ	173.60	3 rd bending XZ
6	651.00	Torsional RZ	197.00	Torsional RZ

The FEA and EMA mode shapes are also compared through the computation of the MAC matrix (defined in Paragraph 5.2). To compare the mode shapes between two different models, firstly it is necessary to verify that they are overlapped in the global reference frame (as shown in left image of Figure 5.5.1.2.3), otherwise translations and rotations of one model with respect the other have to be applied. Then, the function `EmaFeaCoupling` is used to identify the corresponding nodes between the two models; it correlates the nodes, between the two configurations, that have the lowest distance among the others. In this case, the same nodes identified for the experimental test are maintained in the creation of the sell model, thus there is an exact correlation between the nodes.

As visible from the MAC plot (right image of Figure 5.5.1.2.3), there is not a good match between the FEA and EMA mode shapes. Furthermore, as mentioned previously, the 4th and 5th mode shapes are completely different from the ones obtained experimentally.

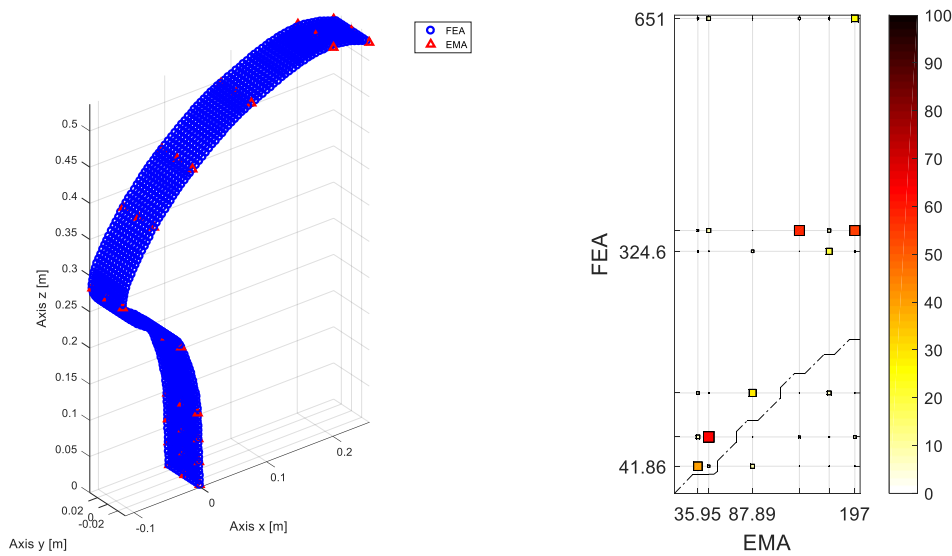


Figure 5.5.1.2.3 – Overlapping verification of the EMA and FEA models (left) and EMA-FEA MAC matrix (right). FEA of the shell model `Prosthetic_006`, isotropic material. The dashed line in the MAC plot is the iso-frequency curve.

5.5.2 3D models

To obtain more reliable results, it is convenient to discretize the model through the use of solid elements. In this way, multiple elements can be set along the thickness, while with the 2D finite element modelling it is not possible. As a result, it is possible to better simulate the component behaviour along the thickness.

The prosthetic is discretized with hexagonal elements on `Lupus 2023`, they are called hexa and define the link between 8 nodes.

The model creation is below described in multiple steps.

1. Firstly, starting from the nodes individuated for the experimental test on the plane of symmetry of the prosthetic, more nodes are identified through the use of the Matlab function `interp1`. In particular, the interpolation method used is the `pchip`, a piecewise cubic interpolation. Given the shape of the prosthetic, in order to have an homogeneous nodes

discretization, it is necessary not to consider a constant stepping on the perpendicular axis, but to compute and set a constant distance (Pitagora's theorem).

2. Then the nodes along the thickness are computed. For the creation of the mesh, the hexagonal elements must be perpendicular to the component shape in order to have as much as possible regular and cubic shapes. To do this, for each node, the angle created in between the adjacent nodes is computed and it is used to calculate the 2D coordinate of the nodes along the thickness. Making reference to the schematic representation of the logic just described (Figure 5.5.2.1), the nodes along the thickness are calculated as:

$$X_q = X_p \pm \left(\frac{t}{num_q - 1} \cdot count_q \right) \cdot \cos \vartheta \quad (5.5.2.1)$$

$$Z_q = Z_p \mp \left(\frac{t}{num_q - 1} \cdot count_q \right) \cdot \sin \vartheta \quad (5.5.2.2)$$

where:

- p refers to the node along the prosthetic shape, while q to the ones along the thickness;
- X_p are the coordinates of the node considered;
- t is the thickness which, from node 101, is decreased for every j node: from 17 mm to 9.5 mm;
- num_q is the number of nodes which describes the component along the thickness;
- $count_q$ is the loop counting which considers the q^{th} node which is being computed;
- ϑ is the computed angle in between the adjacent nodes along the shape.

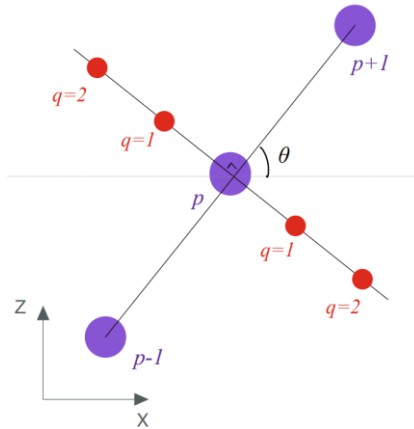


Figure 5.5.2.1 – Schematic representation of the logic considered for the creation of the nodes along the thickness. 3D model discretization.

The nodes ID along the thickness is, starting from the outmost nodes, ID_{p+10} on the right and ID_{p+20} on the left.

3. Afterwards, the discretization along the width is performed. Thus, all the nodes which have been found in the 2D space are extruded adding the Y coordinate value:

$$Y_r = \pm \frac{w}{num_r - 1} \cdot count_r \quad (5.5.2.3)$$

where:

- r refers to the node along the prosthetic width;
- w is the width which is constant till around node 106. Starting from some nodes before the 106th till some nodes after this one (depending on the discretization level), there is a continuous width variation, till reaching a constant value of 70 mm;
- num_r is the number of nodes which describes the component along the width;
- $count_r$ is the loop counting which considers the r^{th} node which is being computed;

The nodes ID along the width is, starting from the outset nodes, ID_p+100 on the right and ID_p+200 on the left (with respect the Y axis).

The .geo file, containing all the nodes coordinates, is thus completely defined.

4. Finally, the hexagonal elements are created. The information required for the .hex document are the ID of the 8 nodes describing the element, the colour and the material properties: density, Young modulus and Poisson ratio. The nodes must be indicated in a proper order, otherwise wrong shapes with respect an hexagon will be created. Below an example of a line of the .hex file and the imagine representing the hexa element created.

[211 10211 10411 411 231 10231 10431 431 11 1.5e+03 6.43e+10 3.0e-01]

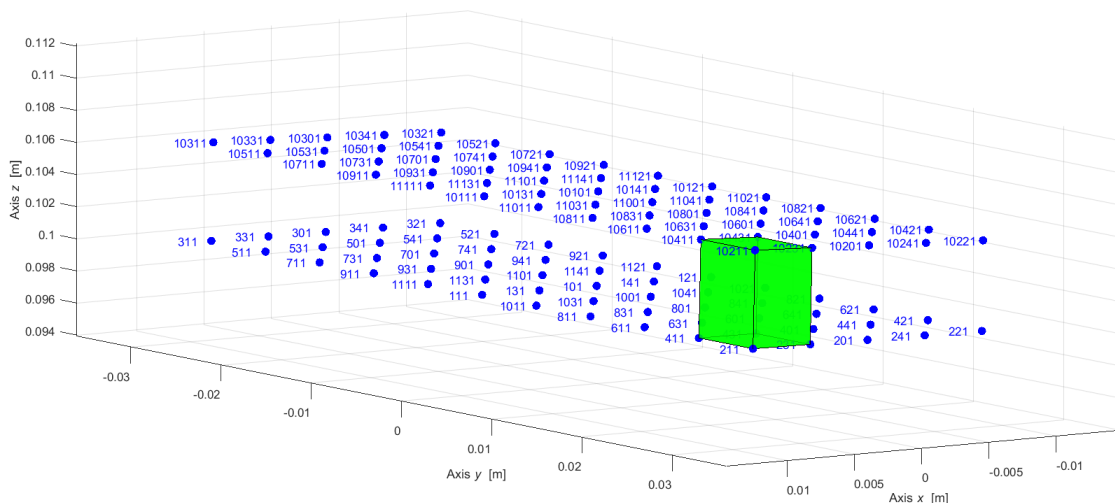


Figure 5.5.2.2 – Creation of one hexa element. Test Rig Control Pannel, Lupos 2023.

5.5.2.1 H-convergence analysis

Firstly, an H-convergence analysis is performed. The number of elements considered to perform this study is reported in Table 5.5.2.1.1. The number of hexa is very high because when a solid mesh is performed, it is suggested to have at least 3 elements along the thickness, otherwise the behaviour along this dimension is not well represented. Thus the less discretize model has 4 hexa along the thickness. Furthermore, the more the elements are regular, thus with a cubic shape, the better are the results, hence the same distance adopted in between the nodes along the thickness is considered also along the other two directions.

The three different discretisations are called Model_1, Model_2 and Model_3. The number of elements they are composed by is reported in Table 5.5.2.1.1. In the table, also the number of hexa present along the thickness and along the width of the component are reported. Having always an even number of elements along the thickness, the central nodes are always placed at the middle of the thickness.

Table 5.5.2.1.1 – Characteristics of the three models considered for the simulation with hexa elements.

Characteristic	Model_1	Model_2	Model_3
Nodes num.	7370	39543	112716
Elements num.	5320	32160	96720
BCs	406	1494	3262
Dofs	43814	235764	673034
Hexa num._thick	4	6	8
Hexa num._width	10	20	30

The three models are displayed below, in isometric (Figure 5.5.2.1.1), lateral (Figure 5.5.2.1.2) and upper view (Figure 5.5.2.1.3). From the upper and lateral views the gradual change in width and thickness are clearly visible. Despite the change in dimension, the number of elements is maintained constant. The models try to replicate as much as possible the real component. In Figure 5.5.2.1.4 Model_2 is overlapped to the Solidworks model, they are really similar, just the two bigger curvature are slightly different and the final rounded part, at the toe level, is not well defined on the Lupos model. However, the not precise shape correspondence at distal end should not affect much the results of the simulation.

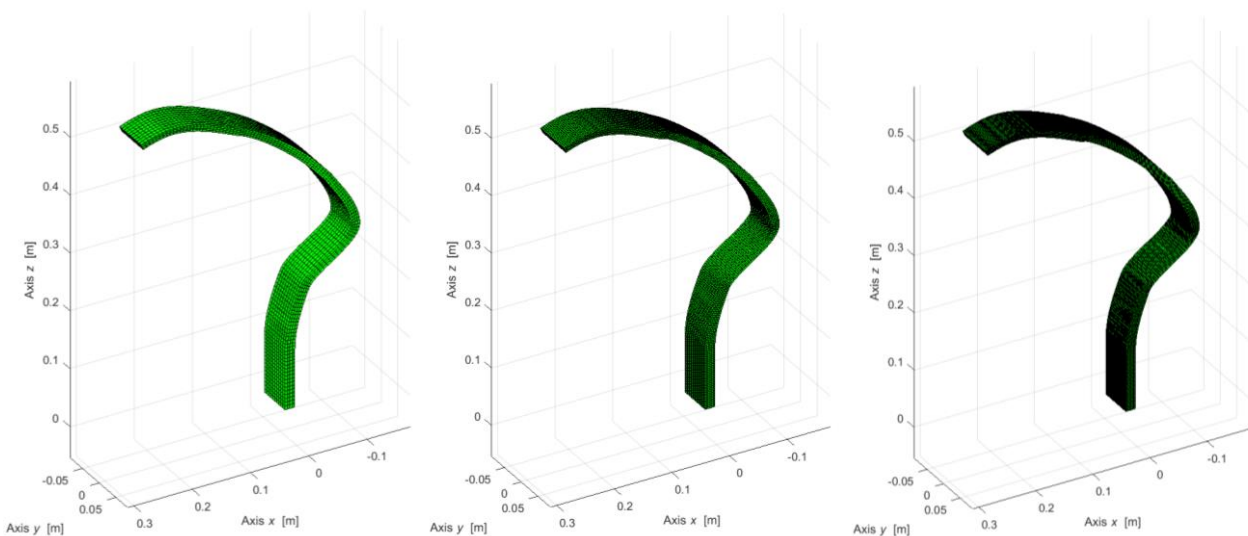


Figure 5.5.2.1.1 – Isometric view of the 3D model discretized by hexa on Lupos 2023. From left to right: Model_1, Model_2 and Model_3.

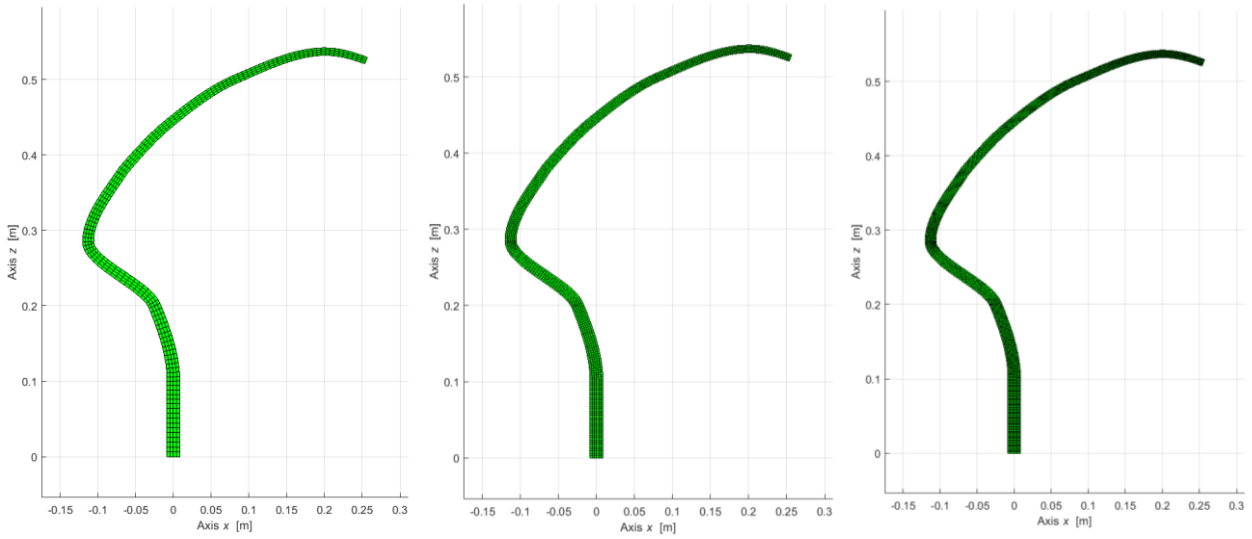


Figure 5.5.2.1.2 – Lateral view of the 3D model discretized by hexa on Lupos 2023. From left to right: Model_1, Model_2 and Model_3.

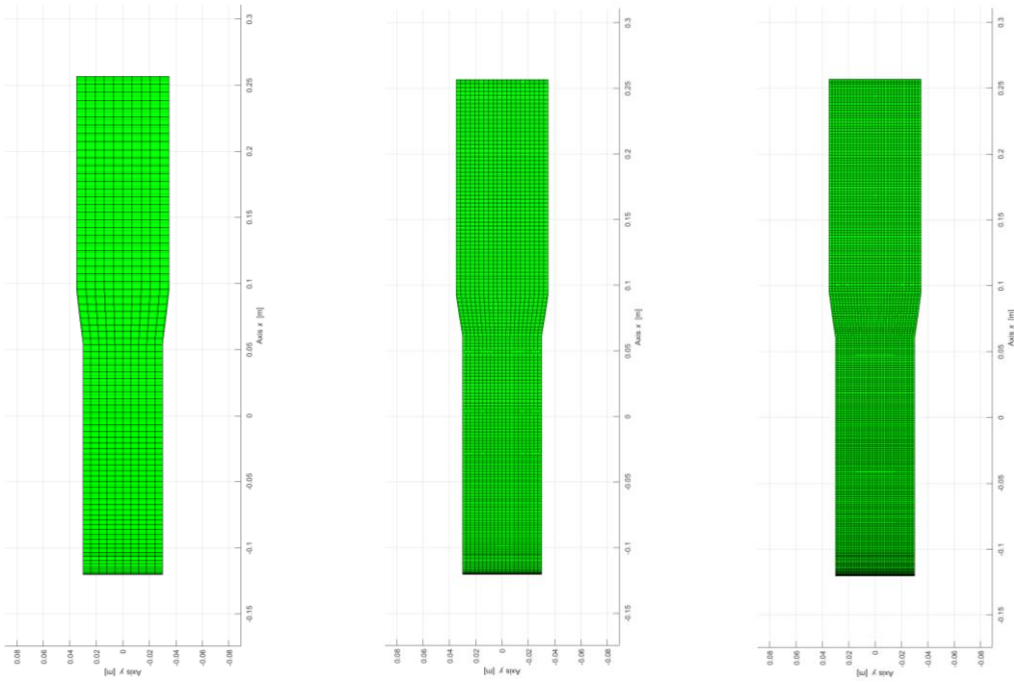


Figure 5.5.2.1.3 – Upper view of the 3D model discretized by hexa on Lupos 2023. From left to right: Model_1, Model_2 and Model_3.

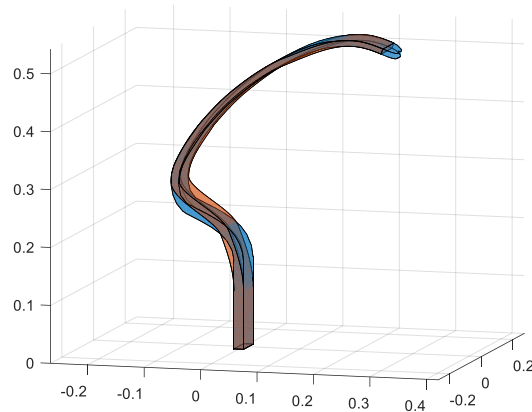


Figure 5.5.2.1.4 – Overlapping of the CAD model created on Solidworks 2015 and the model created on Lupos 2023 discretised with 3D hexa elements.

The same material properties considered in the shell discretization are applied, see Table 5.5.1.2. The boundary conditions applied to the three models are the same. The displacement along X is constrained for all the nodes on the upper and lower surface in the region where the aluminium plates were placed in the experimental test to fix the prosthetic. Then, the Z displacement was also fixed for the nodes at the middle height of the region constrained along X and the Y displacement was constrained for the nodes of the constrained region at the middle of the width. For a better understanding, a schematic drawing of the boundary conditions applied is shown in Figure 5.5.2.1.5, the darker area is the one constrained along X, the violet line represents the nodes fixed also along Z and the red one the nodes constrained also along Y.

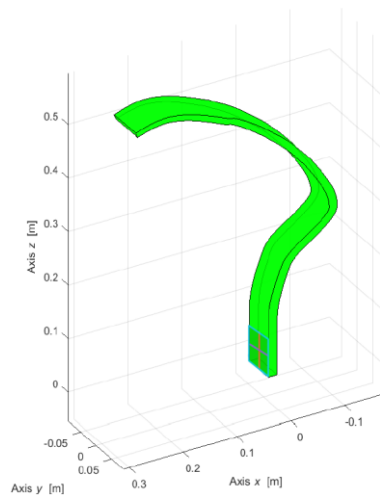


Figure 5.5.2.1.5 – Schematic representation of the constraints for the hexa simulations of Model_1, Model_2 and Model_3. The darker area is the one constrained along X, the violet line represents the nodes fixed also along Z and the red one the nodes constrained also along Y

The models are defined on Lupos and then converted in the .bdf files in order to perform the simulations on MSC Nastran 2017.

An H-convergence analysis is performed considering the first two natural frequencies, as displayed in Figure 5.5.2.1.6. A comparison of the first four natural frequencies among the three discretisations is also reported in Table 5.5.2.1.2. In the last column of the table, the variance in between the results

obtained is computed, according to eq $e = \frac{f_{\max,i} - f_{\min,i}}{f_{\max,i}}$ (5.5.1.1.1). Unexpectedly, in the first

mode, there is a slight increase of the natural frequency of Model_3 with respect the other two. Indeed, when the number of elements describing the component is lower, the model results should be stiffer. In any case, the variation is really small, less than 0.5%, meaning that the stability in the results is already achieved for all the three models. The fact that Model_3 results stiffer can be due to the highest number of nodes constrained.

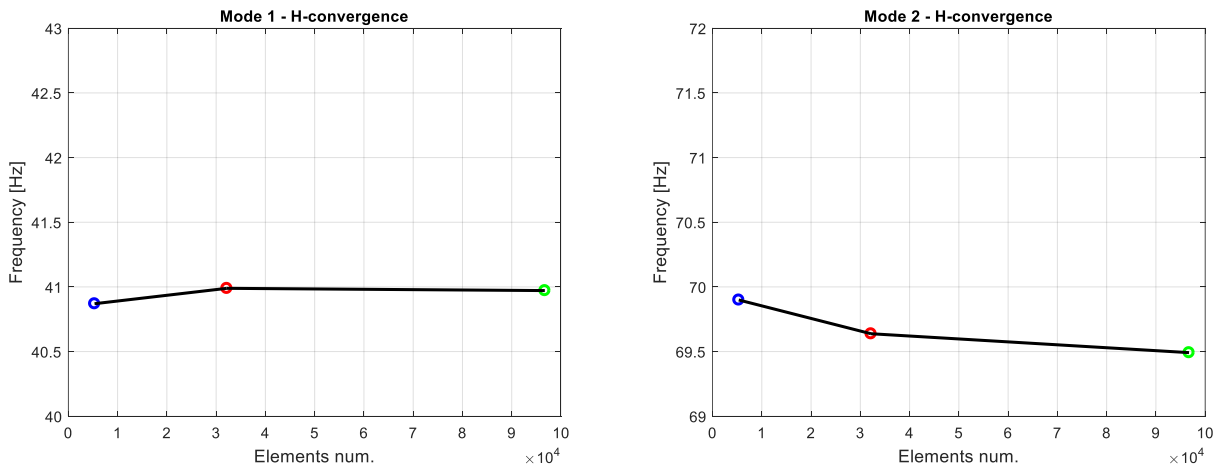


Figure 5.5.2.1.6 – H-convergence results of the prosthetic models described by sh4 elements with the same thickness. First (left) and second (right) modes.

Table 5.5.2.1.2 – Natural frequency results of the three discretisations: Model_1, Model_2 and Model_3.

Natural frequency	Model_1	Model_2	Model_3	e
f_1 [Hz]	40.87	40.99	40.97	0.2%
f_2 [Hz]	69.90	69.64	69.49	0.6%
f_3 [Hz]	113.65	114.23	114.25	0.5%
f_4 [Hz]	273.44	276.09	275.89	1.0%

Of course, since just the number of elements change, and already the roughest one well describes the components, the mode shapes obtained in the three cases are the same. They are displayed in Figure 5.5.2.1.7. The mode shapes are displayed from HyperView since Lupos has difficulties in plotting them given the high number of dofs.

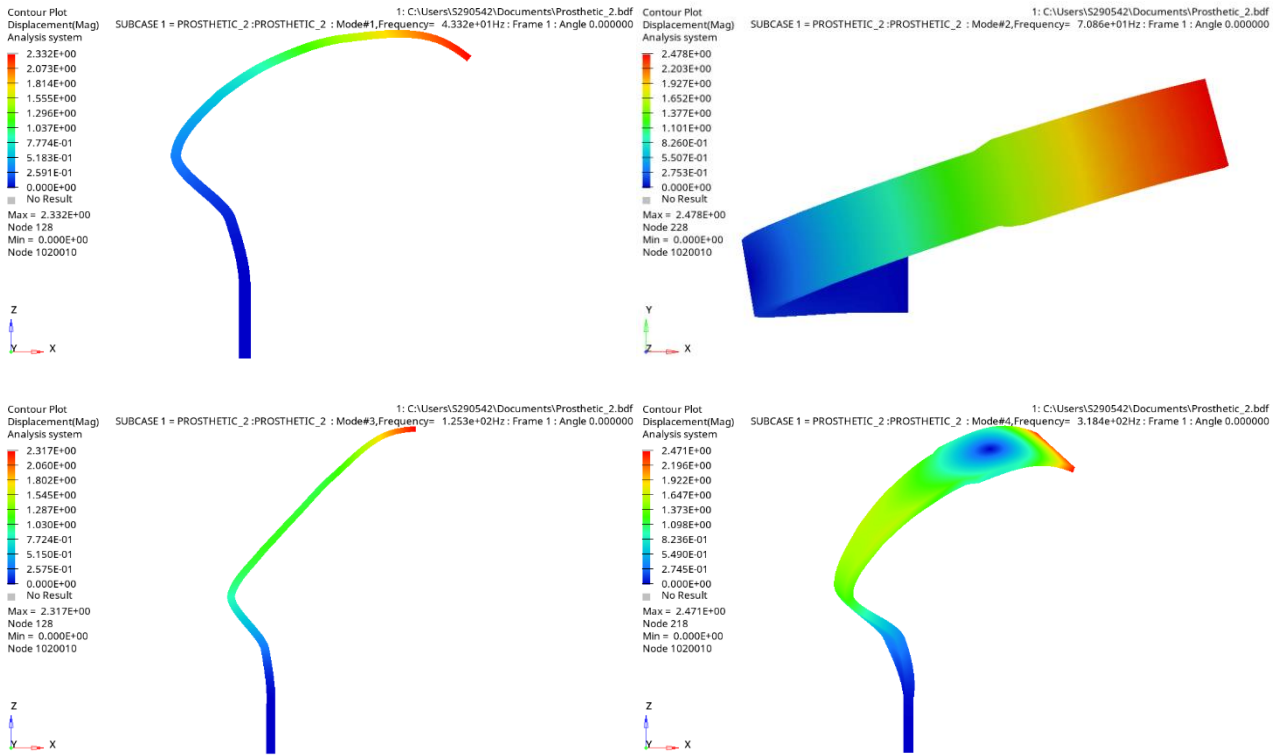


Figure 5.5.2.1.7 – Fist four mode shapes obtained from the hexa discretization of the prosthetic; Hyperview display.

For completeness, in Table 5.5.2.1.3, the first 6 natural frequencies and mode shapes of Model_2 are compared to the EMA results. Even thus there is still a really high discrepancy between the natural frequencies, as verified also in the shell model (Paragraph 5.5.1.2), all the modes correspond to the ones coming out from the experimental test (while in the shell analysis there was a switch between 4th and 5th modes).

Table 5.5.2.1.3 – EMA-FEA comparison. Hexa Model_2, isotropic material.

Mode	FEA		EMA	
	Nat freq. [Hz]	Mode shape	Nat. freq. [Hz]	Mode shape
1	40.99	1 st bending XZ	35.95	1 st bending XZ
2	69.64	1 st bending XY	36.58	1 st bending XY
3	114.23	2 nd bending XZ	87.89	2 nd bending XZ
4	276.09	Torsional RZ	143.80	Torsional RZ
5	362.04	3 rd bending XZ	173.60	3 rd bending XZ
6	609.90	Torsional RZ	197.00	Torsional RZ

The FEA and EMA mode shapes are also compared through the computation of the MAC matrix, displayed in Figure 5.5.2.1.8. As visible from the plot, there is not a good match between the FEA and EMA mode shapes. In any case, as mentioned before, there is an improvement with respect the shell discretization in which the 4th and 5th modes are switched with respect the experimental results.

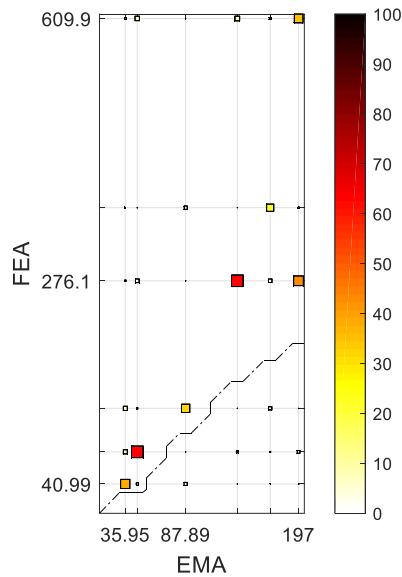


Figure 5.5.2.1.8 – MAC between the EMA and FEA results. Hexa model, Model_2, isotropic material. The dashed line is the iso-frequency curve.

5.5.2.2 Analysis on the constraints definition

Model_2 is considered to perform a study of sensitivity in the change of the boundary conditions definition. The model is described by 32160 hexagonal elements, as already pointed out in Table 5.5.2.1.1.

Three different boundary conditions are considered:

1. all the nodes on the surfaces where the aluminium plates were placed during the experimental test are constrained in all the directions;
2. the displacement along X is constrained for all the surface nodes in the region where the aluminium plates were placed in the experimental test; the Z displacement is also fixed for the nodes at the middle height of the region constrained along X and the Y displacement is constrained for the nodes of the constrained region at the middle of the width, see Figure 5.5.2.1.5;
3. the same boundary conditions of the second case are adopted, but the constrained area has no more the dimensions of the aluminium plates but its height is reduced of 1/3, thus, from 64 mm to 42 mm.

The results of the first four natural frequencies are compared in Table 5.5.2.2.1. As predictable, the frequencies decrease from the first to the last case since the boundary condition become less strict and the degrees of freedom increase. The difference in the results is low in between the case 1 and 2, while is more remarkable in the last case.

Table 5.5.2.2.1 – Natural frequency results of the three boundary conditions cases.

Natural frequency	Case 1	Case 2	Case 3	E
f_1 [Hz]	41.47	40.99	40.05	3.5%
f_2 [Hz]	70.35	69.64	69.26	1.6%
f_3 [Hz]	116.24	114.23	110.51	4.9%
f_4 [Hz]	290.87	276.09	263.92	9.3%

The second case seems to better represent the experimental test conditions, since the prosthetic was fixed along X to the table, although, the latter case could represent better the test since the constraint applied is not ideal and a degree of compliance was registered during the test.

5.5.2.3 Isotropic material tuning

After an H-convergence analysis and a study on the boundary conditions, the material properties are further analysed.

As first attempt, an isotropic material is considered. The aim is to understand if, considering an elastic isotropic behaviour of the component, it is possible to obtain, as resulted experimentally, the first two natural frequencies really close between each other.

The constitutive equation of the isotropic materials is the following:

$$\begin{Bmatrix} \varepsilon_1 \\ \varepsilon_2 \\ \varepsilon_3 \\ \gamma_{23} \\ \gamma_{31} \\ \gamma_{12} \end{Bmatrix} = \begin{bmatrix} \frac{1}{E} & -\frac{\nu}{E} & -\frac{\nu}{E} & 0 & 0 & 0 \\ -\frac{\nu}{E} & \frac{1}{E} & -\frac{\nu}{E} & 0 & 0 & 0 \\ -\frac{\nu}{E} & -\frac{\nu}{E} & \frac{1}{E} & 0 & 0 & 0 \\ 0 & 0 & 0 & \frac{2 \cdot (1+\nu)}{E} & 0 & 0 \\ 0 & 0 & 0 & 0 & \frac{2 \cdot (1+\nu)}{E} & 0 \\ 0 & 0 & 0 & 0 & 0 & \frac{2 \cdot (1+\nu)}{E} \end{bmatrix} \cdot \begin{Bmatrix} \sigma_1 \\ \sigma_2 \\ \sigma_3 \\ \tau_{23} \\ \tau_{31} \\ \tau_{12} \end{Bmatrix} \quad (5.5.2.3.1)$$

where E is the Young modulus, ν is the Poisson ratio and $G = \frac{E}{2 \cdot (1+\nu)}$ is the shear modulus. All

this constants are equal along all the directions.

The relation between stress and strains is equivalent to consider the relation between natural frequencies and mode shapes. Thus also these last depend on the Young modulus, the Poisson ratio and the shear modulus. In particular, for isotropic materials, according to eq

$$\begin{Bmatrix} \varepsilon_1 \\ \varepsilon_2 \\ \varepsilon_3 \\ \gamma_{23} \\ \gamma_{31} \\ \gamma_{12} \end{Bmatrix} = \begin{bmatrix} \frac{1}{E} & -\frac{\nu}{E} & -\frac{\nu}{E} & 0 & 0 & 0 \\ -\frac{\nu}{E} & \frac{1}{E} & -\frac{\nu}{E} & 0 & 0 & 0 \\ -\frac{\nu}{E} & -\frac{\nu}{E} & \frac{1}{E} & 0 & 0 & 0 \\ 0 & 0 & 0 & \frac{2 \cdot (1+\nu)}{E} & 0 & 0 \\ 0 & 0 & 0 & 0 & \frac{2 \cdot (1+\nu)}{E} & 0 \\ 0 & 0 & 0 & 0 & 0 & \frac{2 \cdot (1+\nu)}{E} \end{bmatrix} \cdot \begin{Bmatrix} \sigma_1 \\ \sigma_2 \\ \sigma_3 \\ \tau_{23} \\ \tau_{31} \\ \tau_{12} \end{Bmatrix} \quad (5.5.2.3.1), \quad \text{the two}$$

independent variables are the Young modulus and the Poisson ratio. The natural frequencies depend also on the density of the material, but in this case, the mass and the volume are known, hence ρ is a fixed value.

According to eq

$$\begin{Bmatrix} \varepsilon_1 \\ \varepsilon_2 \\ \varepsilon_3 \\ \gamma_{23} \\ \gamma_{31} \\ \gamma_{12} \end{Bmatrix} = \begin{bmatrix} \frac{1}{E} & -\frac{\nu}{E} & -\frac{\nu}{E} & 0 & 0 & 0 \\ -\frac{\nu}{E} & \frac{1}{E} & -\frac{\nu}{E} & 0 & 0 & 0 \\ -\frac{\nu}{E} & -\frac{\nu}{E} & \frac{1}{E} & 0 & 0 & 0 \\ 0 & 0 & 0 & \frac{2 \cdot (1 + \nu)}{E} & 0 & 0 \\ 0 & 0 & 0 & 0 & \frac{2 \cdot (1 + \nu)}{E} & 0 \\ 0 & 0 & 0 & 0 & 0 & \frac{2 \cdot (1 + \nu)}{E} \end{bmatrix} \begin{Bmatrix} \sigma_1 \\ \sigma_2 \\ \sigma_3 \\ \tau_{23} \\ \tau_{31} \\ \tau_{12} \end{Bmatrix} \quad (5.5.2.3.1),$$

in the isotropic materials, the Young modulus affects the overall behaviour of the component. Thus, by varying it, all the natural frequencies increase or decrease. On the contrary, the Poisson ratio can affect the behaviour in a direction with respect to another direction. Indeed, the Poisson ratio itself

defines the strain along one direction with respect the orthogonal one, see eq $\nu_{ij} = \frac{\varepsilon_j}{\varepsilon_i}$ (5.5.2.3.2).

As consequence, this is the only parameter which could affect differently the eigenvalues.

$$\nu_{ij} = \frac{\varepsilon_j}{\varepsilon_i} \quad (5.5.2.3.2)$$

Therefore, a parametric analysis has been conducted on Lupos by varying just the Poisson ratio value. To be able to perform the analysis on Lupos, the number of elements is reduced with respect Model_2 considered in the previous paragraphs. To maintain a good discretization along the thickness, as in Model_2, 6 hexa elements are considered. On the contrary, along the width and the component shape (XZ plane), the half of the elements number has been selected. As an overall, the number of hexagonal elements of the new model are 7980.

In the LUPOS Control Pannell, the parametric analysis is specified and the Poisson ratio value is made varying in between 0.10 and 0.45 with a step of 0.05. Indeed, the limit values of ν for an isotropic material, according to its definition, are 0 and 0.5. In Table 5.5.2.3.1 and Figure 5.5.2.3.1, the variation of the first four natural frequencies with respect the Poisson ratio is reported. As mentioned before, the effect of changing ν is a different variation in the free response of the component in the two orthogonal planes. Indeed, while the first natural frequency, in which the bending in XZ plane is verified, increases by increasing the Poisson ratio, the second eigenfrequency, related to the flexural mode in the XY plane, decreases. Indeed, having $\nu = 0.45$, means that there is a closer response between transversal and longitudinal behaviours, thus the compliance of the material along the orthogonal direction is closer to the one along the principal one. Thus, by increasing ν , the modes which involve the bending in XZ plane become stiffer, the contrary for the modes on the XY plane. However, the biggest effect is registered for the torsional mode, the fourth one, there is a decrease of 11 Hz, which is remarkable with respect to the variation of the other natural frequencies. From the plot of Figure 5.5.2.3.1, no crossing between the modes are verified.

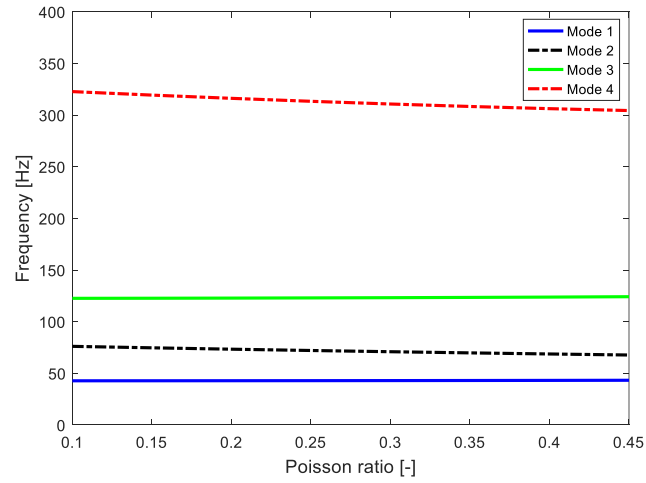


Figure 5.5.2.3.1 – Parametric analysis results, plot of the first four natural frequencies when the Poisson ratio varies between 0.1 and 0.45.

Table 5.5.2.3.1 – Natural frequencies results of the parametric analysis with Poisson ratio variation.

Natural frequencies	ν [-]							
	0.10	0.15	0.20	0.25	0.30	0.35	0.40	0.45
f_1 [Hz]	42.74	42.98	43.02	43.08	43.14	43.24	43.13	43.46
f_2 [Hz]	76.09	74.35	73.01	71.75	69.70	69.44	68.70	67.37
f_3 [Hz]	122.6	124.68	124.82	125.00	125.17	125.50	123.80	126.20
f_4 [Hz]	322.7	326.76	323.53	320.56	298.41	315.35	306.20	311.14

All things considered, the variation in the natural frequencies is not enough to obtain closer results to the experimental ones: the difference between the first two bending is still too high. Thus, it is decided to proceed with a finite element analysis which considers anisotropic properties.

Although, before proceeding with the definition of the orthotropic material, the isotropic properties are firstly tuned in such a way to properly match just the bending modes in the XZ plane and then for properly simulate the flexion in the XY plane and the torsion. In this case, the simulations are performed on MSC Nastran 2017, thus it is no more necessary to considered the reduced model (Model_4), the analyses are again carried out on Model_2.

The flexural modes on the XZ plane are well described for an isotropic material with the following properties:

Table 5.5.2.3.2 – Isotropic material properties, tuning for the bending modes in the XZ plane.

Parameter	Value
Density [kg/m^3]	1548.93
Young modulus [Pa]	$4.5 \cdot 10^{10}$
Poisson ratio [-]	0.15

The natural frequencies resulting are compared to the flexural EMA ones in the XZ plane:

Table 5.5.2.3.3 – FEA-EMA results comparison. Tuning of the isotropic material considering just the bending modes in the XZ plane.

Mode	FEA freq. [Hz]	EMA freq. [Hz]
1	33.64	35.95
2	59.29	-
3	93.75	87.89
4	231.49	-
5	297.26	173.60
6	519.70	-

Regarding the flexural modes on the XY plane and the torsional ones, the isotropic material properties selected are the following:

Table 5.5.2.3.4 – Isotropic material properties, tuning for the bending modes in the XY plane and for the torsional ones.

Parameter	Value
Density [kg/m ³]	1548.93
Young modulus [Pa]	1.8·10 ¹⁰
Poisson ratio [-]	0.25

The natural frequencies resulting are compared to the flexural in the XY plane and torsional EMA ones:

Table 5.5.2.3.5 – FEA-EMA results comparison. Tuning of the isotropic material considering just the bending modes in the XY plane and the torsional ones.

Mode	FEA freq. [Hz]	EMA freq. [Hz]
1	21.31	-
2	36.86	36.58
3	59.38	-
4	145.02	143.80
5	188.23	-
6	322.95	197.00

Notice the big difference in the elastic modulus selected in the two tunings performed, this remarks the impossibility of describing the dynamic behaviour detected experimentally with an isotropic material.

5.5.2.4 Characterization of the carbon fiber composite as an anisotropic material

The carbon fiber composites are materials particularly known for their high strength-to-weight ratio. For this reason they are mainly used in the aeronautical and race fields, where lightweight properties are really important. The composite materials are heterogeneous, they are the result of the mixture between two or more physically and chemically different constituents. Usually the two components are a material with really high strength, in this case the carbon fibers, and a resin which binds together the reinforcement and provides more ductility to the material. The carbon fibers are one of the most costly constituents, they are chosen when high strength and high elastic modulus are required. Usually, composite materials are produced in layers with a thickness of 0.1-1 mm. Hence, the components are made up of a layer stacking sequence, which create the so called laminate. The laminar composition of the blade prosthetic is clearly visible on the lateral surface, as shown in Figure 5.5.2.4.1.

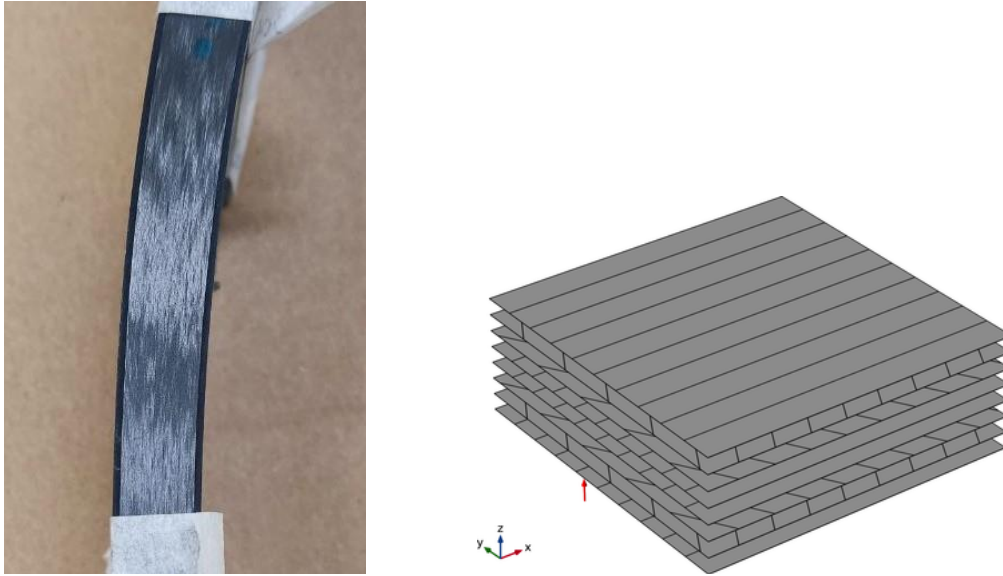


Figure 5.5.2.4.1 – Zoom-in of the lateral side of the Cheetah Xcel Össur. The material composition in laminae, as schematically represented on the right image, is clearly visible on the photo on the left.

The mechanical properties of the composites are really difficult to be predicted due to their anisotropy and not homogeneous characteristics. Furthermore, usually they are subjected to residual thermal stresses and they are sensitive to moisture. To be discretized, composites materials have to be analysed from different scales of measurement. The micromechanics describes the interactions between the different constituents of the material. Indeed, the characteristics of the composite depend on the properties and on the relative quantity of two constituents: the Young moduli, the transversal modulus and the Poisson ratio are calculated according to the rule of mixture:

$$E_L = E_f V_f + E_m V_m \quad (5.5.2.4.1)$$

$$\frac{1}{E_T} = \frac{V_f}{E_f} + \frac{V_m}{E_m} \quad (5.5.2.4.2)$$

$$\frac{1}{G_{LT}} = \frac{V_f}{G_f} + \frac{V_m}{G_m} \quad (5.5.2.4.3)$$

$$\nu_{TL} = E_f \nu_f + E_m \nu_m \quad (5.5.2.4.4)$$

where E_L and E_T correspond to longitudinal and transverse moduli of the composite lamina, G_{LT} and ν_{TL} correspond to in-plane shear modulus and Poisson's ratio, respectively. Suffix f corresponds to fiber property and m corresponds to matrix property. In the above equations, V is the volume fraction.

Then, in the macromechanics, the properties evaluated previously are averaged and the material is considered homogeneous. At this level, the entire lamina is considered. Further, the Classical Laminate Theory allows to predict the properties of a laminate, composed by a stacking sequence of laminae. Finally, the analysis can be performed at the component level to understand its overall behaviour. In this work, just this last step is carried out. Indeed, no information about the material are available from the producers. It is just known that the fibers composing the model are carbon fibers. Nor the resin material, nor the volume fraction of the constituents, nor the stacking sequence, neither the manufacturing processes are disclosed information.

It is assumed that the prosthetic is composed by woven layers. This because on the surface of the bade prosthetic it is visible the bidirectional disposition of the fibers, Figure 5.5.2.4.2 and also because the experimental result of having the bendings in two different planes almost at the same frequency can be due to the fabric disposition of the carbon fibres. Furthermore, the most common resin used for the blade prosthetics are epoxy and vynilester. In this case epoxy matrix is considered.



Figure 5.5.2.4.2 – Cheetah Xcel Össur material, photo of the frontal view.

Since the strength of the fibers is verified just along the length, their orientation and length affect the behaviour of the composite material. Indeed, short fiber composites are usually anisotropic, while the long fibers can be defined orthotropic since three plane of symmetry can be identified.

The orthotropic materials behave as follows:

$$\begin{Bmatrix} \varepsilon_1 \\ \varepsilon_2 \\ \varepsilon_3 \\ \gamma_{23} \\ \gamma_{31} \\ \gamma_{12} \end{Bmatrix} = \begin{bmatrix} \frac{1}{E_1} & -\frac{\nu_{21}}{E_2} & -\frac{\nu_{31}}{E_3} & 0 & 0 & 0 \\ -\frac{\nu_{12}}{E_1} & \frac{1}{E_2} & -\frac{\nu_{32}}{E_3} & 0 & 0 & 0 \\ -\frac{\nu_{13}}{E_1} & -\frac{\nu_{23}}{E_2} & \frac{1}{E_3} & 0 & 0 & 0 \\ 0 & 0 & 0 & \frac{1}{G_{23}} & 0 & 0 \\ 0 & 0 & 0 & 0 & \frac{1}{G_{13}} & 0 \\ 0 & 0 & 0 & 0 & 0 & \frac{1}{G_{12}} \end{bmatrix} \cdot \begin{Bmatrix} \sigma_1 \\ \sigma_2 \\ \sigma_3 \\ \tau_{23} \\ \tau_{31} \\ \tau_{12} \end{Bmatrix} \quad (5.5.2.4.5)$$

where E_1 , E_2 and E_3 are respectively the longitudinal and transversal, in direction 2 and 3, Young moduli; ν_{21} and ν_{12} are the in-plane Poisson ratios; ν_{31} , ν_{13} , ν_{32} and ν_{23} are the out-of-plane Poisson ratios; G_{12} is the in-plane shear modulus; G_{23} and G_{13} are the out-of-plane shear moduli.

The columns of the equation, represent the axes orthogonal to the stress while the rows represent the directions along which the stress is applied.

In order to respect symmetry in the matrix it is necessary that:

$$\frac{\nu_{12}}{E_1} = \frac{\nu_{21}}{E_2} \quad (5.5.2.4.6)$$

$$\frac{\nu_{13}}{E_1} = \frac{\nu_{31}}{E_3} \quad (5.5.2.4.7)$$

$$\frac{\nu_{23}}{E_2} = \frac{\nu_{32}}{E_3} \quad (5.5.2.4.8)$$

To evaluate the existing conditions of Poisson ratios [25] it is necessary that:

$$|\nu_{12}| < \left(\frac{E_2}{E_1} \right)^{1/2} \quad (5.5.2.4.9)$$

$$|\nu_{21}| < \left(\frac{E_2}{E_1} \right)^{1/2} \quad (5.5.2.4.10)$$

$$|\nu_{23}| < \left(\frac{E_2}{E_3} \right)^{1/2} \quad (5.5.2.4.11)$$

$$|\nu_{32}| < \left(\frac{E_3}{E_2} \right)^{1/2} \quad (5.5.2.4.12)$$

$$|\nu_{13}| < \left(\frac{E_3}{E_1} \right)^{1/2} \quad (5.5.2.4.13)$$

$$|\nu_{31}| < \left(\frac{E_1}{E_3} \right)^{1/2} \quad (5.5.2.4.14)$$

As stated in the constitutive equation of the orthotropic material

$$(eq. \left. \begin{matrix} \varepsilon_1 \\ \varepsilon_2 \\ \varepsilon_3 \\ \gamma_{23} \\ \gamma_{31} \\ \gamma_{12} \end{matrix} \right\} = \begin{bmatrix} \frac{1}{E_1} & -\frac{\nu_{21}}{E_2} & -\frac{\nu_{31}}{E_3} & 0 & 0 & 0 \\ -\frac{\nu_{12}}{E_1} & \frac{1}{E_2} & -\frac{\nu_{32}}{E_3} & 0 & 0 & 0 \\ -\frac{\nu_{13}}{E_1} & -\frac{\nu_{23}}{E_2} & \frac{1}{E_3} & 0 & 0 & 0 \\ 0 & 0 & 0 & \frac{1}{G_{23}} & 0 & 0 \\ 0 & 0 & 0 & 0 & \frac{1}{G_{13}} & 0 \\ 0 & 0 & 0 & 0 & 0 & \frac{1}{G_{12}} \end{bmatrix} \cdot \left. \begin{matrix} \sigma_1 \\ \sigma_2 \\ \sigma_3 \\ \tau_{23} \\ \tau_{31} \\ \tau_{12} \end{matrix} \right\} \quad (5.5.2.4.5)), \text{ when they are excited}$$

along the axis of symmetry they behave as isotropic materials: at a shear stress corresponds a shear

strain and at a normal stress corresponds a normal strain; while if they are excited along other directions, they behave as anisotropic material: coupling between normal and shear strains occurs.

As mentioned before, there are many factors which affect the mechanical properties of the composite materials, for instance the production in the autoclave produces a material with a lower amount of resin with respect to the hand lay-up. In any case, for both the manufacturing processes the actual relative amount of filler is unknown and also the amount of impurities, such as voids, is not known. For this reason each composite component produced should be tested in order to know its mechanical properties, as also suggested from the study of Duleba et al. [26]. In this work, indeed, the FE analysis and the tensile test results on a carbon-epoxy composite are compared; the strength values difference is considerable.

The in-plane mechanical properties of carbon-epoxy laminates are taken directly from the producers indications. The company RS, provides the mechanical properties of the carbon-epoxy fabric laminae they manufacture [27], such values are reported in Table 5.5.2.4.1.

Table 5.5.2.4.1 – Properties of the fabric carbon-epoxy composite.

Property	Value
Longitudinal Young modulus E_1 [GPa]	70
Transversal Young modulus E_2 [GPa]	70
Shear modulus G_{12} [GPa]	5
Poisson ratio ν_{12} [-]	0.1

Notice that the characteristics are indicated along the principal axis of the material, thus along the fibres direction. Since, as first attempt, fabrics rotated of $\pm 45^\circ$ with respect the elements local system will be considered, the rotation will be applied to obtain the mechanical values along the elements local system, according to eq. $[\bar{Q}] = [T]^{-1}[Q][R][T][R]^{-1}$ (5.5.2.4.15).

$$[\bar{Q}] = [T]^{-1}[Q][R][T][R]^{-1} \quad (5.5.2.4.15)$$

where:

- $[\bar{Q}]$ is the rotated 2D compliance matrix;
- $[T]$ is the rotation matrix:

$$[T] = \begin{bmatrix} \cos^2(\theta) & \sin^2(\theta) & 2\sin(\theta)\cos(\theta) \\ \sin^2(\theta) & \cos^2(\theta) & -2\sin(\theta)\cos(\theta) \\ -\sin(\theta)\cos(\theta) & \sin(\theta)\cos(\theta) & \cos^2(\theta) - \sin^2(\theta) \end{bmatrix} \quad (5.5.2.4.16)$$

- $[Q]$ is the 2D compliance matrix, which is, for orthotropic materials:

$$[Q] = \begin{bmatrix} \frac{1}{E_1} & -\frac{\nu_{21}}{E_2} & 0 \\ -\frac{\nu_{12}}{E_1} & \frac{1}{E_2} & 0 \\ 0 & 0 & \frac{1}{G_{12}} \end{bmatrix} \quad (5.5.2.4.17)$$

- $[R]$ is the diagonal matrix which takes into account in the rotation, the torsional strain and stress is the half of its actual value:

$$[R] = \begin{bmatrix} 1 & 0 & 0 \\ 1 & 1 & 0 \\ 0 & 0 & 2 \end{bmatrix} \quad (5.5.2.4.18)$$

By solving eq. $[\bar{Q}] = [T]^{-1}[Q][R][T][R]^{-1}$ (5.5.2.4.15), the resulting explicit formulae are the ones

$$\text{reported in eq. } E_x = \frac{1}{\frac{1}{E_1} \cos^4(\theta) + \frac{1}{E_2} \sin^4(\theta) + \left(-\frac{2\nu_{12}}{E_1} + \frac{1}{G_{12}}\right) \sin^2(\theta) \cos^2(\theta)} \quad (5.5.2.4.19)$$

$$\nu_{xy} = E_x \left(\frac{\nu_{12}}{E_1} (\sin^4(\theta) + \cos^4(\theta)) - \left(\frac{2}{E_1} + \frac{2}{E_2} - \frac{1}{G_{12}} \right) \sin^2(\theta) \cos^2(\theta) \right) \quad (5.5.2.4.22), \quad \text{where}$$

direction 1 and 2 are the longitudinal and transversal ones of the material, while x and y belong to the reference system of the element; θ is the rotation angle between the material and the element reference system, in this case it is 45° (see Figure 5.5.2.4.3).

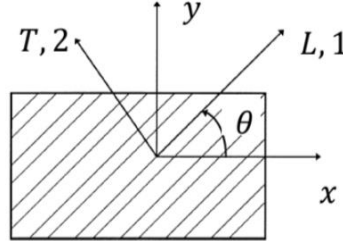


Figure 5.5.2.4.3 – Representation of the in-plane material and element reference systems.

$$E_x = \frac{1}{\frac{1}{E_1} \cos^4(\theta) + \frac{1}{E_2} \sin^4(\theta) + \left(-\frac{2\nu_{12}}{E_1} + \frac{1}{G_{12}} \right) \sin^2(\theta) \cos^2(\theta)} \quad (5.5.2.4.19)$$

$$E_y = \frac{1}{\frac{1}{E_1} \sin^4(\theta) + \frac{1}{E_2} \cos^4(\theta) + \left(-\frac{2\nu_{12}}{E_1} + \frac{1}{G_{12}} \right) \sin^2(\theta) \cos^2(\theta)} \quad (5.5.2.4.20)$$

$$G_{xy} = \frac{1}{2 \left(\frac{2}{E_1} + \frac{2}{E_2} + \frac{4\nu_{12}}{E_1} - \frac{1}{G_{12}} \right) \sin^2(\theta) \cos^2(\theta) + \frac{1}{G_{12}} (\sin^4(\theta) + \cos^4(\theta))} \quad (5.5.2.4.21)$$

$$\nu_{xy} = E_x \left(\frac{\nu_{12}}{E_1} (\sin^4(\theta) + \cos^4(\theta)) - \left(\frac{2}{E_1} + \frac{2}{E_2} - \frac{1}{G_{12}} \right) \sin^2(\theta) \cos^2(\theta) \right) \quad (5.5.2.4.22)$$

The values computed using the formulas of eq ($[\bar{Q}] = [T]^{-1}[Q][R][T][R]^{-1}$) (5.5.2.4.15) -

$$[R] = \begin{bmatrix} 1 & 0 & 0 \\ 1 & 1 & 0 \\ 0 & 0 & 2 \end{bmatrix} \quad (5.5.2.4.18), \text{ reported in Table 5.5.2.4.2, coincide with the ones declared from}$$

the Performance Composites Limited company, a liquidated corporation which has mainly produced carbon-epoxy composites. On their web site, indeed, also the properties of the fabrics with fibres disposition at $\pm 45^\circ$ are indicated, [28].

Table 5.5.2.4.2 – Properties of the fabric carbon-epoxy composite with fibers at $\pm 45^\circ$ (in the local element reference frame).

Property	Value
Longitudinal Young modulus E_x [GPa]	17
Transversal Young modulus E_y [GPa]	17
Shear modulus G_{xy} [GPa]	32

Poisson ratio ν_{xy} [-]	0.6
------------------------------	-----

Thus, such values are considered for the first FE simulation.

The laminae properties define just the in-plane characteristics, this because, given the really low thickness, a plane stress condition can be assumed.

Since the material is directly produced by defining the component shape, there are not accurate values which can be considered. For this reason, usually the components in composite materials are simulated through 2D shells, in this way the material variables along the thickness are not to be specified.

However, in this case a good discretization is reached through the use of 3D elements: the thickness is made varying along the prosthetic shape continuously without jumps, which is difficult to avoid through the use of 2D shells. Thus, the simulation will be conducted with the hexagonal 3D elements discretization. In this case it must be taken into account that, as stated in the work of Gojny et al. [28], the FE simulations with CQUAD elements on Nastran lead to stiffer results with respect to the ones which are obtained through the use of shell.

For the Young modulus along the thickness, as suggested in the composite modelling handbook for FEMAP on NX Nastran [30] and as also done in the work of Gojny et al. [28], the in-plane transverse value indicated in the unidirectional composite laminae is considered. Regarding the Poisson ratio and the shear modulus values, since the lamina is considered bidirectional:

$$\nu_{13} = \nu_{23} \quad (5.5.2.4.23)$$

$$G_{13} = G_{23} \quad (5.5.2.4.24)$$

The values considered are the ones pointed out in the work of Guseinov et al. [31]. Here a new experimental approach is conducted in order to reliably evaluate the interlaminar shear properties of laminates. The material considered in this work has the same in-plane values reported in Table 5.5.2.4.1 are considered. Thus the interlaminar properties used are:

Table 5.5.2.4.3 – Interlaminar and through thickness properties of laminates composed by fabric carbon-epoxy composite.

Property	Value
Through thickness Young modulus E_3 [GPa]	10
Interlaminar shear modulus $G_{13} = G_{23}$ [GPa]	3.4
Through thickness Poisson ratio $\nu_{13} = \nu_{23}$ [-]	0.5

The analysis on the 3D hexagonal elements is then carried out. Model_2, which was described previously and which represents the best compromise between the a good discretization and a not excessive number of elements, is considered. The constraints assigned are the slider along X for all the nodes which were in the region in contact with the aluminium plates during the experimental test, and two lines of nodes constrained one along Y and the other one along Z (see Paragraph 5.5.2.2).

The simulation is performed on Nastran 2017 to be able to define an orthotropic material. For linear structural analyses, MAT9 allows to define anisotropic material properties to axisymmetric 3D solid elements. The bulk entry of MAT9 are used to define the anisotropic material behaviour according to the following constitutive relation:

$$\begin{Bmatrix} \sigma_x \\ \sigma_y \\ \sigma_z \\ \tau_{xy} \\ \tau_{yz} \\ \tau_{zx} \end{Bmatrix} = \begin{bmatrix} C_{11} & C_{12} & C_{13} & C_{14} & C_{15} & C_{16} \\ & C_{22} & C_{23} & C_{24} & C_{25} & C_{26} \\ & & C_{33} & C_{34} & C_{35} & C_{36} \\ & & & C_{44} & C_{45} & C_{46} \\ & & & & C_{55} & C_{56} \\ & & & & & C_{66} \end{bmatrix} \cdot \begin{Bmatrix} \varepsilon_x \\ \varepsilon_y \\ \varepsilon_z \\ \gamma_{xy} \\ \gamma_{yz} \\ \gamma_{zx} \end{Bmatrix} - (T - T_{ref}) \cdot \begin{Bmatrix} A_1 \\ A_2 \\ A_3 \\ A_4 \\ A_5 \\ A_6 \end{Bmatrix} \quad (5.5.2.4.25)$$

where C_{ij} are the elements of the 6×6 symmetric material property matrix in the material coordinate system, A_{ij} are the coefficients of thermal expansion and $(T - T_{ref})$ is the temperature difference used to calculate thermal strain.

In this case, there is no need of considering the effect of the temperature, thus A_{ij} and T_{ref} values are not specified.

As first attempt, the compliance matrix has been calculated by inverting the compliance matrix of the constitutive equation of orthotropic materials

$$(eq. \begin{Bmatrix} \varepsilon_1 \\ \varepsilon_2 \\ \varepsilon_3 \\ \gamma_{23} \\ \gamma_{31} \\ \gamma_{12} \end{Bmatrix} = \begin{bmatrix} \frac{1}{E_1} & -\frac{\nu_{21}}{E_2} & -\frac{\nu_{31}}{E_3} & 0 & 0 & 0 \\ -\frac{\nu_{12}}{E_1} & \frac{1}{E_2} & -\frac{\nu_{32}}{E_3} & 0 & 0 & 0 \\ -\frac{\nu_{13}}{E_1} & -\frac{\nu_{23}}{E_2} & \frac{1}{E_3} & 0 & 0 & 0 \\ 0 & 0 & 0 & \frac{1}{G_{23}} & 0 & 0 \\ 0 & 0 & 0 & 0 & \frac{1}{G_{13}} & 0 \\ 0 & 0 & 0 & 0 & 0 & \frac{1}{G_{12}} \end{bmatrix} \cdot \begin{Bmatrix} \sigma_1 \\ \sigma_2 \\ \sigma_3 \\ \tau_{23} \\ \tau_{31} \\ \tau_{12} \end{Bmatrix} \quad (5.5.2.4.5)), \quad \text{considering the$$

material values pointed out previously, in Table 5.5.2.4.2 and Table 5.5.2.4.3.

The natural frequencies and mode shapes resulting are listed in Table 5.5.2.4.4 and displayed in Figure 5.5.2.4.4.

Table 5.5.2.4.4 – Natural frequencies and mode shapes resulting from the first simulation with orthotropic material discretization. Simulation performed on MSC Nastran 2017.

Mode	Freq. [Hz]	Description
1	20.35	1 st bending XZ
2	26.72	1 st bending XY
3	59.65	2 nd bending XZ
4	115.84	Torsional RZ
5	217.18	3 rd bending XZ
6	233.82	Torsional RZ
7	435.38	4 th bending XZ
8	543.05	Bending XZ
9	649.70	Torsional RZ

10	888.66	5 th bending XZ
----	--------	----------------------------

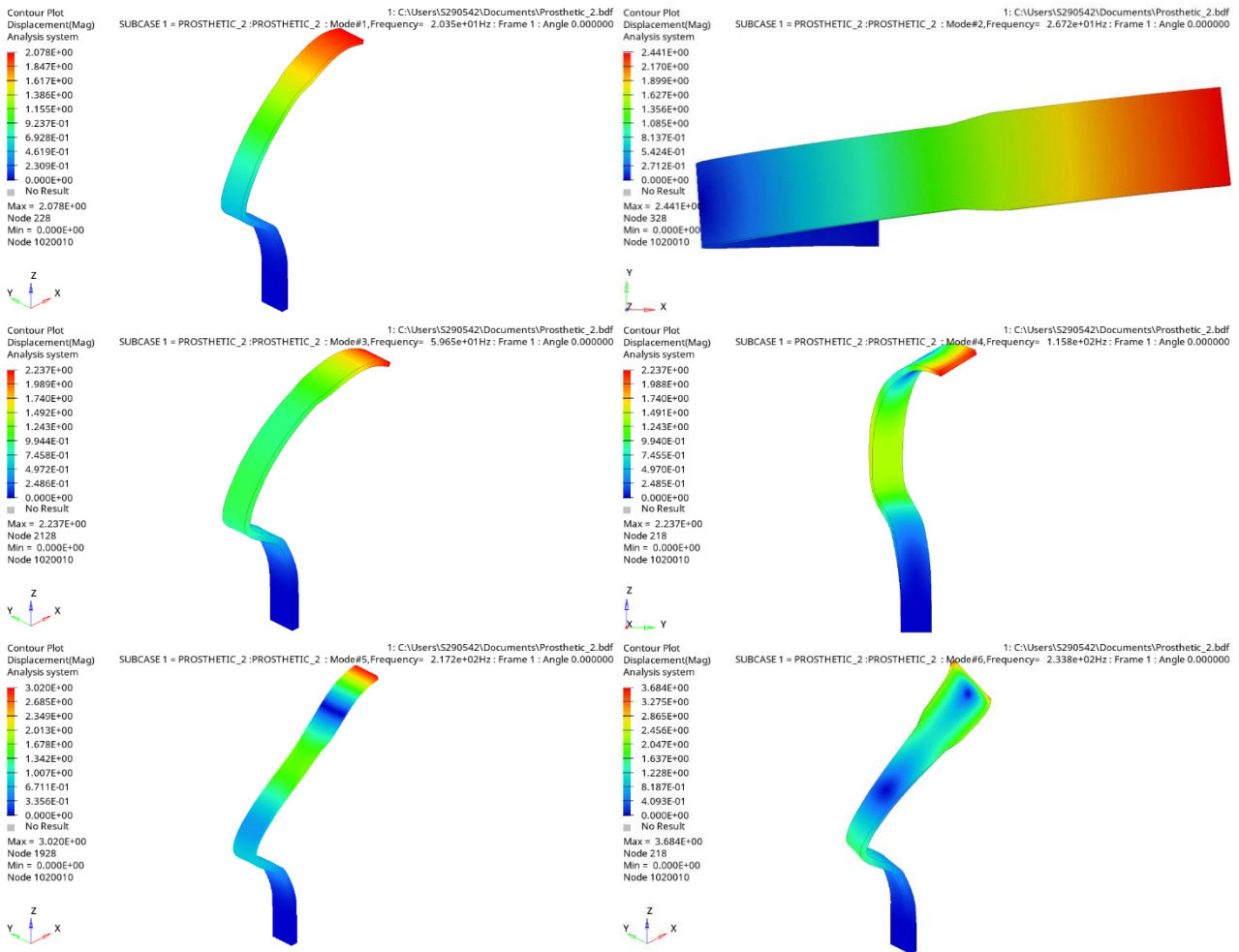


Figure 5.5.2.4.4 – Prosthetic first 6 mode shapes, orthotropic material, first attempt. Simulations on Nastran 2017.

The first natural frequencies result to be lower than the ones obtained experimentally, while the last ones are higher. On the other hand, the mode shapes correspond exactly to the experimental ones. Since just the first six mode shapes are experimentally individuated, the tuning of the material properties will be performed just focusing on these modes.

The first six modes results are reported again in comparison to the EMA ones:

Table 5.5.2.4.5 – Comparison between the FEA and the EMA natural frequencies, first trial.

Mode	FEA freq. [Hz]	EMA freq. [Hz]	Description
1	20.35	35.95	1 st bending XZ
2	26.72	36.58	1 st bending XY
3	59.65	87.89	2 nd bending XZ
4	115.84	143.80	Torsional RZ
5	217.18	173.60	3 rd bending XZ
6	233.82	197.00	Torsional RZ

The fact of having the first FEA natural frequency really low with respect the EMA one, is a result of having an elastic modulus along the thickness lower than the actual one. Thus, a tuning on E_3 is performed, focusing just on the first two natural frequencies values. While increasing E_3 , also the in-plane elastic moduli are increased since, for composite materials, the rigidity is mainly exploited along the fibres, thus on the lamina plane. By increasing just the three Young moduli, there is a switch between the first and second mode shapes. Indeed, if just the Young modulus along Z direction is increased, and not also the shear moduli, the bending in the XZ plane will occur after the bending in the XY plane. Thus also the out-of-plane shear moduli are increased. Hence, the following new values are considered:

Table 5.5.2.4.6 – New material properties considered. FEA analysis with orthotropic material.

Property	Value
In-plane Young moduli $E_1 = E_2$ [GPa]	37
Through thickness Young modulus E_3 [GPa]	36
Interlaminar shear modulus $G_{13} = G_{23}$ [GPa]	5

The following results are obtained:

Table 5.5.2.4.7 – Comparison between the FEA and the EMA natural frequencies, second trial.

Mode	FEA freq. [Hz]	EMA freq. [Hz]
1	33.94	35.95
2	34.03	36.58
3	95.37	87.89
4	162.92	143.80
5	298.35	173.60
6	309.91	197.00

By increasing the elastic moduli, all the natural frequencies are higher. Thus, the fourth, fifth and sixth ones result to be too high with respect the EMA results. Furthermore, a switch in between the fifth and the sixth modes is detected. On the other hand, good results are achieved for the first two modes, the values are really close to the experimental results and the small difference in between these two modes is well simulated.

Further simulations are performed in order to find a good compromise in the FEA resulting natural frequencies with respect the EMA ones. Indeed, in the results reported in Table 5.5.2.4.7, the FEA 6th natural frequency is almost the double of the one obtained experimentally.

Firstly, the in-plane Poisson ratio is decreased in order to have again as 5th mode the bending on the XZ plane and as 6th mode the torsion. This result is achieved by simply decreasing ν_{12} from 0.7 to 0.5.

A compromise can be reached by varying the in-plane Poisson ratio and changing the in-plane shear moduli, which are mainly involved in the torsional modes. Indeed, in this case, two of the modes where the highest difference is registered (the fourth and the sixth) are exactly the torsional one, thus the in-plane shear modulus is decreased. While changing the material properties, it must be paid attention to have the same mode shapes: since the first two modes are really close, the first and second modes can be switched. The final material properties considered and the corresponding results are the reported in Table 5.5.2.4.8, Table 5.5.2.4.9 and Figure 5.5.2.4.5.

Table 5.5.2.4.8 – Final material properties considered. FEA analysis with orthotropic material.

Property	Value
In-plane Young moduli $E_1 = E_2$ [GPa]	40
Through thickness Young modulus E_3 [GPa]	38
In-plane Poisson ratios ν_{12} [-]	0.6
Through thickness Poisson ratio $\nu_{13} = \nu_{23}$ [-]	0.3
Interlaminar shear modulus G_{12} [GPa]	15
Interlaminar shear modulus $G_{13} = G_{23}$ [GPa]	4.5

Table 5.5.2.4.9 – Comparison between the FEA and the EMA natural frequencies. The material properties for the FEA are the final ones chosen.

Mode	FEA freq. [Hz]	EMA freq. [Hz]
1	30.81	35.95
2	32.25	36.58
3	85.84	87.89
4	152.83	143.80
5	273.60	173.60
6	282.48	197.00

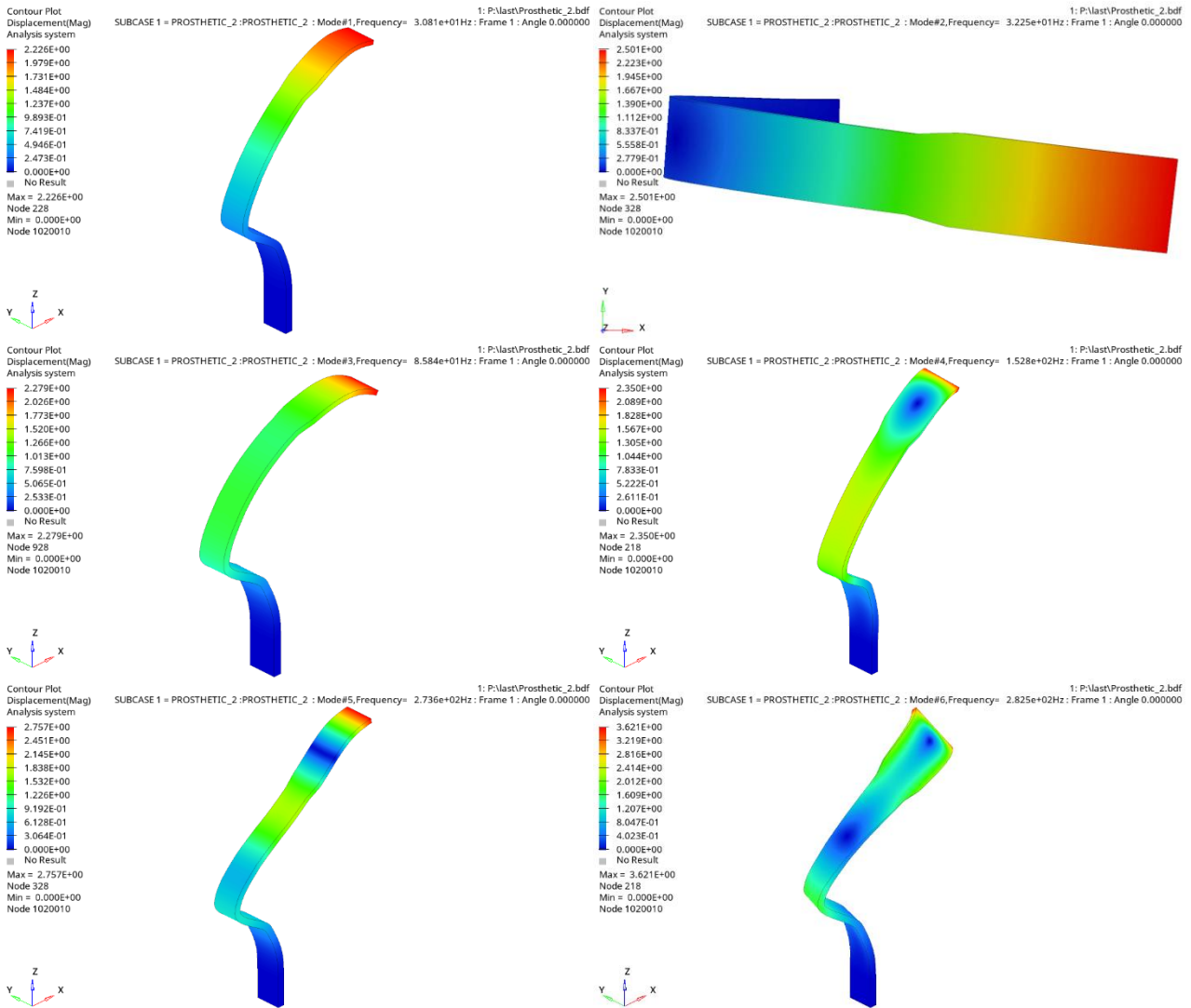


Figure 5.5.2.4.5 – Prosthetic first 6 mode shapes of the FEA simulation on Nastran 2017. Definitive model.

5.5.2.5 Laminate definition

Actually, the prosthetic material is likely to be composted by laminae oriented in different directions. Thus, multiple simulations are performed considering multiple laminae orientation.

To do this, the .hex file is edited by assigning to the elements at different thickness level diverse material properties. Then, on the .bdf file generated the material properties are edited from the isotropic ones to anisotropic with MAT9.

Firstly, the composite properties defined at the end of Paragraph 5.5.2.4, which are referred to the element reference frame, must be computed along the material reference system. To do this, since the fiber direction considered in Paragraph 5.5.2.4 is +/-45°, such rotation angle is applied on

$$\text{eq. } E_x = \frac{1}{\frac{1}{E_1} \cos^4(\theta) + \frac{1}{E_2} \sin^4(\theta) + \left(-\frac{2\nu_{12}}{E_1} + \frac{1}{G_{12}}\right) \sin^2(\theta) \cos^2(\theta)} \quad (5.5.2.4.19)$$

$$\nu_{xy} = E_x \left(\frac{\nu_{12}}{E_1} (\sin^4(\theta) + \cos^4(\theta)) - \left(\frac{2}{E_1} + \frac{2}{E_2} - \frac{1}{G_{12}} \right) \sin^2(\theta) \cos^2(\theta) \right) \quad (5.5.2.4.22) \text{ to find the}$$

material properties along the fibers. The result obtained correspond to the parameters describing the woven lamina at 0°/90°. From these values,

$$\text{eq. } E_x = \frac{1}{\frac{1}{E_1} \cos^4(\theta) + \frac{1}{E_2} \sin^4(\theta) + \left(-\frac{2\nu_{12}}{E_1} + \frac{1}{G_{12}} \right) \sin^2(\theta) \cos^2(\theta)} \quad (5.5.2.4.19) \quad -$$

$$\nu_{xy} = E_x \left(\frac{\nu_{12}}{E_1} (\sin^4(\theta) + \cos^4(\theta)) - \left(\frac{2}{E_1} + \frac{2}{E_2} - \frac{1}{G_{12}} \right) \sin^2(\theta) \cos^2(\theta) \right) \quad (5.5.2.4.22) \text{ are applied to}$$

calculate the lamina properties for different inclinations along the element reference axes. The orientations taken into account are: 0°/90°, +/-45°, 60°/30°, 30°/60°. Below the resulting material properties along the elements local reference frame directions are reported.

Table 5.5.2.5.1 – Laminae mechanical properties along the elements local reference frame. Different laminae orientations are considered.

	E_x [GPa]	E_y [GPa]	G_{xy} [GPa]	ν_{xy} [-]
0°/90°	46.1	46.1	12.5	0.54
+/-45°	40	40	15	0.6
60°/30°	41.4	41.4	14.3	0.59
30°/60°	41.4	41.4	14.3	0.59

To define the anisotropic material on Nastran (MAT9), the stiffness matrix must be specified. It is not enough to consider the properties along the element direction (Table 5.5.2.5.1) and substitute them in the stiffness matrix, in this way the coupling between shear and extension, risen from the rotation of the fibers direction, would be lost. In Paragraph 5.5.2.4 it was possible to neglect the coupling factor just because the fibers are inclined of +/-45° with respect to the element coordinate system, thus negligible coupling rise between shear and extension.

As suggested from the Kaddaha et al. [42] research, the rotation matrix to apply to the 6x6 stiffness matrix referred to the material properties of the 0°/90° lamina, is:

$$[T] = \begin{bmatrix} l_1^2 & m_1^2 & n_1^2 & 2m_1n_1 & 2n_1l_1 & 2m_1l_1 \\ l_2^2 & m_2^2 & n_2^2 & 2m_2n_2 & 2l_2n_2 & 2m_2l_2 \\ l_3^2 & m_3^2 & n_3^2 & 2m_3n_3 & 2l_3n_3 & 2m_3l_3 \\ l_2l_3 & m_2m_3 & n_2n_3 & m_2n_3 + n_2m_3 & l_2n_3 + n_2l_3 & m_2l_3 + l_2m_3 \\ l_3l_1 & m_1m_3 & n_1n_3 & m_1n_3 + n_1m_3 & l_1n_3 + n_1l_3 & m_1l_3 + l_1m_3 \\ ll_2 & m_2m_1 & n_2n_1 & m_2n_1 + n_2m_1 & l_2n_1 + n_2l_1 & m_2l_1 + l_2m_1 \end{bmatrix} \quad (5.5.2.5.1)$$

where l_i , m_i and n_i are the direction cosines, defined as the cosines of the angle between the axes of the material and element coordinate system before and after rotation:

$$\begin{bmatrix} l_1 & m_1 & n_1 \\ l_2 & m_2 & n_2 \\ l_3 & m_3 & n_3 \end{bmatrix} = \begin{bmatrix} \sin(\alpha)\cos(\theta) & -\sin(\theta) & -\cos(\alpha)\cos(\theta) \\ \sin(\alpha)\sin(\theta) & \cos(\theta) & -\cos(\alpha)\sin(\theta) \\ s\sin(\alpha) & 0 & \sin(\alpha) \end{bmatrix} \quad (5.5.2.5.2)$$

where θ is the in-plane angle (on the 1-2 plane) and α is the out-of-plane angle.

Since the rotation occurs just on the lamina plane, $\alpha = 0$, thus the 6x6 rotation matrix is:

$$[T] = \begin{bmatrix} \cos^2(\theta) & \sin^2(\theta) & 0 & 0 & 0 & -2\cos(\theta)\sin(\theta) \\ \sin^2(\theta) & \cos^2(\theta) & 0 & 0 & 0 & 2\cos(\theta)\sin(\theta) \\ 0 & 0 & 1 & 0 & 0 & 0 \\ 0 & 0 & 0 & \cos(\theta) & \sin(\theta) & 0 \\ 0 & 0 & 0 & -\sin(\theta) & \cos(\theta) & 0 \\ \cos(\theta)\sin(\theta) & -\cos(\theta)\sin(\theta) & 0 & 0 & 0 & \cos^2(\theta) - \sin^2(\theta) \end{bmatrix} \quad (5.5.2.5.3)$$

The stiffness matrix of the lamina with the fibers disposed at 0° and 90° is defined exactly as the

$$\text{orthotropic material ones (eq. } \begin{bmatrix} \varepsilon_1 \\ \varepsilon_2 \\ \varepsilon_3 \\ \gamma_{23} \\ \gamma_{31} \\ \gamma_{12} \end{bmatrix} = \begin{bmatrix} \frac{1}{E_1} & -\frac{\nu_{21}}{E_2} & -\frac{\nu_{31}}{E_3} & 0 & 0 & 0 \\ -\frac{\nu_{12}}{E_1} & \frac{1}{E_2} & -\frac{\nu_{32}}{E_3} & 0 & 0 & 0 \\ -\frac{\nu_{13}}{E_1} & -\frac{\nu_{23}}{E_2} & \frac{1}{E_3} & 0 & 0 & 0 \\ 0 & 0 & 0 & \frac{1}{G_{23}} & 0 & 0 \\ 0 & 0 & 0 & 0 & \frac{1}{G_{13}} & 0 \\ 0 & 0 & 0 & 0 & 0 & \frac{1}{G_{12}} \end{bmatrix} \cdot \begin{bmatrix} \sigma_1 \\ \sigma_2 \\ \sigma_3 \\ \tau_{23} \\ \tau_{31} \\ \tau_{12} \end{bmatrix} \quad (5.5.2.4.5),$$

thus no coupling between shear and normal responses are present. The same result is obtained computing the stiffness matrix of the lamina inclined of $\pm 45^\circ$; this validates the hypothesis of no shear-normal coupling assumed in the analyses of Paragraph 5.5.2.4. On the other hand, the stiffness matrix describing the laminae with $30^\circ/60^\circ$ and $60^\circ/30^\circ$ fibres inclination, present coupling between shear and normal responses: the (1,6) and (2,6) entries of the symmetric stiffness matrix are not nil. Furthermore, the matrices of these last two laminae are exactly the same, a part from the (1,6) and (2,6) entries which are opposite in sign in between the two laminae.

A significant advantages of using composites, is that their properties can be tailor-made by having a different stacking sequence depending on the functional requirements. The most common stacking sequence are:

- the symmetric one, because no coupling between bending and extension is present. Indeed, in laminates, bending is critical since there are parts of the material in compression, while the composite works better under tension;
- the cross-ply: all the layers have 0° or 90° fibre orientation. Here shear and extension and bending and twisting are not coupled;
- the balanced angle-ply: there are equal number of plies oriented in either angle directions. No coupling between extension and shear is present, but there can be coupling between bending

and twisting and flection and extension. If this laminate is symmetric, just bending-twisting coupling can occur.

Balanced symmetric angle-ply disposition is assumed for the prosthetic simulations in order to avoid flection-extension and shear-extension couplings.

Firstly, Model_2 is considered for the simulations: it is discretized by hexagonal elements, with 6 hexa along the thickness (see Table 5.5.2.1.1). The results are reported below for each stacking sequence analysed:

Table 5.5.2.5.2 – Natural frequencies results considering different symmetric angle-ply laminate dispositions. The discretization of Model_2 is considered. For each result, the angle disposition is specified, the letter ‘s’ indicates that the laminate is symmetric.

Natural frequencies	[45/45/45]s	[45/0/0]s	[45/60/30]s	[45/60/0]s	[45/30/0]s	[45/0/60]s	[45/0/30]s
f₁ [Hz]	30.81	30.77	30.97	30.94	30.90	30.81	30.81
f₂ [Hz]	32.25	32.25	32.28	32.26	32.27	32.23	32.26
f₃ [Hz]	85.84	85.74	86.02	85.86	86.26	85.80	85.91
f₄ [Hz]	152.83	152.14	152.95	152.56	152.53	152.51	152.57
f₅ [Hz]	273.60	274.72	274.56	274.23	276.14	274.09	275.10
f₆ [Hz]	282.48	282.40	282.69	282.54	282.57	282.39	282.49

The first result is reported just as reference, is the starting one obtained when the material was considered to be entirely composed by plies with +/-45° fibres disposition (Paragraph 5.5.2.4). All the natural frequencies obtained are really close between each laminate definition and the mode shapes correspond exactly to the ones identified in Paragraph 5.5.2.4. The stiffest configuration is the [45/60/30]_s. In general, the biggest difference is registered on the fifth mode, which is the third flection on the XZ plane. In any case, the variance, with respect the reference one is always lower than 1.5%. Probably, such outcome is given to the fact that the number of variables is to low: just the inclination of four laminae, that are also symmetrically coupled, can be changed.

Further consideration can be done on the stacking sequence. In Table 5.5.2.5.3 laminae disposition [45/0/60] and [45/60/0] and also [45/0/30] and [45/30/0] again compared, indicating also the relative

error in between the results, according to eq. $e = \frac{f_{\max,i} - f_{\min,i}}{f_{\max,i}}$ (5.5.1.1.1). A variance in the

results is registered, even if the laminae inclination composing the laminates is the same, just their order changes. The biggest difference is registered for the bending modes on the XZ plane: modes 1, 3 and 5. Setting the 0°/90° laminae close to the +/-45° results to be a more compliance solution rather than having them in the core.

Table 5.5.2.5.3 – Comparison between laminates with the same laminae orientations but different

order disposition. The relative error is computed according to eq. $e = \frac{f_{\max,i} - f_{\min,i}}{f_{\max,i}}$ (5.5.1.1.1).

Natural frequencies	[45/30/0]s	[45/0/30]s	e
f₁ [Hz]	30.90	30.81	0.32%
f₂ [Hz]	32.27	32.26	0.02%
f₃ [Hz]	86.26	85.91	0.41%

f₄ [Hz]	152.53	152.57	-0.03%
f₅ [Hz]	276.14	275.10	0.37%
f₆ [Hz]	282.57	282.49	0.03%

Natural frequencies	[45/60/0]s	[45/0/60]s	e
f₁ [Hz]	30.94	30.81	0.42%
f₂ [Hz]	32.26	32.23	0.09%
f₃ [Hz]	85.86	85.80	0.08%
f₄ [Hz]	152.56	152.51	0.03%
f₅ [Hz]	274.23	274.09	0.05%
f₆ [Hz]	282.54	282.39	0.05%

Another comparison can be done between having the woven lamina at $30^\circ/60^\circ$ or at $60^\circ/30^\circ$. As mentioned previously, indeed, the stiffness matrices are exactly the same in between the two dispositions a part from the shear-extension coupling entries which are equal and opposite in sign. As visible in Table 5.5.2.5.4, also here the biggest difference is registered in the bending on the XZ plane. A part from the first mode, applying the woven lamina at 30° produce a stiffer material with respect to inclining it of 60° .

Table 5.5.2.5.4 – Comparison between laminates with 30° inclination and 60° inclination. The

relative error is computed according to eq.
$$e = \frac{f_{\max,i} - f_{\min,i}}{f_{\max,i}} \quad (5.5.1.1.1)$$

Natural frequencies	[45/60/0]s	[45/30/0]s	e
f₁ [Hz]	30.94	30.90	0.11%
f₂ [Hz]	32.26	32.27	0.02%
f₃ [Hz]	85.86	86.26	0.46%
f₄ [Hz]	152.56	152.53	0.02%
f₅ [Hz]	274.23	276.14	0.69%
f₆ [Hz]	282.54	282.57	0.01%

Natural frequencies	[45/0/60]s	[45/0/30]s	e
f₁ [Hz]	30.81	30.81	0.01%
f₂ [Hz]	32.23	32.26	0.09%
f₃ [Hz]	85.80	85.91	0.13%
f₄ [Hz]	152.51	152.57	0.04%
f₅ [Hz]	274.09	275.10	0.37%
f₆ [Hz]	282.39	282.49	0.03%

A different mesh is then considered in order to have 8 element along the thickness. The discretization of the new model has the following characteristics:

Table 5.5.2.5.5 – Characteristics of the new model created for the laminate analysis. “Hexa num. _thick” and “Hexa num. _width” refers to the number of elements along the thickness and the width.

Characteristic	Model_1
Nodes num.	41157
Elements num.	34304
BCs	862
Dofs	122609
Hexa num. _thick	8
Hexa num. _width	15

Also in this case balanced symmetric angle-ply disposition of the laminae is considered. In the table below, the results obtained for different laminate definition are reported:

Table 5.5.2.5.6 – Natural frequencies results considering different symmetric angle-ply laminate dispositions. The discretization of the new model described in Table 5.5.2.5.5 is considered. For each result, the angle disposition is specified, the letter ‘s’ indicates that the laminate is symmetric.

Natural frequencies	[45/0/0/0] _s	[45/60/0/0] _s	[45/60/30/0] _s	[45/60/0/30] _s	[45/30/60/30] _s	[45/60/30/60] _s
f₁ [Hz]	30.68	31.07	31.11	30.60	31.20	31.24
f₂ [Hz]	32.26	32.28	32.30	32.23	32.33	32.32
f₃ [Hz]	85.63	86.34	86.46	85.32	87.39	86.95
f₄ [Hz]	152.66	153.37	153.92	152.16	154.40	154.48
f₅ [Hz]	272.50	274.46	274.78	272.65	278.48	276.46
f₆ [Hz]	283.10	283.43	283.68	282.34	283.97	283.98

The results variance is still really small, but higher than when just 6 ply were simulated. The most compliant dispositions are [45/0/0/0]_s and [45/60/0/30]_s. The inclination of the lamina at 60° or 30° can give good material stiffness results, furthermore, usually it is suggested to set perpendicular inclinations in between the adjacent plies to have better stiffness results, thus it could be for this reason that the configuration [45/60/0/30]_s is one of the most compliant and the stiffest ones are [45/60/30/60]_s and [45/30/60/30]_s.

Since the number of plies which can be simulated is still really low, not enough considerations can be done on the configuration to select. If it was possible to simulate more plies, the laminae dispositions could have been an important tool in order to tune better the material properties with respect the EMA results. By computing the error in between the FEA and the EMA results, the ply disposition [45/60/30/60]_s results to be the closest to the real prosthetic material behaviour. In any case, as it will be discussed later, the determination of the laminate stacking sequence cannot be the only way for completely matching the EMA results. Indeed, for any laminate definition, there is an increase on the FEA natural frequencies which is far higher than the EMA ones, thus from the fourth one it is anymore possible to match the natural frequencies values with the EMA ones.

Further investigations have been done, considering different material composition at the core. Firstly woven Kevlar inclined at 0°/90° is considered on all the layers a part on the surfaces, where the woven carbon fibres are maintained at +/-45°. Then a simulation is run considering an alternation of Kevlar and carbon fibres layer all at 0°/90°. Finally, at the core unidirectional plies in carbon fibres are simulated. The mechanical properties of the Kevlar composite and of the unidirectional carbon fibres one are reported in Table 5.5.2.5.7. The results of the three simulations are reported in Table 5.5.2.5.7 in comparison to the results obtained considering carbon woven layers at +/-45° on the entire prosthetic. The mode shapes are exactly the same among all the simulations. The natural frequencies are all lower than considering woven carbon fabric on the entire material. Notice that the alternation of Kevlar and carbon plies is a stiffer solution with respect having just Kevlar at the core just for the bending modes on the XZ plane. The unidirectional core, instead makes the component more compliant for all the modes, particularly for the bindings on the XZ plane.

Table 5.5.2.5.7 – Mechanical properties considered for the composite layers in Kevlar (woven) and the ones with the unidirectional carbon fibres.

Property	Kevlar	Unidirectional C
Longitudinal Young modulus E_1 [GPa]	30	135
Transversal in-plane Young modulus E_2 [GPa]	30	38
Through thickness Young modulus E_3 [GPa]	27	38
In-plane Poisson ratios ν_{12} [-]	0.2	0.3
Through thickness Poisson ratio $\nu_{13} = \nu_{23}$ [-]	0.3	0.3
Interlaminar shear modulus G_{12} [GPa]	3	5
Interlaminar shear modulus $G_{13} = G_{23}$ [GPa]	2	4.5

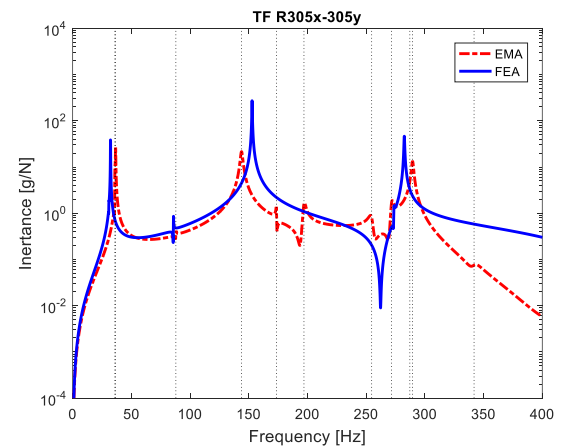
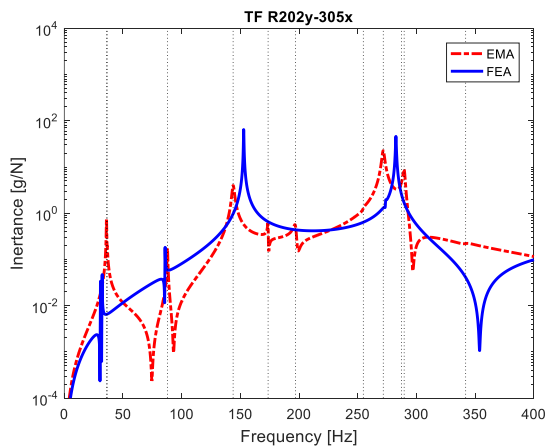
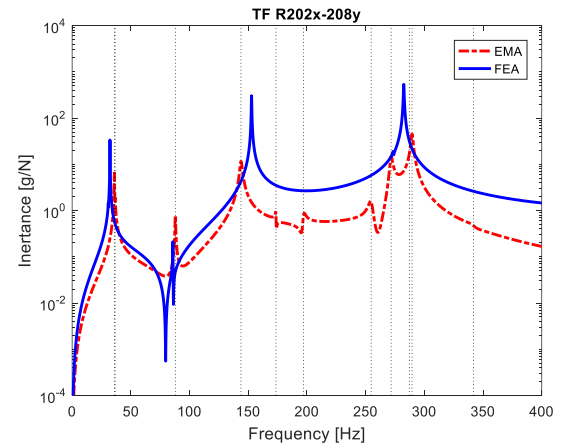
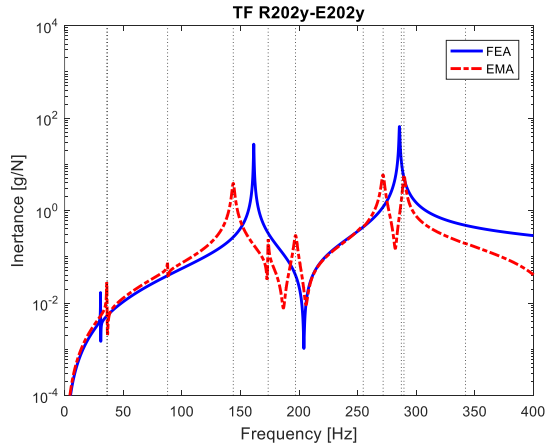
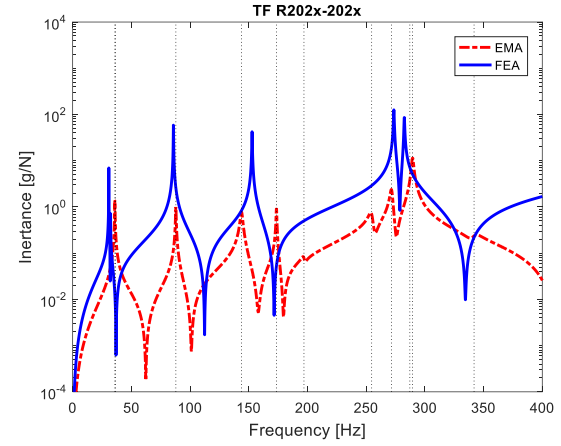
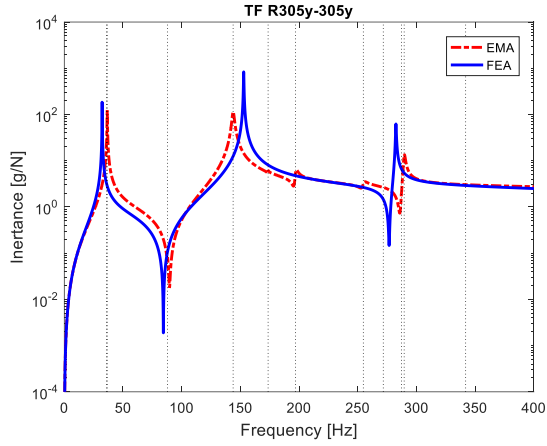
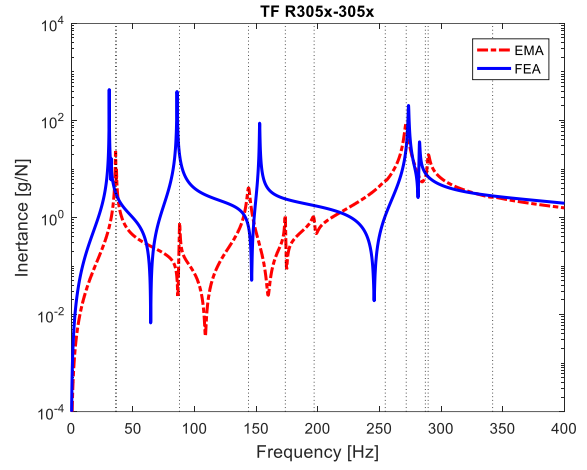
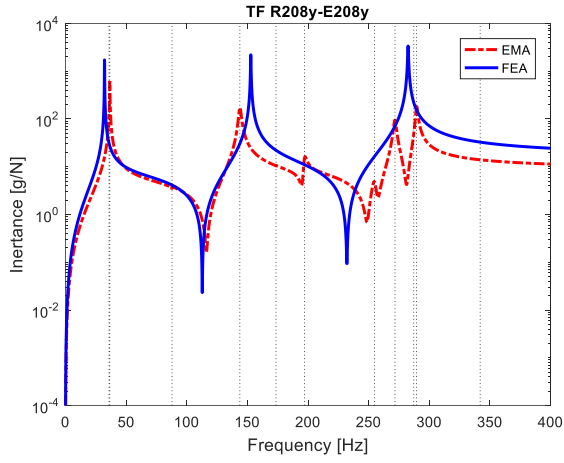
Table 5.5.2.5.8 – Natural frequencies results considering different material composition in the middle layers of the prosthetic.

Natural frequencies	Carbon	Core in Kevlar	Core in Kevlar and carbon	Unidirectional core
f_1 [Hz]	30.81	28.32	29.60	27.26
f_2 [Hz]	32.25	31.78	31.73	31.05
f_3 [Hz]	85.84	79.04	82.50	75.88
f_4 [Hz]	152.83	145.22	145.21	138.10
f_5 [Hz]	273.60	251.26	263.59	240.16
f_6 [Hz]	282.48	278.02	277.69	271.76

5.5.2.6 EMA-FEA comparison

Since the laminate stacking sequence does not affect much the simulation results, the EMA-FEA comparison is performed considering the laminate composed by fabric carbon/epoxy layers all inclined of $\pm 45^\circ$ (thus the outcomes shown at the end of Paragraph 5.5.2.4).

Firstly, the same auto and cross inertances investigated in Paragraph 5.3 are plotted below for the FRF comparison between EMA and FEA.



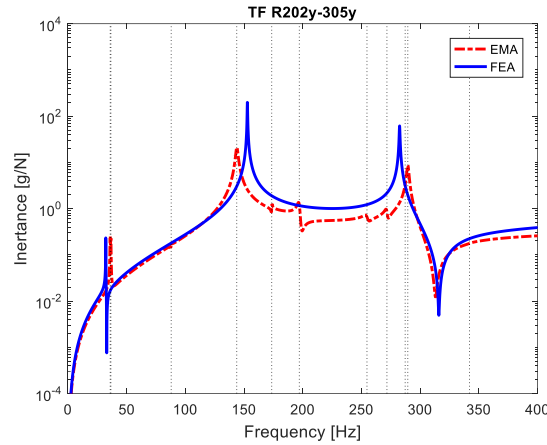


Figure 5.5.2.6.1 – Comparison of the EMA and FEA inertances. The transfer functions are plotted till 400 Hz.

Taking a look to the FRF plots of Figure 5.5.2.6.1, there is a sort of correspondence between the curves. It seems that some modes, the ones which have a lower amplitude, are not detected from the simulations. Thus, the 5th and 6th FEA natural frequencies probably refer to other modes detected in the experimental test. The EMA natural frequencies are again reported in Table 5.5.2.6.1 and the FEA ones are matched to the closest EMA frequency. No considerations can be done on the mode shape matching since from the 6th experimental mode, it is difficult to properly identify a precise mode shape, they seem a mix between torsion and bending on the XZ plane.

Table 5.5.2.6.1 – EMA-FEA natural frequencies match.

Mode	EMA freq. [Hz]	FEA freq. [Hz]
1	35.95	30.81
2	36.58	32.25
3	87.89	85.84
4	143.8	152.83
5	173.6	-
6	197	-
7	254.7	-
8	271.7	273.60
9	287.2	282.48
10	289.5	-

To be more consistent with what just said, the EMA-FEA MAC of the first 6 modes and then of the first 10 modes, is computed and shown in Figure 5.5.2.6.2. Till the 4th mode there is a good correspondence of the modes, then there is a match between the 4th and the 6th mode shape since both are torsions. The most remarkable characteristic is that the EMA modes from the 7th to the 10th have a correspondence just with the 5th and the 6th FEA ones. This is related to the fact that the EMA number of nodes describing the prosthetic shape is low, thus more complicated mode shapes are difficult to identify and to compare to the numerical results.

From Figure 5.5.2.6.2, it is also remarkable the fact that there is an increase in the natural frequency completely different in between the experimental and the simulation results: the FEA 10th mode is around 1250 Hz, while the EMA one is at around 290 Hz.

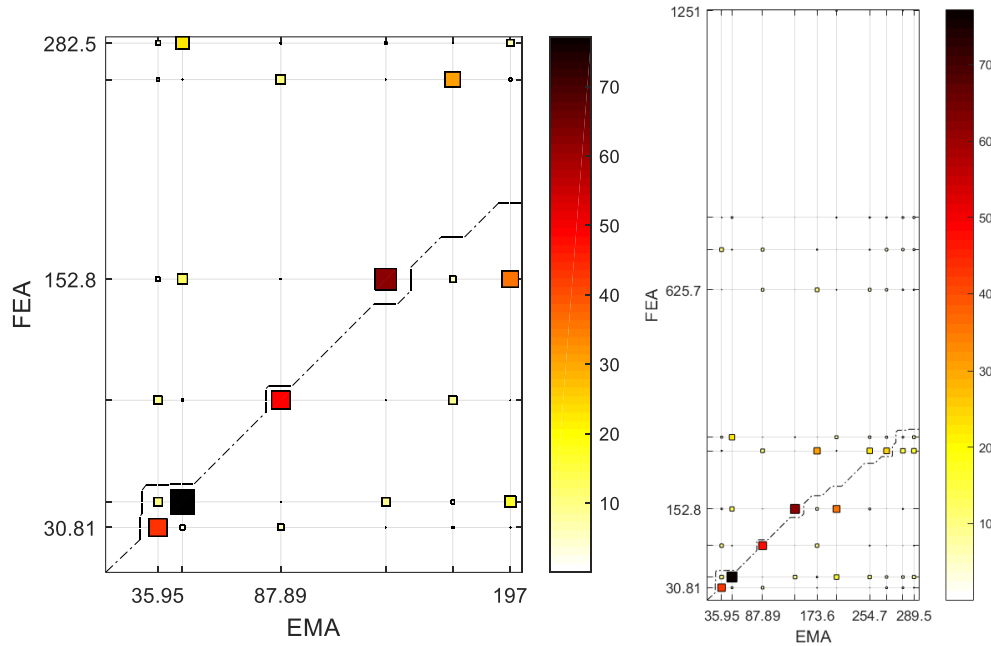


Figure 5.5.2.6.2 – MAC between EMA and FEA. Laminate with carbon/epoxy layers at $\pm 45^\circ$.

5.5.2.7 Changes of the stiffness along the prosthetic shape

As will be further discussed in Paragraph 6, from the EMA 5th mode shape, it seems that the prosthetic upper part is more compliant than the lower one. Here, such possibility is investigated by considering just two materials with different stiffness values along the prosthetic shape, in particular the upper part, the blue one in the left image of Figure 5.5.2.7.1, is made more compliant.

Six simulations are performed:

- sim 1: in the upper part a more compliant woven material is set;
- sim 2: the layers at the surfaces are maintained of the same material considered in Paragraph 5.5.2.4 (stiffer material), while the core of the upper part is made of the more compliant woven material (see Figure 5.5.2.7.1 right image);
- sim 3: on the upper part the unidirectional carbon fibre composite is considered, the fibers are disposed vertically (along the prosthetic shape);
- sim 4: on the upper part the unidirectional carbon fibre composite is considered, the fibers are disposed horizontally (along the prosthetic width);
- sim 5: the core at the upper part is made of unidirectional carbon fibre composite with horizontal disposition.

The material properties considered are reported in Table 5.5.2.7.1 (the stiffer material is the same one identified at the end of Paragraph 5.5.2.4).

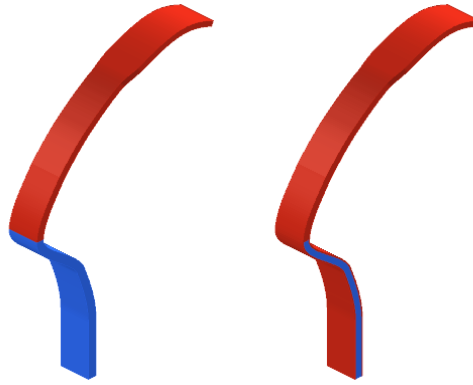


Figure 5.5.2.7.1 – Material distinction between upper and lower part of the prosthetic.

Table 5.5.2.7.1 – Material properties, simulation with the prosthetic upper part more compliant.

Property	Stiffer	More compliant	Unidirectional
Longitudinal Young modulus E_1 [GPa]	40	20	135
Transversal in-plane Young modulus E_2 [GPa]	40	20	38
Through thickness Young modulus E_3 [GPa]	38	19	38
In-plane Poisson ratios ν_{12} [-]	0.6	0.6	0.3
Through thickness Poisson ratio $\nu_{13} = \nu_{23}$ [-]	0.3	0.3	0.3
Interlaminar shear modulus G_{12} [GPa]	15	7.5	5
Interlaminar shear modulus $G_{13} = G_{23}$ [GPa]	4.5	2.25	4.5

The natural frequencies obtained are compared in Table 5.5.2.7.2 to the ones obtained considering the prosthetic composed just by the same woven carbon fibre material at $\pm 45^\circ$ (the one considered at the end of Paragraph 5.5.2.4). Of course the frequencies are lower with respect to have just carbon fibre, since a more compliant material is added. However, in all the cases the natural frequencies of the 5th and 6th mode are still very high. Remarkable effects are sensed for the first natural frequencies: in the first two simulations the first two modes are really close in frequency, while when unidirectional material is applied on the upper part there is any more coupling between these two. Furthermore, notice how much maintaining the same material on the surface affects the results: sim2 and sim 5 have similar outcomes.

Table 5.5.2.7.2 – Natural frequencies of the simulations setting the prosthetic upper part more compliant. They are set in comparison to the case in which the entire prosthetic is composed by the same woven carbon fibre composite.

Natural frequencies	Unique material	sim 1	sim 2	sim 3	sim 4	sim 5
f_1 [Hz]	30.81	23.82	29.08	21.65	20.55	28.78
f_2 [Hz]	32.25	24.03	29.73	30.72	29.74	31.33
f_3 [Hz]	85.84	74.21	82.84	70.51	68.22	82.00
f_4 [Hz]	152.83	115.05	138.29	125.77	123.99	138.55
f_5 [Hz]	273.60	250.43	267.88	243.74	243.55	267.17
f_6 [Hz]	282.48	260.85	274.01	270.90	270.07	276.15

The mode shapes of the new simulations are the same of the ones already obtained in the previous simulations, just the displacement sensed in the lower part is a little bit bigger, but overall the trend is the same. Below are reported the 5th mode shapes of the simulation performed in Paragraph 5.5.2.4, where the material is the same for the entire prosthetic, in comparison to the one of sim 1 and of the EMA. The mode shapes simulated are still different from the one obtained experimentally. Probably other parts of the prosthetic have more compliant properties, for example the toe part tangential to the horizontal point. As it will be discussed in Paragraph 7, further simulations assuming different mechanical properties along the prosthetic should be performed.

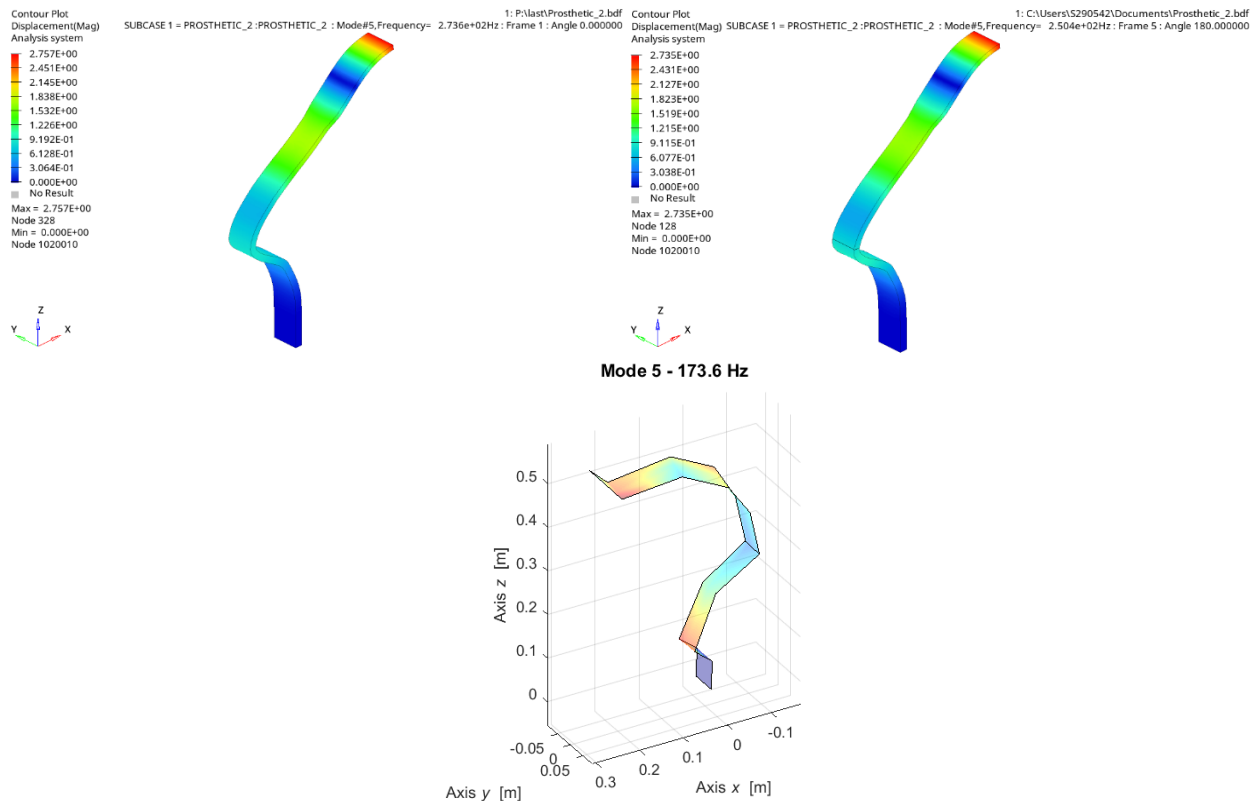


Figure 5.5.2.7.2 – 5th mode shape comparison. From up-left, in reading order: simulation with the same material along the prosthetic, sim 1 and EMA.

Just for completeness, the material properties of sim 2 are switched, thus the upper core part is the stiffer one. The natural frequencies results are compared to the previous sim 5, to the simulation of having just one material in the component and to the EMA. Notice how much the bending modes in the XZ plane are lower, since the main material in the component is the unidirectional with fibers disposed horizontally (along the width). The most remarkable result is the frequency of mode 5 which is close to the EMA one, is the closest result obtained among all the simulations performed till now. This confirms even more the necessity of better knowing the stacking sequence of the material which affect a lot the prosthetic behaviour.

Table 5.5.2.7.3 – Natural frequencies of the simulations setting the prosthetic upper part more compliant. They are set in comparison to the case in which the entire prosthetic is composed by the same woven carbon fibre composite.

Natural frequencies	Unique material	sim 5	sim 5_switched material	EMA
f_1 [Hz]	30.81	28.78	22.348	35.95
f_2 [Hz]	32.25	31.33	31.409	36.58
f_3 [Hz]	85.84	82.00	61.071	87.89
f_4 [Hz]	152.83	138.55	143.78	143.8
f_5 [Hz]	273.60	267.17	197.82	173.6
f_6 [Hz]	282.48	276.15	274.49	197

The 5th mode shape resulting from this simulation is below displayed. The trend is the same of the one coming out from the other simulations.

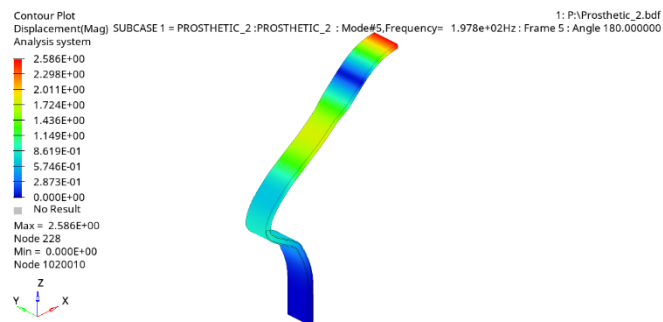


Figure 5.5.2.7.3 – 5th mode shape of sim 5 with the material switched: the upper core part is stiffer.

6. Discussion

The final results obtained point out a discrepancy in the natural frequencies, from the 4th mode, resulting from the experimental test and from the simulation. Multiple considerations have to be underlined in order to understand which are the reasons of such results.

Firstly, the possibility of having acquired wrong results during the test is discarded. Indeed, since the prosthetic was clamped and the constraint is not ideal, there can be the possibility of acquiring vibration modes which actually are the rigid motion of the clamping system. This option is rejected since actually the same test was performed the day before on another table, with the same boundary conditions, and the results were the same of the recorded the day after (reported in Paragraph 5.2). Furthermore, two accelerometers, one mono-axial and the other one tri-axial, were placed on the aluminium plate which constrained the component in order to verify the presence of almost nil displacements. However, the fact that the clamping system is not ideal, is taken into account in the simulations by applying the boundary conditions described in Paragraph 5.5.2.2.

Also the options of individuating more natural frequencies than the actual one during the post processing is discharged. Indeed the EMA auto-MAC matrix, Figure 5.2.3, is almost diagonal, meaning that the modes are orthogonal and not identical between them. Also the plots of the experimental and synthesized auto and cross-instances present visible peaks in correspondence of the natural frequencies individuated, see Paragraph 5.3.

As remarked at the end of Paragraph 5.5.2.6, the first 4 EMA and FEA modes well match between each other, then the discrepancy in the natural frequencies becomes progressively bigger, the simulation is no more able to simulate the experimental results. Thus, there is not an error related just to particular modes. Thus, such discrepancy is not related to wrong simulations of the constraints, in the mesh, in the orthotropic material definition or in the laminate stacking sequence.

Having said this, further are investigated multiple possible reasons for which the blade prosthetic has such unexpected modal behaviour.

Firstly, since the inner composition of the prosthetic is unknown, it was supposed the presence of a different material in the core of the prosthetic, such as foam or plastic. Indeed, usually the material on the surface affects the first modes, then, for higher frequencies also the inner material plays a role, thus for example the 5th and the 6th modes, which are not individuated in the simulations, can be the natural frequencies of the core material. This option was then rejected since some articles mention the presence of just carbon fiber composite in the blade prosthetics, as declared on the “Public Paralympic Heritage Trust” web site [43]. Furthermore, the density of the component is almost the same of the fabric carbon/epoxy laminae considered initially for the characterization of the orthotropic material (Paragraph 5.5.2.4, [27], [28]).

In Paragraph 5.5.2.5, multiple laminate stacking sequences were considered and it was demonstrated that the woven fibre orientations do not affect much the modal behaviour of the prosthetic (if the laminae on the surfaces are maintained inclined of $\pm 45^\circ$). But there is also the possibility of having carbon fibers in short format, or unidirectional, or in particles. As described by Gurdal et. al [51], there is also the possibility of redistributing the fibers of the layers in order to create beneficial stiffening partners against compression and buckling, allowing the fibers to curve within the plane of the laminates. This furnishes an advanced tailoring option to account for non-uniform stress states in a continuous manner. Laminates with curved fibers will have stiffness tailoring possibilities that can lead to alteration of load paths, resulting in favourable stress distributions within the laminate and improving the component performance. Since these laminae do not present a constant in-plane stiffness, theoretical evaluations of such characteristic are almost impossible: there is not a constant distance in between the fibers, they converge and diverge between them. In Gurdal et. al [51] research work, mixing layers with constant and variable stiffness is pointed out as a promising configuration for general loadings. This is just an example of how the internal laminae could be. It demonstrates

how much entropy there is in not knowing how are the internal laminae, there is an infinite number of options in producing composite components.

Also the manufacturing process of the blade prosthetic production is unknown. Prof. Küsefoğlu, in an article posted on the blog of the Kordsa company [44], underlines the possibility of producing blade prosthetics through the combination of different manufacturing techniques, such as the resin transfer moulding and the prepreg. This, can be equivalent to have almost two different materials in the component. Indeed, the production technique affects many parameters such as the quantity of resin remaining in the material and the voids presence. Hence, this is one of the multiple reasons which could explain the difficulties of matching the EMA and FEA natural frequencies.

Prof. Noroozi has dedicated part of his researches to dynamic blade prosthetic analyses. In particular in the articles [16], [17][14], the unknowledge of the exact material composition is pointed out as a big deficit. In the research work [16], the predominant presence of unidirectional layers, which drop off as one from the upper part to the toe, is supposed in order to carry high bending loads. Layers at $\pm 45^\circ$ are also detected on the surfaces to confer good overall properties. However, even here the lack of information on the material (such as the number of layers, the type of carbon and resin, the manufacturing process), due to restriction on access to classified commercial data, makes further investigations on the prosthetic properties impossible. Further, in the conclusions of work [17], the lack of detailed awareness about the dynamic behaviour of composite laminates is also pointed out. More knowledge is needed to understand the influence of variation in carbon lay-up and shape alterations on the frequency, mode shapes and damping of non-linear composite structures.

Here below are further analysed studies regarding the modal composites behaviour, even though as concluded from Prof. Noroozi [17], there is not enough knowledge about this argument to explain the blade prosthetic behaviour.

Actually, the dynamic analysis is largely applied on composites since it is an important tool for providing elastic and viscoelastic properties of the material. The advantage of the impact test is that it can be applied to the entire structure. Indeed, the tests which have to be performed just on specimens, evaluate just the local properties which are not useful for the composites, since they have non-uniform characteristics, thus the need of measuring the ‘in-situ’ globally averaged properties in composite components as well as the distribution of the properties within the component is essential. In the Chen et al. [47] research, it is indeed underlined that if specimens are cut from composite panels, not uniform distribution of the fibers is detected, this cause variations of the physical properties in the material.

Many studies are thus concentrating on the best steps and tools to adopt in order to obtain the most reliable results [52] and on the experimental characterization of different composite parts of racing cars or aircrafts [53]. Moreover, considerable literature is available for the classical solution to the inverse problem, which allows to evaluate the component mechanical properties from the experimental dynamic test data. However, as underlined from the Gibson et al. [49] research, the main issue is the difficulty of performing the inverse solution when the structure has complex geometries, which differ from the simple beam shape. On beam composites, analytical models are developed in order to evaluate the properties variation along the component: changes in the clamping conditions are performed and the natural frequencies are recorded. Hence, in the blade prosthetic case, it should be considered that the mechanical properties change along its shape, but given its particular geometry, from the experimental data no analytical models are available in order to evaluate such properties variation.

There are also studies for simulating the inhomogeneities in the composite beams, such as the Chen et al. [47] one. Here two different models are implemented: the “shifting method” and the “added mass method”, in which respectively the effective length and the mass of the component are changed to simulate the inhomogeneities. Furthermore, composite modulus and density are expressed in terms of the fiber volume fraction based on the micromechanics of composite materials, and the spatial distribution of fiber volume fraction is assumed to be given by a polynomial function. Good theoretical-experimental agreement is obtained for the fundamental modes in clamping-free beam

configuration, while for higher modes it is more difficult to predict the physical properties (“inverse problem”). In the clamped-mass configuration the condition number of the second and third natural results are already really high. This is mainly related to the fact that in the clamped-mass configuration the nonsymmetric condition is more pronounced increasing the bending-extension coupling effect which lowers the natural frequencies. Thus, in general at higher frequencies other factors, such as the bending-extension coupling, become more effective increasing the complexity of the problem. In the prosthetic case the thickness is much higher than the beam considered in this study, making the coupling between in and out-of-plane coupling higher; thus, even if the configuration is clamped-free, the coupling effect could be really significant at the 5th mode.

Since composites are given by the combination of two physically different substances, it is supposed that at higher frequencies the dynamic behaviour of each constituent places an important role in the creation of local modes. The identification of local modes is complicated by the material anisotropy which causes the presence coupled modes, as verified in the 7th -10th EMA modes obtained, where bending and torsion are mixed (as mentioned at the end of Paragraph 5.5.2.6).

Micromechanics is thus investigated in order to understand its influence in the dynamic behaviour of the entire material.

In the Mei et al. [45] research, the local wave transmission and reflection characteristics composite beams in correspondence of various discontinuities is analytically investigated. Here the bending-torsion coupling property of composites is considered. The difference in the results between considering materially coupled materials or uncoupled one is shown in the research work: if coupling is considered, the resulting natural frequencies are progressively lower with respect not coupled materials. Furthermore, it is explained that in correspondence of discontinuities, such as boundary conditions or thickness changes, the incident bending wave component generates the bending of the other type and a torsion, this does not happen if the incident component is torsional. This research just refers to slender beams, in thicker structures also the shear deformation and the rotary inertia must be taken into account. However, this work can already explain part of the dynamic behaviour of the prosthetic: the prosthetic thickness and width changes have an effect on the wave propagation and reflection which should be properly taken into account, together with the coupling effect, which lower the natural frequencies calculated just by considering the standard eigenvalue solution. In another study, Mei et al. [46] underlines that mainly the higher-frequency modes are more sensitive to the bending-torsion material coupling. Indeed, the torsional modes at low frequency are pure, while there is a cut-off frequency from which there is a wave mode transition causing also the torsional modes to be mixed to bendings. This can thus explain the facility in representing numerically just the first modes and also the difficulties of individuating the mode shapes already from the 7th mode.

Further, in the Kim et al. [56] paper, it is explained that in high volume fraction composites in viscoelastic composites with fiber reinforcement (such as the carbon/epoxy one), at low frequencies the wave dispersion effect is given by the viscoelastic matrix properties at low frequencies. Instead, at higher frequencies, the scattering effect becomes predominant. This underlines that the material, at low frequencies behaves as homogeneous, while then the not chemical uniformity in the material become predominant.

The sensibility of the graphite/epoxy laminate to the rate of applied loading is remarked from many studies, as reported in the book of Reid et al. [48]. Thus, the force-displacement relationship between impact and quasi-static tests is different. Not the same elastic modulus can be obtained from the static and modal analysis. This is a consequence also of the fact that the epoxy resin is a viscoelastic material. This means that in vibratory conditions, it is characterised by a dynamic modulus: there is a phase lag between stress and strain. Thus, in the dynamic mechanical analysis, the storage and loss elastic and shear moduli are defined. The storage component (E' and G') represents the elastic portion, thus related to the storage energy, while the loss part (E'' and G'') is related to the viscous characteristic. Thus the complex elastic and shear moduli are defined as follows:

$$E^* = E' + iE'' \quad (6.1)$$

$$G^* = G' + iG'' \quad (5.5.2.7.2)$$

where i is the imaginary unit.

The ratio between the loss and the storage factors is the tangent of the phase angle, it measures the material damping. E' is not equivalent to the Young's modulus since this last is calculated over a range of stress and strains, it is the slope of the curve, while E'' represents the point of a line. Furthermore, the test from which they are measured are different: in one the material is constantly stretched, in the other one stress and strain constantly oscillate (dynamic test, DMA). As underlined in the Menard's book [54], in order to know how the such material behaves, investigating how quickly the viscosity and elastic modulus change in the frequency and temperature domain is necessary. Unexpectedly, the trend of changes of the mechanical properties in the frequency domain is not the same for all the materials, in the Fouad et al. [55] work, different composites are compared and it is discovered that the loss factor of the shear modulus decreases in the frequency domain for the glass and Kevlar composites, while increases for the carbon fibres materials. Such changes with the mechanical characteristics in the frequency domain is not negligible, for example in the Berthe et al. [50] work, it is demonstrated that in the composite T700GC/M21 material, the increase of the apparent shear modulus is verified from a threshold of 10 Hz and the increase is of the 50%. In the work of Naresh et al. [57], the changes in the mechanical properties of composite materials with epoxy resin, in dependence to the temperature and frequency changes. The study demonstrates that depending on the fiber composition and disposition there the dependency to temperature and frequency is different. Furthermore, already in the frequency range analysed: 0-50 Hz the flexural modulus can have a variance of 1.9 GPa. Further, the research activity of Koo et al. demonstrated that for thick beams, unlike the thin ones, the frequency dependence of the mechanical properties of the cross-ply composites cannot be neglected. The frequency dependence of longitudinal and transversal damping and elastic moduli are not negligible already at around 50-100 Hz. In the blade prosthetic case, it is assumed that the viscoelastic properties of the epoxy resin are not that influencing for the first modes, but at higher modes this could be an effect which cannot be neglected and which can considerably lower the natural frequencies.

All things considered, the composite material dynamic behaviour is affected by multiple factors, such as the inhomogeneity of the material, the coupling torsion-bending effect, the viscoelastic properties of the resin material. However, usually, for components of the prosthetic magnitude, such nonlinearities become more significant at frequencies of kHz. Thus the main reasons which could explain the EMA-FEA mismatch for the natural frequencies higher than the 4th one, are probably related to the unknowledge of the exact material composition. There could be the presence of different materials inside the component or some layers could have a particular fibre disposition inside the prosthetic which confer a variable stiffness along the shape. This possibility is also supported to the fact that in the 5th mode shape, the part which is closer to the leg results to be more compliant, in the experimental evaluations with respect to the simulations. The possibility of having the prosthetic upper part more compliant is roughly investigated in Paragraph 5.5.2.7, not relevant results are obtained. But in the last simulation performed, in which the lower part of the prosthetic shape is composed by unidirectional layers and the core upper part by woven ones, reports a natural frequency of the 5th mode really close to the EMA one, demonstrating the high influence of the heterogeneous material composition in the dynamic behaviour and the infinite possible material compositions which can be investigated. Deeper analyses on the possibility of having different material properties along the prosthetic shape should be performed.

7. Conclusions and future works

From the experimental modal analysis on the blade prosthetic carried out at Politecnico of Torino, the dynamic behaviour of the component was successfully identified. 6 mode shapes in the frequency range 0÷240 Hz are identified. The identification of the mode shapes can be considered complete and satisfactory, as it can be noted from the good correspondence among the auto-inertances and the Maxwell reciprocity comparing the respective experimental and synthesised FRFs (Paragraph 5.3.1 - 5.3.2).

The results obtained are compared to the modal analysis performed at the University of Groningen, where just one mono-axial accelerometer and dSpace data analyser were used. From the EMAs results comparison it can be clearly stated the tools used at the University of Groningen were not enough to understand the complex free behaviour of the component (such as the orthogonal coupled modes). However, the good use of the tools available in the laboratory of Groningen allowed to identify at least the overall behaviour of the component: the first two bendings in the XZ plane and the first torsion.

The results obtained from the test performed at Politecnico of Torino, point out the particular dynamic behaviour of the component: there are some couplings between orthogonal modes. For instance, the first two modes, the flexion on the XZ plane and the one on the XY plane, have less than 1 Hz of difference. This behaviour is impossible to be simulated considering isotropic material characteristics (as pointed out in Paragraph 5.5.2.3). The prosthetic is visibly composed by thin layers of composite laminae which confer anisotropic dynamic behaviour to the component.

Since the exact material composition of the blade prosthetic is unknown, the component is supposed to be composed by carbon/epoxy woven laminae (Paragraph 5.5.2.4). The material is thus modelled as orthotropic. In this way, the dynamic characteristic of having some orthogonal modes coupled is well simulated.

Firstly layers of woven laminae oriented at $\pm 45^\circ$, with respect the element local reference frame, are considered. Then, by changing the laminae orientation along the thickness, different stacking sequences are simulated. Not big variations in the natural frequencies are verified. This can be the result of not being able to simulate enough layers. Indeed, for computational issues the finest mesh has 8 elements along the thickness. All the simulations performed are able to catch all the six EMA mode shapes, but the last 5th and 6th natural frequencies are not matching. There is an increase in the frequencies resulting from the simulations that is far higher with respect the experimental results.

Multiple possibilities have been investigated in order to understand the reason of such mismatch. The composite material in general is characterised by nonlinearities and anisotropies which, at high frequencies affect the dynamic performances of the component. However, for the frequencies considered in this work, thus lower than 1 kHz, the EMA-FEA mismatch is more likely to be related to the unknowledge of the exact composition of the material. Probably parts of the component are made more compliant with respect to other parts to improve the prosthetic performance during the run. This possibility is roughly investigated in Paragraph 5.5.2.7, not good matching with the EMA are obtained, but the results, in particular of the last simulation, confirm that this path could be the right one to achieve a better EMA-FEA correspondence. Deeper analyses on this way are needed.

In order to better investigate the dynamic behaviour of the prosthetic, it is suggested to perform other EMAs. One experimental test should be done reproducing the same boundary conditions and comparing it to the results reported in this work. Another EMA should be done in free-free conditions, in such a way to remove the constraints uncertainties and problems in reproducing them. The free-free condition can be achieved by placing the prosthetic on a foam or hanging it with two strings (on the lateral side). Furthermore, in the new EMA it is suggested to increase the number of nodes in order to better compare it to the simulation mode shapes. At least at the upper curvature of the prosthetic (closer to the leg) more nodes should be defined, indeed here, at the 5th mode, a mismatch

in between EMA and FEA mode shape is verified. Hence, in between node 101 and 102 and 102 and 103 (see Figure 5.1.3.2), an additional row of nodes each should be defined.

In general the accelerometer position of the EMA performed in this work can be maintained a part from the two sensors on the clamping system. The tri-axial accelerometer can be moved on the prosthetic in the upper part (closer to the leg), while the mono-axial one could be placed at the toe level, where the prosthetic shape is tangential to the horizontal plane. In this way the mono-axial sensor can sense the Z displacement of the component, which is the main behaviour of the prosthetic, furthermore, at the toe level it is more difficult to excite properly the prosthesis, thus it is convenient to have two sensors instead of just one.

Once the real prosthetic behaviour will be further analysed, deeper considerations can be done about the mechanical characteristic of the component, for example if already experimentally it can be confirmed that there are more compliant regions with respect to others.

All things considered, for the first four modes there is a good match between the EMA and FEA. This is because the orthotropic behaviour of the material is well caught. If the following modes are considered, there is a mismatch in the natural frequencies resulting, something in the characterization of the material is missing. As said before and demonstrated from the last simulation performed in Paragraph 5.5.2.7, this is probably related to the missing information on the material composition and disposition (stacking sequence). Likely other fibres are present in addition to the carbon ones or the fiber disposition is really different from the ones supposed in this work, creating different stiffness properties along the prosthetic shape. New EMAs on the component may help in verifying if there are actually more compliant parts along the prosthetic. This would serve in rejecting some hypothesis and take other paths.

To have a full overview of the prosthetic behaviour, it is also suggested to test it statically. In this way, considerations on the static stiffness can be done: it can be verified if non-linearities in the force-displacement relation are present and the stiffness value when the maximum load on the prosthetic is achieved (which, for sprinting, is around three times the athlete weight). Due to time and costs issues, in this research work, the test was not performed, but the design of the grippers to perform the experimental activity was entirely prepared. Indeed, as explained in Paragraph 3.2, the shape of the Cheetah Xcel does not allow to perform the test using the grippers already present on the MTS machine available in the DIMEAS laboratory at Politecnico of Torino, thus it was necessary to design new ones. In this work all the parameters, such as maximum force and load rate, to set to perform the static test are reported. They are the result of bibliographic researches since, in the case of prosthetics used for high level of activity, such as sprinting, standardize test just refer to walking conditions. Thus, to have a real access to the mechanical characteristic of the prosthetic in the conditions it is intended to be used, different parameters from the standard ones, have to be considered and applied during the test.

Appendix

A.1 Drawings of the aluminium plates and blocks produced by the University of Groningen

A couple of aluminium plates and blocks were designed to perform the static test on the MTS machine available at Politecnico of Torino. The parts were produced by the workshop of the University of Groningen.

Since then issues in performing the static test rose, these parts are integrated in the design of the new supporting system; they will be drilled to be attached to the prosthetic (see Paragraph 3 and Appendix A.2).

Below the drawings of the components.

Appendix

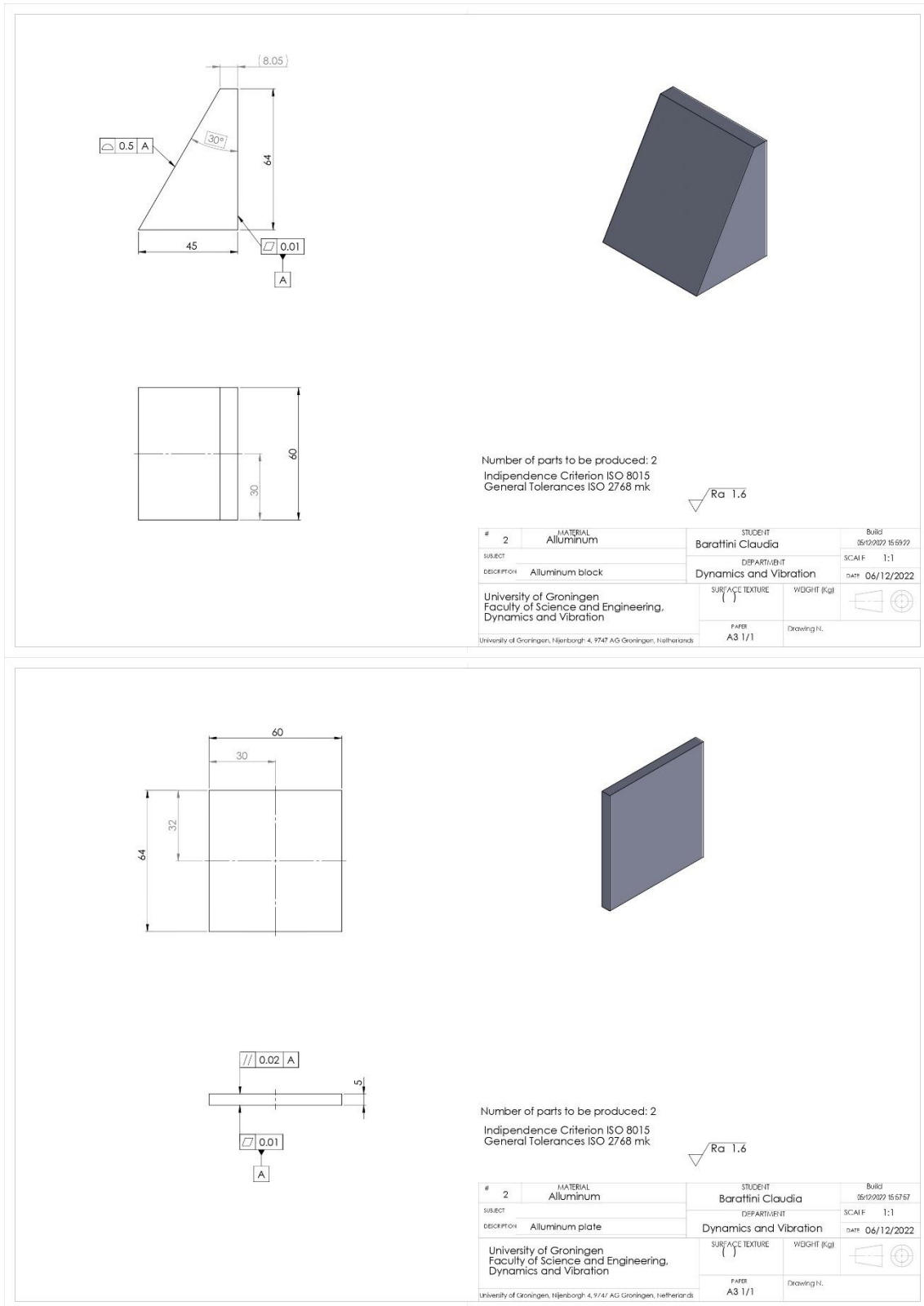


Figure A.1.1 – Drawings of the aluminium plate and block produced by the University of Groningen. Two pieces for each component are manufactured.

A.2 Drawings of the supports designed for the static test on the MTS machine

The drawings realised for the production of the supports for the static test to be performed on the MTS machine at DIMEAS, Politecnico of Torino, are below reported. The drawings were already analysed and discussed with the producers and few tolerances were edited according to the manufacturers suggestions.

In the drawings, the material indicated is steel alloy, actually a free choice was left to the producers between the steel and the aluminium alloy, depending the lowest cost.

A.2.1 Assemblies

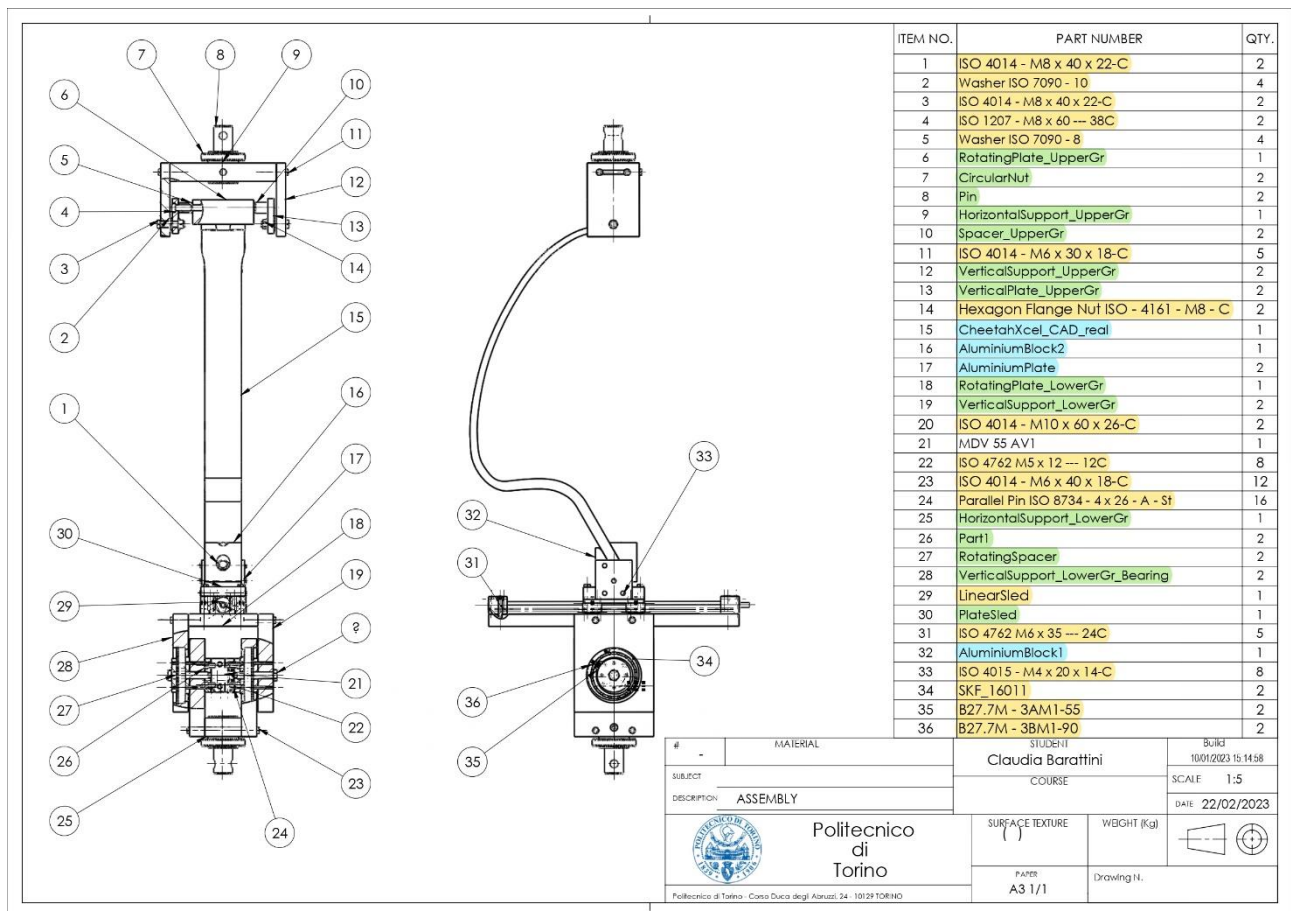


Figure A.2.2.1 – Drawing of the entire assembly. In the BOM table the elements marked in yellow are the commercial ones to buy, the ones in green have to be produced and the ones in blue have just to be drilled.

The blocks drills have to be performed positioning them in assembly with the prosthetic and drilling also the prosthetic.

Independence Criterion ISO 8015
General Tolerances ISO 2768 mk

Surface texture: $\sqrt{Ra\ 1.6}$

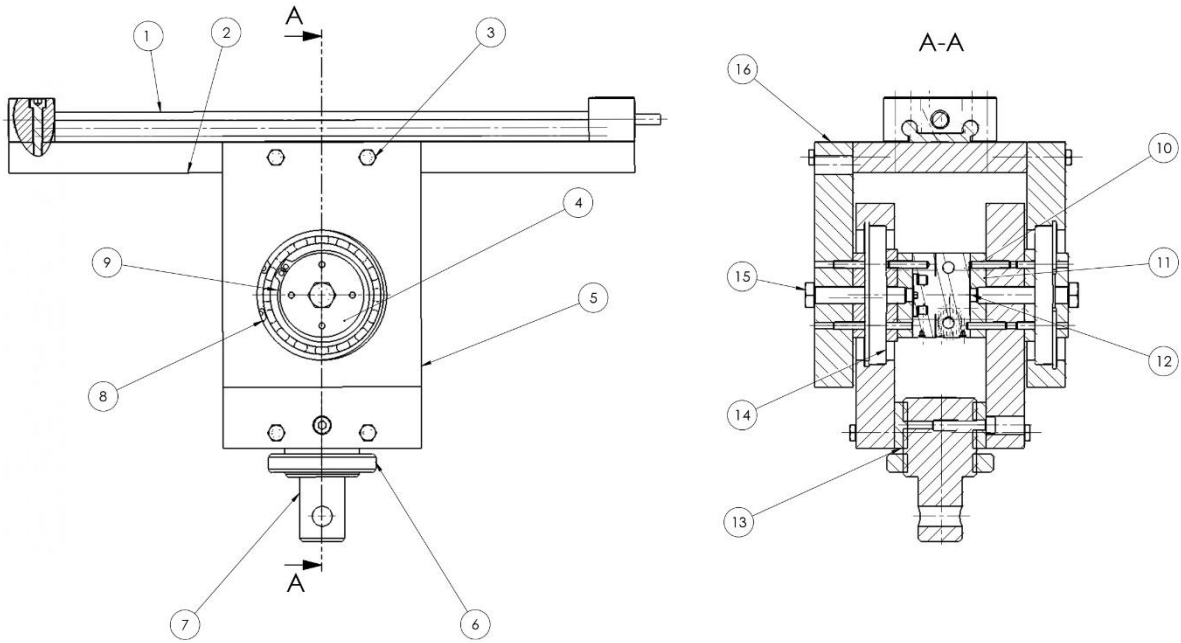
ITEM NO.	PART NUMBER	QTY.
1	CheetahXcel_CAD_real	1
2	AluminiumBlock2	1
3	AluminiumBlock1	1
4	ISO 4014 - M8 x 40 x 22-C	2

#	MATERIAL	STUDENT	BUIK3
SUBJECT		Barattini Claudia	28/12/2022 17.38.02
DESCRIPTION	ASSEMBLY_CheetahBlocks	COURSE	SCALE 1:5
Politecnico di Torino Corso Duca degli Abruzzi, 24 - 10129 TORINO		SURFACE TEXTURE	WEIGHT (Kg)
		PAPER A3 1/1	Drawing N.

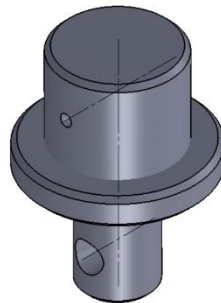
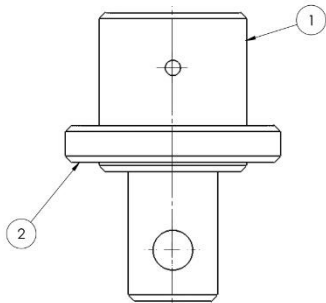
ITEM NO.	PART NUMBER	MATERIAL	Rotation of the prosthetic position/QTY.
1	HorizontalSupport_LowerGr	Steel alloy	1
2	VerticalSupport_LowerGr	Steel alloy	1
3	VerticalSupport_LowerGr_Bearing	Steel alloy	1
4	ISO 4014 - M6 x 40 x 18-C		4
5	SKF_16011		1

#	MATERIAL	STUDENT	BUIK3
SUBJECT		Claudia Barattini	21/12/2022 19.22.09
DESCRIPTION	ASSEMBLY_FixedLowerGripper	COURSE	SCALE 1:2
Politecnico di Torino Corso Duca degli Abruzzi, 24 - 10129 TORINO		SURFACE TEXTURE	WEIGHT (Kg)
		PAPER A3 1/1	Drawing N.

Appendix



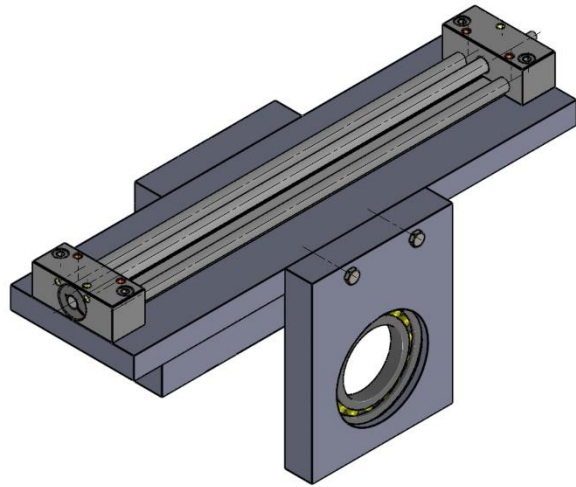
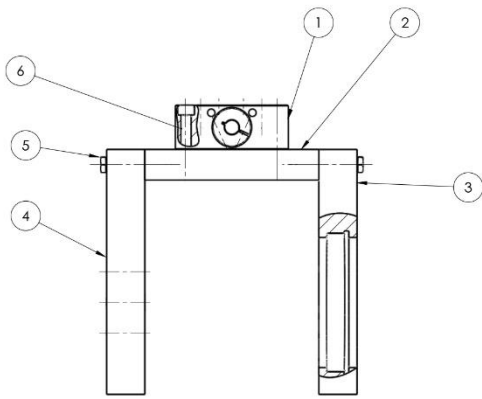
ITEM NO.	PART NUMBER	QTY.	ITEM NO.	PART NUMBER	QTY.	#	MATERIAL	STUDENT	Bulk3
1	LinearSled	1	9	B27.7M - 3AM1-55	2	-		Claudia Barattini	10/01/2023 15:14:58
2	RotatingPlate_LowerGr	1	10	Parallel Pin ISO 8734 - 4 x 26 - A - St	16	SUBJECT		COURSE	SCALE 1:2
3	ISO 4014 - M6 x 40 x 18-C	8	11	Part1	2	DESCRIPTION	ASSEMBLY_LowerGripper		DATE 21/02/2023
4	RotatingSpacer	2	12	MDV 55 AV1	1	 Politecnico di Torino	SURFACE TEXTURE	WGHT (Kg)	
5	VerticalSupport_LowerGr_Bearing	2	13	HorizontalSupport_LowerGr	1		PAPER	Drawing N.	
6	CircularNut	1	14	SKF_16011	2	A3 1/1			
7	Pin	1	15	ISO 4014 - M10 x 60 x 26-C	2	<small>Politecnico di Torino - Corso Duca degli Abruzzi, 24 - 10129 TORINO</small>			
8	B27.7M - 3BM1-90	2	16	VerticalSupport_LowerGr	2				



ITEM N.	PART NAME	MATERIAL	QTY.
1	Pin	Steel alloy	1
2	CircularNut	Steel alloy	1

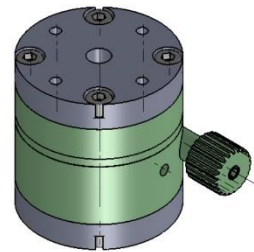
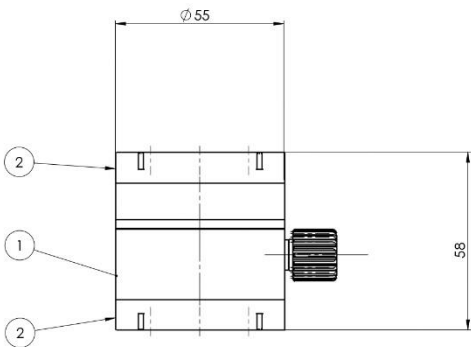
#	MATERIAL	STUDENT	Bulk3
-		Claudia Barattini	03/01/2023 11:31:59
SUBJECT		COURSE	SCALE 1:1
DESCRIPTION	ASSEMBLY_Pin		DATE 28/01/2023
 Politecnico di Torino	SURFACE TEXTURE	WGHT (Kg)	
	PAPER	Drawing N.	
<small>Politecnico di Torino - Corso Duca degli Abruzzi, 24 - 10129 TORINO</small>			

Appendix



ITEM NO.	PART NAME	MATERIAL	QTY.
1	LinearSled		1
2	RotatingPlate_LowerGr	Steel alloy	1
3	VerticalSupport_LowerGr_Bearing	Steel alloy	1
4	VerticalSupport_LowerGr	Steel alloy	1
5	ISO 4014 - M6 x 40 x 18-C		4
6	ISO 4762 M6 x 35 -- 24C	Steel alloy	4
7	SKF_16011		1

#	MATERIAL	STUDENT	Bulk3
SUBJECT		Claudia Barattini	30/12/2023 09:39:52
DESCRIPTION	ASSEMBLY_RotatingLowerGripper	COURSE	SCALE 1:2
			DATE 21/02/2023
 Politecnico di Torino <small>Politecnico di Torino - Corso Duca degli Abruzzi, 24 - 10129 TORINO</small>	SURFACE TEXTURE	WEIGHT (Kg)	
	PAPER A3 1/1	Drawing N.	



ITEM NO.	PART NAME	MATERIAL	QTY.
1	RotatingTable		1
2	Part1	Steel alloy	2

#	MATERIAL	STUDENT	Bulk3
SUBJECT		Claudia Barattini	15/01/2023 18:10:23
DESCRIPTION	ASSEMBLY_RotatingTable	COURSE	SCALE 1:1
			DATE 02/02/2023
 Politecnico di Torino <small>Politecnico di Torino - Corso Duca degli Abruzzi, 24 - 10129 TORINO</small>	SURFACE TEXTURE	WEIGHT (Kg)	
	PAPER A3 1/1	Drawing N.	

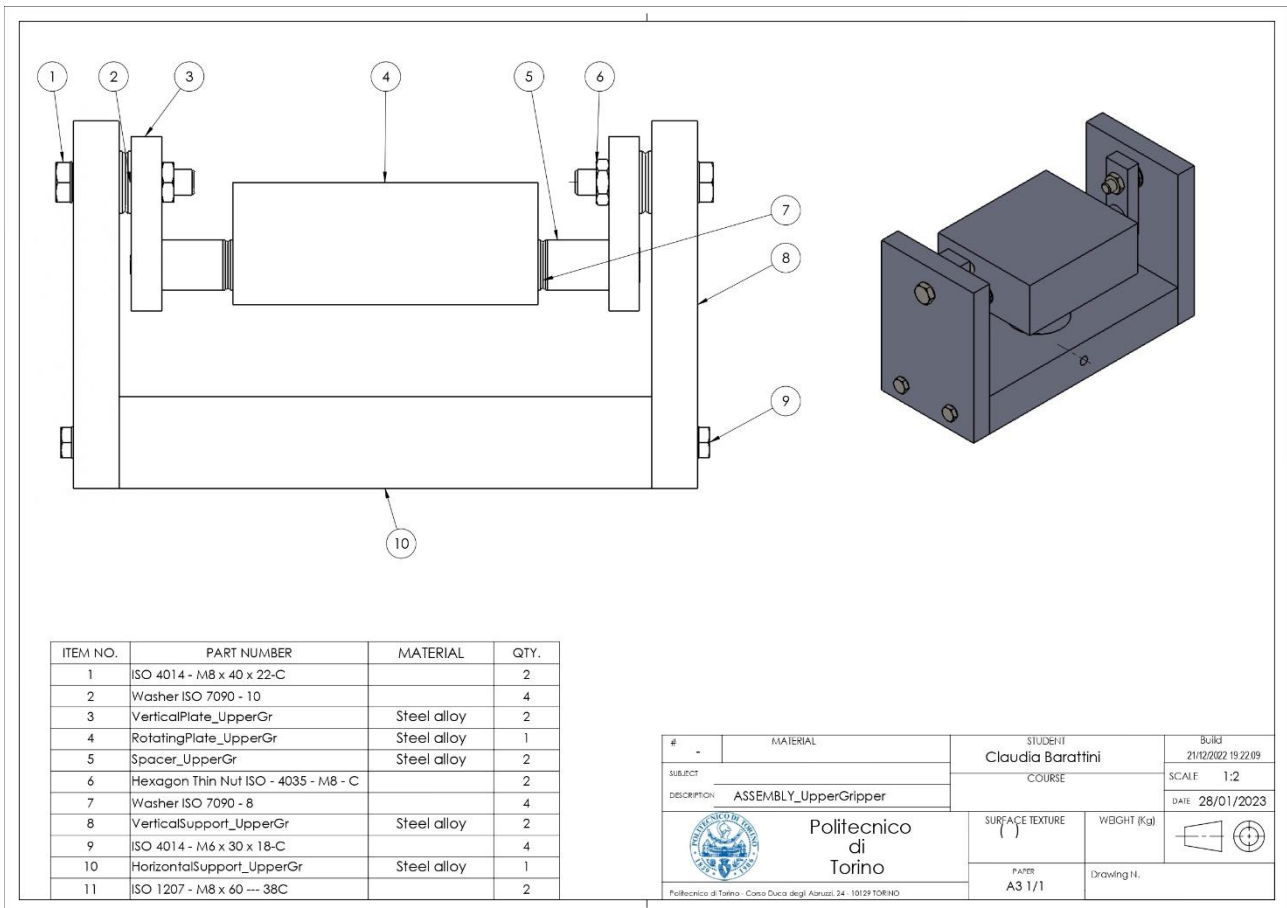
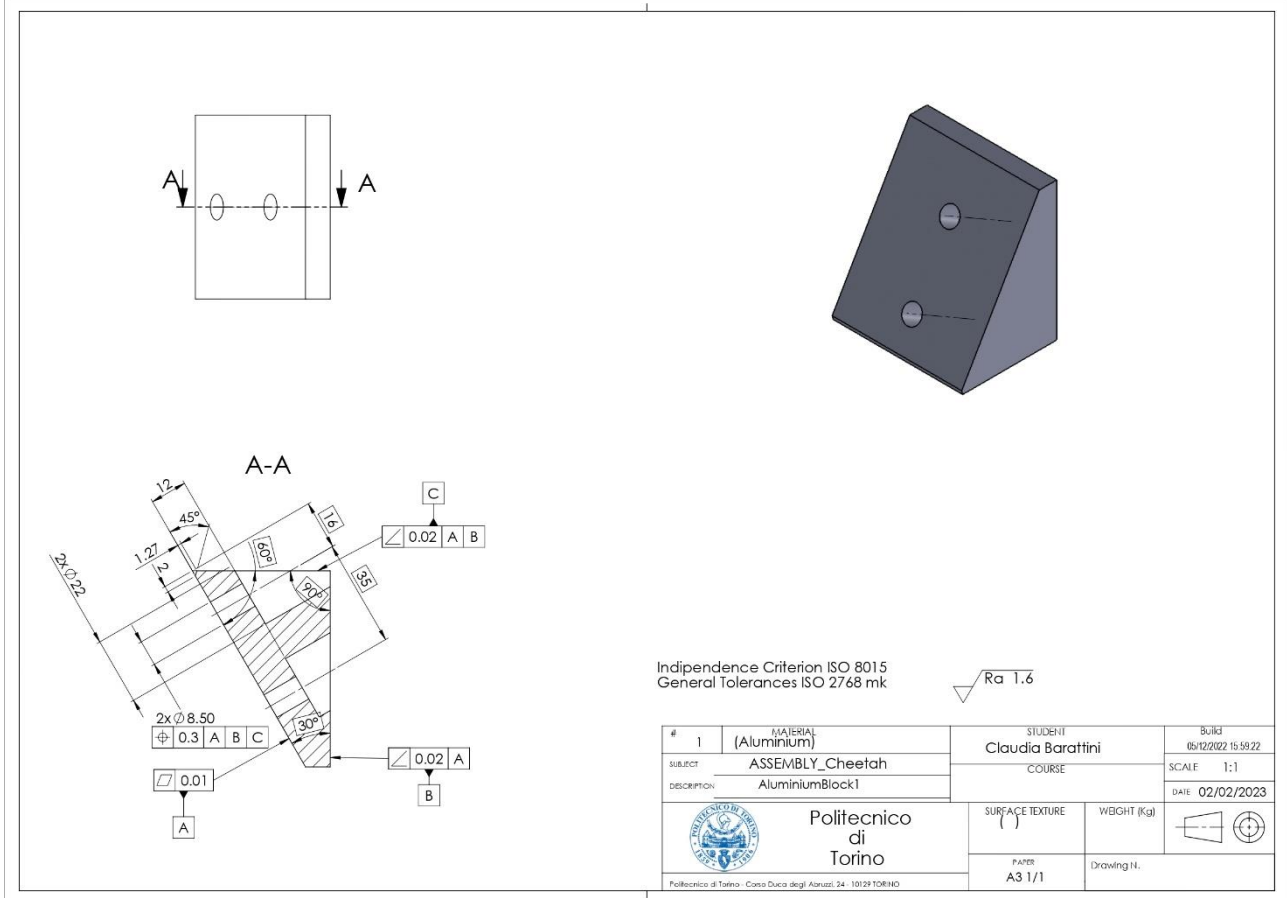
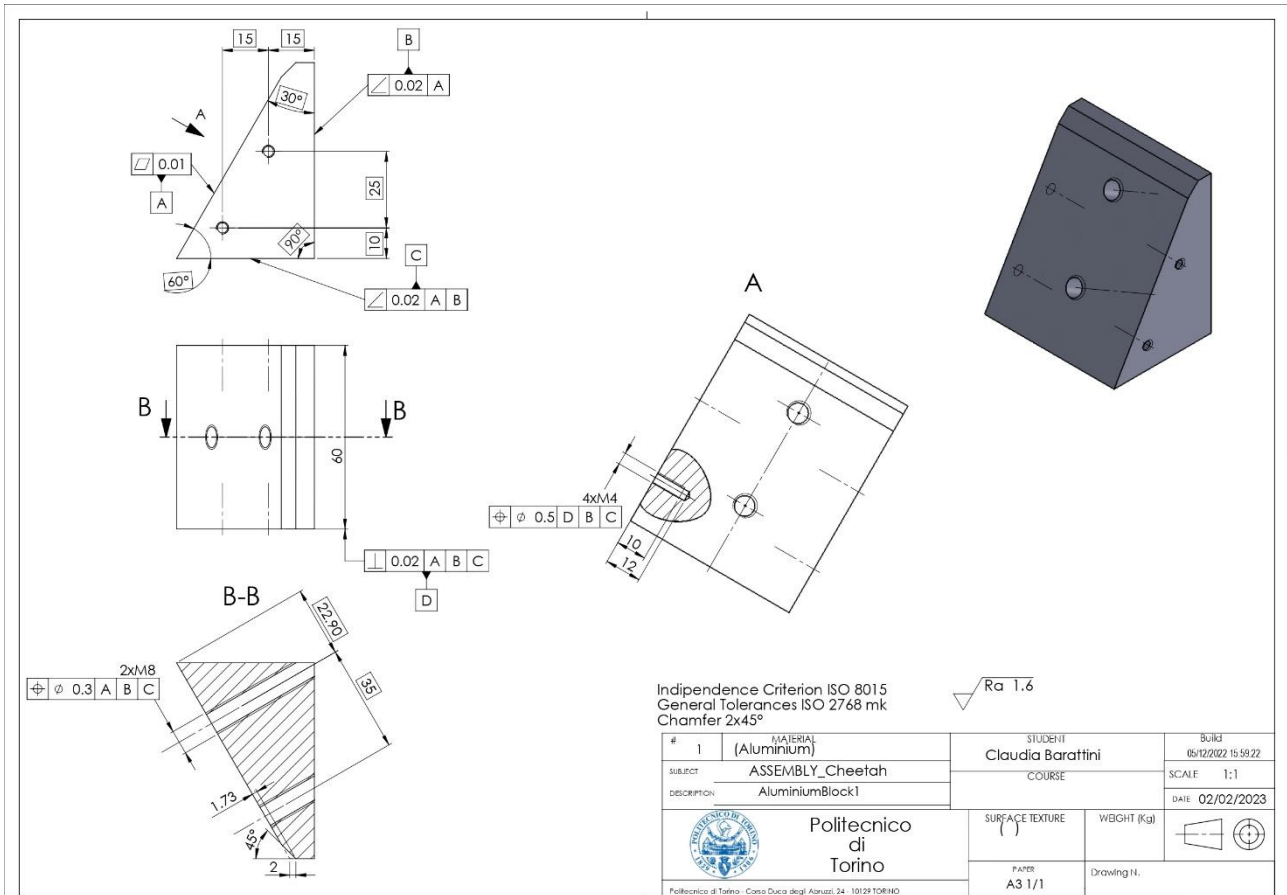


Figure A.2.1.3 – Assemblies drawings..

A.2.2 Parts to be drilled

The drawing of the holes to realise on the prosthetic are not present. Indeed, as also agreed with the manufacturer, the drills will be firstly realised on the aluminium blocks, then they will be assembled to with the prosthesis and this last will be drilled.

Appendix



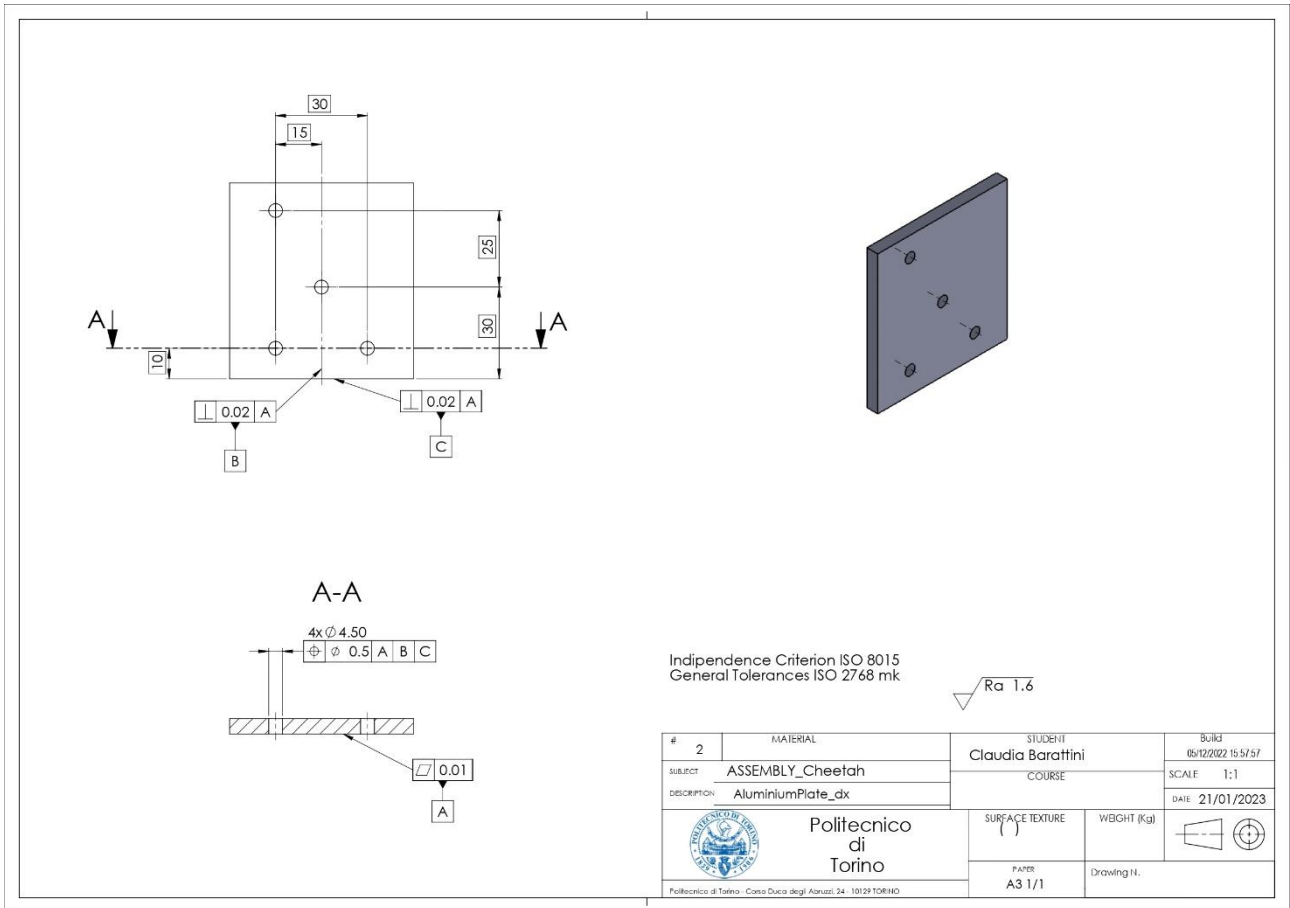
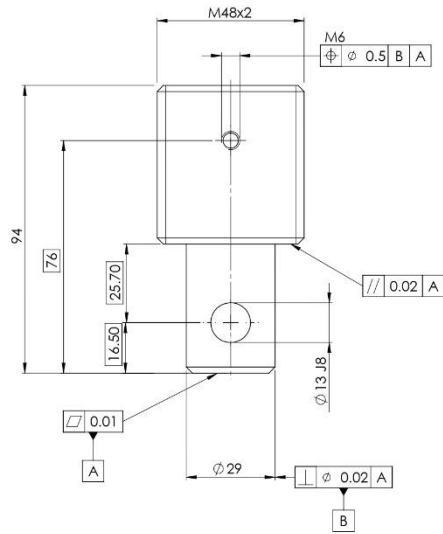


Figure A.2.2.1 – Drawings of the parts to be drilled.

A.2.3 Parts to be produced

As mentioned before, in the drawings the material indicated is steel alloy, actually a free choice was left to the producers between the steel and the aluminium alloy, depending the lowest cost.

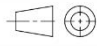
Appendix

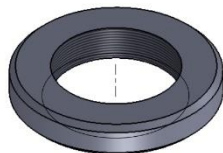
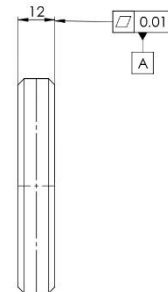
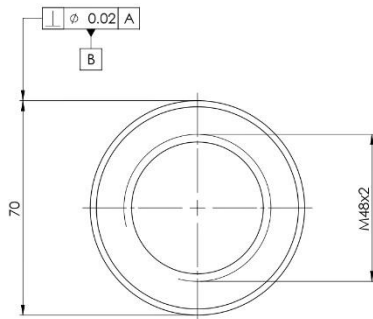


Parts to be produced: 2

Independence Criterion ISO 8015
General Tolerances ISO 2768 mk
Chamfers 2x45°

✓ Ra 1.6



#	2	MATERIAL	Steel	STUDENT	Barattini Claudia	Bulk3	21/12/2022 15:55:49
SUBJECT	Upper and lower Grippers			COURSE		SCALE	1:1
DESCRIPTION	Pin					DATE	02/02/2023
 Politecnico di Torino Corso Duca degli Abruzzi, 24 - 10129 TORINO				SURFACE TEXTURE	()	WEIGHT (Kg)	
				PAPER	A3 1/1	Drawing N.	



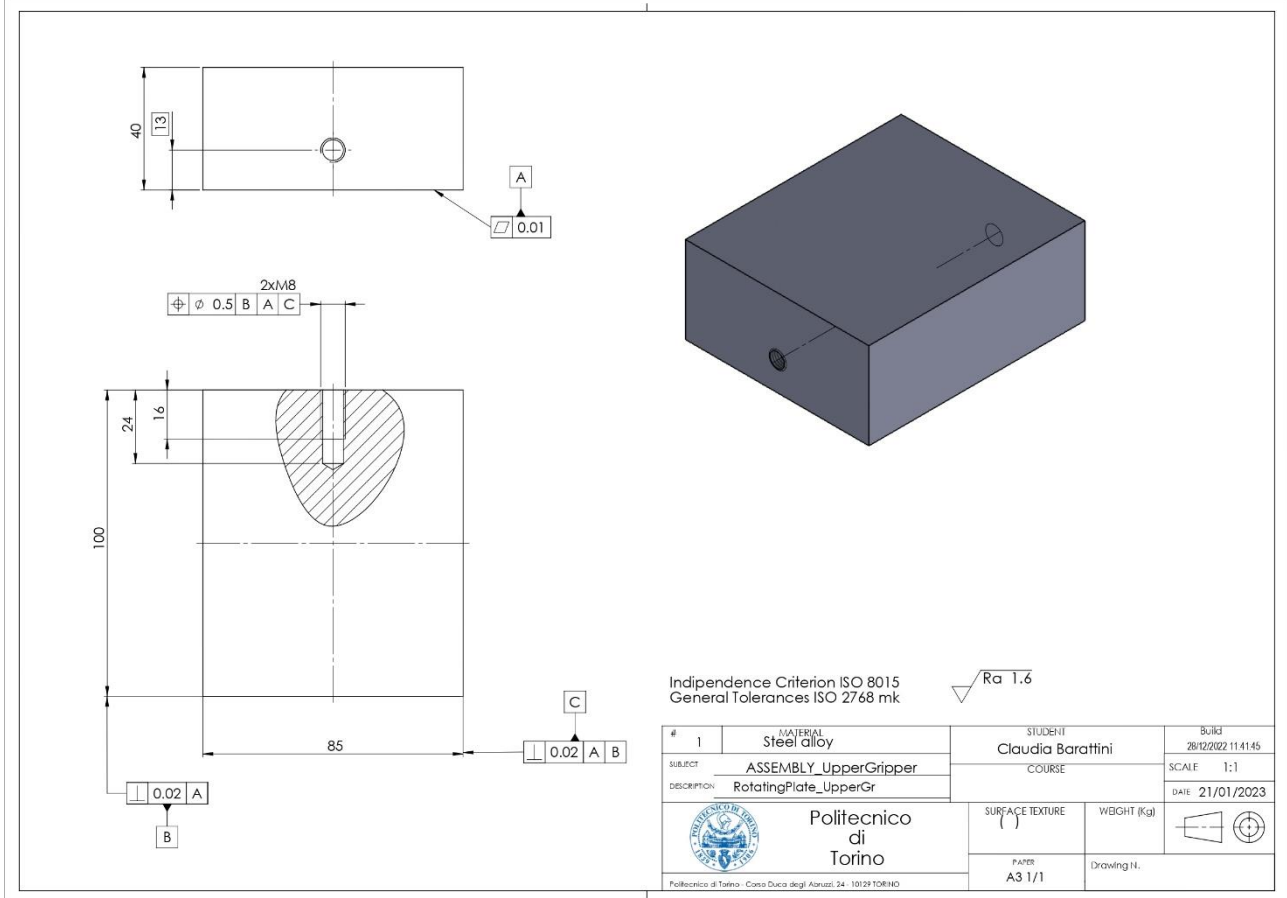
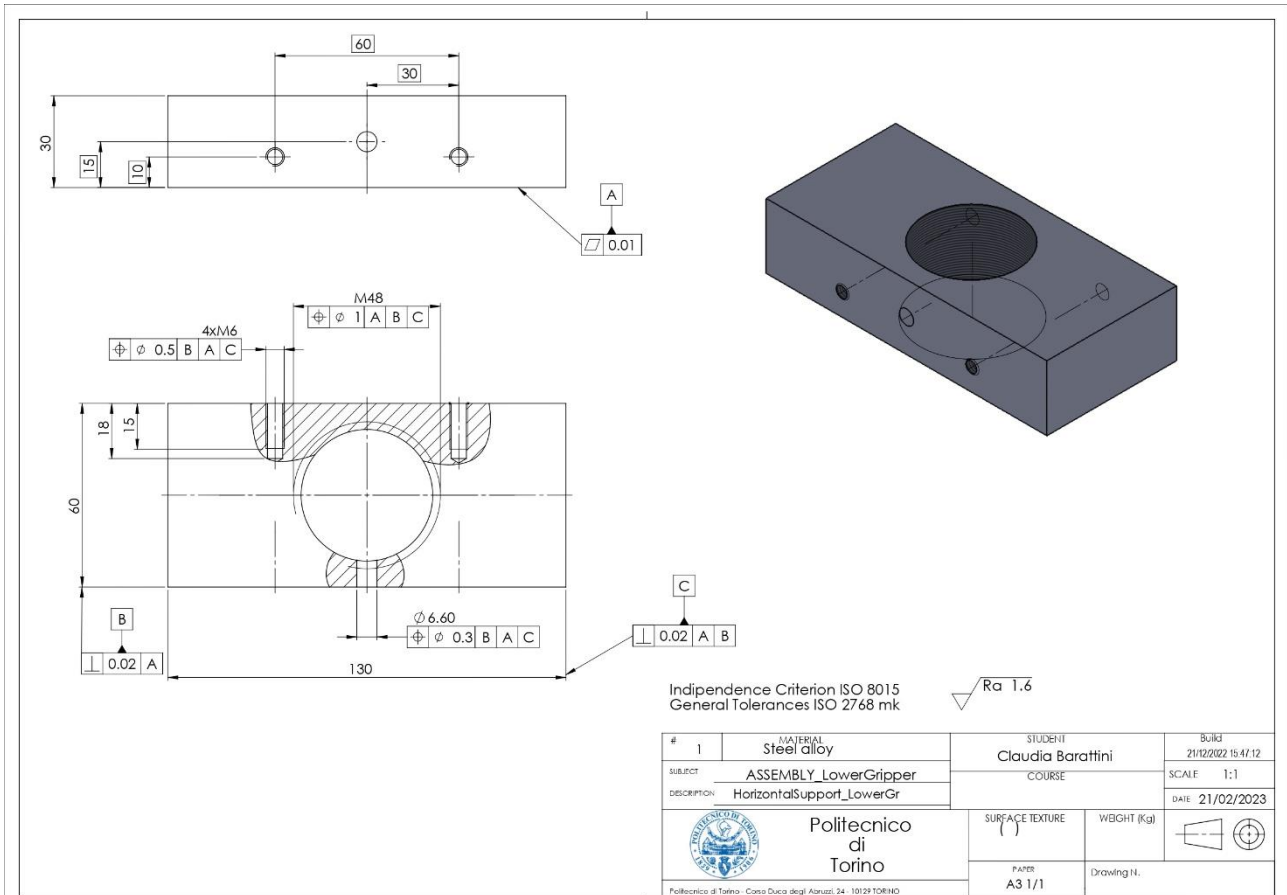
Number of parts to be produced: 2

Independence Criterion ISO 8015
General Tolerances ISO 2768 mk
Chamfers 2x45°

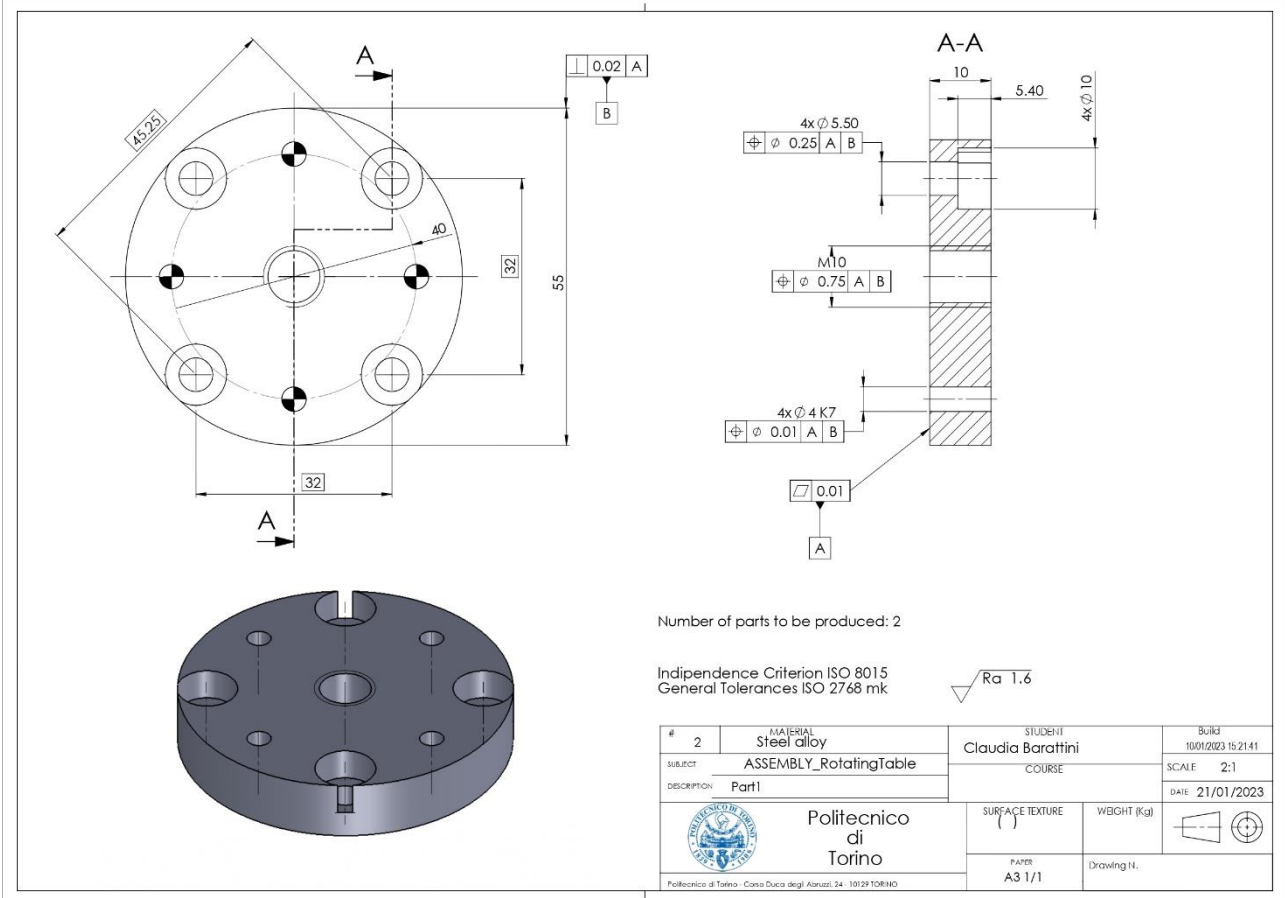
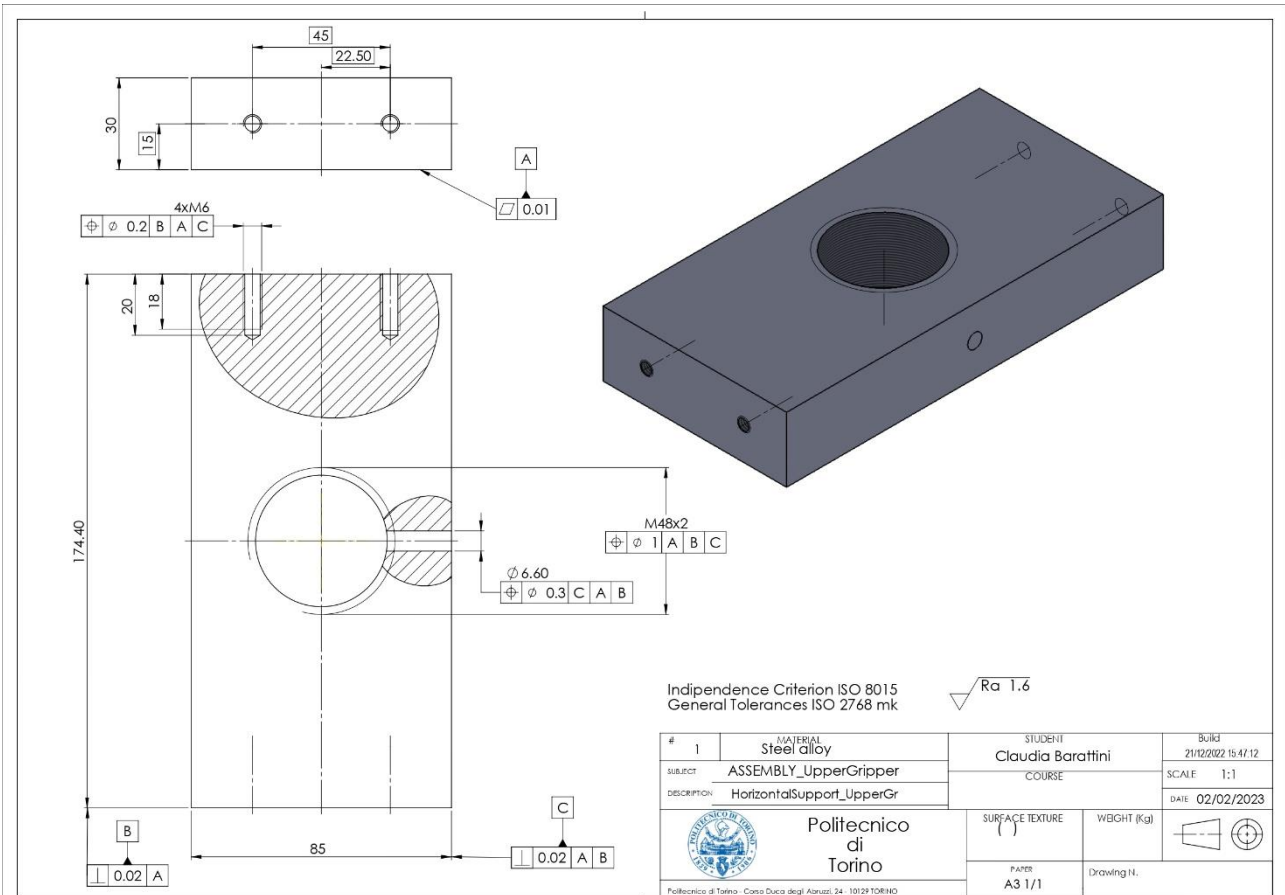
✓ Ra 1.6

#	2	MATERIAL	Steel alloy	STUDENT	Claudia Barattini	Bulk3	21/12/2022 15:26:23
SUBJECT	Upper and lower grippers			COURSE		SCALE	1:1
DESCRIPTION	CircularNut					DATE	02/02/2023
 Politecnico di Torino Corso Duca degli Abruzzi, 24 - 10129 TORINO				SURFACE TEXTURE	()	WEIGHT (Kg)	
				PAPER	A3 1/1	Drawing N.	

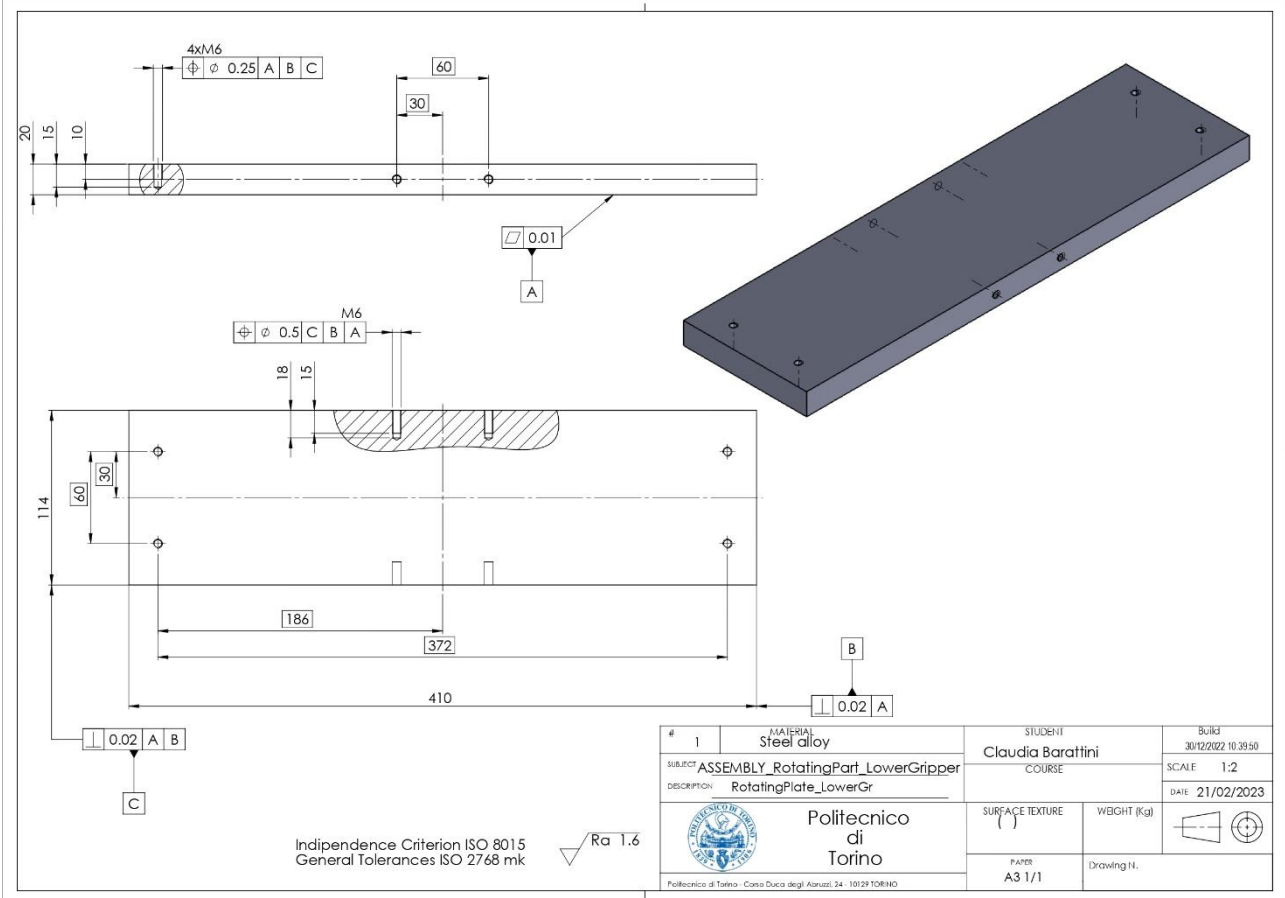
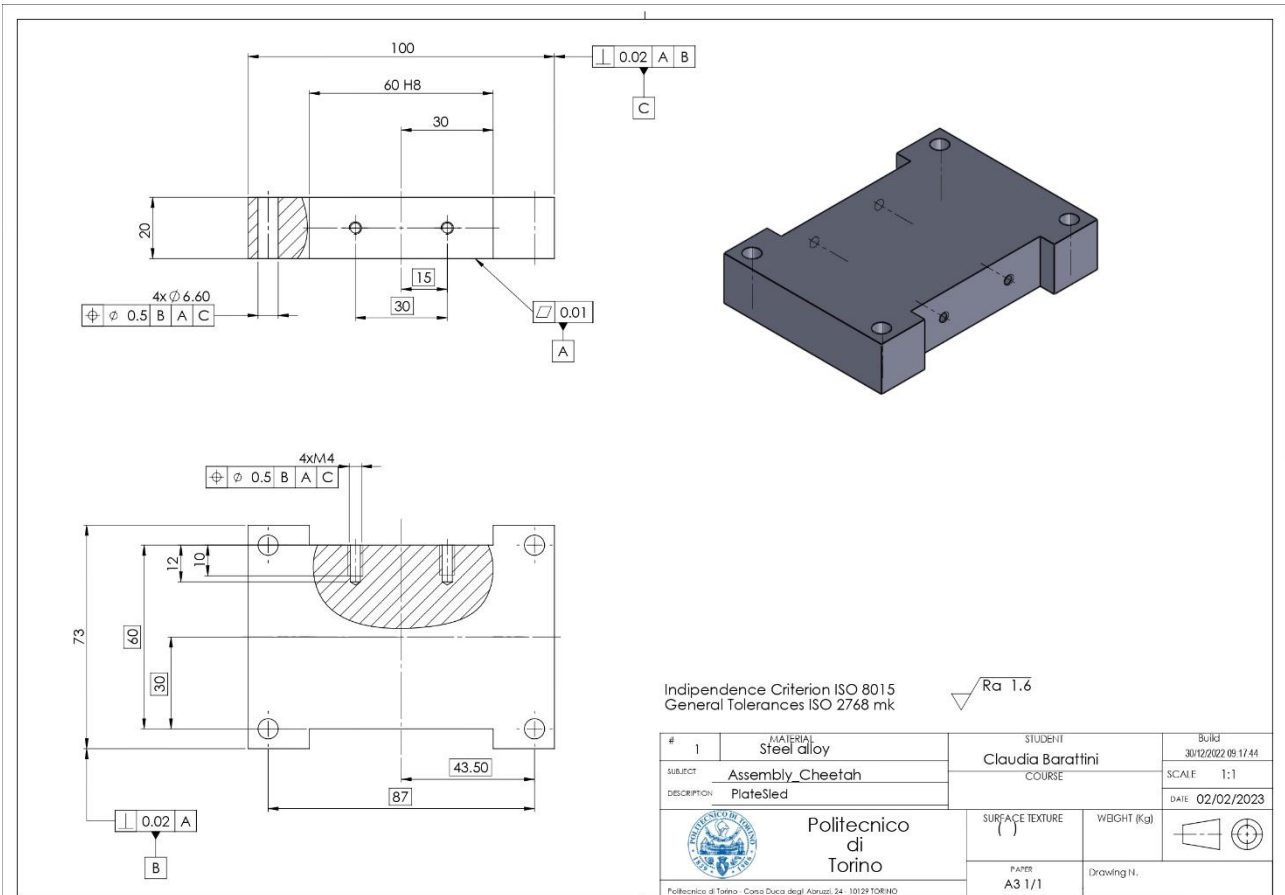
Appendix



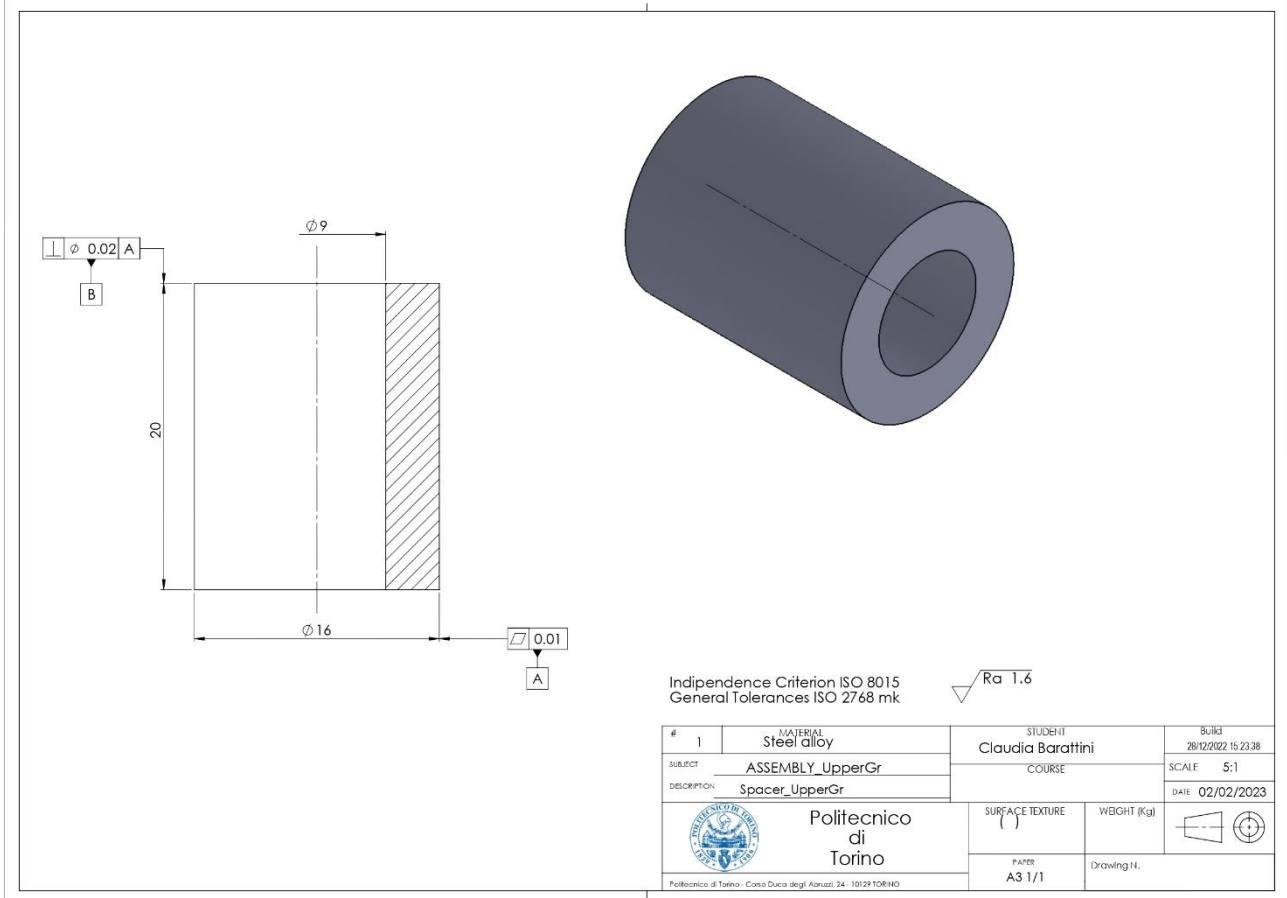
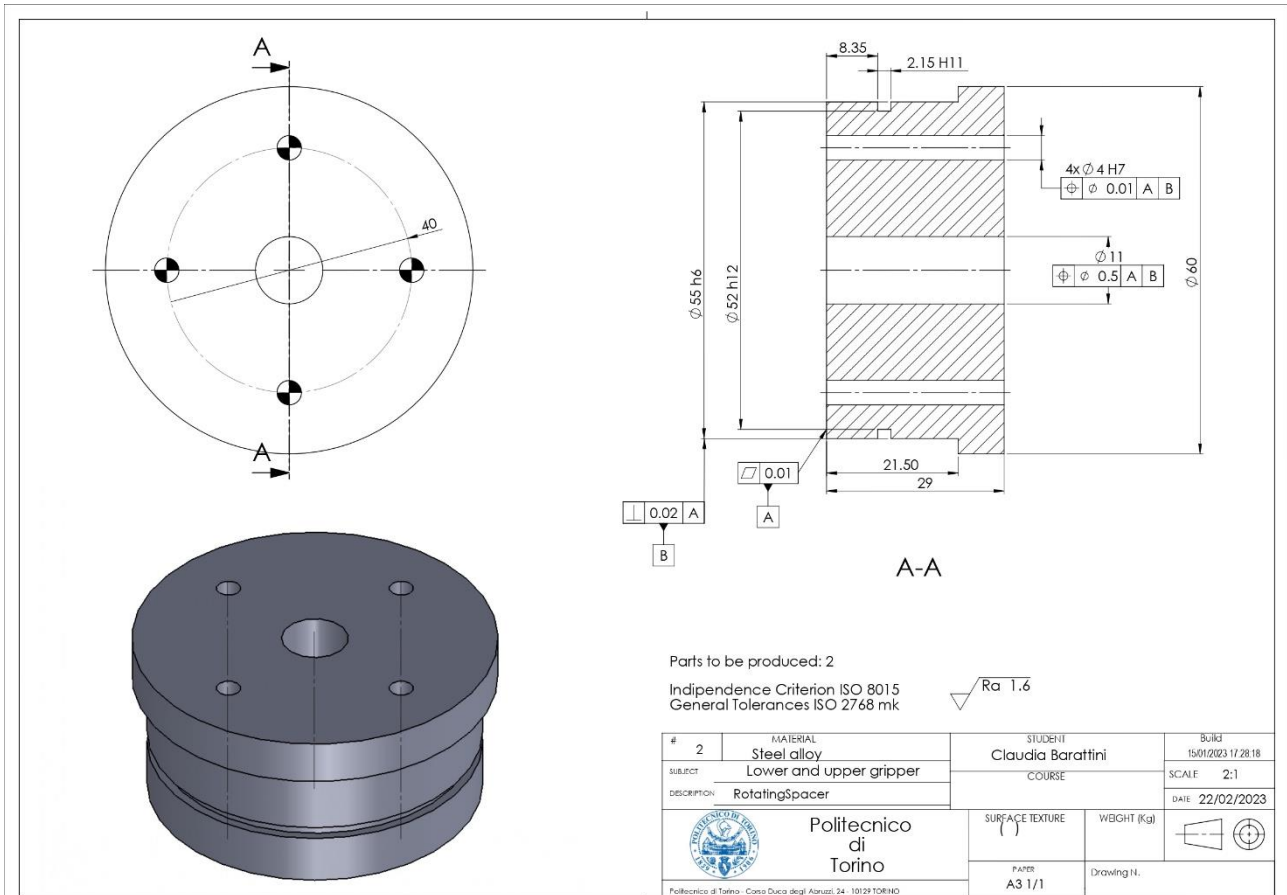
Appendix



Appendix



Appendix



Appendix

Technical drawing of a vertical plate with two holes. The top view shows a width of 27 and a hole spacing of 13.50. The side view shows a total length of 57, a hole diameter of 9, and a bottom flange with a diameter of 15 and a thickness of 5. Surface texture is Ra 1.6. Tolerances are specified for various features.

Independence Criterion ISO 8015
General Tolerances ISO 2768 mk

# 1	MATERIAL Steel alloy	STUDENT Claudia Barattini	BUK3 28/12/2022 09:52:00
SUBJECT	ASSEMBLY_UpperGripper	COURSE	SCALE 2:1
DESCRIPTION	VerticalPlate_UpperGr		DATE 21/01/2023
 Politecnico di Torino <small>Politecnico di Torino - Corso Duca degli Abruzzi, 24 - 10129 TORINO</small>	SURFACE TEXTURE ()	WEIGHT (Kg)	
	PAPER A3 1/1	Drawing N.	

Technical drawing of a vertical support plate with four holes. The top view shows a width of 160 and a hole spacing of 130. The side view shows a total height of 110, a hole diameter of 11, and a bottom flange with a diameter of 12 and a thickness of 25. Surface texture is Ra 1.6. Tolerances are specified for various features.

Number of parts to be produced: 2
Independence Criterion ISO 8015
General Tolerances ISO 2768 mk

# 2	MATERIAL Steel alloy	STUDENT Claudia Barattini	BUK3 28/12/2022 10:01:59
SUBJECT	ASSEMBLY_LowerGripper_Rotating and not rotating	COURSE	SCALE 1:2
DESCRIPTION	VerticalSupport_LowerGr		DATE 22/02/2023
 Politecnico di Torino <small>Politecnico di Torino - Corso Duca degli Abruzzi, 24 - 10129 TORINO</small>	SURFACE TEXTURE ()	WEIGHT (Kg)	
	PAPER A3 1/1	Drawing N.	

Appendix

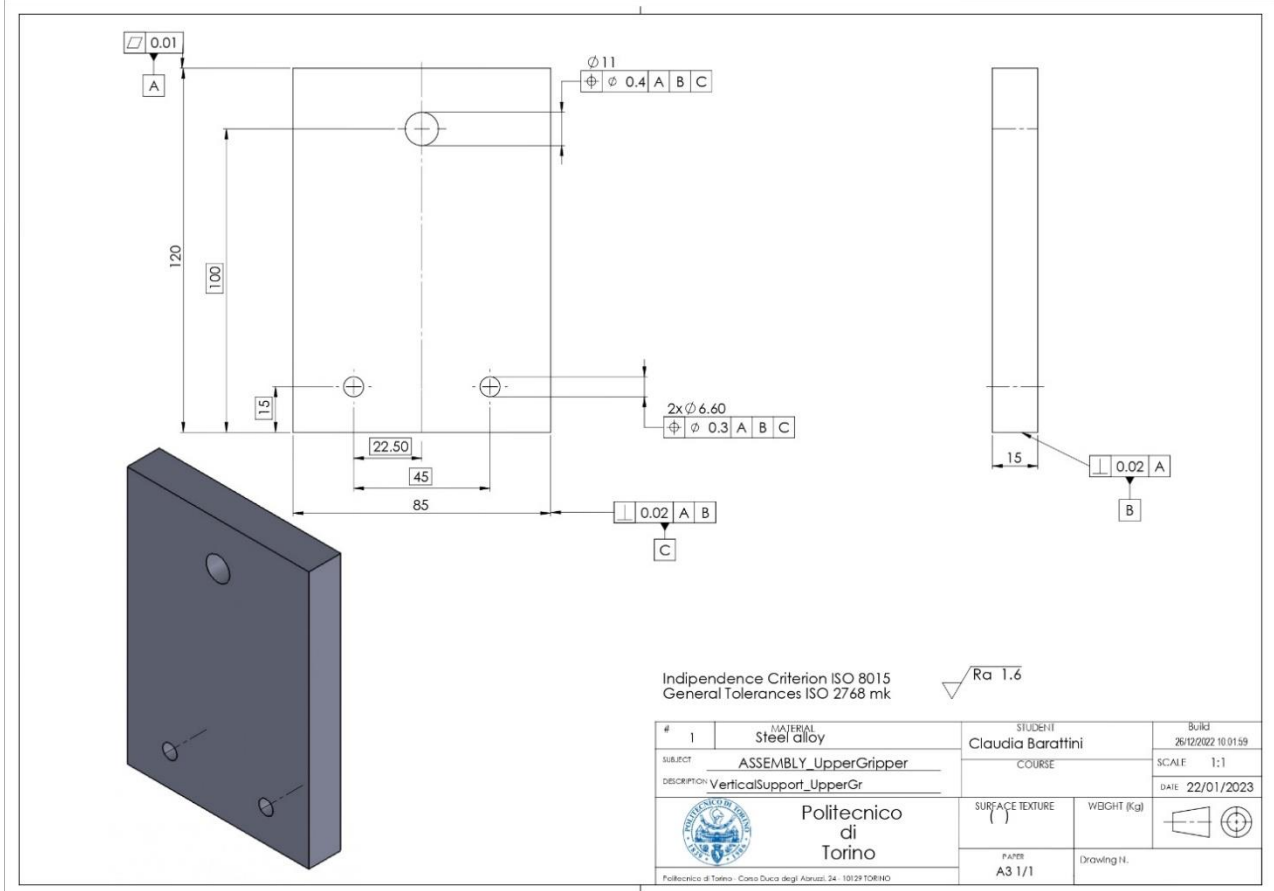
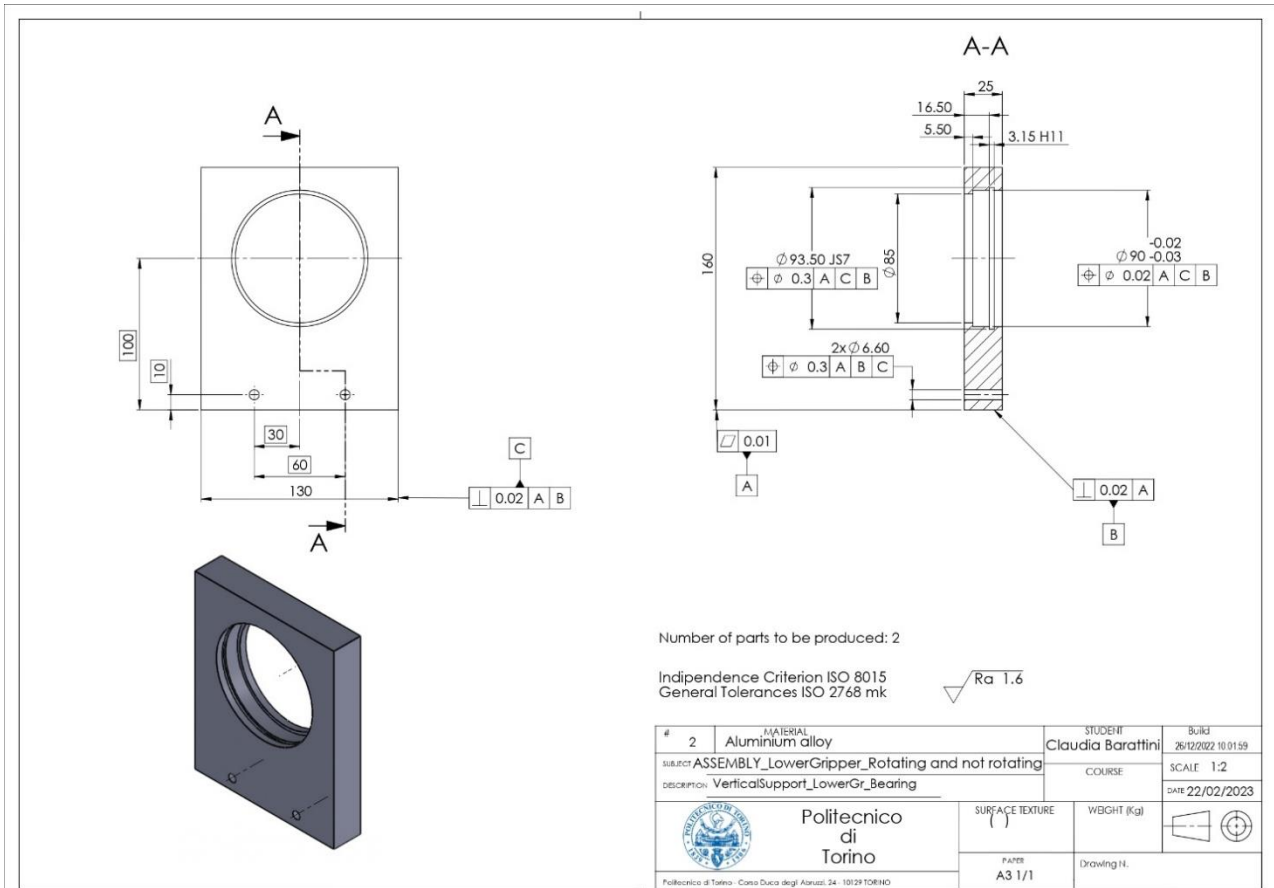


Figure A.2.3.1 – Drawings of the parts to be produced.

Reference

- [1] Bonisoli E., “LUPOS Lumped Parameters Open Source FEM code”, PoliTo, DIMEAS, 2022-09-16.
Lupos_Tutorial_2022-09-16.pdf
- [2] Godfrey B. S., Pechman K. M., Lau T. M., “Lower Limb Prosthetics”, American Academy of Physical Medicine and Rehabilitation, 20 September 2013.
<https://now.aapmr.org/lower-limb-prosthetics/>, available: 2022-11-06
- [3] Catto E., *Realization and evaluation of a prosthetic foot*, Mater Thesis, Politecnico di Torino, Italy, 2019.
Catto_Realization and evaluation of a prosthetic foot_MMS2019.pdf
- [4] Chan C. W., Rudins A., “Foot Biomechanics During Walking and Running,” *Mayo Clin Proc*, vol. 69, pp. 448-461, 1994.
Chan,Rudins_Foot biomechanics during walking and running_1994.pdf
- [5] Hansen A. H., Meier M. R., Sessoms P. H., Childress D. S., “The effects of prosthetic foot roll-over shape arc length on the gait of trans-tibial prosthesis users”, *Journal of Prosthetics and Orthotics*, 16 (2), April 2004, pp. 41-45.
<https://doi.org/10.1080/03093640600816982>, available in 2022-11-04, PMID: 17162519
- [6] Koehler-McNicholas S., Nickel E., Barrons K., Blaharski K., Dellamano C., Ray S., Schnall B., Hendershot B., Hansen A., “Mechanical and dynamic characterization of prosthetic feet for high activity users during weighted and unweighted walking”, 2018.
<https://journals.plos.org/plosone/article?id=10.1371/journal.pone.0202884> available in 2022-11-03
- [7] Hansen A. H., Childress D. S., “Investigations of roll-over shape: implications for design, alignment, and evaluation of ankle-foot prostheses and orthoses”, *Disability and Rehabilitation*, 32(26), November 26, 2010, pp. 2201–2209.
- [8] International Standards Organisation. Prosthetics - Structural testing of lower- limb prostheses - requirements and test methods. ISO 10328:20 0620 06.
- [9] Takahashi K. Z., Kepple T. M., Stanhope S. J., “A unified deformable (UD) segment model for quantifying total power of anatomical and prosthetic below-knee structures during stance in gait”, *J Biomech*, 45 (15), 2012, pp 2662–2667.
<https://doi.org/10.1016/j.jbiomech.2012.08.017>, available on 2022-11-04, PMID: 22939292
- [10] Tabucol J.,Brugo T. M.,Povolo M.,Leopaldi M.,Oddsson M.,Carloni R.,Zucchelli A., “Structural FEA-based design and functionality verification methodology of energy-storing-and releasing prosthetic feet”, *Applied Sciences*, Switzerland, 2021.
<https://doi.org/10.3390/app12010097> available 2022-11-07
- [11] Tryggvason H., Starker F., Lecomte C., Jonsdottir F., “Use of dynamic FEA for design modification and energy analysis of a variable stiffness prosthetic foot”, University of Iceland, Reykjavík, Iceland, 16 January 2020.
Tryggvason,Starker,Lecomte,Jonsdottir_Use of dynamic FEA for design modification and energy analysis of a variable stiffness prosthetic foot_2020.pdf
- [12] Rigneya S. M., Simmons A., Karka L., “Mechanical characterization and comparison of energy storage and return prostheses”, *Medical Engineering and Physics*, 41, 2017, pp 90–96.
Rigneya,Simmons,Karka_Mechanical characterization and comparison of energy storage and return prostheses_2017.pdf

- [13] Beck N. B., Taboga P., Grabowski A. M., “Characterizing the mechanical properties of running-specific prostheses”, Steven Allen Gard, Northwestern University, US, December 2016.
DOI:10.1371/journal.pone.0168298
- [14] Dyer B. J. D., Sewell P., Noroozi S., “An investigation into the measurement and prediction of mechanical stiffness of lower limb prostheses used for running”, *The Official Journal of RESNA*, 26 (3), 2014, pp 157-163.
DOI: 10.1080/10400435.2014.888599
<http://dx.doi.org/10.1080/10400435.2014.888599> available on the 2022-11-16
- [15] Nakayama H., Takahashi Y., Tanaka K., “Measurement of dynamic behavior of running-specific prostheses by an impact test”, 13th conference of the International Sports Engineering Association, 15 June 2020.
<https://www.mdpi.com/2504-3900/49/1/145/htm>
- [16] Noroozi S., Ong Z. C., Khoo S. Y., Aslani N., Sewell P., “Dynamic characterisation of Össur Flex-Run prosthetic feet for a more informed prescription”, *Prosthetics and Orthotics International*, 43(1), 2019, pp 62-70.
DOI: 10.1177/0309364618789449
- [17] Noroozi S., Sewell P., Rahman A. G. A., Vinney J., Chao O. Z., Dyer B., “Modal analysis of composite prosthetic energy-storing-and-returning feet: an initial investigation”, *Journal of Sports Engineering and Technology* , 227 (1), March 2013, pp 39-48.
DOI: 10.1177/1754337112439274
- [18] Ossur, Technical Presentation, Cheetah Xcel.
Ossur, Cheetah Xcel_Technical Presentation.pdf
- [19] Ossur sport solutions, pp. 275-578.
Ossur sport solutions, Cheetah Xcel_Technical information.pdf
- [20] Ossur, Instructions for use, Alignment adapters.
Ossur, Cheetah Xcel_Alignment adapters.pdf
- [21] Ossur, Instructions for use.
Ossur, Cheetah Xtreme_Instructions for Use.pdf
- [22] “LMS Test.Lab Modal Analysis”, LMS.
- [23] “LMS Test.Lab Modal Impact”, LMS.
- [24] S. Toledo, “NX Nastran User's Guide”, Siemens, MSC.Software Corporation, 2001.
- [25] “MSC.Nastran 2017_Quick reference guide”, MSC.Software Corporation, 2016-11-25.
- [26] Duleba B., Dulebová L’U, Spišák E., “Simulation and evaluation of carbon/epoxy composite systems using FEM and tensile test”, *Procedia Engineering* 96, 2014, pp. 70 – 74.
DOI: <https://doi.org/10.1016/j.proeng.2014.12.099>.
- [27] “Datasheet_Carbon/Epoxy Composite”, RS company.
RS company_Datasheet_Carbon-epoxy composite.pdf
- [28] Mechanical Properties of Carbon Fibre Composite Materials, Fibre / Epoxy resin (120°C Cure), Performance Composites Ltd.
http://www.performance-composites.com/carbonfibre/mechanicalproperties_2.asp available on the 2023-03-31
- [29] Gojny K., Dacko A., “Investigation of finite element (FE) modelling of composite materials: shell, solid and solid layered composite modelling – comparison of impact on simulation results”, *Polish Society of Composite Materials*, 21: 1-2, 2021, pp. 29-39
- [30] “Composite modeling_Handbook for FEMAP”, NX Nastran and LS-DYNA_2020.

Composite modeling_Handbook for FEMAP_NX Nastran and LS-DYNA_2020.pdf

- [31] Guseinov K., Kudryavtsev O., Bezmelnitsyn A. and Sapozhnikov S., “Determination of interlaminar shear properties of fibre-reinforced composites under biaxial loading a new experimental approach”, *Polymers* 2022, 14 (13), 2575.
DOI: <https://www.mdpi.com/2073-4360/14/13/2575>
- [32] Yin H., Li Q., Iannucci L., “Meso-scale Finite Element (FE) modelling of biaxial carbon fibre non-crimp-fabric (NCF) based composites under uniaxial tension and in-plane shear”, *Composite Structures* 290, 15 June 2022, 115538.
- [33] AL-Zubaidy H., Zhao X.-L., Al-Mihaidi R., “Mechanical behaviour of normal modulus carbon fibre reinforced polymer (CFRP) and epoxy under impact tensile loads”, *Procedia Engineering* 10, 2011, pp. 2453–2458.
- [34] Jin H., Lu W.-Y., Nelson K., Nissen A., Briggs T., “Mechanical properties of woven composites at ambient temperature”, Sandia National Laboratories, 2018.
- [35] Noroozi S., Sewell P., Rahman A. G. A., Vinney J., Chao O. Z., Dyer B., “Modal analysis of composite prosthetic energy-storing-and-returning feet: an initial investigation”, *Journal of Sports Engineering and Technology* , 227 (1), March 2013, pp 39-48.
DOI: 10.1177/1754337112439274
- [36] D’Imperio S., *Violin mode shapes parametric analysis*, Master Thesis, Politecnico di Torino, Italy, 2016/2017.
DImperio_Violin mode shapes parametric analysis_BSc2017.pdf
- [37] Paolino D., *Introduction Lightweight, Design of lightweight and composite structures*, DIMEAS Politecnico di Torino, Italy, 2022.
Paolino_Introduction Lightweight_Design of lightweight and composite structures.pdf
- [38] Paolino D., *Micromechanics, Design of lightweight and composite structures*, DIMEAS Politecnico di Torino, Italy, 2022.
Paolino_Micromechanics_Design of lightweight and composite structures.pdf
- [39] Paolino D., *Lamina, Design of lightweight and composite structures*, DIMEAS Politecnico di Torino, Italy, 2022.
Paolino_Lamina_Design of lightweight and composite structures.pdf
- [40] Paolino D., *Laminate, Design of lightweight and composite structures*, DIMEAS Politecnico di Torino, Italy, 2022.
Paolino_Laminate_Design of lightweight and composite structures.pdf
- [41] Paccola R., Sampaio M., Coda H., “Continuous stress distribution following transverse direction for FEM orthotropic laminated plates and shells”, *Applied Mathematical Modelling*, 40, 2016, pp. 7382–7409.
- [42] Kaddaha M. A. , Younes R., Lafon P., “Homogenization method to calculate the stiffness matrix of laminated composites”, *MDPI*, 2, 2021, pp. 416-434.
<https://doi.org/10.3390/>
- [43] “Running Blades and their evolution”, Public Paralympic Heritage Trust.
<https://www.paralympicheritage.org.uk/running-blades-and-their-evolution#:~:text=Modern%20running%20blades%20are%20made,carbon%20fibre%20are%20fused%20together.> available on the 2023-02-31.
- [44] Küsefoğlu S., “Carbon fiber / epoxy composites: ideal materials for orthopedic prosthetics.”, *Kodsa, The reinforcer blog*.
<https://www.reinforcer.com/en/category/detail/Carbon-Fiber-Epoxy-Composites-Ideal-Materials-for-Orthopedic-Prosthetics->

Reference

/46/235/0#:~:text=Conventional%20wood%2C%20fiberglass%2Fpolyester%20composites,also%20be%20used%20in%20prosthetics. available on the 2023-03-31

- [45] Mei C., “Global and local wave vibration characteristics of materially coupled composite beam structures”, *Journal of Vibration and Control*, 11, 11, 2005, pp. 1413–1433.
DOI: 10.1177/1077546305058651
- [46] Mei C., “Effect of material coupling on wave vibration of composite Timoshenko beams”, *Journal of Vibration and Control*, 127, 4, 2005, pp. 333–340.
DOI: 10.1115/1.1924641
- [47] Chen W. H., Gibson R. F., “Property distribution determination for nonuniform composite beams from vibration response measurements and Galerkin's method”, *Journal of Applied Mechanics*, 65, March 1998, pp. 127-133.
- [48] Reid S. R., Zhou G., *Impact behaviour of fibre-reinforced composite materials and structures*, Woodhead Publishing Ltd and CRC Press LLC, 2000.
- [49] Gibson R. F., “Modal vibration response measurements for characterization of composite materials and structures”, *Composite Science and Technology*, 60, 2000, pp. 2769-2780.
- [50] Berthea J., Deletombe E., Brieva M., Portemontb G., Paulmier P., “Dynamic characterization of CFRP composite materials – Toward a pre-normative testing protocol – Application to T700GC/M21 material”, *Procedia Engineering*, 80, 2014, pp. 165-182.
- [51] Gurdal Z., B.F. Tatting B. F., Wuc C. K., “Variable stiffness composite panels: Effects of stiffness variation on the in-plane and buckling response”, *Composites, A* 39, 2008, pp. 911-922.
- [52] Cuadrado M., Pernas-Sánchez J., Artero-Guerrero J.A., Varas D., “Model updating of uncertain parameters of carbon/epoxy composite plates using digital image correlation for full-field vibration measurement”, *Measurement*, 159, 2020, 107783.
<https://doi.org/10.1016/j.measurement.2020.107783>
- [53] Molina-Viedma A., López-Alba E., Felipe-Sesé L., Díaz F., “Full-field operational modal analysis of an aircraft composite panel from the dynamic response in multi-impact test”, *Sensors*, 21, 1602, 2021.
<https://doi.org/10.3390/s21051602>
- [54] Menard K. P., *Dynamic mechanical analysis: a practical introduction*, CRC Press LLC, Florida, 2000.
- [55] Fouad H., Mourad A.-H. I., ALshammari B. A., Hassan M. K., Abdallah M. Y., Hashem M., “Fracture toughness, vibration modal analysis and viscoelastic behavior of Kevlar, glass, and carbon fiber/epoxy composites for dental-post applications”, *Journal of the mechanical behavior of biomedical materials*, 101, 103456, 2020.
<https://doi.org/10.1016/j.jmbbm.2019.103456>
- [56] Kim J. Y., Guon J., Lee B. H., “Dispersive wave propagation in a viscoelastic matrix reinforced by elastic fibers”, *The Journal of the Acoustical Society of America*, 95, 1213, (1994).
DOI: 10.1121/1.408565
- [57] Naresh K., Khan K. A., Umer R. and Vasudevan A., “Temperature-frequency–dependent viscoelastic properties of neat epoxy and fiber reinforced polymer composites: experimental characterization and theoretical predictions”, *Polymers*, 12, 1700, 2020.
DOI:10.3390/polym12081700
-

- [58] Koo K. N., Lee I., “Dynamic behaviour of thick composite beams”, *Journal of reinforced plastic and composites*, 14, March 1995, pp. 196-210.